VOLUME 35 SEPTEMBER 1957 NUMBER 9

Canadian Journal of Physics

Published by THE NATIONAL RESEARCH COUNCIL
OTTAWA CANADA

CANADIAN JOURNAL OF PHYSICS

(Formerly Section A, Canadian Journal of Research)

Under the authority of the Chairman of the Committee of the Privy Council on Scientific and Industrial Research, the National Research Council issues THE CANADIAN JOURNAL OF PHYSICS and five other journals devoted to the publication, in English or French, of the results of original scientific research. Matters of general policy concerning these journals are the responsibility of a joint Editorial Board consisting of: members representing the National Research Council of Canada; the Editors of the Journals; and members representing the Royal Society of Canada and four other scientific societies.

Manuscripts for publication should be submitted to Dr. H. E. Duckworth, Editor, Canadian Journal of Physics, Hamilton College, McMaster University, Hamilton, Ontario.

(For instructions on preparation of copy, see **Notes to Contributors** (inside back cover).)

Proof, correspondence concerning proof, and orders for reprints should be sent to the Manager, Editorial Office (Research Journals), Division of Administration and Awards, National Research Council, Ottawa 2, Canada.

Subscriptions, renewals, requests for single or back numbers, and all remittances should be sent to Division of Administration and Awards, National Research Council, Ottawa 2, Canada. Remittances should be made payable to the Receiver General of Canada, credit National Research Council.

The journals published, frequency of publication, and prices are:

Canadian Journal of Biochemistry and Physiology	Monthly	$3.00 a year
Canadian Journal of Botany	Bimonthly	$4.00 a year
Canadian Journal of Chemistry	Monthly	$5.00 a year
Canadian Journal of Microbiology	Bimonthly	$3.00 a year
Canadian Journal of Physics	Monthly	$4.00 a year
Canadian Journal of Zoology	Bimonthly	$3.00 a year

The price of single numbers of all journals is 75 cents.

Canadian Journal of Physics

Issued by THE NATIONAL RESEARCH COUNCIL OF CANADA

VOLUME 35 SEPTEMBER 1957 NUMBER 9

THE PHOTOPROTONS EMITTED FROM CARBON AND NITROGEN NUCLEI[1]

D. L. LIVESEY[2]

ABSTRACT

The photoprotons from carbon have been studied by exposing propane gas to bremsstrahlung of maximum energy 35 Mev. and recording the charged particles produced in photographic plates. The energy distribution displays a peak near 6.0 Mev. which is related to the position of the dipole resonance in C^{12} nuclei. The angular distribution of protons near the peak energy agrees closely with a function $f(\theta) = A + B\sin^2\theta$, but at higher energies most of the protons are emitted at forward angles. Nitrogen gas has also been bombarded with bremsstrahlung of maximum energies 30 and 70 Mev. The energy distributions of the photoprotons are interpreted in terms of known reactions in the N^{14} nucleus.

1. INTRODUCTION

Several experiments have been performed to determine the energy distributions and angular distributions of protons emitted by nuclei bombarded by high energy bremsstrahlung. In a previous paper (Livesey 1956) the author has described the results obtained with apparatus containing oxygen gas at high pressure and employing photographic plates to record the tracks of the photoprotons from oxygen-16 nuclei. It was found that with bremsstrahlung of maximum energies 30 Mev. and 35 Mev. the proton energy distributions showed features explicable in terms of the electric-dipole resonance in oxygen near 22 Mev. Similar results may be expected with other light nuclei but in most cases the interpretation of data is less direct because the residual nucleus has several accessible levels in addition to the ground state. This paper describes the results obtained with the same apparatus as before containing propane gas or nitrogen instead of oxygen and bombarded with bremsstrahlung from the target of the 70 Mev. electron synchrotron at Queen's University. The photoprotons recorded were due chiefly to the following reactions:

$$\text{In propane:} \quad C^{12} + h\nu = H^1 + B^{11} - 16.0 \text{ Mev.},$$

$$\text{In nitrogen:} \quad N^{14} + h\nu = H^1 + C^{13} - 7.6 \text{ Mev.},$$

$$N^{14} + h\nu = n^1 + H^1 + C^{12} - 12.5 \text{ Mev.}$$

The details of the experimental procedure were in nearly all respects identical with those described in the paper on oxygen.

[1]Manuscript received May 28, 1957.
Contribution from the Department of Physics, Queen's University, Kingston, Ontario.
[2]Formerly National Research Council Postdoctorate Fellow. Present address: Oundle School, Oundle, Northants, England.

2. RESULTS WITH PROPANE

Previous experiments on the photoprotons emitted from carbon have been carried out with solid foils of graphite or polymerized hydrocarbons. Halpern, Mann, and Rothman (1952) used 23 Mev. bremsstrahlung and detected the protons above about 3 Mev. energy by a scintillation method. The angular distributions of these particles showed a peak near 80°. Later work by Cohen, Mann, Patton, Reibel, Stephens, and Winhold (1956) showed that the energy distribution has a broad maximum which is probably due to the electric-dipole resonance in carbon if most of the transitions leave B^{11} in its ground state. This maximum included subsidiary peaks at 5.1 and 6.0 Mev., of the same type as those shown by the photoprotons from oxygen, and possibly corresponding to discrete levels in C^{12} at 21.5 and 22.6 Mev.

The present experiment employed propane gas at a pressure of 2.2 atmospheres and bremsstrahlung of maximum energy 35 Mev. It differs from the Pennsylvania experiments chiefly in the higher photon energies, which give enhanced possibilities of protons other than those from the (γ, p) reaction being recorded, and in the use of a gas stopping-power for calculating corrections added to the observed ranges of protons in the photographic emulsion. In this work the most significant results were for protons of energies above 4.5 Mev., and a constant stopping-power of 2.2 for propane relative to air was adopted, this being deduced from Bragg's results quoted in Hirschfelder and Magee (1948). Two sets of plates were exposed simultaneously, one having 200 μ and the other 400 μ coatings, and the total X-ray dosage at the center of the apparatus was about 1200 roentgens.

After being processed by the method described by Dawson and Livesey (1956), the 200 μ plates were thoroughly scanned by one observer who measured 1600 tracks. The preliminary analysis showed that the proton energy distribution had a peak near 5.5 Mev. and extended as far as 12 Mev., although the theoretical maximum energy was about 17 Mev. Very few tracks were seen to go right through the emulsions, but in order to check the distribution at high energies a second observer measured 750 tracks in one of the 400 μ plates. Fig. 1 shows the final energy distribution of 1940 protons accepted as being within the correct range of dips in the plates and in the angular range 35° to 145°. The minimum energy recorded was 3.0 Mev. but data below 4.5 Mev. were rejected because protons at extreme angles were cut off in this region. In the diagram the distribution definitely rises from 4.5 Mev. to 5.5 Mev. and there is a broad peak centered at 6.0 Mev. Subsidiary peaks may occur at 5.3 and 6.0 Mev., in agreement with the Pennsylvania results, also at 6.7 Mev., corresponding to a discrete level in C^{12} at 23.3 Mev. The lack of adequate resolution of these peaks is presumably due to the presence of protons leaving B^{11} in excited states, and other protons from multiple reactions of the (γ, pn) type. At high energies the distribution of Fig. 1 falls uniformly except for a possible peak at 9.0 Mev., corresponding to photons of energy 25.8 ± 0.2 Mev. if these protons left B^{11} in the ground state.

The angular distributions of the protons were obtained by plotting the numbers observed in intervals of 10° divided by $\sin\theta$ to give ordinates pro-

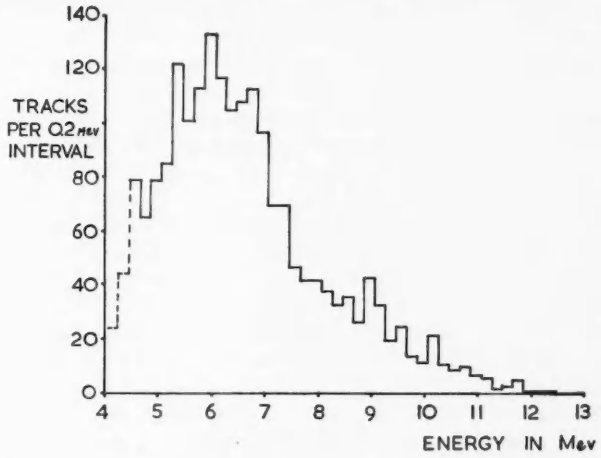

FIG. 1. Energy distribution of 1940 proton tracks from propane exposed to 35 Mev. bremsstrahlung.

portional to the differential cross-section per unit solid angle. At first the data were divided into several energy groups but the only significant differences were between those protons in the region around 6 Mev. and those at higher energies. Fig. 2 shows the results collected for two energy ranges

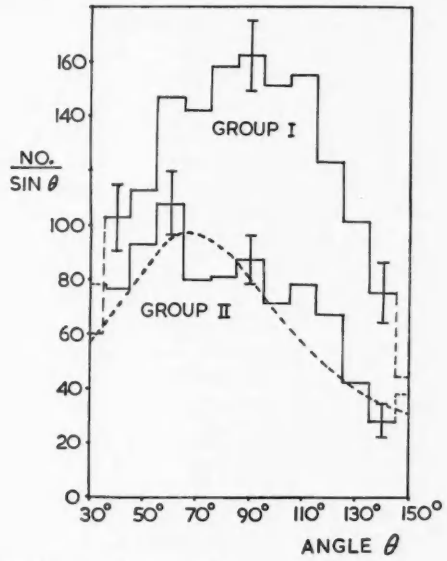

FIG. 2. Angular distributions of protons from propane in two energy groups: I, protons between 4.5 and 6.9 Mev.; II, protons above 6.9 Mev., with a dashed curve showing the function $f(\theta) = A + B(\sin\theta + p\sin\theta\cos\theta)^2$.

only: Group I (4.5 to 6.9 Mev.) and Group II (7.0 Mev. upwards), the latter including the small number of protons penetrating the 200 μ emulsions.

The angular distribution for Group II has a marked forward peak near 60° and the asymmetry is also shown by the fact that 370 protons were recorded in the angular range 35°–85° against 253 in the range 95°–145°. An attempt was made to fit the results by a function of the type:

$$f(\theta) = A + B(\sin\theta + p\sin\theta\cos\theta)^2,$$

with $A/B = 0.5$ and $p = 0.6$. This function gives the dotted line in Fig. 2 but no very close agreement is obtained.

The angular distribution for Group I protons in Fig. 2 is almost symmetrical about the 90° line, the actual numbers of protons recorded being 569 between 35° and 85° and 521 between 95° and 145°. The results were further treated by averaging the ordinates for supplementary angles and plotting these against $\sin^2\theta$, as is shown in Fig. 3. The straight line shows that the data agree with the function

$$f(\theta) = A + B\sin^2\theta,$$

where $A/B = 0.23$ with a probable error of ± 0.1.

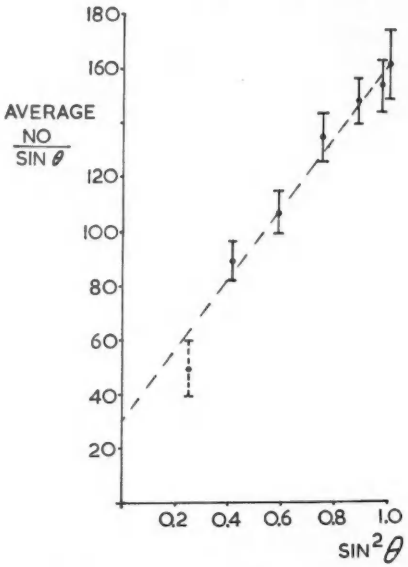

FIG. 3. Numbers of protons in Group I averaged over supplementary angles and plotted against $\sin^2\theta$.

3. RESULTS WITH NITROGEN

The behavior of nitrogen differs markedly from that of carbon and oxygen because of the low energy threshold for the (γ, p) reaction in N^{14} nuclei, and

the large number of ways in which protons can be emitted by incident photons exceeding 20 Mev. in energy. According to Horsley, Haslam, and Johns (1952) the electric-dipole resonance is near 22 Mev., while Ferguson, Halpern, Nathans, and Yergin (1954) found a large cross-section for the (γ, pn) reaction, comparable with the (γ, p) cross-section, near 22 Mev. This result was supported by the cloud-chamber experiments of Wright, Morrison, Reid, and Atkinson (1956), who also detected sharp peaks in the (γ, p) excitation function near 10 Mev. Apart from these latter experiments and those of Spicer (1953) very little work has been done on the photoprotons from nitrogen.

During the present experiments the camera was filled with nitrogen at various pressures and exposed to 70 Mev. bremsstrahlung several times to test the behavior of the apparatus. Later in the sequence a set of Ilford 200 μ plates was used in nitrogen at 6 atmospheres, and a long run was carried out with 30 Mev. bremsstrahlung, the total dosage being approximately 600 roentgens. The 30 Mev. plates were first examined by two observers working at the edges nearest the beam during exposure. The preliminary results showed a proton energy distribution extending from 5 Mev. at least as far as 11 Mev., and a large proportion of the longer tracks went right through the emulsion layers. In order to investigate the longer tracks the author scanned a large area on one plate near the far edge where the angles of dip were considerably reduced. Despite this change in procedure escape effects still curtailed the numbers of measurable tracks above 13 Mev.

The final energy distribution of 800 tracks measured in the 30 Mev. plates is shown in Fig. 4(A), which has not been corrected for the escape effects. A continuous distribution extends from 5 Mev. to 8 Mev. where there is a fairly sharp drop, followed by a broad peak between 10 and 11 Mev. At energies above 13 Mev. there is some evidence of another broad group, allowing for the rapidly-varying escape correction in this region. For comparison Fig. 4(B) is the energy distribution of 384 tracks measured in 70 Mev. plates, and this shows some similarity to Fig. 4(A) but with reduced resolution. In two of the 70 Mev. plates measurements were extended down to 2 Mev. but this led to no new results except the angular distribution shown in Fig. 5.

The interpretation of the nitrogen results given here is as follows:

(i) the (γ, p) reaction in N^{14} with a dipole resonance at 22.5 ± 0.5 Mev. gives rise to a proton group at 13.7 ± 0.5 Mev. when the residual nucleus is left in its ground state;

(ii) the excited states in C^{13} reported at 3.1, 3.7, and 3.9 Mev. (Ajzenberg and Lauritsen 1955) give rise to overlapping proton groups between 9.5 and 11.0 Mev.;

(iii) the (γ, pn) reaction, believed to be of major importance in the resonance region, yields protons of energies up to 8 Mev. but these are mixed with (γ, p) protons leaving C^{13} in highly-excited states.

If this interpretation is correct the numbers of protons in groups (i) and (ii) can be used to find the relative abundance of transitions to the ground state and excited states of C^{13}. In a typical plate 30 protons occurred in

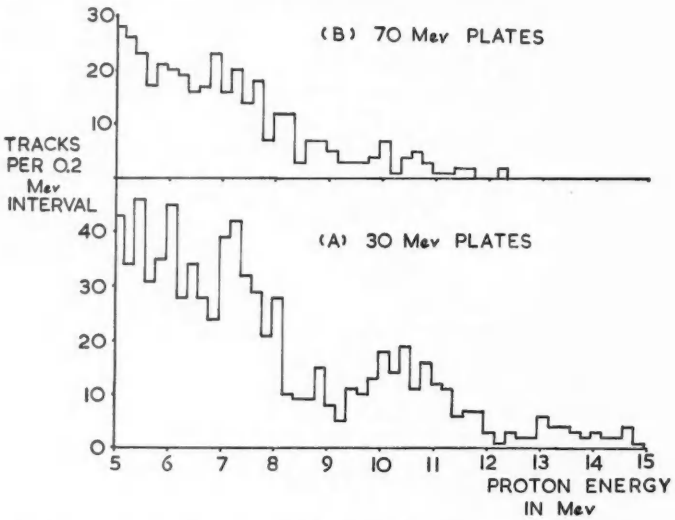

FIG. 4. (A) Energy distribution of 800 proton tracks from nitrogen exposed to 30 Mev. bremsstrahlung. (B) Distribution of 384 tracks in 70 Mev. nitrogen plates.

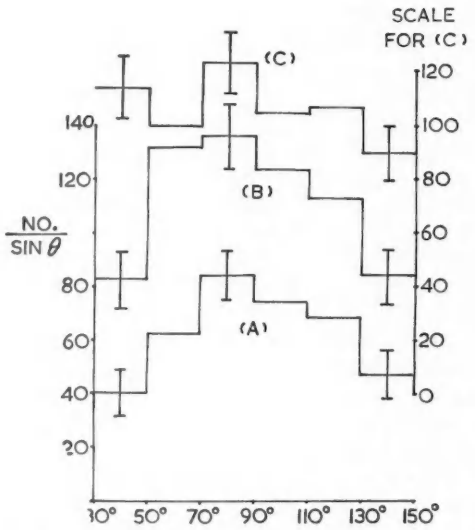

FIG. 5. Angular distributions of photoprotons from nitrogen. (A) Protons above 8.5 Mev. in 30 Mev. plates. (B) Protons between 5.0 and 8.5 Mev. in 30 Mev. plates. (C) Protons between 2.0 and 8.5 Mev. in 70 Mev. plates.

category (i) and 60 protons in (ii), while the fractions escaping in the two cases were 60% and 12% respectively. The true abundances of the two groups are therefore nearly equal.

We may also study the angular distributions of the observed protons, divided up in Fig. 5 so that (A) refers to protons above 8.5 Mev. in 30 Mev. plates, (B) to protons between 5.0 and 8.5 Mev. in 30 Mev. plates, and (C) to protons between 2.0 and 8.5 Mev. in the 70 Mev. plates. The data are grouped in 20° intervals in order to provide sufficient statistical accuracy in the ordinates. The distribution of Fig. 5(A) is essentially symmetrical about 90°, and is consistent with a function of the type $A+B\sin^2\theta$. The lower-energy protons of Fig. 5(B) also show a peak near 90°, but there is some slight forward asymmetry, and the data of Fig. 5(C) give a basically isotropic distribution.

4. DISCUSSION

The results available for carbon and nitrogen may be compared with those for oxygen to yield conclusions about the photodisintegration of these light nuclei. Although the nuclei C^{12}, N^{14}, and O^{16} have very different thresholds for photoproton emission, in all three cases the proton energy distribution includes a peak attributed to the electric-dipole resonance at 22 Mev., with protons leaving the residual nuclei in their ground states. In favorable cases it is possible to detect sharp peaks within the main resonance, and in C^{12} these probably correspond to photons of energies 21.8, 22.6, 23.3, and 25.8 Mev. These figures should agree with the "breaks" in (γ, n) yield curves determined by betatron experiments, but the proton experiments are limited in accuracy at present.

Angular distributions of photoprotons emitted by photons close to the main dipole resonance are in all cases anisotropic, symmetrical about the 90° line, and in agreement with a function of the type $f(\theta) = A+B\sin^2\theta$. At higher energies the protons show a markedly forward distribution, and efforts have been made to fit the data with a function representing a certain amount of electric-quadrupole interference with the main dipole term. Values obtained for the ratio A/B have been low, usually between 0.1 and 0.3. In the nitrogen results, low-energy protons showed a distribution essentially isotropic, and this is explicable on the grounds that these protons can be produced by several reactions and can leave the residual nuclei in many different states.

Estimates of the cross-sections for these processes are confined to partial cross-sections for transitions to the ground states of residual nuclei. The carbon results yield a value of 20 Mev-mb. for the integrated partial cross-section of the (γ, p) reaction for photons above 21 Mev. This agrees roughly with the oxygen results, but on the other hand the nitrogen data indicate that the partial cross-section for photons above 20 Mev. is very low, of the order of 2 Mev-mb., probably because of the larger number of excited states accessible in the residual nucleus C^{13}.

ACKNOWLEDGMENTS

I wish to thank Dr. B. W. Sargent for his continued interest and help with

these experiments, which formed part of the program at Queen's University supported by the Atomic Energy Control Board. Mrs. E. MacPhail carried out many of the microscope measurements and Mr. H. Janzen operated the synchrotron. Thanks are due to Dr. L. Katz and Dr. W. E. Stephens for discussions and correspondence.

REFERENCES

AJZENBERG, F. and LAURITSEN, T. 1955. Revs. Mod. Phys. **27**, 77.
COHEN, L., MANN, A. K., PATTON, B. J., REIBEL, K., STEPHENS, W. E., and WINHOLD, E. J. 1956. Phys. Rev. **104**, 108.
DAWSON, W. K. and LIVESEY, D. L. 1956. Can. J. Phys. **34**, 241.
FERGUSON, G. A., HALPERN, J., NATHANS, R., and YERGIN, P. F. 1954. Phys. Rev. **95**, 776.
HALPERN, J., MANN, A. K., and ROTHMAN, M. 1952. Phys. Rev. **87**, 164.
HIRSCHFELDER, J. O. and MAGEE, J. L. 1948. Phys. Rev. **73**, 207.
HORSLEY, R. J., HASLAM, R. N. H., and JOHNS, H. E. 1952. Can. J. Phys. **30**, 159.
LIVESEY, D. L. 1956. Can. J. Phys. **34**, 1022.
SPICER, B. M. 1953. Australian J. Phys. **6**, 391.
WRIGHT, I. F., MORRISON, D. R. O., REID, J. M., and ATKINSON, J. R. 1956. Proc. Phys. Soc. (London), A, **69**, 77.

MEASUREMENT OF THE COMPLEX DIELECTRIC CONSTANT OF LIQUIDS AT CENTIMETER AND MILLIMETER WAVELENGTHS[1]

A. G. Mungall and John Hart

ABSTRACT

The measurement of the complex dielectric constant of lossy liquids in the millimeter and centimeter wave region by a free-space technique is described. The method involves the measurement of absorption per wavelength and of reflectance at normal incidence. Families of curves are given for the relations between these two quantities and the real and imaginary parts of the complex dielectric constant. Results for ethyl and methyl alcohol at 9 and 13 mm. wavelength are compared with those obtained by waveguide techniques.

INTRODUCTION

The determination of the complex dielectric constant at wavelengths between 6 millimeters and 10 centimeters by the measurement of the standing-wave pattern set up in a waveguide terminated by a sample of the material being examined has been developed very successfully. These techniques, however, become more difficult and less accurate as the wavelength decreases, and 6 mm. seems to be almost the lower limit of their practicability.

Recent investigations (Poley 1955) have indicated that the frequency spectrum between 6 mm. and the long wavelength end of the far infrared may well yield further regions of dielectric absorption, especially for liquids such as the alcohols. With a view to extending our measurements to this region, we have developed a free-space technique of dielectric constant measurement the accuracy of which does not decrease with decreasing wavelength, which can be extended to far infrared wavelengths as generators become available.

This method is similar in principle to that used by Saxton and Lane (1946) in their measurements at 1.24 and 1.58 cm. of the refractive index, absorption coefficient, and dielectric constant of water, in that two sets of measurements, reflectance and absorption, are required. We have, however, carried out measurements at shorter wavelengths, simplified the experimental procedure, and developed a simple means of computing the complex dielectric constant from the experimental data. From the values of attenuation per wavelength and normal reflectance, the real and imaginary parts of the complex dielectric constant may be obtained directly from two sets of universal curves, given in this paper.

The purpose of this paper is to show that at even long wavelengths of 9 and 13 mm. where diffraction effects are troublesome, the method yields results comparable with those obtained by waveguide standing-wave techniques on lossy liquids such as methyl and ethyl alcohol, for which the real and imaginary permittivities are of about the same magnitude.

[1]Manuscript received April 12, 1957.
Contribution from the Division of Applied Physics, National Research Council, Ottawa, Canada.
Issued as N.R.C. No. 4430.

METHOD

The method involves two measurements:

1. The attenuation or absorption experienced by a wave travelling through the dielectric material being examined.

2. The reflectance at normal incidence of a wave entering an infinitely thick slab of the dielectric.

It can be shown (Von Hippel 1954) that the attenuation coefficient α of a plane electromagnetic wave of free-space wavelength λ_0 travelling through a dielectric material with complex dielectric constant k_e^*,

where $$k_e^* = k_e' - jk_e'',$$

is given by

$$\alpha = \frac{2\pi}{\lambda_0}\left[\frac{k_e'(1+\tan^2\delta)^{\frac{1}{2}}-1}{2}\right]^{\frac{1}{2}}, \tag{1}$$

where $\tan\delta = k_e''/k_e'$.

The attenuation coefficient α is defined by the usual expression for the time and distance variation of the electric field in the dielectric

$$E = E_0\, e^{j\omega t-(\alpha+j\beta)z},$$

where E_0 is the maximum value of the electric field, ω is the angular frequency, t is the time, z is the distance along the direction of propagation, and β is the propagation constant.

From the expression it is apparent that a determination of α for a particular dielectric at a wavelength λ_0 specifies a set of values of k_e' and k_e'', but not a unique pair.

Further information is required to specify this unique pair, and this may be obtained from the normal reflectance of an infinitely thick slab of the dielectric. Since the dielectrics in question are always lossy (we are interested in regions of absorption), in practice a slab of only a few millimeters thickness is required.

The expression for the ratio, r_0, between reflected field and incident field at normal incidence at a dielectric interface between infinitely thick dielectrics of intrinsic impedances Z_2 and Z_1 is well known, and is

$$r_0 = (Z_2-Z_1)/(Z_2+Z_1),$$

where Z_1 and Z_2 are related to the complex magnetic permeability μ^* and the complex electric permittivity ϵ^* by

$$Z = [\mu^*/\epsilon^*]^{\frac{1}{2}}.$$

At an air–dielectric interface, where μ^* is continuous and ϵ_{air}^* is assumed to be ϵ_0, r_0 reduces to

$$r_0 = \frac{1-(k_e'-jk_e'')^{\frac{1}{2}}}{1+(k_e'-jk_e'')^{\frac{1}{2}}}.$$

The ratio of reflected to incident power, R_0, can then be computed to be

$$R_0 = |r_0|^2 = \frac{(1-k_e)^2+4k_e \sin^2\delta/2}{(1+2\sqrt{k_e}.\cos\delta/2+k_e)^2}, \tag{2}$$

where $k_e^2 = k_e'^2+k_e''^2$.

This expression yields the further necessary information, another set of values of k_e' and k_e''. This, together with the first set from the transmission measurements, specifies a unique pair of values satisfying simultaneously both sets of experimental information.

In practice, since relative power measurements are usually expressed in terms of decibels, both α and R_0 are expressed in this manner. In Fig. 1, the attenuation coefficient α is shown as a function of k_e' for a number of values of k_e'', and is expressed in terms of decibels per free-space wavelength. This method is particularly appropriate to the mathematical form of α, yielding a set of curves independent of wavelength. In Fig. 2, the normal reflectance R_0, expressed in terms of decibels difference in intensity between reflected and incident wave, is also shown as a function of k_e' for a number of values of k_e''.

The determination of the complex dielectric constant is thus reduced to the measurement of two physical quantities quite accessible at any wavelength, the absorption loss per wavelength and the normal reflectance.

EXPERIMENTAL

Two sets of equipment are required, one for the absorption and one for the reflectance measurements.

I. Absorption Measurements

The absorption loss per wavelength is determined by measuring the transmission of a cell of continuously adjustable thickness, and plotting the cell loss in decibels as a function of the cell thickness. For thicknesses beyond which multiple reflections within the cell become unimportant, this plot is a straight line, the slope of which yields directly the attenuation in decibels per wavelength.

Fig. 3 shows the construction of the cell, the important elements of which are the thin (0.003 in.) mica windows, which absorb and reflect negligibly, and the millimeter thread for cell thickness adjustment. The diameter of the cell is 6 cm. The face of the right end of the cell is indexed so that fractions of a millimeter change of thickness are directly indicated. In the experimental setup this cell was placed over a hole of slightly smaller diameter in a metal baffle, and an approximately collimated beam of microwaves was passed through it; this beam was derived from a lens–horn combination which gave a negligible amount of stray radiation.

A typical plot of cell loss as a function of cell thickness is shown in Fig. 4, for ethyl alcohol at a wavelength of 1.3 cm. The effect of multiple internal reflections for small thicknesses is evident at the lower end of the graph, but the upper portion of the graph follows a straight line.

II. Reflectance Measurements

Since the measurement of reflectance at normal incidence implies placing

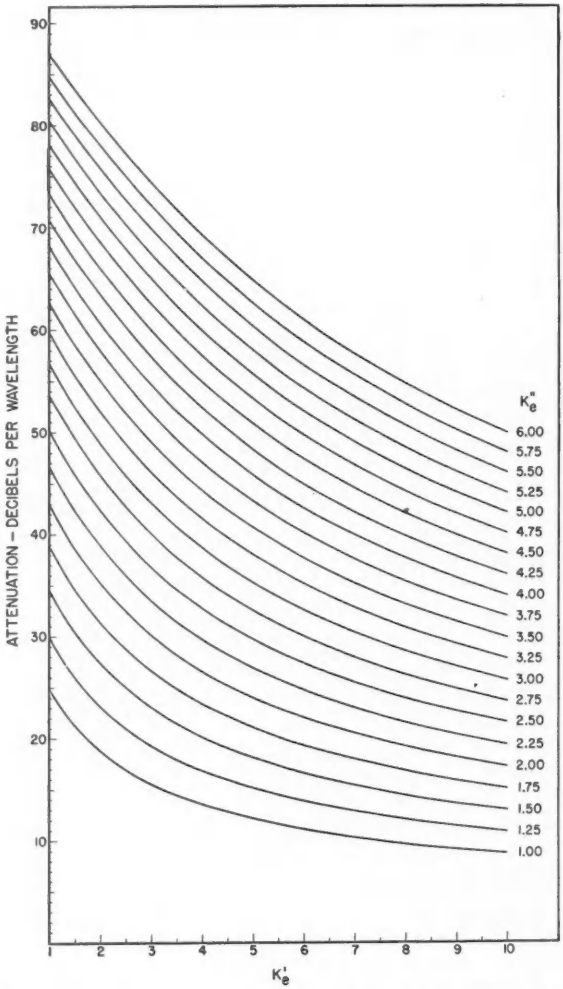

FIG. 1. The attenuation coefficient α as a function of k_e' for various values of k_e''.

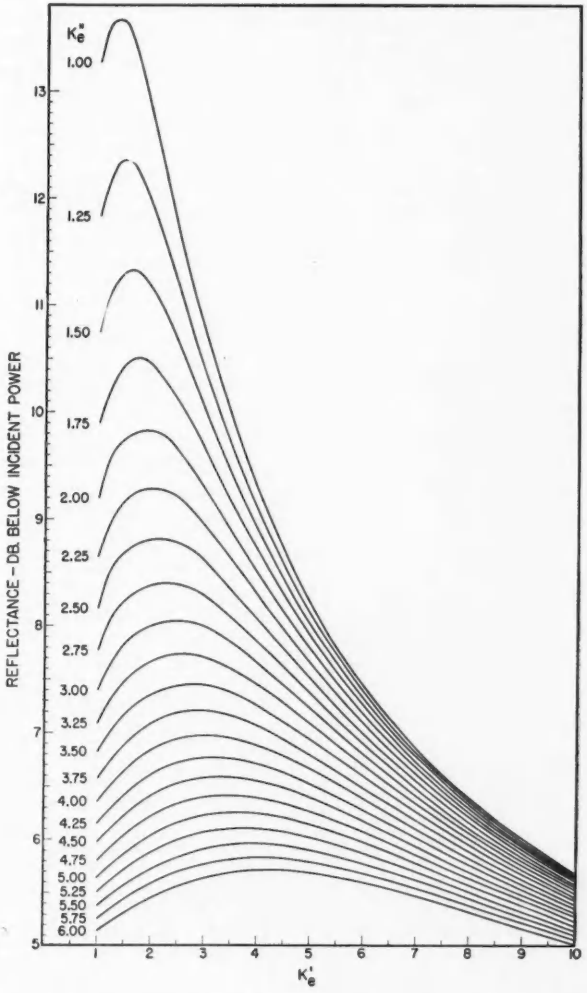

FIG. 2. Power loss on normal reflection as a function of k_e' for various values of k_e''.

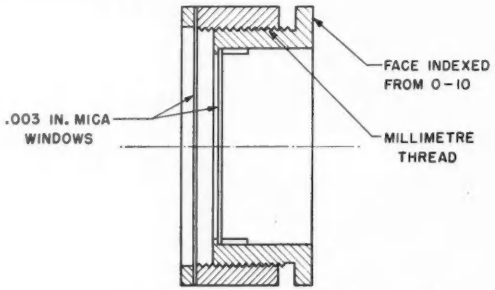

FIG. 3. The absorption cell.

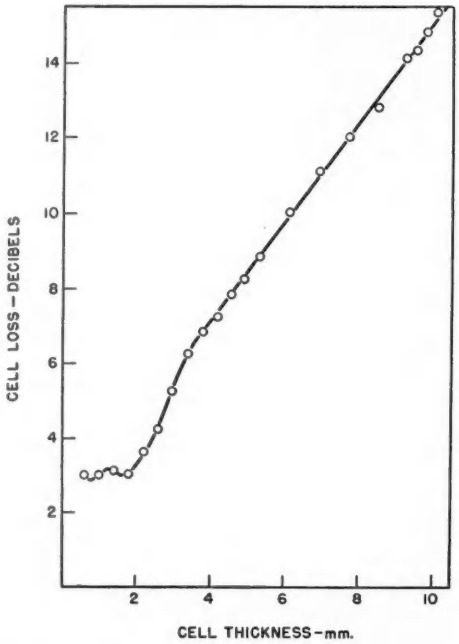

FIG. 4. Cell absorption as a function of cell thickness for ethyl alcohol at 1.3 cm. wavelength.

the source and detector both in the normal to the plane of the dielectric surface, direct measurement of the normal reflectance cannot be made by any simple method. Our solution of the problem was to build a goniometer to measure the reflected power over a range of angles as close to normal incidence as possible. The reflectance is plotted as a function of the angle of incidence, and the normal reflectance obtained by extrapolation. A typical

plot appears in Fig. 5, which shows the reflectance of methyl alcohol as a function of angle of incidence at a wavelength of 9.0 mm. The flatness of the curve indicates that errors incurred by such extrapolation are small.

It is apparent also from Fig. 5 that the precision of the reflectance measurements must be higher than that of the cell loss measurements, since a relatively small change of reflectance shifts the allowable values of k_e' and k_e'' (Fig. 2) appreciably. The reflectance was determined by comparison of the powers reflected specularly first by a level plane brass surface, and then by a tray filled to the same level with the liquid in question, the incident power being held constant during the procedure. The two specimens rested on a plate which moved on a pair of parallel level ways, so that first one and then the other could be moved into position beneath the transmitting and receiving horns. Both the standard reflector and the tray containing the liquid were about 17 cm. square, and were placed in identical positions for each measurement.

III. Determination of the Complex Dielectric Constant from the Reflection and Absorption Measurements

The sets of values of k_e' and k_e'' obtained from the two measurements described above are plotted and the point of intersection obtained. Fig. 6 shows such a plot for methyl alcohol at a wavelength of 9 mm. The points on each curve are obtained from Figs. 1 and 2. The figure shows that the slopes of the two curves at the point of intersection are such as to cause little uncertainty in the determination of the point.

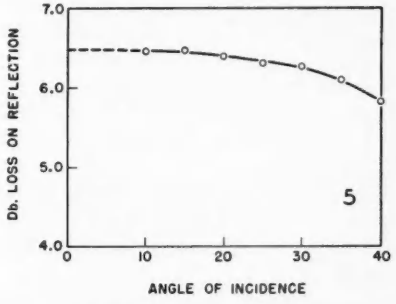

FIG. 5. Power loss on specular reflection as a function of angle of incidence for methyl alcohol at a wavelength of 9 mm.

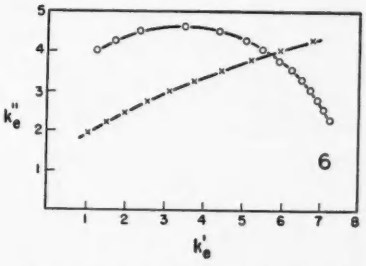

FIG. 6. Determination of the complex dielectric constant from the reflectance (circles) and absorption (crosses) data on methyl alcohol at 9 mm. wavelength.

DISCUSSION

The method outlined above was tested by applying it to both methyl and ethyl alcohol at wavelengths of 9 mm. and 1.3 cm. Table I shows these values in comparison with those obtained by waveguide techniques (Poley 1955; Lane and Saxton 1952), all measurements being taken at room temperature.

From these tables it is apparent that our values are in agreement with

those quoted in the literature. Comparable deviations in the results exist in both the waveguide standing-wave techniques and our free-space method.

TABLE I

	Methyl alcohol		Ethyl alcohol		
λ_0	k_e'	k_e''	k_e'	k_e''	Source
1.3 cm.	7.1	4.3	4.4	1.4	Ours
1.25 cm.	5.98	4.48	4.13	1.42	Poley
1.24 cm.	6.88	4.76	4.23	1.56	Lane and Saxton
9.0 mm.	5.7	3.9	3.8	1.25	Ours
8.0 mm.	5.68	3.23	3.89	1.30	Poley
6.2 mm.	6.04	3.15	3.47	1.11	Lane and Saxton

As with any free-space technique using finite apertures there is the problem of accounting for diffraction effects. Errors due to diffraction can be greatly reduced by at least two methods. First, the apertures of the system may be increased so that variations of power in the diffraction pattern in the vicinity of the receiving horn are small enough that movement of the apertures results in negligible variations in the total power received by the horn. Second, if this cannot be done, the apparatus must be so arranged that any alteration of the system during measurements does not shift the diffraction pattern with respect to the receiving horn. The first method was applied in the reflectance measurements by making both the standard reflector and the tray containing the liquid sufficiently wide that no measurable change in reflected power occurred as a result of the lateral movement of the reflecting surface through several wavelengths. In the absorption measurements it was, of course, necessary to alter the thickness of the cell during measurements, and this required the movement of one of the cell apertures. When the cell was empty, with both mica windows removed, this movement resulted in a noticeable periodic variation of power in the receiving horn, which was interpreted as a shift of the diffraction pattern. Placing a tubular baffle in front of the receiving horn greatly reduced this power variation; from this we inferred that over the normal range of cell adjustment, the diffraction pattern at the mouth of the horn did not alter appreciably.

Direct transmission between the two horns in the reflectance measurements, discussed in some detail by Saxton and Lane (1946), was much reduced in our case by the use of collimating lenses over each horn.

The relative power measurements were carried out by means of precision attenuators, calibrated at both frequencies used by comparison with a precision audio-attenuator. In all calibrations, the microwave detecting element was a bolometer, operated only in its square-law region. All sets of data were self-consistent within 0.2 db.

Even at centimeter wavelengths, where diffraction effects are troublesome, it is apparent that free-space methods of measurement of the dielectric constant yield results of about the same validity as do the more-established standing-

wave techniques, and for shorter wavelengths, it seems that they will be preferable.

REFERENCES

LANE, J. A. and SAXTON, J. A. 1952. Proc. Roy. Soc. A, **213**, 400.
POLEY, J. Ph. 1955. Appl. Sci. Research, B, **4**, 337.
SAXTON, J. A. and LANE, J. A. 1946. Meteorological factors in radio-wave propagation (The Physical Society, London), p. 278.
VON HIPPEL, A. R. 1954. Dielectrics and waves (John Wiley and Sons, Inc., New York), p. 28.

THE VARIATION WITH SIDEREAL TIME OF RADIO STAR SCINTILLATION RATES[1]

G. C. Reid

ABSTRACT

Long-term analysis of the scintillation rate of the radio star Cassiopeia A at a frequency of 50 Mc./s. has been carried out using data obtained at Ottawa and Saskatoon. It is found that the variation of scintillation rate with sidereal time can be explained by assuming the ionospheric irregularities responsible for the scintillations to be greatly extended along the direction of the earth's magnetic field, and to have a drift motion whose average direction appears to be around an axis passing through the earth's dip-pole.

INTRODUCTION

Continuous recording of the 50 Mc./s. radiation from the intense radio star Cassiopeia A has been carried out at the Radio Physics Laboratory near Ottawa since September, 1953. Results obtained with the original version of the equipment, consisting of a phase-switching interferometer employing two spaced folded-dipole antennas, have been described by Hartz (1955). Several improvements have been made in the equipment, including the substitution of three-element Yagi antennas for the original folded dipoles, and these have resulted in increased over-all sensitivity without decreasing the length of time during which the source is observable. The time-constant of the equipment has also been reduced from 1 minute to about 6 seconds, permitting the recording of more rapid fluctuations in the received signal strength. The second version of the equipment has been in almost continuous operation since July, 1955.

Equipment of a similar type, employing a 2-second time-constant, has been constructed at the University of Saskatchewan, and has been in operation continuously at Saskatoon for a period of over 2 years. The author is deeply indebted to the operators of the Saskatoon equipment for supplying their raw data on which much of the analysis in this paper is based.

The purpose of the paper is to present the results obtained from recordings over a period of 1 year, and to discuss the bearing of these results on our knowledge of the mechanism responsible for the scintillations.

ANALYSIS OF RECORDS

The equipment design is such that any localized source of 50 Mc./s. radiation moving through the antenna lobes will produce a sinusoidal trace on a pen recorder, the amplitude of the sinusoid being proportional to the received signal. The typical pattern produced by the Cassiopeia source is shown in Fig. 1. The strong radio source in Cygnus produces a sinusoid of different period which can be observed occasionally when the Cassiopeia source passes through a region of minimum antenna sensitivity. The amplitude of this

[1]Manuscript received May 1, 1957.
Contribution from the Defence Research Telecommunications Establishment, Ottawa, Canada. Work performed under Defence Research Board project number D-48-28-01-02.

signal is very low, however, owing both to the decreased sensitivity of the antennas in the direction of the Cygnus orbit and to the fact that the source is intrinsically weaker than Cassiopeia A. A more serious source of interference comes from occasional solar noise storms which can distort or completely obscure the Cassiopeia signal. Usually, such storms can easily be recognized from their characteristic forms, and the corresponding recordings rejected. The 50 Mc./s. radiation from the quiet sun cannot be detected.

Routine analysis of the scintillation records is carried out by assigning to each hour two indices, one representing the average scintillation amplitude during the hour (i.e. a measure of the ratio of the r.m.s. deviation of the amplitude to the mean amplitude of the signal), and one representing the average scintillation rate during the hour (i.e. the number of peaks per minute). In this paper we shall be concerned only with variation of the scintillation rate index, which can take values from 0 to 4. Index 0 means that no appreciable scintillation appeared during that hour, and the other indices are chosen in such a way that rapid analysis is possible merely by inspection of the records. Very roughly, index 4 is assigned when the time interval between fading peaks is $\frac{2}{3}$ minute or less, and indices 3 and 2 correspond respectively to intervals of about 1 and $1\frac{1}{2}$ minutes.

Typical examples of the scintillation rate indices are shown in Fig. 1.

RESULTS OF ANALYSIS

In this discussion we shall be concerned mainly with the time variation of the scintillation rate index. It can be seen that two effects can contribute to this variation, since the scintillation rate may depend both on time of day (solar time variation) and on position of the source in the sky as seen by the receiving antennas (sidereal time variation).

At the latitudes of Ottawa and Saskatoon (45° 23′ N. and 52° 07′ N. respectively) the radio star Cassiopeia A is circumpolar, reaching a minimum elevation above the horizon of 13° 57′ at Ottawa and 20° 39′ at Saskatoon. Since the beamwidth of the antennas is sufficient to include the entire orbit, recording is possible 24 hours per day. In order to separate completely the solar and sidereal time variations, at least one year of continuous recording is necessary, since during the course of a year the star will have occupied each point on its orbit at all times of the solar day. The solar time variation can then be eliminated by using the whole year's data for each sidereal hour.

One method of carrying out the analysis would be simply to sum all the indices for each particular hour of the day, and plot the sums as a function of time. This procedure might give valid results if all the index assignments were carried out by one observer, but it has been found that two observers analyzing the same records will frequently differ in their results, particularly in the assignment of indices 3 and 4. As these indices have the greatest weight in a simple addition, intercomparison of results between two stations would be seriously affected. Differences in individual record analysis will have a much smaller effect if the indices are divided into two groups, corresponding to slow scintillation (indices 0, 1, 2) and fast scintillation (indices 3, 4). The

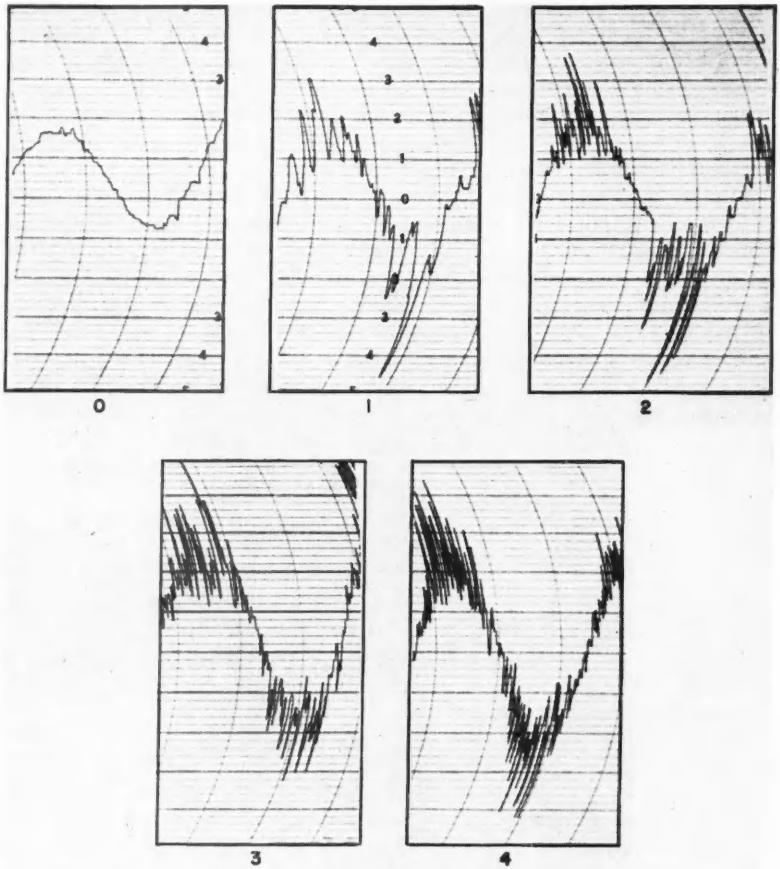

FIG. 1. Typical examples of the scintillation rate indices assigned to the Ottawa records. The spacing between vertical curved lines represents 15 minutes.

weighting effect of the large indices is now eliminated and the only important difference in analysis occurs in the assignment of indices 2 and 3. In practice, these are much more readily distinguishable than are indices 3 and 4.

This type of procedure has been carried out for the Ottawa data from August, 1955, to August, 1956, and for the Saskatoon data from April, 1955, to April, 1956. In Figs. 2 and 3 the percentages of occurrence of indices 3 and 4 are plotted as a function of sidereal time measured from the time of upper transit of Cassiopeia A at the station. It can be seen that the scintillation rate is fairly low when the source is near upper transit and high in the sky, and increases as the source approaches the horizon, reaching a maximum around the time of lower transit. In the case of the Ottawa data the increase

in rate after upper transit is fairly steady, and the curve is quite symmetrical about the time of lower transit. At Saskatoon, however, the scintillation rate appears to fall after upper transit, reaching a minimum at about $4\frac{1}{2}$ hours, and the curve is symmetrical about a time of 1 hour after lower transit. In what follows an explanation of these features of the two curves is proposed by making certain assumptions as to the nature and motion of the ionospheric irregularities responsible for scintillation.

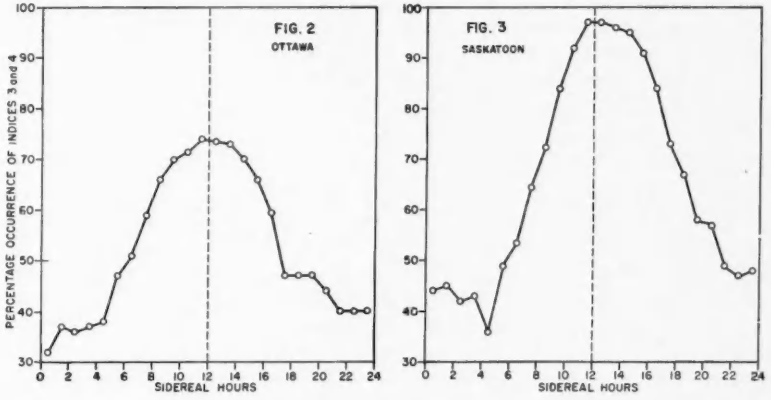

FIG. 2. Percentage occurrence of indices 3 and 4 at Ottawa, August, 1955, to August, 1956. The vertical dotted line indicates the time of lower transit of the source.
FIG. 3. Percentage occurrence of indices 3 and 4 at Saskatoon, April, 1955, to April, 1956.

THEORY OF SIDEREAL VARIATION

The nature, location, and cause of the atmospheric irregularities responsible for radio star scintillations are not yet fully known, although certain of their characteristics have been deduced from previous evidence. It must be pointed out, however, that deductions made from data covering only a limited period of time and secured at one geographical location cannot immediately be assumed to apply to all times and locations. The properties of the upper atmosphere are known to vary widely with both geographic and geomagnetic location, and with time, particularly with reference to the sunspot cycle.

Scintillation phenomena tend to show rather more correlation with the behavior of the F2 layer than with that of any other atmospheric region, and accordingly the irregularities have been assumed for the most part to lie in the uppermost reaches of the ionosphere. Hewish (1952) has shown that by assuming that the scintillations are caused by a thin diffracting screen, fair agreement can be obtained between theory and observation if the height of the screen is taken as approximately 400 km. This region of the ionosphere is not normally accessible to sounding techniques. The fairly high correlation found by various workers between scintillation rate and geomagnetic disturbance may be additional evidence for the great height of the scintillating

region, since the F2 region is more strongly influenced by the geomagnetic field than other ionospheric regions. In the present work a tentative height of 350 km. has been assumed, although it will be seen that the results are very little changed by adopting another value. It has also been assumed that the scintillation is caused by the drift of the irregularities across the line of sight between the observer and the source rather than by rapid changes in electron density in a static ionosphere. This fact has been fairly well established by observations taken by Hewish (1952) at two points separated by a few kilometers. A similar pattern is seen at both points, individual peaks being slightly displaced in time, indicating a drift of the irregularities along the line joining the two points.

A great deal of evidence has been accumulated recently showing that ionospheric irregularities tend to be elongated along the direction of the earth's local magnetic field, sometimes to a very marked degree (Peterson 1955; Phillips and Spencer 1955; Spencer 1955). This result might be expected from the fact that at ionospheric heights the ratio of collisional frequency to gyro-frequency for electrons is such that motion along the direction of the field is much more likely than motion across the field lines. Consequently, once an irregular patch of ionization is formed, the electrons will tend to diffuse along the direction of the field, and the patch will become elongated in this direction. We shall assume here that all the scintillation is due to irregularities which are greatly extended along the direction of the field, and attempt to explain the shape of the curves in Figs. 2 and 3 by a simple theory of their motion.

The observed scintillation rate must be proportional, among other things, to the number of irregularities encountered by the radiation in its passage through the ionosphere. If the irregularities are randomly scattered within a defined region, this number is simply proportional to t, the path-length of the ray from the star through this region. t can be shown to be given by

$$t = [(R+h_1)^2 - R^2\sin^2\phi]^{\frac{1}{2}} - [(R+h_2)^2 - R^2\sin^2\phi]^{\frac{1}{2}}, \tag{1}$$

where R is the radius of the earth, h_1 and h_2 are the limiting heights of the region containing the irregularities, and ϕ is the zenith angle of the star as seen by the observer. The zenith angle, ϕ, can be computed in terms of the hour-angle, H, after upper transit by the formula given by Spencer (1955):

$$\cos\phi = \sin\lambda\sin\delta + \cos\lambda\cos\delta\cos H, \tag{2}$$

where λ and δ are the observer's latitude and the declination of the star respectively.

Assuming the layer in question to lie between 300 and 400 km. above the earth's surface, the sidereal variations of t at Ottawa and Saskatoon have been computed, and are shown in Figs. 4 and 5, normalized in such a way that the maxima coincide with the maxima in Figs. 2 and 3 respectively. Comparison of Figs. 2 and 4 and of Figs. 3 and 5 shows a certain amount of agreement, particularly in the case of the Ottawa data. The path-length curves, however, are necessarily symmetrical about the time of lower transit, while

the Saskatoon experimental data show a marked degree of asymmetry which must be explained by some additional factor. The choice of different levels in defining the region of irregularities changes the curves by an amount which becomes appreciable only near the lower transit point. It has been found that the choice of the layer between 300 km. and 400 km. gives a better fit to the experimental data than the choice of a lower region, such as that defined by the 200 km. and 100 km. levels.

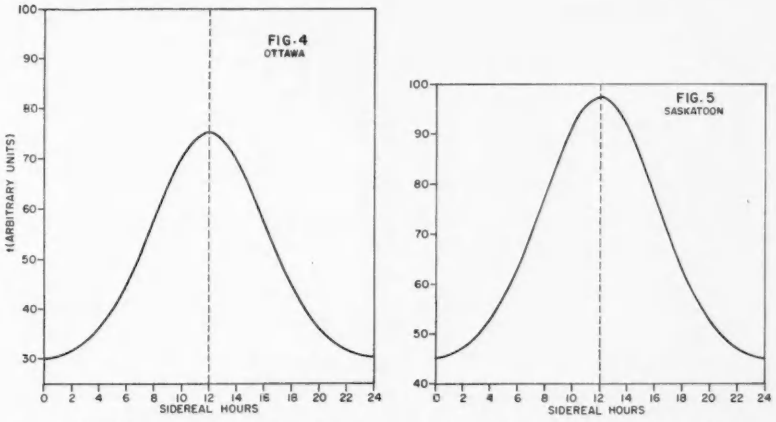

FIG. 4. Variation with sidereal time of the atmospheric path-length between 400 and 300 km. heights of radiation received at Ottawa.

FIG. 5. Variation with sidereal time of the atmospheric path-length between 400 and 300 km. heights of radiation received at Saskatoon.

The radiation from the star will cast a "shadow" of the ionospheric irregularities on the ground, and the drift motion of this ground pattern past the receiving antennas produces the observed scintillation. The velocity and direction of motion of the ground pattern is the second major factor which must be considered in any explanation of the time variation of scintillation rate.

If we assume that the irregularities are greatly extended along the direction of the earth's local magnetic field, the ground pattern will have a major axis lying in the direction of the "shadow" of the lines of force of the earth's field in the neighborhood of the 350 km. region. The angle between this major axis and geographic north at the point of observation can be calculated as a function of sidereal time by considering Fig. 6, in which a flat earth has been assumed for simplicity.

The line AB represents a segment of a line of force of the geomagnetic field between the heights h and h' above the earth. The line OP is the projection of AB on the ground by parallel rays from the infinitely distant source, and is inclined to the northerly direction (the y-axis) at an angle α. The source has zenith angle ϕ and azimuth θ as seen by an observer at O, both θ and α being measured positively to the east of north and negatively to the west.

The direction cosines of the line of force and of the rays from the source with respect to the coordinate axes shown are given respectively by $(V/F, N/F, E/F)$ and $(-\cos\phi, \sin\phi\cos\theta, \sin\phi\sin\theta)$, where V, N, E, and F are

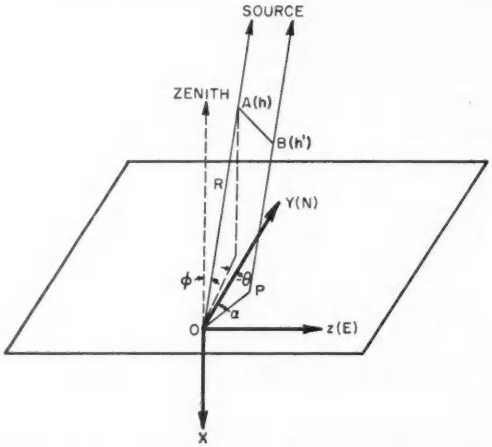

FIG. 6. Ground pattern cast by irregularities. The line AB represents a segment of a line of force of the earth's magnetic field between heights h and h'. OP is the shadow cast by an irregularity lying along this segment.

respectively the vertical, northerly, and easterly field components and the total field strength. Using these values and the coordinates of points A and B, it can be shown that the point P has coordinates given by

$$x = 0,$$
$$y = (h-h')(\tan\phi\cos\theta + N/V),$$
$$z = (h-h')(\tan\phi\sin\theta + E/V),$$

and hence the angle α is given by the expression

$$\tan\alpha = (\tan\phi\sin\theta + E/V)/(\tan\phi\cos\theta + N/V). \tag{3}$$

Thus the orientation of the ground pattern with respect to north can be computed for any zenith angle and azimuth of the source, knowing the three components of the earth's magnetic field in the neighborhood of the irregularities.

According to Mitra (1948) the difference between the magnetic field at ground level and that in the F region is not more than 10%, and in the following analysis ground level values have been used without applying any correction. Fig. 7 shows the loci of the points on the earth's surface below the points where rays observed at Ottawa and Saskatoon meet the 350 km. level. The loci are seen to be approximate ellipses covering quite a large area. Values of the components of the earth's field in the neighborhood of the irregularities have been found by plotting these ellipses on maps showing

the variation of V, N, and the magnetic declination D (E is given by $\tan D = E/N$). The zenith angle, ϕ, of the source can be computed from equation (2) in terms of the hour-angle after upper transit, and it can be shown that the azimuth angle θ is given by

$$\sin \theta = -\cos \delta \sin H / \sin \phi, \tag{4}$$

where the notation is the same as in equation (2). The angle θ is positive if measured to eastward of north, and negative if measured westward.

FIG. 7. Map showing loci of points on the earth's surface below the points where the radiation from Cassiopeia A intersects the 350 km. level of the ionosphere.

Substitution of the values of θ, ϕ, E, N, and V in equation (3) yields values of α as a function of sidereal time after upper transit at the two stations. Values of α obtained in this way are shown in Fig. 8. The direction of the major axis of the ground pattern is seen to oscillate back and forth about the north–south direction as the star moves around the pole.

If now we assume that the observed scintillation effects are produced by the drift of this pattern across the ground, we have to consider how the direction of motion will affect the observed scintillation rate. Since we have assumed the individual shadows to be very greatly elongated along one axis, it is obvious that any drift motion along the direction of this axis will not be detectable, and hence we can assume that the observed scintillation rate will be proportional to the component of the drift lying along the minor axis of the ground pattern. If the drift is in an east–west direction, then the scintillation rate will be proportional to $t \cos \alpha$, where t is a factor representing

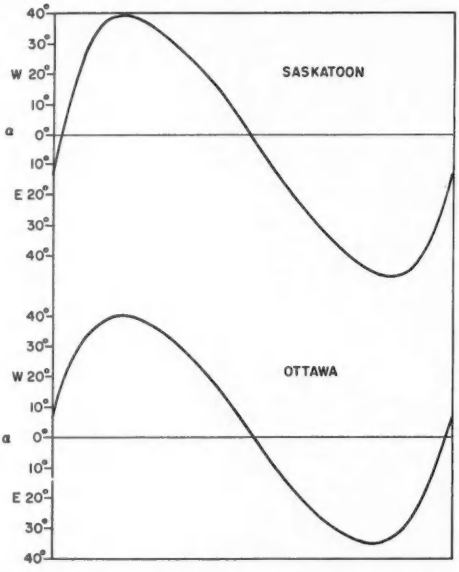

FIG. 8. Variation with sidereal time of the angle α between the major axis of the ground pattern and geographic north. The horizontal scale represents the time between successive upper transits of the source at the two stations.

the number of irregularities encountered in passing through the ionosphere, i.e. t is proportional to the ionospheric thickness in the line of sight. If the drift is predominantly north–south, the rate should be proportional to $t \sin \alpha$. If the drift is along a direction inclined at angle β to the north–south direction, β being measured positively to the east of north, simple geometrical considerations show that the scintillation rate would be expected to be proportional to $t \sin(\beta - \alpha)$.

This function has been computed for various values of β for both Saskatoon and Ottawa, using the values for t plotted in Figs. 4 and 5. The results are shown in Figs. 9 and 10.

DISCUSSION OF RESULTS

Comparison of Figs. 3 and 10 indicates that the true value of β for Saskatoon lies somewhere between $-60°$ and $-90°$. In Fig. 11 the experimental points are shown superimposed on the curve of $t \sin(\beta - \alpha)$ for $\beta = -75°$, the value which was found to give the best fit. The slight flattening which is apparent near the maximum of the experimental points indicates that some form of saturation may be taking place in the assignment of indices. This is quite conceivable, since the maximum possible experimental percentage is 100, and a measured value of 97 might indicate a 3% error in index assignment, a figure which is remarkably low considering the relatively crude method of

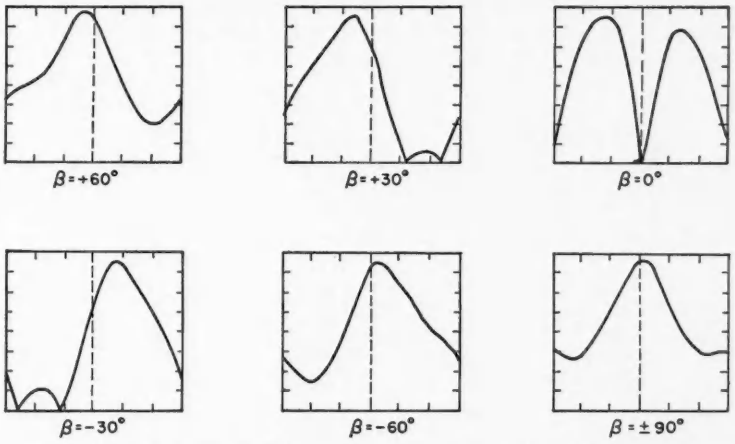

FIG. 9. Variation with sidereal time of $t \sin(\beta-\alpha)$ at Ottawa for selected values of β. In both Figs. 9 and 10 the horizontal scale is one sidereal day in length and the vertical scale, in arbitrary units, is the same for both. The vertical dashed line indicates the time of lower transit.

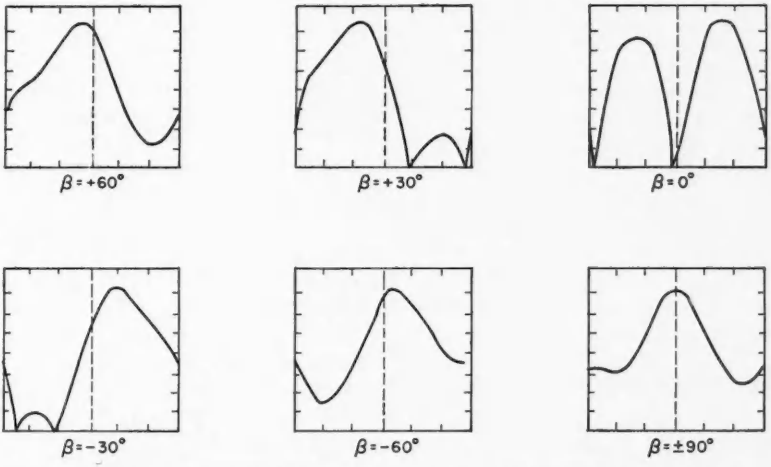

FIG. 10. Variation with sidereal time of $t \sin(\beta-\alpha)$ at Saskatoon for selected values of β.

analysis. The theoretical curve in Fig. 11 has been normalized to fit the experimental data in the neighborhood of 75% and all values greater than 97 have been reduced to 97.

The agreement between the curve and the experimental points is seen to be fairly good, implying that the Saskatoon results can be explained by assuming that the irregularities are greatly extended along the direction of

the geomagnetic field, and that their average drift over a period of 1 year is in a direction 15° north of west, or south of east. (Directly opposed directions of drift cannot be distinguished.)

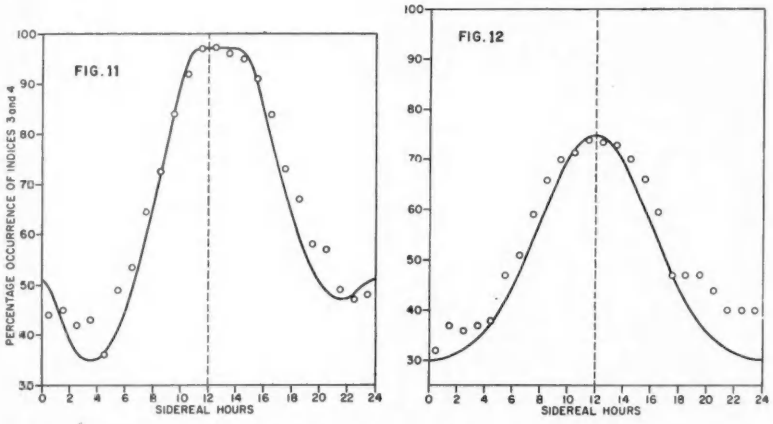

FIG. 11. Experimental data for Saskatoon superposed on curve of $t \sin(\beta - \alpha)$ for $\beta = -75°$.
FIG. 12. Experimental data for Ottawa superposed on a curve of path-length between the 400 and 300 km. levels. The curve has been normalized to fit the data near the maximum.

Comparison of Figs. 2 and 9 shows that the detailed agreement between theoretical and experimental curves is not quite as good for the Ottawa data. The curve of path-length alone (Fig. 4) gives a much better fit to the data than any of the curves of Fig. 9. This is illustrated in Fig. 12, where the experimental data for Ottawa are shown together with the curve of path-length between the 400 and 300 km. levels, normalized to fit the experimental data at the maximum. The agreement is seen to be quite close, though the fact that most of the points lie above the curve indicates that a slight saturation effect may be taking place near the maximum, with normalization at about 50% giving a closer over-all fit.

The conclusion to be drawn from this is that in the case of the Ottawa data the number of irregularities encountered plays a more important part in determining the observed scintillation rate than does their direction of motion. It must be pointed out, however, that any analysis of fading-rate data may be critically dependent on the effective time-constant of the equipment, since finer detail will become apparent as the time-constant is shortened. Throughout the period under discussion the time-constants employed at Ottawa and Saskatoon were respectively 6 seconds and 2 seconds, so that the Saskatoon data would be expected to yield a better picture of events than would the Ottawa data.

In order to test this hypothesis the Ottawa time-constant was changed to 1.5 seconds in October, 1956, and preliminary analysis of the data obtained between October 4, 1956, and January 18, 1957, indicates an average drift in

a direction inclined at 20° south of west (or north of east). This is illustrated in Fig. 13, where the observed percentages of indices 3 and 4 are plotted as a function of sidereal time after upper transit of the source, together with the computed curve for $\beta = +70°$.

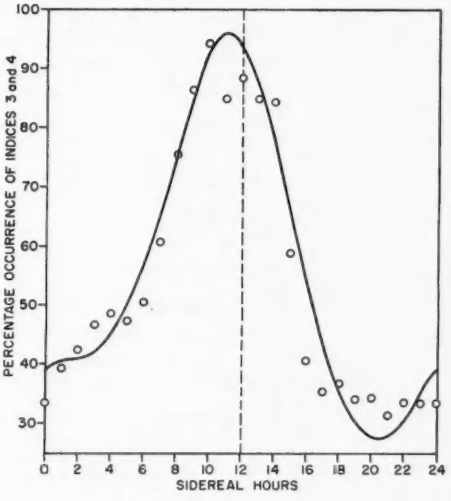

FIG. 13. Preliminary fast time-constant data for Ottawa (October, 1956, to January, 1957) superposed on curve of $t \sin(\beta - \alpha)$ for $\beta = +70°$.

While these results can be regarded only as preliminary, it is interesting to note that both at Saskatoon and Ottawa the average direction of drift is roughly at right angles to the direction of the horizontal component of the local geomagnetic field. Perpendiculars drawn to the directions of drift at the two stations have been found to intersect in a point having approximate geographic coordinates of 70° N., 97° W. This point is very close to the dip-pole of the earth's magnetic field, a fact which would appear to indicate an average drift of the irregularities around this pole. Confirmation of this result will await the collection of data from other stations, particularly those having a greater local magnetic declination than does either Ottawa or Saskatoon.

It should be pointed out that this technique can yield only a limited amount of information about ionospheric drifts, in that only the average line of drift over a fairly long period of time can be found. The average magnitude of the velocity cannot be determined and there is an ambiguity in the direction of drift along the specified line. The method does have the advantage, however, that motion in any direction can be detected, while the conventional spaced-receiver type of experiment gives direct information only on the velocity component at right angles to the direction of elongation.

CONCLUSIONS

Data concerning the rate of scintillation of the circumpolar radio star Cassiopeia A observed at Saskatoon using a 2-second time-constant and at Ottawa using a 6-second time-constant have been examined over a period of 1 year. While the dependence on sidereal time at Ottawa could be explained simply in terms of path-length through the ionosphere the Saskatoon results can be explained only by assuming that the irregularities causing the scintillation are greatly elongated along the direction of the earth's magnetic field, and have a general drift motion along a direction inclined at 15° north of west or south of east.

Preliminary data obtained at Ottawa over a period of $3\frac{1}{2}$ months using a time-constant of 1.5 seconds give evidence of a general drift in a direction about 20° south of west or north of east. These results appear to favor an average drift of the irregularities around the dip-pole.

ACKNOWLEDGMENTS

The author wishes to express his deep indebtedness to Mr. C. H. Costain and Mr. H. Grigg of the University of Saskatchewan, who very kindly supplied the raw data obtained from the Saskatoon equipment, and to Mr. T. R. Hartz, Mr. W. A. Sharf, and Mr. W. E. Mather for design, construction, and maintenance of the Ottawa equipment.

The author is also indebted to Mr. T. R. Hartz for much valuable discussion and advice, and to Dr. P. A. Forsyth for his continued interest in and encouragement of the project.

REFERENCES

HARTZ, T. R. 1955. Can. J. Phys. **33**, 476.
HEWISH, A. 1952. Proc. Roy. Soc. A, **214**, 494.
MITRA, S. K. 1948. The upper atmosphere (Royal Asiatic Society of Bengal).
PETERSON, A. M., VILLARD, O. G., LEADABRAND, R. L., and GALLAGHER, P. B. 1955. J. Geophys. Research, **60**, 497.
PHILLIPS, G. J. and SPENCER, M. 1955. Proc. Phys. Soc. (London), B, **68**, 481.
SPENCER, M. 1955. Proc. Phys. Soc. (London), B, **68**, 493.

A PROPOSED β-DECAY INTERACTION[1]

M. A. PRESTON

ABSTRACT

It is shown that one can retain the two-component neutrino theory and time reversal with scalar and tensor interactions in the β-decay Hamiltonian, if one postulates that the scalar term produces neutrino emission and the tensor term antineutrino emission. This is consistent with all present experimental data.

It has been pointed out (for example by Wu and Lee at the Rochester Conference, 1957, and in Ambler *et al.* 1957) that the results on the angular distribution of positrons from aligned Co^{58} nuclei (Ambler *et al.* 1957; Postma *et al.* 1957) present serious difficulties for the two-state neutrino theory if one preserves invariance under time reversal. The nature of this difficulty can be expressed in the following way. Let $C_{GT}^2 = |C_T|^2+|C_A|^2+|C_T'|^2+|C_A'|^2$, $C_F^2 = |C_S|^2+|C_V|^2+|C_S'|^2+|C_V'|^2$, with the coupling constants defined by Lee and Yang (1956). The experiment (Ambler *et al.* 1957) on Co^{60} shows that the quantity

$$(1) \qquad A = 2\,\mathrm{Re}[C_T C_T'^* - C_A C_A'^* + i(\alpha Z/p)(C_A C_T'^* + C_A' C_T^*)]/C_{GT}^2$$

is, within experimental accuracy, independent of the electron momentum p and very near -1 in value. If we define

$$(2) \qquad B = 2\,\mathrm{Re}[C_T' C_S^* + C_T C_S'^* - C_A' C_V^* - C_A C_V'^* - i(\alpha Z/p)(C_A' C_S^* + C_A C_S'^* - C_T' C_V^* - C_T C_V'^*)]/C_{GT}^2$$

the asymmetry parameter β defined in Ambler *et al.* (1957) is for Co^{58}

$$(3) \qquad \beta = \frac{v}{c}\,\frac{-A+\sqrt{6}B|M_F|/|M_{GT}|}{1+(C_F^2/C_{GT}^2)(|M_F|^2/|M_{GT}|^2)}.$$

The quantity $(C_F^2/C_{GT}^2)(|M_F|^2/|M_{GT}|^2)$ has been measured (Griffing and Wheatley 1956) as 0.125 ± 0.04 from the angular distribution of the Fe^{58} γ-ray following the decay of Co^{58}. In order to evaluate $|M_F|^2/|M_{GT}|^2$ one needs the value of C_F^2/C_{GT}^2, which can in principle be determined from the half-lives of O^{14} and of the neutron; Gerhart (1954) quotes a value of 0.73 ± 0.2 for this ratio. However the neutron half-life is rather uncertain and, if one takes account of the tritium half-life in a manner suggested by Blatt (1953), one can obtain as a reasonable estimate

$$C_F^2/C_{GT}^2 = 0.57\pm0.15.$$

We shall use this value in the following, but the arguments are not seriously affected by this choice. The experimenters have not suggested a mean value for $\beta c/v$, but from the figures given by Ambler *et al.* (1957) a not unreasonable value would appear to be 0.84 ± 0.10. Using these numbers one finds $B = -(0.05\pm0.2)$, a value consistent with zero.

[1]Manuscript received May 21, 1957.
Contribution from McMaster University, Hamilton, Ontario, and the University, Birmingham, England.

In the two-state neutrino theory with time reversal invariance, all the coupling constants are real and the coupling constant ratio C'/C is -1 for all five interactions in β-decay (Lee and Yang 1957). With these assumptions the very small value (<0.02) of $\mathrm{Re}(C_A C_T^* + C_A' C_T'^*)$ determined by the Na^{22} experiment (Sherr and Miller 1954) requires that C_A and C_A' be essentially zero. Also B becomes simply $-2C_S/C_T$ and we have

$$(C_S/C_T)^2 = 0.0006 \pm 0.01. \tag{4}$$

On the other hand, the angular correlation in the neutron decay (Robson 1955) shows that

$$|C_T|^2+|C_T'|^2-|C_A|^2-|C_A'|^2+|C_V|^2+|C_V'|^2-|C_S|^2-|C_S'|^2 = (0.09\pm0.11)(3C_{GT}^2+C_F^2). \tag{5}$$

Putting $C_A = C_A' = 0$, this, together with the adopted value of C_F^2/C_{GT}^2, gives

$$(|C_S|^2+|C_S'|^2)/C_{GT}^2 = 0.62\pm0.25, \tag{6a}$$

$$(|C_V|^2+|C_V'|^2)/C_{GT}^2 = -0.05\pm0.25. \tag{6b}$$

Equations (4) and (6*a*) are clearly inconsistent, so that the theory used to derive equation (4) is apparently in need of modification. It can be seen that very substantial changes in the values of the measured quantities would be needed to bring the neutron angular correlation experiment and the Co^{58} experiments into agreement. The absence of strong angular correlation in the neutron decay seems to rule out the suggestion that the Fermi component of the β-decay interaction might be vector rather than scalar. It should also be recalled that the presence of vector would introduce V–T interference terms which would tend to destroy the straight Kurie plots of many first-forbidden spectra (Konopinski and Langer 1953). A possible solution of the contradiction, still retaining the framework of the two-component theory, is to abandon time reversal invariance.

The purpose of this note, however, is to suggest another possible theory. This suggestion is that the two-state neutrino theories remain valid, time reversal remains valid, and the β-decay interaction is a mixture of scalar and tensor interactions, but that in the decay of a neutron the scalar interaction emits a ***neutrino*** while the tensor term emits an ***antineutrino***, using the terminology of Lee and Yang. In their notation the proposed interaction Hamiltonian is

$$C_S(\psi_p {}^H O_S \psi_N)(\psi_e {}^H O_S \psi_\nu') + C_T(\psi_p {}^H O_T \psi_N)(\psi_e {}^H O_T \psi_\nu) + \text{c.c.}$$

So far as processes involving only one neutrino are concerned, this is equivalent to writing $C_S' = C_S$, $C_T' = -C_T$ in the standard four-component neutrino theory. In processes involving both neutrino emission and absorption, the four-component and two-component theories will give different results, since in the two-component theory neutrinos of opposite screw sense are charge conjugate (Serpe 1952), but this is not so in the four-component theory. In Majorana or two-component theory, we are abandoning the principle

of lepton conservation*; most of the remainder of this paper is devoted to showing that this does not contradict experiment. Neither does the four-component theory.

It is clear that this theory is consistent with the situation already described, since it requires that B be identically zero and since none of the other quantities discussed depends on the sign of C_S or C_S'. It is also consistent with the experimental evidence that the double β-decay of even–even nuclides does not occur without the emission of neutrinos. The possibility of such decay requires the existence of virtual intermediate states from which the neutrino emitted by the scalar matrix element can be absorbed in going to the final state through a tensor matrix element, or vice versa. However, the scalar interaction connects the initial 0+ state only with intermediate states which are themselves 0+ and these cannot decay to the final 0+ state through the tensor interaction. Nor are there any alternative low-lying 1+ states in even–even nuclei. Similarly the tensor interaction connects both initial and final states only to intermediate states 1+. Hence even–even nuclides can perform double β-decay only with the emission of two neutrinos (or antineutrinos) and consequent reduced probability. Odd A nuclei can emit two electrons and no neutrinos on this theory, but such a process would be in competition with ordinary single β-decay and would thus be extremely difficult to detect.

Another consequence of this theory is that inverse β^+ processes such as $Cl^{37} \rightarrow A^{37}$ should occur with pile neutrinos. However this will be at a rate markedly less than that calculated on the basis of the older Majorana theory. In Cl^{37} neutrino capture, both scalar and tensor interactions play a role. However, owing to statistical and other factors the probability of capture through the tensor term is perhaps three to eight times as great as through the scalar term. On the other hand, only the *neutrinos* emitted by the pile can be captured by the tensor interaction, and these, produced in the pile by the scalar term, are probably of the order 1/5 to 1/10 of the antineutrinos emitted. Consequently the capture rate would be reduced by a factor of say 2 to 5, allowing for the doubled cross-section due to the removal of spin degeneracy (Lee and Yang 1957). The detection of neutrino capture in Cl^{37} or alternatively a reduction in the upper limit on its cross-section is a test of the proposed theory.

On this theory, the absence of the axial vector interaction depends on the absence of double β-decay and not on the smallness of $C_AC_T+C_A'C_T'$. The latter could be arranged by having $C_A' = C_A$, but since A and T have the same selection rules there would then be intermediate states for double β-decay of even–even nuclei. It is important to increase the accuracy of the He^6 angular correlation experiment to obtain a direct measurement of $|C_A|^2/|C_T|^2$.

One other aspect of β-decay theory which would be affected by this proposal is the shape of certain forbidden spectra. Since the scalar–tensor terms have coefficient $C_SC_T+C_S'C_T'$, they would be absent. A preliminary examination

*The writer has benefited from remarks by W. Pauli and from a preprint of a paper by K. M. Case.

suggests that the shapes of these spectra are not inconsistent with the absence of cross terms. A more exact statement requires considerable numerical work.

The proposed theory would appear to permit the retention of the two-component or Majorana neutrino with time reversal invariance and a β-decay interaction consisting only of scalar, tensor (and pseudoscalar) terms without contradicting any present experimental data.

The author is indebted to Professor R. E. Peierls for extending the hospitality of his department during a sabbatical leave, and to the Nuffield Foundation and the British Council for travel grants.

REFERENCES

AMBLER, E., HAYWARD, R. W., HOPPES, D. D., HUDSON, R. P., and WU, C. S. 1957. Phys. Rev. **106**, 1361.
BLATT, J. M. 1953. Phys. Rev. **89**, 83.
GERHART, J. B. 1954. Phys. Rev. **95**, 288.
GRIFFING, D. F. and WHEATLEY, J. C. 1956. Phys. Rev. **104**, 389.
KONOPINSKI, E. J. and LANGER, L. M. 1953. Annual Revs. Nuclear Sci. **2**, 261.
LEE, T. D. and YANG, C. N. 1956. Phys. Rev. **104**, 254.
——— 1957. Phys. Rev. **105**, 1671.
POSTMA, H., HUISKAMP, W. J., MIEDMA, A. R., STEENLAND, M. J., TOLHOEK, H. A., and GORTER, C. J. 1957. Physica, **23**, 259.
ROBSON, J. M. 1955. Phys. Rev. **100**, 933.
SERPE, J. 1952. Physica, **18**, 295.
SHERR, R. and MILLER, R. H. 1954. Phys. Rev. **93**, 1076.

A REVISED SEMIEMPIRICAL ATOMIC MASS FORMULA[1]

A. G. W. CAMERON

ABSTRACT

A new mass formula has been constructed which contains volume and surface energies, each with a symmetry energy contribution, Coulomb and Coulomb exchange energies, and shell correction and pairing energies. A nuclear model with a trapezoidal radial-density distribution was used. The central density was assumed constant, and the dimensions were adjusted to fit the Stanford electron-scattering results. The symmetry energy coefficients were determined by a least-squares fit to the valley of beta stability. The volume and surface energy coefficients were determined by a least-squares fit to 89 odd–odd masses uniformly spaced in mass number. The shell correction and pairing energies were assumed to be independent functions of the proton and neutron numbers; they were empirically determined from the differences between masses computed from the formula without corrections and those tabulated by Wapstra and Huizenga. The median energy difference between the corrected formula and the Wapstra–Huizenga masses is about 300 kev. Some remarks are made concerning the implication of these results for nuclear deformations and fission thresholds.

INTRODUCTION

The semiempirical atomic mass formula, originally introduced by Weizsacker (1935), has been treated by many authors who have given different determinations of the coefficients. Among the more thorough treatments of the problem are those of Feenberg (1947) and Green (1954).

The semiempirical formula traditionally includes terms representing a volume energy (proportional to A), a surface energy (proportional to $A^{2/3}$), a symmetry volume energy (dependent on the isotopic number), a Coulomb energy, and a pairing energy (which expresses the extra stability of nuclei with paired neutrons and protons). These terms contain coefficients which have been determined from the energy differences of mirror nuclei, from the position of the valley of beta stability, and by fitting masses.

Fixing a coefficient in the Coulomb energy is equivalent to determining a radius of the nuclear charge distribution. In the early formulas this was usually done by assuming that the energy differences between mirror nuclei resulted from the Coulomb energy difference between two uniform charge distributions differing by one proton. This assumption exaggerates the charge radius, since the odd nucleon in a mirror pair tends to lie near the nuclear surface (Fitch and Rainwater 1953). These early mass formulas differ from the mass measurements at the middle of the periodic table by amounts of the order of 10 to 20 Mev.

Green (1954) showed that these differences were reduced if the Coulomb energy coefficient was determined by fitting masses. If the nuclear radius is written $R = r_0 A^{1/3}$, then the radius constant for a uniform charge distribution found by Green is $r_0 = 1.22 \times 10^{-13}$ cm. This is comparable to the values obtained from the Stanford electron-scattering results (Hofstadter 1956).

[1]Manuscript received June 20, 1957.
Contribution from the Physics Division, Atomic Energy of Canada Limited, Chalk River, Ontario.
Issued as A.E.C.L. No. 433.

A similar approach was tried by Mathews (1956). He computed the Coulomb energy for a trapezoidal radial nuclear charge distribution with skin thickness fixed by the Stanford electron-scattering results, and he added a Coulomb exchange-energy term. He obtained a radius constant $r_0 = 1.205\times10^{-13}$ cm. This is considerably larger than the Stanford determinations which lie in the vicinity of $r_0 \approx 1.08\times10^{-13}$ cm.

The present mass computations were undertaken in an effort to obtain realistic atomic masses in the vicinity of the valley of beta stability and also at considerable distances from it. It was decided to base all terms on the trapezoidal radial model of the nucleus and to use new mass terms which can be physically justified and which seem necessary in order to get a good fit to the trend of atomic mass values.

THE REVISED MASS FORMULA

For convenience in this paper all atomic masses M have been expressed as mass excesses, $M-A$, in Mev. energy units. The mass-excess equation is written in the following symbolic form:

$$(1) \qquad M-A = 8.367A-0.783Z+E_v+E_s+E_c+E_{ex}+S(Z, N)+P(Z, N),$$

where the subscripts v, s, c, and ex denote respectively volume, surface, Coulomb, and Coulomb exchange energies. The first two terms on the right-hand side give the mass excess of the neutrons and protons in the nucleus. $S(Z, N)$ and $P(Z, N)$ are empirical shell correction and pairing energies.

The volume energy is expressed as the sum of two contributions. The first of these is the volume saturation energy, which is taken proportional to the number of particles A. The second contribution is a volume symmetry energy assumed proportional to $(A-2Z)^2/A^2$. The volume energy term is therefore written:

$$(2) \qquad E_v = \alpha\left[1-\frac{\beta}{\alpha}\frac{(A-2Z)^2}{A^2}\right]A,$$

where α and β are constants to be determined.

The Stanford electron-scattering results (Hofstadter 1956) established two properties of the nuclear density distribution. The first of these is the rough proportionality to $A^{1/3}$ of the distance from the center of the nucleus to the point at which the charge density has fallen to 50% of its central value. The second property is the constancy of the charge skin thickness. It is found that the distance between the points at which the charge density has fallen to 90% and to 10% of its central value is independent of the nucleus and equal to 2.5×10^{-13} cm. These two properties are most conveniently expressed in a trapezoidal radial model of the nucleus such as is shown in Fig. 1.

In Fig. 1 the nuclear radius R is defined as the distance from the center to the point at which the nuclear density has 50% of the central value ρ_0. The half skin thickness z is set equal to a constant, 1.5×10^{-13} cm. The Stanford results show that R is roughly proportional to $A^{1/3}$, but in fact it is possible to obtain a better fit to the Stanford results if the alternative assumption is

made that the central density ρ_0 is constant. The Stanford results are then fitted by the formula

$$R = 1.112A^{1/3}\left[1-\frac{0.62025}{A^{2/3}}\right]\times 10^{-13}\ \text{cm}. \tag{3}$$

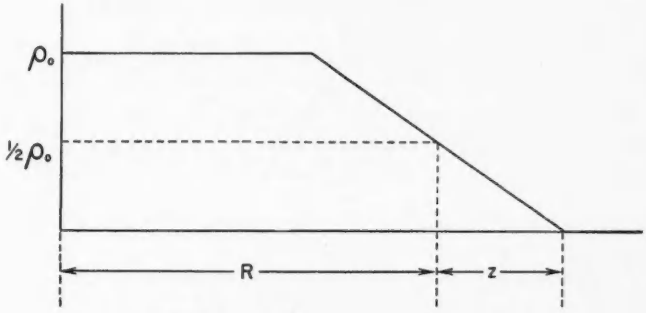

FIG. 1. The trapezoidal radial model of the nucleus.

The surface of the nucleus is an ill-defined quantity when its edge is diffuse as in Fig. 1. However, it seems appropriate to take the sphere of radius R as the reference surface for the surface energy, and that assumption is made here. It is assumed that the surface energy is proportional to the area of this reference surface.

Feenberg (1947) has pointed out that the surface energy should contain a symmetry energy contribution. This is logical when it is realized that the surface energy is a consequence of the failure of nuclear saturation at the edge of the nucleus and that the volume saturation energy contains a symmetry energy term. Therefore the surface energy is written in the form

$$E_s = \gamma\left[1-\frac{\phi}{\gamma}\frac{(A-2Z)^2}{A^2}\right]\left[1-\frac{0.62025}{A^{2/3}}\right]^2 A^{2/3}, \tag{4}$$

where γ and ϕ are constants to be determined.

For very small liquid drops the surface energy becomes less than one would expect for a strict proportionality to the reference surface area (Hirschfelder, Curtiss, and Bird 1954). Attempts were made to introduce a similar relationship in the surface energy used here, but the results so obtained were poor compared to those without such a relationship.

The Coulomb energy E_c can be calculated for the nuclear model of Fig. 1 by well-known methods (see, for example, Bethe and Bacher 1936). The result is

$$E_c = 0.779\frac{Z(Z-1)}{A^{1/3}}\left[1-\frac{1.5849}{A^{2/3}}+\frac{1.2273}{A}+\frac{1.5772}{A^{4/3}}\right]. \tag{5}$$

The Coulomb exchange energy arises from the correlations in the motions of the protons in the nucleus. Since it is a small term, it was decided to adapt

the calculation of Bethe and Bacher (1936) for the nuclear model of Fig. 1. The result is

$$(6) \qquad E_{ex} = -0.4323 \frac{Z^{4/3}}{A^{1/3}}\left[1-\frac{0.57811}{A^{1/3}} - \frac{0.14518}{A^{2/3}} + \frac{0.49597}{A}\right].$$

The terms $S(Z, N)$ and $P(Z, N)$ were determined empirically as discussed in the following section.

An attempt was made to include in the mass formula a term involving a nuclear compression energy (Feenberg 1947). However, it was found that the formula without such a term fitted the trend of masses in the range $25 \leqslant A \leqslant 250$ so well that it was not possible to determine a coefficient for a compression energy term. Therefore no such term is included in the mass formula.

Equation (1) without the shell correction and pairing energy terms will be referred to as the reference mass formula:

$$(7) \qquad (M-A)_{ref} = 8.367A - 0.783Z + E_v + E_s + E_c + E_{ex}.$$

Ignoring shell effects, the valley of beta stability is obtained by differentiating the reference mass formula with respect to Z and setting the resulting expression equal to zero. One obtains

$$(8) \qquad \frac{\partial E_v}{\partial Z} + \frac{\partial E_s}{\partial Z} = 0.783 - \frac{\partial E_c}{\partial Z} - \frac{\partial E_{ex}}{\partial Z}.$$

The terms on the left-hand side of equation (8) are linear in the unknown coefficients β and ϕ.

In order to average out shell effects it is necessary to determine β and ϕ by a least-squares procedure in which the properties of the actual valley of beta stability at many points are substituted into equation (8). The bottom of the valley of beta stability was taken to be that drawn on the General Electric Chart of the Nuclides (Stehn and Clancy 1956). For every even mass number in the range $70 \leqslant A \leqslant 250$ the stability line was read to the nearest 0.1 in atomic number, and the resulting pairs of values of "Z" and A were substituted into equation (8). The least-squares solution of these equations gives

$$\beta = -31.4506 \text{ Mev.},$$

$$\phi = 44.2355 \text{ Mev.}$$

The remaining two constants in the reference mass formula, α and γ, were determined by a least-squares fit of the reference mass formula to experimental atomic masses. The measured masses adopted for this purpose were those given by Wapstra (1956*a*, 1956*b*) and by Huizenga (1956). It has been shown by Newton (1956) that an appropriate reference level for nuclear level densities is the ground state of odd–odd nuclei. Therefore it was decided to fit the reference mass formula only to odd–odd masses and to define the pairing energy $P(Z, N)$ to be zero for odd–odd nuclei. Eighty-nine odd–odd masses were chosen in the range $26 \leqslant A \leqslant 254$ which were as uniformly spaced as possible and which otherwise had the least possible assigned errors. It was

hoped that this procedure would minimize errors due to shell effects in the determination of α and γ. The mass excesses of the 89 nuclei were substituted into equation (7), and a least-squares solution of the resulting equations gave

$$\alpha = -17.0354 \text{ Mev.},$$

$$\gamma = 25.8357 \text{ Mev.}$$

It is interesting to note the near equality of the ratios $\beta/\alpha = 1.846$ and $\phi/\gamma = 1.712$. One would expect these ratios to be of the same order of magnitude but not necessarily equal.

The differences between the masses calculated from equation (7) with the constants determined above and the 89 odd–odd masses are plotted in Fig. 2. These differences have a trend the course of which crosses the axis of zero

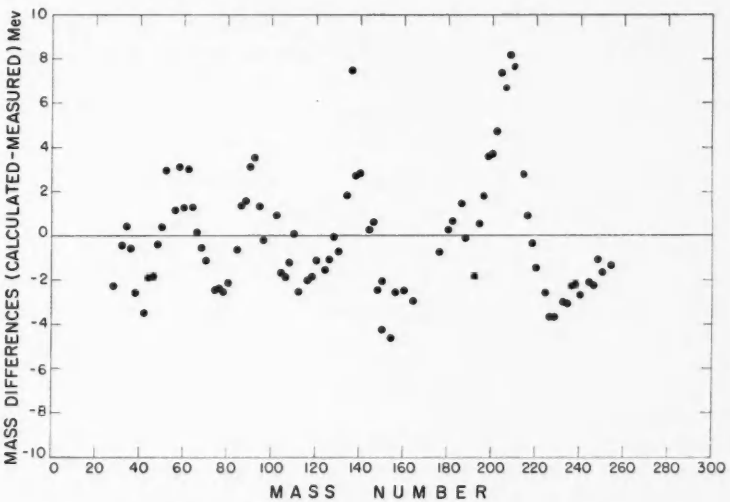

FIG. 2. Comparison of 89 odd–odd masses with the reference mass formula.

difference many times. Accordingly, equation (7) is considered to give a good fit to the trend of the masses over the entire mass range shown. Most of the attempts mentioned above, in which somewhat different forms for some of the terms were tried, resulted in fits in which the differences would cross the zero axis only twice, thus indicating the unsuitability of the assumed terms.

THE SHELL CORRECTION AND PAIRING ENERGIES

The trend of the mass differences in Fig. 2 shows large and fairly smooth deviations from the zero axis. This indicates that important corrections to the reference mass formula should be made which depend upon the energies of the individual particle orbits in the nuclear potential well and upon certain

mutual interactions between particles in these orbits. Following the procedure of Green and Edwards (1953), it is assumed that the shell correction and pairing energies can be written as independent functions of the neutron and proton numbers:

$$S(Z, N) = S(Z)+S(N),$$
$$P(Z, N) = P(Z)+P(N).$$

It was desired to attribute the odd–even effect in neutron and proton binding energies to the pairing energy. It was hoped that residual energy differences between pairing-corrected reference masses and measured masses would be smooth functions of the neutron and proton numbers. The functions $S(Z)$, $S(N)$, $P(Z)$, and $P(N)$ were determined by an empirical procedure.

The following quantities were formed from the Wapstra–Huizenga masses:

$$\Delta = (M-A)_{\text{meas}}-(M-A)_{\text{ref}}.$$

Trial quantities $P(Z, N)$ were assumed (the pairing energies of Newton (1956) were used in the first approximation). The shell corrections were then approximately given by

$$S(Z, N) = \Delta(Z, N)-P(Z, N).$$

A separation was made between proton and neutron effects by forming shell correction differences, which (for protons) are

$$\begin{aligned}\delta S(Z) &= S(Z)-S(Z-1)\\ &=\Delta(Z, N)-\Delta(Z-1, N)-P(Z, N)+P(Z-1, N).\end{aligned}$$

These differences were weighted inversely as the squares of the errors in them, and weighted averages of the differences were computed over all possible values of the neutron number N for each proton number Z. These average differences were smoothed. Similar average differences $\delta S(N)$ were obtained and smoothed.

These smooth differences were summed to form $S(Z)$ and $S(N)$, and the analysis was inverted to obtain empirical values for $P(Z)$ and $P(N)$. These in turn were used to improve $\delta S(Z)$ and $\delta S(N)$.

The final step in the empirical determinations was to form the quantities

$$\Delta(Z, N)-P(Z, N)-S(Z, N).$$

Weighted averages of these quantities were computed for constant Z and for constant N, and it was insisted that these weighted averages should approach zero as closely as possible. This was done by adjusting $\delta S(Z)$ and $\delta S(N)$ in a manner consistent with the errors in the weighted averages and in such a way as to leave the functions as smooth as possible.

The functions $\delta S(Z)$ and $\delta S(N)$ which finally resulted are shown in Figs. 3 and 4. It was gratifying to find that these functions were quite smooth except for discontinuities at shell edges. These shell correction differences can be given a physical interpretation in the following way. Presumably the reference mass surface corresponds roughly to the highest occupied levels in a Fermi gas of nucleons. The derivatives of the shell correction differences then are

corrections to the spacing of the individual particle levels at the Fermi level in the gas.

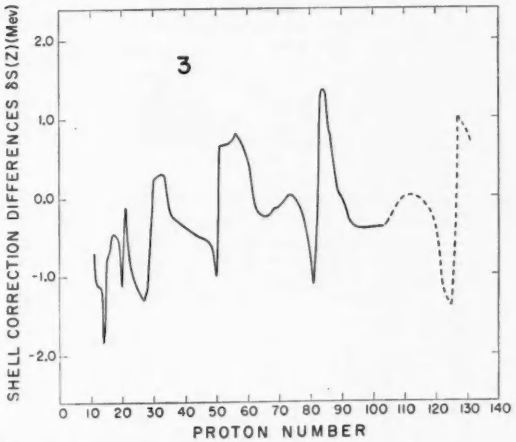

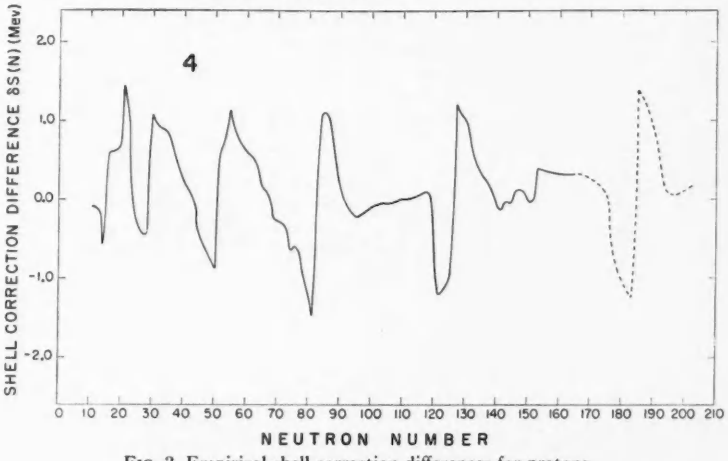

FIG. 3. Empirical shell correction differences for protons.
FIG. 4. Empirical shell correction differences for neutrons.

It is interesting to note that the shell correction differences change almost linearly as a shell fills in the lighter spherical nuclei, but in the heavier nuclei the onset of nuclear deformation causes the shell correction differences to become flat fairly abruptly. This is consistent with Nilsson's (1955) picture of a roughly even spacing of particle orbits in deformed nuclei.

It should be noted that the shell correction differences for protons are predominantly negative for low Z. This suggests that the reference mass surface should have some small additional dependence on Z.

Extrapolations of the shell correction differences to higher nucleon numbers are shown as dashed lines in Figs. 3 and 4. These extrapolations are based on the physical interpretation given above and involve assumptions of a closed proton shell at $Z = 126$ and a closed neutron shell at $N = 184$.

The quantities $S(Z)+P(Z)$ and $S(N)+P(N)$ are listed in Table I.

Histograms of the differences between the masses calculated from the final mass formula and those in the Wapstra–Huizenga tables are plotted in Figs. 5, 6, 7, and 8, corresponding to different ranges of mass number.

TABLE I

SHELL PLUS PAIRING CORRECTIONS AS FUNCTIONS OF PROTON AND NEUTRON NUMBERS
(The values are extrapolated for $Z > 100$ and $N > 160$; all energies are in Mev.)

Z or N	$S(Z)+P(Z)$	$S(N)+P(N)$	Z or N	$S(Z)+P(Z)$	$S(N)+P(N)$	Z or N	$S(Z)+P(Z)$	$S(N)+P(N)$
11	18.26	−12.81	75	0.59	2.06	138		−0.13
12	15.05	−15.40	76	−0.35	0.51	139		0.70
13	16.01	−13.07	77	0.32	0.74	140		−0.06
14	12.04	−15.80	78	−0.96	−1.18	141		0.49
15	13.27	−13.81	79	−0.52	−1.26	142		−0.20
16	11.09	−14.98	80	−2.08	−3.54	143		0.40
17	12.17	−12.63	81	−2.46	−3.97	144		−0.22
18	10.26	−13.76	82	−3.64	−5.26	145		0.36
19	11.04	−11.37	83	−1.55	−4.18	146		−0.09
20	8.41	−12.38	84	−0.96	−3.71	147		0.58
21	9.79	−9.23	85	0.97	−2.10	148		0.12
22	7.36	−9.65	86	0.88	−1.70	149		0.75
23	8.15	−7.64	87	2.37	−0.08	150		0.15
24	5.63	−9.17	88	1.75	−0.18	151		0.70
25	5.88	−8.05	89	2.72	0.94	152		0.17
26	3.17	−9.72	90	1.90	0.27	153		1.11
27	3.32	−8.87	91	2.55	1.13	154		0.89
28	0.82	−10.76	92	1.46	0.08	155		1.85
29	1.83	−8.64	93	1.93	0.91	156		1.62
30	0.97	−8.89	94	0.86	−0.31	157		2.54
31	2.33	−6.60	95	1.17	0.49	158		2.29
32	1.27	−7.13	96	0.08	−0.78	159		3.20
33	2.92	−4.77	97	0.39	0.08	160		2.91
34	1.61	−5.33	98	−0.76	−1.15	161		3.84
35	2.91	−3.06	99	−0.39	−0.23	162		3.53
36	1.35	−3.79	100	−1.51	−1.41	163		4.48
37	2.40	−1.72	101	−1.17	−0.42	164		4.15
38	0.89	−2.79	102	−2.36	−1.55	165		5.12
39	1.74	−0.93	103	−1.95	−0.55	166		4.78
40	0.36	−2.19	104	−3.06	−1.66	167		5.75
41	0.95	−0.52	105	−2.62	−0.66	168		5.39
42	−0.65	−1.90	106	−3.55	−1.73	169		6.31
43	−0.04	−0.45	107	−2.95	−0.75	170		5.91
44	−1.73	−2.20	108	−3.75	−1.74	171		6.87
45	−0.96	−1.22	109	−3.07	−0.78	172		6.33
46	−2.87	−3.07	110	−3.79	−1.69	173		7.13
47	−2.05	−2.42	111	−3.06	−0.78	174		6.61
48	−4.05	−4.37	112	−3.77	−1.60	175		7.30
49	−3.40	−3.94	113	−3.05	−0.75	176		6.31
50	−5.72	−6.08	114	−3.78	−1.46	177		6.27
51	−3.75	−4.49	115	−3.12	−0.67	178		4.83
52	−4.13	−4.50	116	−3.90	−1.26	179		4.49
53	−2.42	−3.14	117	−3.35	−0.51	180		2.85
54	−2.85	−2.93	118	−4.24	−1.04	181		2.32
55	−1.01	−1.04	119	−3.86	−0.53	182		0.58
56	−1.33	−1.36	120	−4.92	−1.84	183		−0.11
57	0.54	0.69	121	−5.06	−2.42	184		−0.98
58	−0.02	0.21	122	−6.77	−4.52	185		0.81
59	1.74	2.11	123	−7.41	−4.76	186		1.77
60	0.75	1.33	124	−9.18	−6.33	187		3.37
61	2.24	3.29	125	−10.16	−6.76	188		4.13
62	1.00	2.46	126	−11.12	−7.81	189		5.60
63	1.98	4.30	127	−9.76	−5.80	190		6.15
64	0.79	3.32	128	−9.23	−5.37	191		7.29
65	1.54	4.79	129	−7.96	−3.63	192		7.35
66	0.39	3.62	130	−7.65	−3.35	193		7.95
67	1.08	4.97	131		−1.75	194		7.67
68	0.00	3.64	132		−1.88	195		8.16
69	0.78	4.63	133		−0.61	196		7.83
70	−0.35	3.07	134		−0.90	197		8.31
71	0.58	4.06	135		0.09	198		8.01
72	−0.55	2.49	136		−0.32	199		8.53
73	0.59	3.30	137		0.55	200		8.27
74	−0.61	1.46						

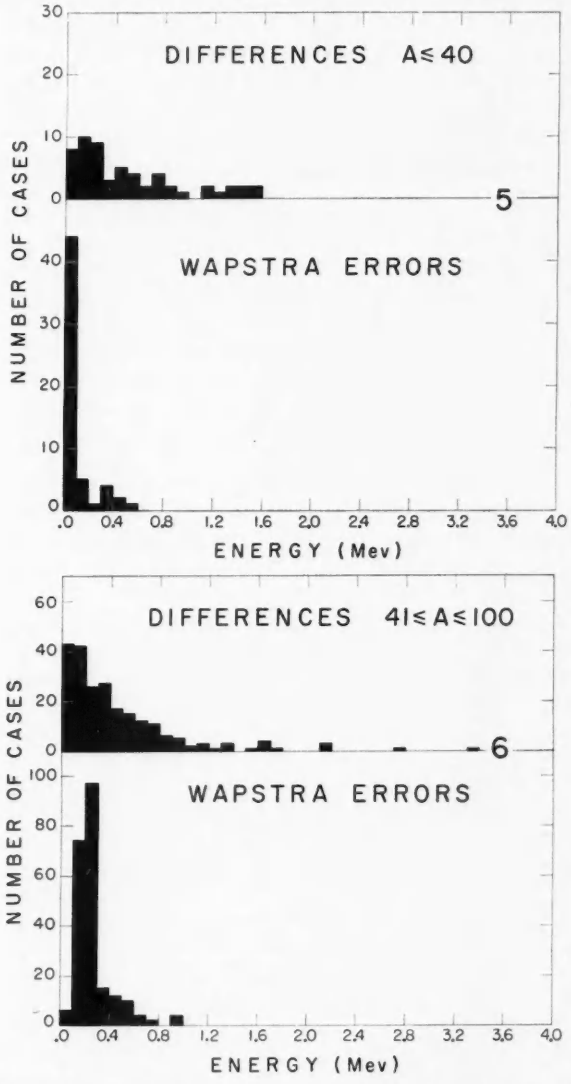

FIG. 5. Differences between measured masses and the mass formula, compared with the errors assigned by Wapstra, for $A \leqslant 40$.

FIG. 6. Differences between measured masses and the mass formula, compared with the errors assigned by Wapstra, for $41 \leqslant A \leqslant 100$.

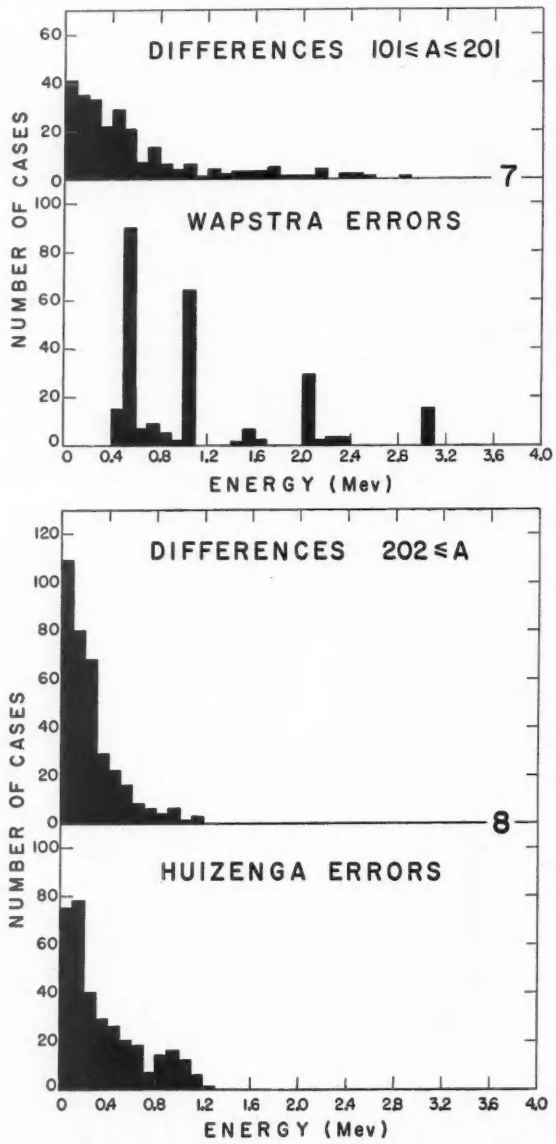

FIG. 7. Differences between measured masses and the mass formula, compared with the errors assigned by Wapstra, for $101 \leqslant A \leqslant 201$.

FIG. 8. Differences between measured masses and the mass formula, compared with the errors assigned by Huizenga for $202 \leqslant A$.

These differences are compared with the errors assigned by Wapstra and by Huizenga. The median difference is in the range 200 to 300 kev., and, although this is comparable with the median assigned error, it is also a reasonably good measure of the error likely to be encountered near the valley of beta stability when using the new formula. It is evident from Fig. 5 that larger errors are to be expected for very light masses, and it is probable that a mass formula based on supermultiplet theory or the shell model would enjoy more success in the light region.

NUCLEAR DEFORMATIONS AND FISSION THRESHOLDS

It is interesting to examine the influence of the new mass formula on the theory of fission thresholds. When a nucleus is deformed the surface energy increases and the Coulomb energy decreases. In the past these energy changes have been calculated for the deformation of a liquid-drop model of the nucleus with a sharp edge (see, for example, Swiatecki 1956). In such calculations a parameter x is defined as the Coulomb energy divided by twice the surface energy of the undeformed nucleus. For U^{236} the theory requires $x \approx 0.74$.

In the present mass formula (but neglecting for convenience the small Coulomb exchange energy) for U^{236}, $E_c = 1019$ Mev. and $E_s = 878$ Mev. This gives $x = 0.58$ (an even smaller value would result if the Coulomb exchange energy were included). According to Swiatecki (1956), for $x = 0.58$, the fission threshold is $0.0665E_s = 58.4$ Mev. This is an order of magnitude too large. However, it should be noted that this threshold is still a small difference of two large quantities. At the symmetric saddle point the Coulomb energy is 777 Mev. and the surface energy is 1159 Mev. (Swiatecki 1956).

When a nuclear model of the type illustrated in Fig. 1 is deformed the amount of nuclear matter in the skin is increased. Hence it should not be expected that the reference surface for the surface energy will deform like the sharp edge of a liquid drop. If the reference surface of the nucleus is the locus of points at which the central density has decreased to 50%, as assumed above, then the deformed reference surface must lie inside the surface generated by deforming at constant volume. In this case the deformed surface energy computed by Swiatecki (1956) would be too large.

In order to see how important such effects may be, consider the following very crude calculation which can be expected to overestimate the effect somewhat. In the undeformed U^{236} nucleus 47% of the nuclear matter is inside the skin. This has decreased to 30% at the symmetric saddle point if the number of nucleons in the skin varies as the surface energy computed by Swiatecki (1956). The scale length of the central portion of the nucleus is thus diminished in the ratio $(30/47)^{1/3}$. The reference surface area would be decreased in the ratio $[(R-z)(30/47)^{1/3}+1.5]^2/[(R-z)+1.5]^2 = 0.892$ for U^{236}. The deformed surface energy now becomes $1159 \times 0.892 = 1031$ Mev. The fission threshold is $1031-878-1019+777 = -83$ Mev.

This crude procedure points to the difficulty of defining a reference surface for a nucleus with a diffuse edge and indicates that small values of the par-

ameter x may not be inconsistent with small fission thresholds. It may also be noted that small values of x favor asymmetric fission (Swiatecki 1956). The writer believes that a fundamentally new approach to the problem of the fission barrier is needed.

It is evident that if large nuclear deformations produce only a small barrier against fission then it is reasonable to expect that quite small amounts of energy may be sufficient to produce fairly extensive nuclear deformations. Since such energies can easily be obtained by internal nuclear reorganizations, it is easy to understand why heavy nuclei are commonly deformed.

The writer is indebted to Dr. L. G. Elliott and Dr. T. D. Newton for useful discussions and to Mr. J. Riddell for early computations. He wishes to thank Mr. Jon Mathews for giving him a copy of his notes on computations with the trapezoidal radial model of the nucleus.

More than 8000 mass excesses have been computed with equation (1). These are given in Chalk River Report CRP-690, together with associated neutron, proton, and alpha-particle binding energies and positive and negative beta decay energies. More extensive tables of nuclear reaction energies are being computed. The energies released in fission as a function of the fragment pairs are also being computed.

REFERENCES

BETHE, H. A. and BACHER, R. F. 1936. Revs. Mod. Phys. **8**, 82.
FEENBERG, E. 1947. Revs. Mod. Phys. **19**, 239.
FITCH, V. L. and RAINWATER, J. 1953. Phys. Rev. **92**, 789.
GREEN, A. E. S. 1954. Phys. Rev. **95**, 1006.
GREEN, A. E. S. and EDWARDS, D. F. 1953. Phys. Rev. **91**, 46.
HIRSCHFELDER, J. O., CURTISS, C. F., and BIRD, R. B. 1954. Molecular theory of gases and liquids (John Wiley & Sons, Inc., New York).
HOFSTADTER, R. 1956. Revs. Mod. Phys. **28**, 214.
HUIZENGA, J. R. 1956. Physica, **21**, 410.
MATHEWS, J. 1956. Privately circulated notes.
NEWTON, T. D. 1956. Can. J. Phys. **34**, 804.
NILSSON, S. G. 1955. Kgl. Danske Videnskab. Selskab, Mat.-fys. Medd. **29**, No. 16.
STEHN, J. R. and CLANCY, E. F. 1956. Knolls Atomic Power Laboratory publication.
SWIATECKI, W. J. 1956. Phys. Rev. **104**, 993.
WAPSTRA, A. H. 1956*a*. Physica, **21**, 367.
——— 1956*b*. Physica, **21**, 385.
WEIZSACKER, C. F. VON. 1935. Z. Physik, **96**, 431.

THE FORWARD-SCATTERING OF RADIO WAVES FROM OVERDENSE METEOR TRAILS[1]

C. O. Hines and P. A. Forsyth

ABSTRACT

The forward-scattering of radio waves from overdense meteor trails is treated from an elementary point of view. The results indicate that the same geometric factors enter this problem as enter the problem of forward-scattering from underdense trails, and that the transition between underdense and overdense trails occurs at the same value of charge density as in the backscatter case. These conclusions are not expected to be generally valid when applied to individual trails, but at least they should provide a valid basis for the interpretation and prediction of the effects produced statistically by a large number of trails.

INTRODUCTION

A number of meteor studies now employ the radar technique of observation, whereby radio waves from a local transmitter are detected at a nearby receiver after being scattered by the ionized meteor trails. Normally, the scattering process is effectively specular, so that a trail must lie at right angles to the radar beam if it is to be detected with appreciable amplitude.

Two qualitatively distinct mechanisms have been suggested for the specular process, and these are now recognized as limiting cases of a complex phenomenon. They appear to be applicable separately to trails of high and low ionization, with a fairly well-defined transition region linking the two. The original suggestions were made by Pierce (1938) and by Lovell and Clegg (1948), the latter authors developing an earlier idea of Blackett and Lovell (1941). The two suggestions were developed further by Herlofson (1947), Huxley (1952), and Greenhow (1952), and they were united in the generalized treatments given by Kaiser and Closs (1952) and by Eshleman (1952). The final formalisms, including corrections to earlier works, are summarized by Kaiser (1953) and Eshleman (1955).

The outstanding qualitative distinction between the two processes lies in the degree to which the incident wave can penetrate the meteor trail without undergoing serious modification. If the line density of ionization along the trail is sufficiently high, then a region of negative dielectric constant which surrounds the axis of the trail prevents full penetration, and the incident wave is reflected as though a metallic cylinder comprised the region in question. Meteor trails which behave in this way are known as 'overdense'. If the line density of ionization is sufficiently small, the incident wave can penetrate the trail without serious change (despite a small axial region of negative dielectric constant, which may exist momentarily), and the scattered signal then results from the uncoupled motions of individual electrons. The meteor trails in this case are termed 'underdense'.

Even in the limiting cases of very high and very low ionization, these

[1]Manuscript received May 24, 1957.
Contribution from the Radio Physics Laboratory of the Defence Research Board, Ottawa. The work was performed under project PCC No. D48-95-11-01.

simple approaches are subject to various complicating modifications (Herlofson 1951; Feinstein 1951; Manning 1953). Nevertheless, the simple pictures provide an excellent background for the interpretation of much experimental data, particularly when the data are statistical in nature.

Radio studies of meteors have been extended by the use of widely separated transmitters and receivers, in which case the signals are received from the meteor trails after undergoing a 'forward-scattering' process. The theoretical analysis of this process poses many problems which are not encountered in the backscatter work, and only limited advances have been made. For example, a wave-matching formalism has been developed for the case of normal incidence (Kaiser and Closs 1952; Eshleman 1952), and the numerical integration of the resultant equations has been completed for three selected ionization densities (Keitel 1955*a*, *b*), but no analytic expression for the received signal has been obtained by this approach nor can one be expected. The further complications inherent in non-normal incidence have been discussed by Keitel (1955*b*) and Wait (1955), while the latter author has developed the relevant formalism for a homogeneous scattering column.

Perhaps the most successful, and certainly the most useful, attack on the problem of forward-scattering was conducted by Eshleman (1952). He derived an analytic formula for the received signal to be expected from an underdense trail, on the assumptions of (*a*) free penetration of the trail by the incident wave, and (*b*) uncoupled oscillation of the scattering electrons. In spite of these simplifications, Eshleman's formula provides a legitimate basis for predicting many statistical characteristics of forward-scatter circuits (Eshleman and Manning 1954; Villard, Eshleman, Manning, and Peterson 1955; Hines, Forsyth, Vogan, and Pugh 1955; Hines 1956) and for interpreting experimental data already obtained (Forsyth, Hines, and Vogan 1955; Hines and Vogan 1957).

Eshleman's restriction to underdense trails does not impose any serious limitation in practice, so long as systems of high sensitivity are employed and so long as attention is confined to the more numerous (and even overlapping) signals of smaller amplitude and shorter duration. However, if the system sensitivity is decreased, or if analyses are made in which the individual effects of the larger signals become important, serious discrepancies between the theory and the observations may be expected. In view of this, it seems desirable to obtain a simplified forward-scatter formula which may be applied to overdense trails. The derivation of such a formula constitutes the purpose of this paper.

The method to be adopted may be considered a naive extension of the elementary treatment appropriate to the overdense backscatter process. The meteor trail is replaced, in effect, by a perfectly reflecting metallic cylinder having a radius appropriate to the particular forward-scatter angle involved. The received signal is then determined directly by geometric optics, with the further inclusion, somewhat arbitrarily, of a polarization factor. The net result is a formula which is undoubtedly faulty, and which may, on occasion, have only casual relation to the true picture in a detailed comparison of

individual cases. It is known, for example, that even the exact theory for reflection from metallic cylinders is inappropriate if the incident electric field is polarized in the plane perpendicular to the axis of the trail (Keitel 1955*a*, *b*), and the geometric-optics approach can hardly be expected to improve the prediction. Nevertheless, it is felt that this approach will provide functional relations and order-of-magnitude estimates which can be combined in a valid statistical picture. Because such a picture is highly desirable, and because it is not likely to be achieved by the more refined methods, the simplifying assumptions adopted here appear to be warranted.

SUMMARY OF EARLIER FORMULAE

For present purposes, it is appropriate to adopt a highly idealized model for the ionization distribution in a meteor trail. It will be assumed that the trail is formed instantaneously, at time $t = 0$, with a uniform line density of electrons, q, along a straight line of zero cross-section. The trail is assumed to expand radially from this line, under the effects of diffusive forces and polarization fields. The latter act to equalize the rates of diffusion of ions and electrons, and lead to a modified diffusion coefficient, D, applicable to both types of charge. In these circumstances, the volume density of electrons (or ions) is given by

$$N = (q/4\pi Dt)\exp(-\rho^2/4Dt) \qquad (t \geqslant 0), \tag{1}$$

where ρ measures distance radially from the axis of the trail.

If q is sufficiently small, the trail is underdense and the scattered signal may be calculated from simple scatter theory. In the radar (backscatter) case, the power available from a matched receiving antenna is given by

$$P_R(0) = P_T\left[\frac{G_T G_R \lambda^3}{32\pi^3 r^3}\right]\left[\frac{\mu_0 e^2}{4m}\right]^2 q^2 \tag{2}$$

at time $t = 0$, and by

$$P_R(t) = P_R(0)\exp(-32\pi^2 Dt/\lambda^2) \qquad (t \geqslant 0) \tag{3}$$

at later times. Here P_T is the transmitted power, r is the distance from the radar site to the 'reflection point' on the trail (i.e., the point on the trail nearest the radar site, such that $\mathbf{r}$ is perpendicular to the axis of the trail), G_T and G_R are the transmitting and receiving antenna gains (relative to isotropic radiators) in the direction of the reflection point, λ is the radio wavelength, e is the electronic charge, m is the electronic mass, and $\mu_0 = 4\pi\times10^{-7}$ henry/meter (= the permeability of free space, in a rationalized system of units). In practice, q is to be evaluated at the reflection point, and the trail need extend only for a distance of the order $(\lambda r/2)^{\frac{1}{2}}$ on either side of this point. The time constant

$$\tau = \lambda^2/16\pi^2 D \tag{4}$$

of the exponential decay of signal amplitude is often taken as a measure of the signal duration.

If q is sufficiently great, the trail is overdense and its back-scattering

properties are calculated from those of a perfectly reflecting cylinder. This cylinder is such that it just encloses the region of negative dielectric constant, and its radius is therefore the value of ρ in (1) which makes N just critical for the frequency concerned. This value is given by

$$\rho_c = \left[4Dt \cdot \ln\left(\frac{\mu_0 e^2}{4m}\frac{q\lambda^2}{4\pi^3 Dt}\right)\right]^{\frac{1}{2}} \tag{5}$$

since the critical electron density is

$$N_c = \pi^2 4m/\mu_0 e^2 \lambda^2 \tag{6}$$

at wavelength λ. The back-scatter cross section of a cylinder of radius ρ_c at radar range r ($\gg \rho_c$) is $\pi r \rho_c$, so the received power is given by

$$P_R'(t) = P_T\left[\frac{G_T G_R \lambda^2}{64\pi^2 r^3}\right]\left[4Dt \cdot \ln\left(\frac{\mu_0 e^2}{4m}\frac{q\lambda^2}{4\pi^3 Dt}\right)\right]^{\frac{1}{2}} \qquad (t \geqslant 0) \tag{7}$$

in the overdense case. This expression applies only until time

$$\tau' = \frac{\mu_0 e^2}{4m}\frac{q\lambda^2}{4\pi^3 D}, \tag{8}$$

when the trail reaches such a diffuse state that $N < N_c$ everywhere within it. Near and after time τ', the dominant signal is that scattered by uncoupled electrons, and formula (3) becomes applicable again. This contribution is relatively minor, however, and it is usually ignored; τ' is then taken to be the duration of the signal. The maximum signal occurs at time τ'/ϵ, and has the value

$$P_R'(\tau'/\epsilon) = \frac{P_T G_T G_R \lambda^3}{32\pi^4 r^3}\left[\frac{\pi}{4\epsilon}\frac{\mu_0 e^2}{4m}\right]^{\frac{1}{2}} q^{\frac{1}{2}}, \tag{9}$$

where $\epsilon = \exp 1$.

It is clear that some smooth transition between the two types of signal will occur, and that neither set of formulae will be accurate in the transition region. However, it is often useful to treat each set as being correct in a part of the transition region, with the change from one set to the other occurring abruptly. The point at which the change is assumed to occur varies with the criteria used in its determination, but the commonly quoted transitional values of q lie in the range $1\text{–}2.4\times10^{14}$ electrons per meter. From a phenomenological point of view, it is convenient to assume a transition at a value of q equal to

$$\begin{aligned} q_T &= (\pi/4\epsilon)^{1/3}(4m/\mu_0 e^2) \\ &= 0.75\times10^{14} \text{ electrons/meter}, \end{aligned} \tag{10}$$

since the peak signals predicted by (2) and (9) are then equal. On this basis, the peak received power would be expected to vary as q^2 for q's up to the value (10), and as $q^{\frac{1}{2}}$ for higher values; the whole variation, though not smooth, would be continuous.

In the case of forward-scattering, the generalizations of (2)–(4) for underdense trails are

$$P_R(0) = P_T\left[\frac{G_T G_R \lambda^3 \sin^2\alpha}{16\pi^4 r_T r_R (r_T+r_R)(1-\cos^2\beta\sin^2\phi)}\right]\left[\frac{\mu_0 e^2}{4m}\right]^2 q^2, \tag{11}$$

$$P_R(t) = P_R(0)\exp(-32\pi^2 Dt/\lambda^2\sec^2\phi), \qquad (t \geqslant 0) \tag{12}$$

$$\tau = \lambda^2 \sec^2\phi/16\pi^2 D. \tag{13}$$

Here r_T and r_R are the distances from the reflection point P to the transmitter T and receiver R, respectively, 2ϕ is the angle TPR, β is the angle between the axis of the trail and the plane TPR, and α is the angle between the (plane-polarized) incident electric vector and the direction PR of the scattered ray. (It is assumed that the receiving antenna can accept all polarizations equally well; otherwise, a further polarization factor must be included.) The 'reflection point' in this case is that point on the axis of the trail whose total distance from transmitter and receiver, r_T+r_R, is a minimum. In practice, q is to be evaluated at this point, and the trail must extend for a distance of the order $[\lambda r_T r_R/(r_T+r_R)(1-\cos^2\beta\sin^2\phi)]^{\frac{1}{2}}$ or more on each side of the reflection point for the full signal to be realized.

As already noted, forward-scatter generalizations of (7)–(9) for overdense trails have not yet been given. They are to be derived, from the simplest assumptions, in the following sections.

CRITICAL ELECTRON DENSITY AND CRITICAL RADIUS

The critical electron density quoted in (6) applies only in the case of normal incidence. For oblique incidence onto a plane interface, at angle of incidence i, the density required for total reflection is reduced by a factor $\cos^2 i$. The angle ϕ appears to be the forward-scatter counterpart of i, for it is half the angle between the incident and scattered rays. Accordingly, the forward-scatter generalization of (6) appears to be

$$N_c = \pi^2 4m/\mu_0 e^2 \lambda^2 \sec^2\phi, \tag{14}$$

which gives the electron density at the effective surface of reflection. The axial distance of this surface is then given by

$$\rho_c = \left[4Dt \cdot \ln\left(\frac{\mu_0 e^2}{4m}\frac{q\lambda^2\sec^2\phi}{4\pi^3 Dt}\right)\right]^{\frac{1}{4}}. \tag{15}$$

The strength of the received signal will be determined from geometric optics, assuming it to be equal to that received from a perfectly reflecting cylinder of radius ρ_c. It may be noted that the duration of the signal can be predicted even at this point, by determining the time required for ρ_c to collapse to zero.

GEOMETRIC REFLECTION FROM A CYLINDER

Consider a circular cylinder of radius ρ which lies along the z axis of a cartesian coordinate system, and a transmitter located at

$$\mathbf{r}_T = [x_T, y_T, z_T].$$

By symmetry, a ray incident on the cylinder at $\rho, 0, 0$ would be reflected

along a line passing through x_T, $-y_T$, $-z_T$. A general point on this line can be specified (by projection) by

$$\mathbf{r}_R = [(r_R/r_T)x_T, -(r_R/r_T)y_T, -(r_R/r_T)z_T]$$

provided that $x_T \gg \rho \ll (r_R/r_T)x_T$, a condition which will be assumed throughout. The vector $\mathbf{r}_R$ will, of course, locate the receiver.

Similarly, a ray incident on ρ, 0, ζ will be reflected through the point x_T, $-y_T$, $-z_T+2\zeta$, and so (by projection) through

$$\mathbf{r}_R' = [(r_R/r_T)x_T, -(r_R/r_T)y_T, -(r_R/r_T)z_T+\zeta+(r_R/r_T)\zeta]$$

provided that $\zeta \ll r_R, r_T$. Lastly, a ray incident at $\rho, \alpha\rho, 0$, (with $\alpha \ll 1$) can be shown to pass through $x_T+2y_T\alpha$, $-y_T+2x_T\alpha$, $-z_T$. (This is demonstrated most readily by rotating the x and y axes through the small angle α, applying symmetry again, and then rotating the axes back to their original position, all the while keeping the transmitter position fixed in the original coordinate system. Only first-order terms in α are retained.) By projection, the reflected ray also passes through

$$\mathbf{r}_R'' = [(r_R/r_T)(x_T+2y_T\alpha), (r_R/r_T)(-y_T+2x_T\alpha), -(r_R/r_T)z_T].$$

The three points which have been specified on the cylinder define a small rectangular area which can be represented both in magnitude and in orientation (of its normal) by the vector

$$\begin{aligned}\mathbf{a}_1 &= [(\rho, \alpha\rho, 0)-(\rho, 0, 0)]\times[(\rho, 0, \zeta)-(\rho, 0, 0)] \\ &= [\alpha\rho\zeta, 0, 0].\end{aligned}$$

By symmetry, this vector bisects the angle between $\mathbf{r}_T$ and $\mathbf{r}_R$, and so forms an angle ϕ with each of these radial vectors. Accordingly, $\mathbf{a}_1$ presents a cross section $\alpha\rho\zeta \cos\phi$ to energy incident from the transmitter. The power radiated towards the rectangle is, then, $P_TG_T\alpha\rho\zeta \cos\phi/4\pi r_T^2$.

After reflection, this power passes through a rectangle whose sides are

$$\boldsymbol{\delta}' = \mathbf{r}_R'-\mathbf{r}_R = [0, 0, \zeta+(r_R/r_T)\zeta] = [0, 0, \{(r_T+r_R)/r_T\}\zeta]$$

and

$$\boldsymbol{\delta}'' = \mathbf{r}_R''-\mathbf{r}_R = [(r_R/r_T)2y_T\alpha, (r_R/r_T)2x_T\alpha, 0].$$

The area of this rectangle can be represented by

$$\mathbf{a}_2 = \boldsymbol{\delta}''\times\boldsymbol{\delta}' = [\{r_R(r_T+r_R)/r_T^2\}2x_T\alpha\zeta, -\{r_R(r_T+r_R)/r_T^2\}2y_T\alpha\zeta, 0]$$

and its cross section as seen from the reflection point is

$$(\mathbf{r}_R.\mathbf{a}_2)/r_R = 2\alpha\zeta[r_R(r_T+r_R)/r_T^3][x_T^2+y_T^2].$$

Accordingly, the power flux at the receiver is

$$\begin{aligned}&[P_TG_T\alpha\rho\zeta \cos\phi/4\pi r_T^2]/2\alpha\zeta[r_R(r_T+r_R)/r_T^3][x_T^2+y_T^2] \\ &\qquad = P_TG_T\rho \cos\phi\, r_T/8\pi r_R(r_T+r_R)(x_T^2+y_T^2).\end{aligned}$$

Then, since the effective area of a matched receiving antenna is $G_R\lambda^2/4\pi$, the received power is

$$P_TG_TG_R\lambda^2\rho \cos\phi\, r_T/32\pi^2r_R(r_T+r_R)(x_T^2+y_T^2).$$

The factor $(x_T^2+y_T^2)$ can be replaced by a function of the more usual forward-scatter parameters as follows. A unit vector, $\mathbf{u}$, normal to the plane of incidence, can be determined from

$$\begin{aligned}\mathbf{r}_T\times\mathbf{a}_1 &= r_T a_1 \sin\phi\,\mathbf{u}\\ &= \alpha\rho\zeta\, r_T \sin\phi\,\mathbf{u}\end{aligned}$$

and

$$\begin{aligned}\mathbf{r}_T\times\mathbf{a}_1 &= [x_T, y_T, z_T]\times[\alpha\rho\zeta, 0, 0]\\ &= [0, \alpha\rho\zeta\, z_T, -\alpha\rho\zeta\, y_T]\end{aligned}$$

whence

$$\mathbf{u} = [0, z_T/r_T \sin\phi, -y_T/r_T \sin\phi].$$

A unit vector along the axis of the cylinder is given by

$$\mathbf{k} = [0, 0, 1],$$

and the angle $(\pi/2-\beta)$ between $\mathbf{u}$ and $\mathbf{k}$ is then given by

$$\sin(\pi/2-\beta) = |\mathbf{u}\times\mathbf{k}| = z_T/r_T \sin\phi,$$

whence

$$\cos\beta \sin\phi = z_T/r_T = [1-(x_T^2+y_T^2)/r_T^2]^{\frac{1}{2}}$$

and

$$x_T^2+y_T^2 = r_T^2[1-\cos^2\beta \sin^2\phi].$$

Accordingly, the received power can be written as

$$P_R = P_T G_T G_R \lambda^2 \rho \cos\phi/32\pi^2 r_T r_R (r_T+r_R)(1-\cos^2\beta \sin^2\phi). \tag{16}$$

POLARIZATION EFFECTS

The geometric-optics approach, which has been employed in the problem so far, precludes any explicit effects of wave polarization. That is, no factor analogous to the $\sin^2\alpha$ factor of (11) can be expected to appear in the treatment given up to this point.

There seems to be little doubt, however, that some polarization effects must be operating at least near the transition region. Keitel's computations for forward-scatter at normal incidence ($\beta = \pi/2$) show a pronounced dip in the effective reflection coefficient, in cases corresponding to $\sin\alpha \to 0$, for ionizations as high as 10^{17} electrons per meter (the highest he treated). The signal does not vanish in these conditions, nor does it reach a minimum precisely at $\alpha = 0$, but some tendency towards a $\sin^2\alpha$ variation in received power does persist. This tendency undoubtedly decreases as q increases, but so too does the number of meteor trails concerned. The $\sin^2\alpha$ factor will be inserted in the formula for overdense trails, as the simplest representation of a variation which is known to occur and which is not taken into account in the direct geometric-optics approach. Fortunately, it is often the case in practice that $\alpha \approx \pi/2$ for the most readily detected trails, so the inclusion of this factor need not affect theoretical predictions to any great extent.

FORWARD-SCATTERED SIGNAL FROM OVERDENSE TRAILS

The signal received from an overdense trail can now be obtained by replacing ρ in (16) by ρ_c from (15), and introducing the $\sin^2\alpha$ factor:

$$(17)\quad P_R'(t) = P_T\left[\frac{G_TG_R\lambda^2\sin^2\alpha}{32\pi^2r_Tr_R(r_T+r_R)(1-\cos^2\beta\sin^2\phi)} \times \frac{4Dt}{\sec^2\phi}\ln\left(\frac{\mu_0e^2}{4m}\frac{q\lambda^2\sec^2\phi}{4\pi^3Dt}\right)\right]^2.$$

In this, the $\cos\phi$ factor of (16) has been replaced by a $1/\sec^2\phi$ factor under the square root. This regrouping has been done simply for convenience of comparison with (7): the transition from backscatter to forward-scatter can be made by expanding the backscatter time scale by a $\sec^2\phi$ factor, and by expanding the backscatter power scale by the factor $2r^3\sin^2\alpha/r_Tr_R(r_T+r_R)\times(1-\cos^2\beta\sin^2\phi)$. It is then immediately evident that the maximum received power is likewise increased by this power factor, and that the time of maximum and the duration of the signal are increased by $\sec^2\phi$ over their backscatter values:

$$(18)\quad (P_R')_{\max} = P_R'(\tau'/\epsilon) = P_T\left[\frac{G_TG_R\lambda^3\sin^2\alpha}{16\pi^4r_Tr_R(r_T+r_R)(1-\cos^2\beta\sin^2\phi)}\right]\left[\frac{\pi}{4\epsilon}\frac{\mu_0e^2}{4m}\right]^2q^2$$

where

$$(19)\qquad \tau' = \frac{\mu_0e^2}{4m}\frac{q\lambda^2}{4\pi^3D}\sec^2\phi$$

is the total duration of the forward-scattered signal.

A comparison of equations (11)–(13) with equations (2)–(4) will show that exactly the same factors are employed in scaling power and time for the underdense trails. Accordingly, if the transition is still taken to occur when the peak powers predicted by the underdense and overdense formulae are equal, then the value quoted in (10) continues to give the transition value of ionization. As in the backscatter case, the peak received power may then be expected to vary as q^2 for q's up to q_T, and as q^2 for greater q's.

CONCLUSION

Formulae have been presented in the past giving the received power to be expected from both underdense and overdense trails in the case of backscatter, and from underdense trails in the case of forward-scatter. No general explicit formula had been given for forward-scatter from overdense trails, nor could one of any great accuracy be expected. Nevertheless, an approximate formula for this case can be of considerable value in the prediction and interpretation of certain forward-scatter data. Accordingly, an attempt has been made here to deduce such a formula, and the relation (17) has been obtained. This is not presented as an accurate relation, but only as a working relation based on a reasonable working model.

On this basis, it is found that the received power still varies as q^2 for over-

dense trails, even in the forward-scatter case. This is a conclusion that has often been assumed tacitly, but never justified.

Finally, if continuity of peak power at the transition is accepted (intuitively, if for no other reason), then the transition value of the ionization is found to be the same for forward-scatter as for backscatter. This is a question that has been at issue for some time in the past.

REFERENCES

BLACKETT, P. M. S. and LOVELL, A. C. B. 1941. Proc. Roy. Soc. (London), A, **177**, 183.

ESHLEMAN, V. R. 1952. Electronic Research Lab., Stanford University, Stanford, Calif., Tech. Rept. No. 49.

——— 1955. Radio Propagation Lab., Stanford University, Stanford, Calif., Tech. Rept. No. 44.

ESHLEMAN, V. R. and MANNING, L. A. 1954. Proc. Inst. Radio Engrs. **42**, 530.

FEINSTEIN, J. 1951. J. Geophys. Research, **56**, 37.

FORSYTH, P. A., HINES, C. O., and VOGAN, E. L. 1955. Can. J. Phys. **33**, 600.

GREENHOW, J. S. 1952. Proc. Phys. Soc. B, **65**, 169.

HERLOFSON, N. 1947. Repts. Progr. in Phys. **11**, 444.

——— 1951. Arkiv Fysik, **3**, 247.

HINES, C. O. 1956. J. Atmospheric and Terrest. Phys. **9**, 229.

HINES, C. O., FORSYTH, P. A., VOGAN, E. L., and PUGH, R. E. 1955. Can. J. Phys. **33**, 609.

HINES, C. O. and VOGAN, E. L. 1957. Can. J. Phys. **35**, 703.

HUXLEY, L. G. H. 1952. Australian J. Sci. Research, **5**, 10.

KAISER, T. R. 1953. Research Revs., Phil. Mag. Suppl. **2**, 495.

KAISER, T. R. and CLOSS, R. L. 1952. Phil. Mag. **43**, 1.

KEITEL, G. H. 1955*a*. Proc. Inst. Radio Engrs. **43**, 1481.

——— 1955*b*. Radio Propagation Lab., Stanford University, Stanford, Calif., Sci. Rept. No. 1.

LOVELL, A. C. B. and CLEGG, J. A. 1948. Proc. Phys. Soc. **60**, 491.

MANNING, L. A. 1953. J. Atmospheric and Terrest. Phys. **4**, 219.

PIERCE, J. A. 1938. Proc. Inst. Radio Engrs. **26**, 892.

VILLARD, O. G., ESHLEMAN, V. R., MANNING, L. A., and PETERSON, A. M. 1955. Proc. Inst. Radio Engrs. **43**, 1473.

WAIT, J. R. 1955. Can. J. Phys. **33**, 189.

THE LOW LEVELS OF Si^{29} [1]

D. A. Bromley, H. E. Gove, E. B. Paul,[2] A. E. Litherland, and E. Almqvist

ABSTRACT

Information on the low levels in Si^{29} has been obtained by studying the gamma radiation associated with the $Si^{29}(p, p'\gamma)Si^{29}$ inelastic-scattering reaction in the proton-energy range from 2.5 to 3.0 Mev. and with the $Al^{29}(\beta^-)Si^{29}$ negatron decay. Angular-distribution measurements have shown that the 2.03 Mev. level in Si^{29} has spin 5/2, and are consistent with a 3/2 assignment to the 1.28 Mev. level. The $E2/M1E2$ branching ratio for the de-excitation of the 2.03 Mev. state has been measured to be approximately 100. Log ft values of < 5.2, > 6.5, and 5.2 have been determined for the branches of the Al^{29} decay to the 2.43, 2.03, and 1.28 Mev. states in Si^{29}.

INTRODUCTION

Recent work on the $Mg^{24}(p, \gamma)Al^{25}$ reaction (Litherland *et al.* 1956, 1957) has shown that many features of the structure of the $A = 25$ system can be correlated with the predictions of a collective model (Nilsson 1955; Bohr and Mottelson 1953, 1955). Such models have in common the prediction that the nuclear distortion should reach a maximum value in the middle region of a shell and that the sign of this distortion should change in this region as well as at the shell boundaries. This prediction is borne out, for example, by the behavior of the observed nuclear quadrupole moments as a function of atomic weight (Townes, Foley, and Low 1949).

In particular, it is known that Al^{27} has a quadrupole moment of $+0.15$ barn while S^{33}, the next measurable nuclide, has a quadrupole moment of -0.06 barn (Blin-Stoyle 1956). Sheline (1956) has analyzed the available data on Al^{28} and concludes that they are consistent with a prolate shape for this nucleus. A study of the low levels of the intermediate nuclide Si^{29} was considered to be of interest in that it provides a further test for the relevance of a collective model to this mass region, as well as providing information on the magnitude and sign of the distortion. The case of Si^{29} was of particular interest in that, in analogy with the case of O^{17}, it seems reasonable to consider the nuclide as consisting of a single nucleon, in this case a neutron, outside of the closed Si^{28} shell. Fortunately there exists a relatively large amount of experimental information bearing on these levels as summarized by Endt and Kluyver (1954). In particular, the $Si^{28}(d, p)Si^{29}$ differential-cross-section measurements of Holt and Marsham (1953), coupled with the work of Roderick, Lönsjö, and Meyerhof (1955) on the beta decay of Al^{29} and P^{29}, determine the parities of these levels and the 3/2 spin of the first and third excited states and, furthermore, restrict the spins of the remaining states below 4 Mev. to one of two possible values. The level excitations have been measured by high-resolution magnetic analyses of the proton groups from the $Si^{28}(d, p)Si^{29}$

[1]Manuscript received May 21, 1957.
Contribution from Atomic Energy of Canada Limited, Chalk River, Ontario.
Issued as A.E.C.L. No. 472.
[2]Present address: Atomic Energy Research Establishment, Harwell, England.

reaction (Endt *et al.* 1951; Van Patter and Buechner 1952). In this paper the results of an experimental study of the gamma radiation produced by inelastic proton scattering on Si^{29}, as well as that associated with the beta decay of Al^{29}, will be presented. In the paper which follows this (Bromley *et al.* 1957), a discussion of these and other data available on the $A = 29$ system in terms of a collective model will be presented. This will include a detailed comparison of the experimental data with the predictions of the Nilsson model, as well as evidence which suggests that the particle-core coupling in the $A = 29$ system is appreciably weaker than that in the $A = 25$ system.

EXPERIMENTAL APPARATUS AND PROCEDURE

The proton beam of the Chalk River electrostatic generator has been used to study the inelastic scattering for proton energies in the range 2.5 to 3.0 Mev. The target consisted of a 30 μg. per sq. cm. metallic silicon deposit electromagnetically enriched to over 90% Si^{29} and deposited directly on a 0.020 in. tantalum backing. This target was prepared by the Isotope Branch at A.E.R.E., Harwell. Gamma radiation associated with the inelastic scattering was detected in sodium-iodide crystal spectrometers consisting of 5 in. diameter by 4 in. long crystals viewed by 5 in. Dumont 6364 photomultipliers. The coincidence circuits available for use in this work were slow, having a resolving time of 1 μsecond, and particular care has been necessary in correcting for the accidental coincidence yield. The system geometry has been described in greater detail in previous publications (Litherland *et al.* 1956; Gove *et al.* 1956) and is shown schematically in Fig. 1. In measuring angular distributions, the geometry is as is shown in this figure with a 5 in. spacing between the front

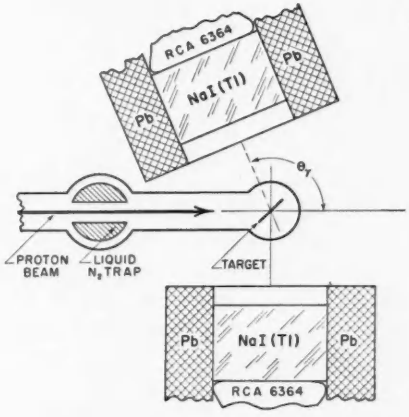

FIG. 1. Schematic representation of the experimental assembly. In studying neutron-produced activities, the target was replaced by the activated sample; the remainder of the experimental geometry remained fixed. The acceptance angle of the crystals was varied by moving them radially with respect to the target.

face of the crystal and the wall of the target tube. In the coincidence measurements, on the other hand, the crystal was moved closer to this tube to obtain maximum solid angle.

The Al^{29} was produced by the $Si^{29}(n, p)Al^{29}$ reaction in 1 in. by 1 in. by $\frac{1}{8}$ in. quartz plates mounted some $\frac{1}{8}$ in. from a tritium target bombarded with deuterons from a 100 kv. Cockcroft–Walton generator. The intensity of 14 Mev. neutrons from the target was monitored to be about 10^9 per second, and activation bombardments of approximately 6 minutes duration were used. In one case to be described later a small, 3-mg. sample of elemental Si^{29} was also activated in similar fashion. After bombardment the samples were inserted in the same target mount and geometry as were used for the inelastic-scattering measurements as shown in Fig. 1.

EXPERIMENTAL RESULTS

$Si^{29}(p, p'\gamma)Si^{29}$

Fig. 2 shows the excitation curve for the 1.28 Mev. radiation from the reaction $Si^{29}(p, p'\gamma)Si^{29}$, corresponding to the de-excitation of the first excited

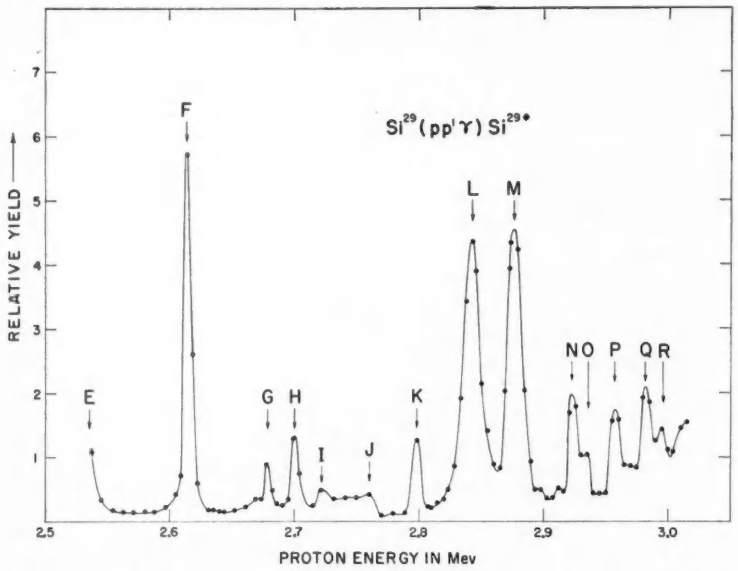

FIG. 2. Yield of 1.28 Mev. radiation from the $Si^{29}(p, p'\gamma)Si^{29}$ reaction as a function of the bombarding proton energy. The alphabetical labelling of the resonances is for identification only.

state in Si^{29}, as a function of the proton bombarding energy. Radiation yield from the 2.03 Mev. second excited state was resonant at only six of these resonances, labelled *G*, *H*, *K*, *M*, *O*, and *P*. The 2.43 Mev. radiation from the third excited state was detected only at resonance *Q*, near the highest

energy available, and then so weakly that further measurements on it were not feasible. The energy scale for this curve is based on the $Li^7(p, n)$ threshold at a proton energy of 1.882 Mev.

Deuteron stripping measurements (Holt and Marsham 1953) showed that the orbital angular momentum l_n of the neutrons captured in the $Si^{28}(d, p)Si^{29}$ reaction leading to the 2.03 Mev. state was equal to two, requiring that the 2.03 Mev. state be either $3/2+$ or $5/2+$. In order to fix the assignment to this level, the angular distribution of the 2.03 Mev. radiation relative to the proton beam was measured at two of the above resonances, namely *K* and *O*. The results of these measurements are shown in parts A and B of Fig. 3

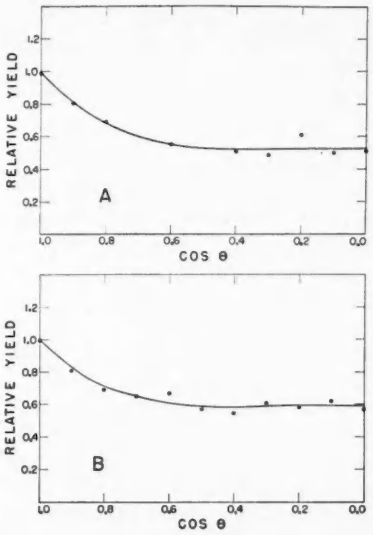

FIG. 3. Angular distributions of the 2.03 Mev. radiation relative to the direction of the incident proton beam. The solid curves are least-squares fits to the experimental points. Curve A was measured at resonance *K*, curve B at resonance *O*.

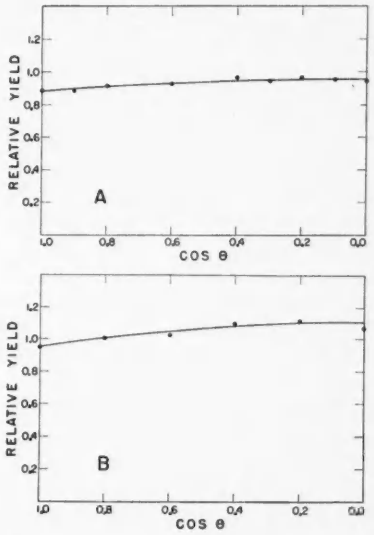

FIG. 4. Angular distributions of the 1.28 Mev. radiation relative to the direction of the incident proton beam. The solid curves are least-squares fits to the experimental points. Curve A was measured at resonance *K*, curve B at resonance *N*.

respectively, where the solid curves are the least-squares fits to expansions in even Legendre polynomials up to and including P_4; these are

$$W(\theta_2) = \alpha\{P_0(\cos\theta_2)+[0.41\pm0.03]P_2(\cos\theta_2)+[0.25\pm0.05]P_4(\cos\theta_2)\},$$

$$W(\theta_2) = \alpha\{P_0(\cos\theta_2)+[0.31\pm0.02]P_2(\cos\theta_2)+[0.20\pm0.03]P_4(\cos\theta_2)\}$$

respectively. These fits have been obtained using the standard program on the FERUT computer at the University of Toronto. Similar measurements on the 1.28 Mev. gamma radiation at resonances *K* and *N* are shown in parts A and B of Fig. 4; the solid curves here represent

$$W(\theta_2) = \alpha\{P_0(\cos\theta_2) - [0.055 \pm 0.006]P_2(\cos\theta_2) + [0.010 \pm 0.015]P_4(\cos\theta_2)\},$$
$$W(\theta_2) = \alpha\{P_0(\cos\theta_2) - [0.110 \pm 0.013]P_2(\cos\theta_2) + [0.001 \pm 0.007]P_4(\cos\theta_2)\}$$

respectively. The subscript 2 in these expressions identifies the radiation measured as shown in a later figure (Fig. 11), and α is an arbitrary intensity factor. Since a $3/2+ \rightarrow 1/2+$ transition can have no terms higher than P_2, the presence of a P_4 term in the 2.03 Mev. gamma-ray distribution eliminates the 3/2 possibility and shows that the 2.03 Mev. state must be $5/2+$. Similarly the absence of a P_4 term in the 1.28 Mev. gamma distribution is consistent with the assignment of $3/2+$ which had been made to this state on the basis of stripping and the beta-decay measurement. This results from the fact that the stripping angular distributions in the $Si^{28}(d, p)Si^{29}$ reaction to this state also show a characteristic $l_n = 2$ pattern, restricting the spin to either 3/2 or 5/2, whereas the beta decay (Roderick *et al.* 1955) from the $1/2+$, P^{29} ground state (Calvert *et al.* 1957) to this state with a log *ft* value of 4.7 is presumably allowed, thus restricting the spin to 3/2.

Branching Ratio of the 2.03 Mev. State

A series of measurements was carried out to determine the branching ratio of the 2.03 Mev. level. Fig. 5A is a typical spectrum of the gamma radiation from the Si^{29} target as obtained with a 30-channel pulse-height analyzer and the 5 in. by 4 in. crystals described previously. This clearly shows both the 1.28 and the 2.03 Mev. radiation and was measured at resonance *K*. The spectrum in Fig. 5B was obtained by setting a voltage gate about the 1.28 Mev. line in Fig. 5A and examining the spectrum of the radiation from the target in coincidence with this gate. The peak section of a Pr^{144} calibration spectrum giving a gamma-ray line at 0.695 ± 0.005 Mev. (Alburger and Kraushaar 1952) has been superposed for comparison and indicates that the peak observed in the coincidence spectrum corresponds to gamma radiation of 780 ± 25 kev. Before being able to identify this gamma radiation as the stopover gamma from the 2.03 to the 1.28 Mev. states in Si^{29}, it was essential to show that it did not result from the de-excitation of the first excited state in P^{30}. Two measurements of the excitation energy of this state have been published; a nuclear emulsion study of the $Si^{29}(d, n)P^{30}$ reaction (Mandeville *et al.* 1952) indicated an excitation of 0.75 ± 0.06 Mev., whereas a more recent measurement of this excitation in a study of the $Si^{29}(p, \gamma)P^{30}$ reaction (Broude *et al.* 1956) yielded a value of 0.690 ± 0.010 Mev.

In order to demonstrate that the 0.780 ± 0.025 Mev. radiation shown in Fig. 5 did not correspond to this radiation, a voltage gate was set on all gamma radiation from the Si^{29} target having energy greater than 3 Mev., and the coincidence spectra were examined. Since only gamma radiation from the $Si^{29}(p, \gamma)P^{30}$ reaction would be expected in this energy region, cascading from the capturing states through the first excited state of P^{30} would be expected to result in a corresponding line in the coincidence spectra. As shown in Fig. 6, this is indeed the case; a Pr^{144} calibration spectrum has again been superposed for comparison, and the observed line has an energy of 0.710 ± 0.020 Mev. in agreement with the measurement of Broude *et al.* (1956).

From the $Si^{28}(d, p)Si^{29}$ magnetic spectrograph measurements (Endt *et al.* 1951; Van Patter and Buechner 1952), the energy of the $M1E2$ cascade transition from the second to the first excited state in Si^{29} should be 0.749 ± 0.010 Mev. Within the quoted errors, the previously quoted energy of 0.780 ± 0.025 Mev. is in agreement with this energy. The difference between the energies of the lines shown in Figs. 5 and 6 is greater than the experimental

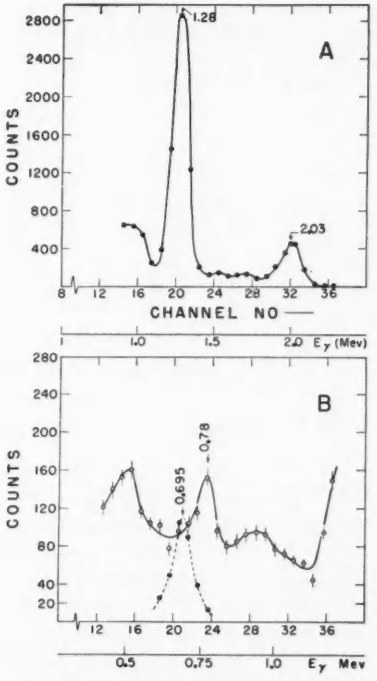

FIG. 5. Gamma radiation associated with the $Si^{29}(p, p'\gamma)Si^{29}$ reaction. Part A is a direct spectrum of this radiation measured at resonance K. Part B is the spectrum of radiation in coincidence with a voltage gate set on the 1.28 Mev. peak appearing in Part A. The dashed line in Part B is the peak of the 0.695 Mev. line in the gamma radiation from a Pr^{144} source which has been superposed for comparison.

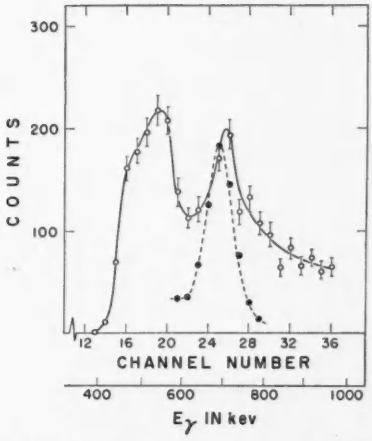

FIG. 6. Gamma radiation associated with the $Si^{29}(p, \gamma)P^{30}$ reaction. This spectrum shows radiation in coincidence with all radiation from the Si^{29} target with energy in excess of 3 Mev. The dashed curve is the 0.695 Mev. Pr^{144} line which has been superposed for comparison. The cutoff at 450 kev. is instrumental.

errors could encompass; consequently the identification of the 0.780 ± 0.025 Mev. radiation as the cascade transition from the 2.03 Mev. Si^{29} state appears reasonable. In the remainder of the paper the energy will be referred to as 0.75 Mev. for purposes of discussion.

The angular correlation of this radiation was measured in coincidence with a voltage gate set on the 1.28 Mev. radiation in a second detector fixed at

90° to the beam axis as a function of the angle between the 0.75 Mev. gamma detector and the beam axis. The results of this measurement at resonance K (2.80 Mev.) are shown in Fig. 7. The solid line in this figure represents a least-

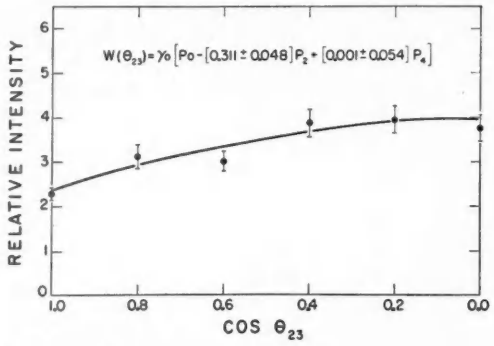

FIG. 7. Angular correlation of the 0.750 Mev. radiation in coincidence with a voltage gate set on the 1.28 Mev. radiation. The solid curve is a least-squares fit to the experimental points having the indicated coefficients.

squares fit to the data, again using even Legendre polynomials up to and including P_4, and is given by

$$W(\theta_{23}) = \alpha_0\{P_0(\cos\theta_{23}) - [0.311 \pm 0.048]P_2(\cos\theta_{23}) + [0.001 \pm 0.053]P_4(\cos\theta_{23})\}$$

(see Fig. 11).

In obtaining the relative intensities of the 1.28, 2.03, and 0.75 Mev. radiations, standard spectral shapes and efficiencies determined for these spectrometers using calibrated radioactive sources have been used. The methods used have been described previously (Litherland *et al.* 1956). These intensities were corrected for the measured angular distributions of the 1.28 and 2.03 Mev. radiations and for the measured correlation of the 0.75 Mev. radiation, with the final result that 99.5% of the de-excitations of the 2.03 Mev. state are by $E2$ radiation directly to the ground state and only about 0.5% by $M1E2$ stopover radiation via the 1.28 Mev. state. Uncertainties in the crystal efficiencies and in the extraction of intensities from the observed spectra would contribute at most a factor of two uncertainty in this value of 0.5%.

As noted previously, the proton energies available were not sufficiently high to allow investigation of the 2.43 Mev. state branching ratio in the inelastic-scattering measurements.

$Al^{29}(\beta^-)Si^{29}$ Measurements

The activation of the Al^{29} was carried out as previously described; Fig. 8 shows two spectra of the gamma radiation associated with the decay of the neutron-produced activity in the quartz samples. Curves A and B in this figure show data obtained in runs of 1 minute duration taken 10 and 20 minutes respectively after the end of the activation bombardments. On the basis of the indicated energies, the 1.28 and 2.43 Mev. radiation has been

identified as associated with the $Al^{29}(\beta^-)$ decay to the corresponding states in Si^{29}. The 1.78 Mev. gamma radiation is then identified with the β^- decay

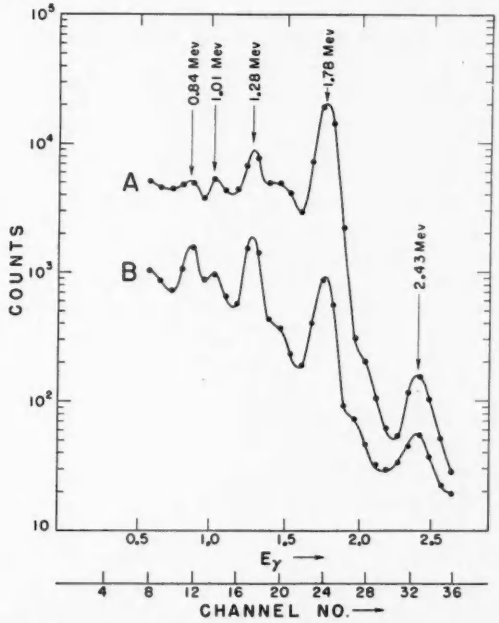

FIG. 8. Gamma radiation associated with the decay of 14 Mev. neutron-produced activity in quartz samples. Curves A and B represent the counts obtained in runs of 1 minute duration starting 10 and 20 minutes respectively after the termination of a 6 minute activation bombardment. Note that the ordinate is logarithmic.

of Al^{28} produced by the $Si^{28}(n, p)Al^{28}$ reaction on the abundant silicon isotope in the samples to the first excited state of Si^{28}, and the 0.84 and 1.01 Mev. radiation with the β^- decay of Mg^{27} produced by the (n, α) reaction on the Si^{30} isotope to the first and second excited states of Al^{27}. From the relative intensities of these radiations, obtained by fitting standard spectral shapes to the total gamma spectra measured at various intervals after the end of the activation bombardments, it was possible to construct the rough decay plots shown in Fig. 9. The indicated half-lives of these decays of 2.3, 6.2, and 6.7 minutes are in good agreement with the published half-lives of 2.3 minutes for Al^{28} and 6.5 minutes for Al^{29} (Endt and Kluyver 1954). The 0.84 and 1.01 Mev. radiations were not sufficiently intense to allow the construction of such a plot.

As a further check on the correctness of these identifications, a 3 mg. sample of separated elemental silicon, enriched to over 90% in Si^{29}, was activated as described previously and the spectrum shown in Fig. 10 measured with this sample inserted in the target chamber. The statistical accuracy

was, of necessity, low, and, after the background is subtracted, several points lie below the base line of this logarithmic plot. The results of the measurement are, however, in agreement with the previous assignments, since the 0.84 and 1.01 Mev. radiations are missing; the 1.78 Mev. radiation results from the activation of residual Si^{28} remaining in this enriched source.

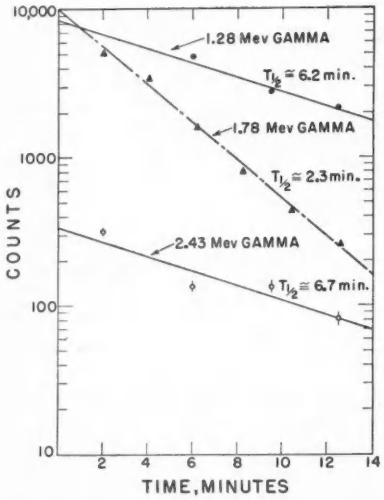

FIG. 9. Decay plots for three of the radiations observed in Fig. 7. The straight lines on the figure correspond to the indicated half-lives. The abscissa is measured from the termination of the activation bombardment.

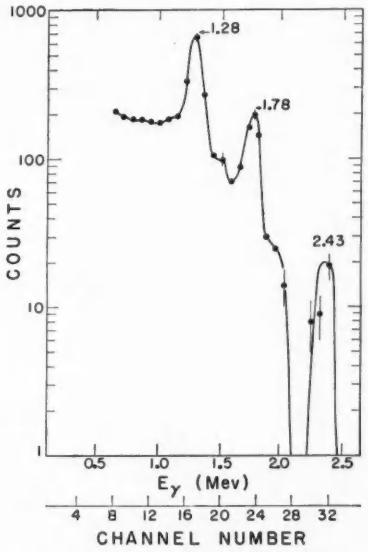

FIG. 10. Gamma radiation associated with the decay of 14 Mev. neutron-produced activity in a 3 mg. sample of elemental silicon enriched to over 90% Si^{29}. Subtraction of background has dropped several points below the base line of this logarithmic plot.

The measurements just described give a ratio of the intensities of the 1.28 Mev. and 2.43 Mev. gamma radiations of 15.2 ± 1.5. This is over a factor of two greater than has previously been reported (Roderick, Lönsjö, and Meyerhof 1955). On the assumption that the de-excitation of the 2.43 Mev. state in Si^{29}, populated in this decay, is entirely via direct transitions to the ground state, these measurements correspond to log ft values of 5.2 for both decay branches, since a branching of the Al^{29} decay to the $1/2+$ Si^{29} ground state has not been reported (Endt and Kluyver 1954). Any branching of the de-excitation of the 2.43 Mev. state in Si^{29} would reduce the corresponding log ft value below 5.2.

The shell-model assignments for the ground states of Al^{29} and P^{29} are $5/2+$ and $1/2+$ corresponding to a single vacancy in the $d_{5/2}$ proton shell and a single proton in the $s_{1/2}$ shell respectively (Mayer and Jensen 1955). These assignments are consistent with the log ft values of <5.2 and 5.2 reported

here for the Al^{29} decay branches to the 3/2+, 2.43 and 1.28 Mev. states in Si^{29}, with the absence of transitions to the Si^{29} ground state, and with the log *ft* values of 4.5, 5.0, and 3.7 found previously (Roderick, Lönsjö, and Meyerhof 1955) for the P^{29} decay branches to the 2.43, 1.28 Mev., and ground states of Si^{29}. Since the ground-state spin of 1/2 of Si^{29} has been determined directly by nuclear magnetic resonance methods (Williams, McCall, and Gertowsky 1954), the observed log *ft* value of 3.7 is consistent with the mirror nature of the decay from the 1/2+, P^{29} ground state. The assignment of 1/2+ to this state has been confirmed by the observation of an $l_p = 0$ pattern in the corresponding $Si^{28}(d, n)P^{29}$ reaction (Calvert *et al.* 1957). A compilation of these data is given in Fig. 1 of the following paper (Bromley *et al.* 1957).

However, with the assignment of 5/2+ to the Al^{29} ground state, the beta-decay branch to the 5/2+, 2.03 Mev. level in Si^{29} would *a priori* be expected to be allowed, with a log *ft* value $\lesssim 5$. By fitting standard spectral shapes to the 1.28 and 2.43 Mev. peaks in spectra such as those in Fig. 8, it has been possible to show that no branching of the Al^{29} decay occurs to the 2.03 Mev. state with a log *ft* value less than 6.5. This is consistent with the lower limit of 6.0 quoted by Roderick *et al.* (1955).

Similarly, no evidence has been found for 1.15 Mev. radiation which would result from cascade de-excitation of the 2.43 Mev. state through that at 1.28 Mev. Because of the presence of the intense 1.78 and 1.28 Mev. radiations in these measurements it is not possible to set a low upper limit on the intensity of this transition if it is present. From spectra such as those shown in Fig. 8 it is, however, possible to show that the intensity of the 1.15 Mev. radiation is not greater than about 100 times that of the 2.43 Mev. radiation. It was not possible in these decay measurements to obtain information on the 400 kev. radiation corresponding to the cascade from the 2.43 to the 2.03 Mev. states because of the high background in this energy range. Consequently it has not been possible to establish other than an upper limit for the log *ft* value for the Al^{29} negatron decay transition to the 2.43 Mev. state. Examination of the $Si^{30}(He^3, \alpha)Si^{29}$ reaction using a $(He^3)^{++}$ beam is planned in this laboratory. Since the *Q* value for the reaction as calculated from current nuclear mass values (Mattauch *et al.* 1956) is 9.96 Mev., it should be possible to excite the 2.43 Mev. level and thus study its de-excitation.

DISCUSSION

The coefficients listed previously for the Legendre polynomial fits to the angular-distribution measurements on the 1.28 and 2.03 Mev. radiation and to the correlation measurement on the 0.75 Mev. radiation must be corrected for attenuation resulting from the finite acceptance angle of the detectors. In making this correction the theoretical treatment of this effect due to Rose (1953) was used. At the spacing of 6.2 in. used in these measurements, between the target and front crystal face, the calculated (Rutledge 1957) attenuation of the a_2 and a_4 coefficients on the angular distributions is 6.5% and 20% respectively, whereas for the correlation measurement, since two identical detectors were used, the corresponding attenuations amount to 13% and 40%

respectively. The coefficients listed in Table I have been corrected for this attenuation.

TABLE I

COEFFICIENTS AND THEIR STANDARD DEVIATIONS IN THE LEAST-SQUARES FIT OF THE DATA OF FIGS. 3, 4, AND 7 TO AN EXPANSION OF THE FORM

$$W(\theta) = \sum_{n=0}^{2} a_{2n} P_{2n}$$

The coefficients have been normalized to a value of unity for a_0 and have been corrected for the finite counter acceptance angles (Rose 1953); proton and gamma-radiation energies are quoted in Mev.; the alphabetical resonance designations refer to the excitation curve of Fig. 2

E_γ'	Resonance	E_p	a_2	a_4
2.03	K	2.80	0.44±0.03	0.30±0.06
	O	2.93	0.33±0.02	0.24±0.04
1.28	K	2.80	−0.058±0.006	0.012±0.018
	N	2.92	−0.110±0.013	0.001±0.007
0.75	K	2.80	−0.351±0.054	0.001±0.073

An attempt has been made, using standard correlation theory (Sharp *et al.* 1954), to obtain information from these measurements on the multipole mixture of the 1.28 and 0.75 Mev. radiations as well as on the resonance K parameters. Using the formalism for a triple angular correlation with intermediate radiation unobserved, the predicted angular distribution of the 2.03 Mev. radiation was calculated for a number of different assumed input channel spins and orbital momenta as well as different values for the total angular momentum for the compound state. The observation of a $P_4(\cos\theta_2)$ term in the angular distribution of the 2.03 Mev. radiation (Fig. 3 and Table I) immediately precludes the possibility of incident s or p waves. The notation adopted is shown in Fig. 11, where I_1 is the spin of the target nucleus, s_1 and l_1 are the input channel spin and orbital angular momentum respectively, j_1 is

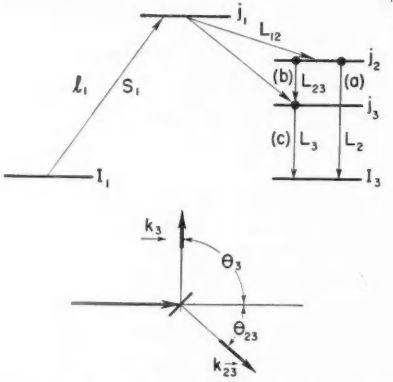

FIG. 11. Schematic illustration of the quadruple-correlation parameter assignments and of the experimental geometry during the measurement. The vectors k_3 and k_{23} represent the detector axes for the final and cascade gamma radiations respectively.

the total angular momentum of the compound state, j_2 that of the intermediate state, and I_3 that of the final state; L_{12} is the total angular momentum carried by the unobserved intermediate radiation or particle and L_2 is that carried by the final radiation. The results obtained are listed in Table II. It should be noted that in this instance the fact that $j_2 = 5/2$ and $I_3 = 1/2$ restricts the value of L_2 to 2—that is, pure quadrupole radiation—and thus appreciably simplifies the computations.

TABLE II

PREDICTED ANGULAR DISTRIBUTIONS OF THE 2.03 MEV. RADIATION IN Si^{29} MEASURED RELATIVE TO THE BEAM AXIS

The entries are the coefficient ratios in the Legendre polynomial expressions for the predicted correlations. The parameters are as shown in Fig. 11

I_1	s_1	l_1	j_1	L_{12}	j_2	L_2	I_3	a_2/a_0	a_4/a_0
1/2	0	2	2	1/2	5/2	2	1/2	0.571	−0.571
1/2	1	2	2	1/2	5/2	2	1/2	0.286	0.381
1/2	1	2	3	1/2	5/2	2	1/2	0.490	−0.299
1/2	1	3	2	1/2	5/2	2	1/2	0.114	−0.190
1/2	1	3	2	3/2	5/2	2	1/2	0.163	0.218
1/2	0	3	3	1/2	5/2	2	1/2	0.571	−0.571
1/2	0	3	3	3/2	5/2	2	1/2	0.314	0.286
1/2	1	3	3	1/2	5/2	2	1/2	0.428	−0.095
1/2	1	3	3	3/2	5/2	2	1/2	0.236	0.048

A comparison of these results with the experimentally determined coefficients at resonance K, corrected for attenuation, as presented in Table I, indicates that, although the agreement is not excellent, the most reasonable set of parameter assignments, assuming no incident channel-spin mixing, is $s_1 = 0$, $l_1 = 3$, $j_1 = 3^-$, and $L_{12} = 3/2$, in addition to those previously fixed, corresponding to f-wave formation and p-wave decay of the 3^- compound state.* Clearly, admixing the $s_1 = 1$ contribution increases the discrepancy with experiment, as does admixture of $L_{12} = 1/2$ (it should be noted that the $L_{12} = 1/2$ and 3/2 contributions add incoherently when the corresponding radiation is unobserved). If one defines the channel-spin mixing parameter t in the usual way (Sharp *et al.* 1954), then on the assumption of d-wave formation and s-wave decay of a 2^+ compound state, while it is not possible to fit the observed coefficients with any value of t, it is of some interest to note that a value of $t = 9$ gives precisely the same prediction for the angular correlation of the 2.03 Mev. radiation as does the set of parameters previously listed for f-wave formation and p-wave decay, namely $W(\theta) = P_0 + 0.314P_2 + 0.286P_4$. Using the expressions given by Sharp *et al.* (1954) to compute the values of t to be expected for pure j–j coupling (neglecting interference) in terms of appropriate Racah coefficients, namely

$$t = \frac{(2s_a+1)W^2(l_1 i_p j_1 I_1, j_p s_a)}{(2s_b+1)W^2(l_1 i_p j_1 I_1, j_p s_b)},$$

*The single-particle width for f-wave formation is approximately 60 kev.

where s_a and s_b are the two allowed channel spins, i_p is the intrinsic spin of the incident particle, j_p its total angular momentum, and the remaining parameters are as defined previously, one obtains, for $j_p = 3/2$, $t = 0.66$, and, for $j_p = 5/2$, $t = 0.15$. These values of t correspond to predicted coefficient ratios of $a_2/a_0 = 0.457$, $a_4/a_0 = -0.194$ and $a_2/a_0 = 0.534$, $a_4/a_0 = -0.446$ respectively and are clearly not in agreement with the measured values as shown in Table I. Examination of the predicted coefficients as functions of t shows that it is not possible to obtain agreement with experiment for any value of t.

It should be noted that the arguments just advanced for the measurements at resonance K are equally applicable to the measurements at resonance O. The fact that these two neighboring resonances show such similar characteristics may well reflect a generic relationship between the corresponding levels in P^{30} as multiplet members.

Because of the remaining discrepancies just noted it is not possible to make a unique parameter assignment at these resonances. Since, however, any information bearing on the multipolarity of the 0.75 Mev. radiation is of considerable interest in any discussion of these data in terms of a particular model (see following paper, Bromley *et al.* 1957), a preliminary analysis of the available data assuming pure channel spin 0, f-wave formation, and p-wave decay of a 3^- compound state has been carried out.

The calculation, analogous to that just presented for the 2.03 Mev. radiation, for that of 1.28 Mev. involves an additional parameter, since the spins involved $(3/2 \rightarrow 1/2)$ do not preclude $M1E2$ multipole mixtures. The result obtained for this assignment for resonance K is

$$W(\theta_2) = P_0(\cos\theta_2) + \frac{0.40}{1+x^2}(x^2-3.46x-1)P_2(\cos\theta_2),$$

where $x = |S_E|/|S_M|$ is the multipole-mixture parameter as defined by Sharp *et al.* (1954).

Comparison of this expression with the data of Table I gives $x = 3.25$ or -0.23 depending upon whether the relative phases of the $M1$ and $E2$ components of the radiation differ by 180° or 0°.*

The expressions given in CRT-556 (Sharp *et al.* 1954) may be extended to the case of a quadruple correlation with the first intermediate radiation unobserved. In general such a calculation is of formidable proportions; however, with the assumptions just listed it becomes feasible. The parameters involved are shown schematically in Fig. 11 as well as the geometric arrangement of the detectors when measuring this correlation. Neglecting interference between compound states, the expression for the correlation components of the cascade gamma ray, in coincidence with the final gamma ray detected in a fixed counter at 90° to the incident beam, is given by (Sharp 1957)

$$W(L_{23}L'_{23}; L_3L'_3) = \sum_{k_1k_3k_{23}} (-1)^{s_1-I_3+j_2+j_3+L_{12}+L'_{23}} Z_0(l_1j_1l_1j_1, s_1k_1)$$

*The Huby phase correction (1954) has been included here.

$$\times W(j_1 j_2 j_1 j_2, L_{12} k_1) \cdot G_1 \begin{pmatrix} j_2 L_{23} j_3 \\ k_1 k_{23} k_3 \\ j_2 L'_{23} j_3 \end{pmatrix} Z_1(L_3 j_3 L'_3 j_3, I_3 k_3) \Omega_{k_1 k_3 k_{23}},$$

where $\Omega_{k_1 k_3 k_{23}}$ is a geometric factor given by

$$\Omega_{k_1 k_3 k_{23}} = \sum_{\mu_1 \mu_3} (k_1 k_3 \mu_1 \mu_3, k_{23}\, \mu_1 + \mu_3) \left\{ \frac{(4\pi)^3}{(2k_1+1)(2k_3+1)(2k_{23}+1)} \right\}^{1/2}$$
$$\times Y_{k_1}^{\mu_1}(\theta_1 \phi_1) \cdot Y_{k_3}^{\mu_3}(\theta_3 \phi_3) \cdot Y_{k_{23}}^{\mu_1+\mu_3 *}(\theta_{23} \phi_{23}).$$

If the multipole parameter for the final 1.28 Mev. radiation is taken as x as in the case just considered and that of the 0.75 Mev. cascade radiation as y, then the predicted correlation is of the form

$$W(\theta_{23}) = W(11:11) + 2xW(11:12) + x^2 W(11:22) + y^2 W(22:11)$$
$$+ 2y^2 x W(22:12) + x^2 y^2 W(22:22) + 2yW(12:11)$$
$$+ 4xyW(12:12) + 2x^2 yW(12:22).$$

If the coefficients in the resulting expression are compared with those obtained in the Legendre polynomial fit to the measured correlation as listed in Table I and $x = 3.25$ is assumed from the previous calculation, the indicated value of y is 25.87 or 0.05, whereas assuming $x = -0.23$ results in a value of y of 40.32 or 0.05. The available information is not adequate to obtain unique values for x and y. It is, however, interesting to note that the above values for y indicate that, on the assumption of f-wave formation and p-wave decay of the resonance involved, the 0.75 Mev. radiation is either almost pure $E2$ or pure $M1$.

As will be discussed in the following paper (Bromley *et al.* 1957), if this radiation is pure $E2$, the branching ratio of 100 observed for the de-excitation of the 2.03 Mev. state is in rough agreement with the predictions of a simple single-particle model (Wilkinson 1956); if, on the other hand, it is pure $M1$, the predicted value is 1.7×10^{-5}. It must be emphasized, however, that the analysis just presented is preliminary and may well not be unique. A similar calculation is not feasible for the case of d-wave formation with incident channel-spin mixing, since the additional parameters thus introduced cannot be determined from the available data.

Further discussion of the results presented herein and other information bearing on the low levels of Si^{29} will be deferred to the following paper (Bromley *et al.* 1957), where it will be shown that the experimental data can be correlated with the predictions of a collective model. Detailed comparisons of these data with the predictions of the Nilsson (1955) strong-coupling collective model, which has been used to describe the properties of the $A = 25$ isobaric system (Litherland *et al.* 1957), will be presented together with some evidence which suggests that collective vibrational oscillations characteristic of an intermediate-coupling model may also play a role in this mass region.

The comparison with the strong-coupling model indicates that Si^{29} has an

oblate shape with a value for the spheroidicity parameter $\delta \approx -0.15$.* Here $\delta \approx \Delta R/R_0$, where R is the mean radius of the spheroid and ΔR is the difference between the major and minor semi-axes. Although agreement between the experimentally observed quantities and the model predictions is in some cases only qualitative, it will be shown that current collective models have relevance for the description of the static and dynamic properties of nuclides in this mass region.

REFERENCES

ALBURGER, D. E. and KRAUSHAAR, J. 1952. Phys. Rev. **87**, 448.
BLIN-STOYLE, R. J. 1956. Revs. Mod. Phys. **28**, 75.
BOHR, A. and MOTTELSON, B. R. 1953. Kgl. Danske Videnskab. Selskab, Mat.-fys. Medd. **27**, No. 16.
——— 1955. Beta- and gamma-ray spectroscopy, *edited by* K. Siegbahn (Interscience Publishers, Inc., New York), Chap. XVII.
BROMLEY, D. A., GOVE, H. E., and LITHERLAND, A. E. 1957. Can. J. Phys. **35**, 1057.
BROUDE, C., GREEN, L. L., SINGH, J. J., and WILLMOTT, J. C. 1956. Phys. Rev. **101**, 1052.
CALVERT, J. M., JAFFE, A. A., and MASLIN, E. E. 1957. Proc. Phys. Soc. (London), A, **70**, 78.
ENDT, P. M. and KLUYVER, J. C. 1954. Revs. Mod. Phys. **26**, 95.
ENDT, P. M., VAN PATTER, D. M., BUECHNER, W. W., and SPERDUTO, A. 1951. Phys. Rev. **83**, 491.
GOVE, H. E., BARTHOLOMEW, G. A., PAUL, E. B., and LITHERLAND, A. E. 1956. Nuclear Phys. **2**, 132.
HOLT, J. R. and MARSHAM, T. N. 1953. Proc. Phys. Soc. (London), A, **66**, 467.
HUBY, R. 1954. Proc. Phys. Soc. (London), A, **67**, 1103.
LITHERLAND, A. E., MCMANUS, H., PAUL, E. B., BROMLEY, D. A., and GOVE, H. E. 1957. Can. J. Phys. (To be published).
LITHERLAND, A. E., PAUL, E. B., BARTHOLOMEW, G. A., and GOVE, H. E. 1956. Phys. Rev. **102**, 208.
MANDEVILLE, C. E., SWAN, C. P., CHATTERJEE, S. D., and VAN PATTER, D. M. 1952. Phys. Rev. **85**, 193.
MATTAUCH, J., WALDMANN, L., BIERI, R., and EVERLING, F. 1956. Z. Naturforsch. **11a**, 525.
MAYER, M. G. and JENSEN, J. H. D. 1955. Elementary theory of nuclear shell structure (John Wiley & Sons, Inc., New York).
NILSSON, S. G. 1955. Kgl. Danske Videnskab. Selskab, Mat.-fys. Medd. **29**, No. 16.
RODERICK, H., LÖNSJÖ, O., and MEYERHOF, W. E. 1955. Phys. Rev. **97**, 97.
ROSE, M. E. 1953. Phys. Rev. **91**, 610.
RUTLEDGE, A. R. 1957. Private communication.
SHARP, W. T. 1957. Private communication.
SHARP, W. T., KENNEDY, J. M., SEARS, B. J., and HOYLE, M. G. 1954. Chalk River Report CRT-556 (unpublished).
SHELINE, R. K. 1956. Nuclear Phys. **2**, 382.
TOWNES, C. H., FOLEY, H. M., and LOW, W. 1949. Phys. Rev. **76**, 1415.
VAN PATTER, D. M. and BUECHNER, W. W. 1952. Phys. Rev. **87**, 51.
WILKINSON, D. H. 1956. Phil. Mag. **1**, 127.
WILLIAMS, G. A., MCCALL, D. W., and GERTOWSKY, H. S. 1954. Phys. Rev. **93**, 1428.

*This assumes a value of $\kappa = 0.05$, where κ is the parameter introduced by Nilsson as a measure of the strength of the spin–orbit interaction assumed. There is evidence which suggests that a larger value of κ may be more appropriate for d-shell nuclei; since δ is approximately proportional to κ, increase in κ will be reflected in δ (see Eq. 8 of the following paper (Bromley *et al.* 1957)).

APPLICATION OF A COLLECTIVE MODEL TO Si^{29} [1]

D. A. Bromley, H. E. Gove, and A. E. Litherland

ABSTRACT

A strong-coupling collective model has been applied to a description of the low levels of Si^{29}. Detailed comparisons of the predictions of this model with static and dynamic properties of the low levels of the $A = 29$ isobaric system have been made; experimental data on the level spectrum, ground-state magnetic moment, decoupling parameter, reduced widths for nucleon capture in deuteron-induced stripping reactions, as well as gamma- and beta-ray transition widths have been used in the comparisons. These indicate that Si^{29} has an oblate shape with a spheroidicity parameter $\delta \simeq -0.15$. Although agreement between experiment and theory is in some cases only qualitative, it is shown that current collective models have relevance for the description of nuclear properties in this mass range.

INTRODUCTION

As noted in the preceding paper (Bromley *et al.* 1957), the apparent qualitative success obtained in correlating the experimental data on the $A = 25$ isobaric system with the predictions of a collective model (Litherland *et al.* 1956, 1957), together with the strong $E2/M1E2$ branching ratio observed in Si^{29}, suggests the possibility of a collective interpretation of the properties of the $A = 29$ system and, in particular, of the low levels of Si^{29}.

Before going on to a detailed comparison of the experimental data available on the low levels of this system, as shown in Fig. 1, with the predictions of the rotational collective model, a brief discussion of two other models will be given. These two models might *a priori* be expected to have more relevance to Si^{29}.

Single-Particle Model

If Si^{29} is considered as a single neutron outside of a closed Si^{28} core, a single-particle model with assignments of $d_{5/2}$, $d_{3/2}$, and $s_{1/2}$ to the 2.03 Mev., 1.28 Mev., and ground states of Si^{29} (Fig. 1) might be expected to be particularly applicable. The following data are of interest in examining this applicability:

(*a*) If one considers the gamma-ray transition probabilities given by Moszkowski (1955) for the Weisskopf (1951) single-particle model and includes the effective charge factors arising from nuclear recoil (Bohr and Mottelson 1953), one obtains for a radius of $1.45\times10^{-13}A^{1/3}$ cm. and E_γ in Mev. the following expressions:

$$T_{sp}(M1) = 2.8\times10^{13}E_\gamma^{3}\ \text{sec.}^{-1}\ \text{(odd proton)}, \tag{1a}$$

$$= 1.95\times10^{13}E_\gamma^{3}\ \text{sec.}^{-1}\ \text{(odd neutron)}; \tag{1b}$$

$$T_{sp}(E2) = 1.6\times10^{8}(1+Z/A^{2})^{2}A^{4/3}E_\gamma^{5}\ \text{sec.}^{-1}\ \text{(odd proton)}, \tag{2a}$$

$$= 1.6\times10^{8}Z^{2}A^{-8/3}E_\gamma^{5}\ \text{sec.}^{-1}\ \text{(odd neutron)}. \tag{2b}$$

[1]Manuscript received May 21, 1957.
Contribution from Physics Division, Atomic Energy of Canada Limited, Chalk River, Ontario.
Issued as A.E.C.L. No. 474.

In the case of the 0.75 Mev. cascade radiation from the 2.03 to the 1.28 Mev. state in Si^{29} (Bromley *et al.* 1957), equations (1) and (2) lead to a predicted branching ratio for the 2.03 Mev. state de-excitation of 1.66×10^{-5} for a single-neutron transition characteristic of Si^{29}; for comparison, the corresponding prediction for a single-proton transition is 4.31×10^{-2}. The observed branching ratio is $\sim$100. Since this transition is between $d_{5/2}$ and $d_{3/2}$ states, it is not possible to invoke l forbiddenness or other selection rules in this model to provide the inhibition of the $M1$ component of this radiation by the factor of at least 10^4 which would be required to bring the model predictions into agreement with this observation. A direct measurement of the multipole mixture in this radiation would be of considerable interest; unfortunately the preliminary analysis of the angular correlation of this radiation, presented in the preceding paper (Bromley *et al.* 1957), does not give a unique result. The analysis carried out by Wilkinson (1956) on some 34 $M1$ transitions in relatively light nuclei (albeit all in the p shell) indicates that the widths for these $M1$ transitions have a distribution centering on 0.15 of the Weisskopf prediction and a spread such that 85% of them occur within factors of 0.015 and 1.5 times these predictions. The inhibition factors $\sim$100 indicated for the low edge of this distribution are in many instances attributable to l forbiddenness. The experimental observations on the 0.75 Mev. radiation require an inhibition by at least a factor of 100 beyond this without the possibility of invoking l forbiddenness; these observations are therefore not consistent with this model.

(*b*) The preliminary analysis of the angular distribution of the 1.28 Mev. radiation presented in the preceding paper indicates that this radiation has an appreciable $M1$ component. Here the $M1$ component of such a transition from a $d_{3/2}$ to an $s_{1/2}$ state would be l forbidden (Mayer and Jensen 1955); it should be noted, however, that the inhibition factors normally associated with this forbiddenness are at most $\sim$100 and that these are not sufficiently great to indicate a significant discrepancy between the model predictions and the experimental results.

(*c*) The predicted magnetic moment for Si^{29} is -1.91 n.m., whereas the experimental value is -0.555 n.m. (Blin-Stoyle 1956). It should be noted here that, in the analogous case of O^{17}, with a measured moment of -1.89 n.m. (Blin-Stoyle 1956), the agreement is excellent, suggesting appreciably greater relevance for this model for O^{17}. Bohr and Mottelson (1953) have suggested that the relatively small magnitude of the Si^{29} magnetic moment may be understood in terms of a small $d_{3/2}$ admixture in the $s_{1/2}$ ground state consistent with an oblate shape for the nuclear surface.

(*d*) Finally, the model does not accord with the high log ft value >6.5 observed for the branch of the Al^{29} beta decay to the 2.03 Mev. state in Si^{29}.

Vibrational Collective Model

The fact that the Si^{28} core, on a pure j–j coupling picture, corresponds to the closing of the $d_{5/2}$ shell for both protons and neutrons suggests that collective effects of a vibrational nature may be important. Thus if the core is sufficiently symmetric to prefer a spherical shape, the collective behavior is

manifested in vibrational oscillations of the nuclear shape about this spherical shape (Alder *et al.* 1956) rather than in rotational motion of the entire nucleus about an axis perpendicular to the symmetry axis of the assumed fixed distortion. In this model the nucleon-to-core coupling strength is intermediate between the strong and weak coupling limits considered in the original treatments (Bohr and Mottelson 1953). For these nuclides the model is characterized by a level sequence $0+$, $2+$, $(0+\ 2+\ 4+)$, where the last three bracketed levels are expected to form a relatively closely spaced triplet, by excitations such that $2 \leqslant E_2/E_1 \leqslant 2.5$, where E_2 and E_1 are the observed excitation energies of the second and first excited states respectively, and by marked inhibition of $M1$ transitions, in agreement with experimental data in the range $66 < A < 150$ (Scharff-Goldhaber and Weneser 1955). Similar predictions were obtained for even–even nuclei by Wilets and Jean (1956) using a collective model which retains strong coupling and includes γ-instability (Bohr and Mottelson 1953). That these models may have relevance to the nuclides in the region of Si^{28} is evidenced by the fact that for Si^{28} $E_2/E_1 = 2.5$, and measurements on the $Al^{27}(p, \gamma)Si^{28}$ reaction (Gove *et al.* 1957) indicate a level in Si^{28} at 4.64 ± 0.02 Mev. with $J \geqslant 3$ as well as the possibility of a further level at 4.62 with $J \leqslant 2$ (see also Endt and Paris 1956). However, there is as yet no evidence for a $J = 0$ level in this energy region, nor is there evidence of an $l_n = 0$ stripping pattern for the $Al^{27}(d, n)Si^{28}$ reaction leading to a level at $\sim$4.6 Mev. in Si^{28} (Calvert *et al.* 1955; Rubin 1957). Further measurements on Si^{28} are required, therefore, before any final conclusions can be drawn regarding the relevance of this model to this region.

It may be of interest to note that a smooth curve drawn through the points of the plot of the ratio E_2/E_1 against the parameter $E_1/\hbar\omega$ given by Wilets and Jean (1956), for heavier nuclides where the vibrational collective model appears to be applicable, indicates a value of $E_1/\hbar\omega = 0.15$ corresponding to $E_2/E_1 = 2.59$ for Si^{28}. If a value of $\hbar\omega \approx 5$ Mev. as given by Bohr and Mottelson (1953, Fig. 2) is assumed for Si^{28}, then $E_1/\hbar\omega \cong 0.36$. This discrepancy is greater than that for all but two of the 60 cases considered by Wilets and Jean (1956).

If, instead, a value of $\hbar\omega = \hbar\omega_\beta = \hbar\omega_\gamma \approx 12$ Mev., as is consistent with the magnitude of the vibration–rotation term in the energy level spectra of nuclides in this mass region, is assumed for Si^{28}, $E_1/\hbar\omega \approx 0.15$ in agreement with the extrapolated curve. (See the following section on the Decoupling Parameter.)

Comparison of the available data with the intermediate-coupling model would require detailed eigenfunctions and eigenvalues for the single-particle orbits analogous to those published by Nilsson for the strong-coupling model. As yet, no such calculations are available.

Rotational Collective Model

The experimental evidence just presented is not in complete accord with the predictions of either the single-particle or the vibrational collective model.

The strong $E2$ crossover radiation observed in Si^{29} from the 2.03 Mev. state is suggestive of the predictions of a rotational collective model for similar

transitions in heavy nuclides. The Nilsson model, which has been used with qualitative success in the $A = 25$ system (Litherland *et al.* 1956, 1957), is a generalized single-particle one in that the single nucleon is considered to be strongly coupled to a deformed core consisting of the remaining nucleons. Nilsson has considered only the case of axially symmetric spheroidal deformations and has calculated the eigenfunctions and eigenvalues for the single-particle orbits in the resulting spheroidal potential, including spin–orbit coupling. On each of the levels so defined, corresponding to different intrinsic nuclear structure, rotation of the nucleus as a whole produces rotational bands of levels, all with the same intrinsic structure. This model would be expected to apply to nuclides with well-developed rotational level spectra, which, in the case of even–even nuclides, results in a low-energy level sequence with energies $E = [\text{constant}] \times I(I+1)$, where I is the total angular momentum of the level with characteristic assignments of $0+$, $2+$, $4+$ to the first three levels in ascending order. This expression does not include the vibration–rotation interaction terms, which will be discussed later. The predicted ratio for the excitations of the second and first excited states in this model is clearly $E_2/E_1 = 3.33$. As an example, Mg^{24} is known to have the characteristic level sequence $0+$, $2+$, $4+$ with $E_2/E_1 = 3.0$ (Endt and Kluyver 1954); Al^{25} and Mg^{25}, corresponding respectively to the addition of a single proton and neutron to the Mg^{24} core, have been shown to have characteristics which accord well with the predictions of this model, as noted above.

It has been suggested by Bohr and Mottelson (1955) that a criterion for the transition between rotational spectra characteristic of a strong-coupling model and vibrational spectra characteristic of an intermediate-coupling model is that, for even–even nuclides, the excitation energy of the first excited $(2+)$ state is such that

$$E(2) \approx 3\hbar^2/0.23\mathcal{I}_{\text{rigid}} \approx 32\hbar^2/MAR_0^2. \tag{3}$$

Rotational spectra are to be expected for even–even nuclides with $E(2)$ less than this critical value. For Mg^{24} and Si^{28}, $E(2) = 1.37$ and 1.77 Mev. respectively, and the corresponding critical values as computed from equation (3) are 3.54 and 2.22 Mev. respectively. This is consistent with the observation that Al^{25} and Mg^{25}, with single nucleons outside the Mg^{24} core, appear to have well-defined rotational characteristics (Litherland *et al.* 1957) and suggests that the strong-coupling model may also have relevance for the description of the properties of Si^{29} despite the fact that, as noted previously, on a pure j–j coupling assumption, Si^{28} would be expected to be spherically symmetric with consequent lack of a stable distortion for Si^{29} (Alder *et al.* 1956).

The spirit of the discussion to follow will be to examine, in as great detail as possible, the comparison between the predictions of this model and the available experimental information; this includes the decoupling parameter for the rotational band based on the ground state, the moment of inertia also deduced from the level spectrum, the ground-state magnetic moment, the level sequence itself, the reduced widths for nucleon capture in deuteron-

induced stripping reactions, as well as gamma- and beta-ray transition widths. In addition, the model predictions for the total binding energy of Si^{29} will be presented as a function of the nuclear shape. The intent of this examination is, first, to attempt to establish the extent to which this model is applicable to Si^{29}, and, second, to this extent, to arrive at the sign and magnitude of the Si^{29} spheroidicity.*

RESULTS

Decoupling Parameter

In this model the $K = 1/2$ (Nilsson orbit 9, see Fig. 3) rotational band based on the $1/2+$ ground state could comprise either the level sequence at excitations of 0, 1.28, and 2.03 Mev. or that at 0, 2.03, and 2.43 Mev., both of which contain levels of total angular momentum $I = 1/2$, $3/2$, and $5/2$. The second of these sequences would leave the state at 1.28 Mev. as the base for a $K = 3/2$ (orbit 8) rotational band. K, the quantum number introduced by Bohr and Mottelson (1953), is the projection of the total angular momentum I on the nuclear-symmetry axis. In Fig. 1, two sets of K values are listed corresponding to these two sequences, the first, in parentheses, corresponding

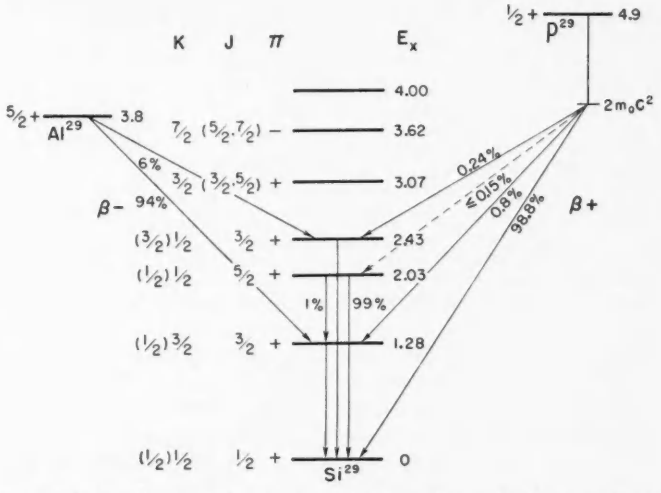

FIG. 1. Compilation of some of the experimental information available on the low levels of Si^{29} and the $A = 29$ isobaric system. Energies are referred to the ground state of Si^{29}. The values of K in parentheses are those corresponding to a prolate shape. The evidence presented in this paper favors the alternate K assignments corresponding to oblate shape.

to a prolate shape (positive spheroidicity) and the second corresponding to an oblate shape (negative spheroidicity).

*The term "spheroidicity" is used instead of the more usual "distortion" or "deformation" since it more correctly implies that only a special set of "distortions" or "deformations" is considered, namely those with axial symmetry.

In either case, for $K = 1/2$, the rotational spectrum is modified (Bohr and Mottelson 1953) and is given by

$$(4) \quad E_K(I) = E_K{}^0 + (\hbar^2/2\mathscr{I})\{I(I+1) + \delta_{K,1/2}\, a(-1)^{I+\frac{1}{2}}(I+\tfrac{1}{2})\} - 4(\hbar^2/2\mathscr{I})^3[3/(\hbar\omega_\beta)^2 + (1/\hbar\omega_\gamma)^2]\{I(I+1) + \delta_{K,1/2}\, a(-1)^{I+\frac{1}{2}}(I+\tfrac{1}{2})\}^2,$$

where $\mathscr{I}$ is the moment of inertia, a is the decoupling parameter characterizing the partial decoupling of the intrinsic particle spin from the rotational motion of the core, and $\hbar\omega_\beta$ and $\hbar\omega_\gamma$ are vibrational quanta associated with the quantum numbers n_β and n_γ defined by Bohr and Mottelson (1953). The third term in this expression is the vibration–rotation interaction energy which was neglected in the previous discussion.

Since the $I = 7/2+$ fourth member of the rotational band in Si^{29} has not been identified, it is not possible to solve for the five unknowns in this equation using only measured excitations in Si^{29}. In order to obtain values of a and $\hbar^2/2\mathscr{I}$ for this band, the factor $[3/(\hbar\omega_\beta)^2 + (1/\hbar\omega_\gamma)^2]$ appearing in equation (4) was obtained from the measured level excitations in the core nucleus, Si^{28}, by taking, for purposes of argument, the level at 4.64 Mev. as the $4+$ member of the ground-state rotational band, as is consistent with the $Al^{27}(p, \gamma)Si^{28}$ measurements (Gove *et al.* 1957), and solving the above equations for $\hbar^2/2\mathscr{I}$ and this factor. The value obtained for $\hbar^2/2\mathscr{I}$ was 0.32 Mev., and for comparison purposes, if one makes the assumption that $\hbar\omega_\beta = \hbar\omega_\gamma = \hbar\omega$, the indicated value is $\hbar\omega = 12$ Mev., which is of the expected order of magnitude for nuclides in this mass region.

Using this value for the vibrational quanta in the vibration–rotation term in equation (4), the resulting sets of equations for both of the level sequences postulated for the $K = 1/2$ ground-state band in Si^{29} have been solved numerically, giving for an assignment of $K = 3/2$ to the 1.28 Mev. state $\hbar^2/2\mathscr{I} = 0.40$ Mev. and $a = +1.20$ and for an assignment of $K = 1/2$ to this state $\hbar^2/2\mathscr{I} = 0.31$ Mev. and $a = +0.46$. The vibration–rotation correction decreases the values of a by 3% and raises the $\hbar^2/2\mathscr{I}$ value by 8%.

In Fig. 2, the values of a obtained have been superposed on a plot of the decoupling parameter as a function of the nuclear spheroidicity δ as calculated using the Nilsson eigenfunctions. From the figure, a value of $a = +1.20$ is consistent with $\delta \simeq -0.20$ or -0.05, whereas $a = +0.46$ is consistent with $\delta = +0.15$. Consequently a $K = 3/2$ assignment to the 1.28 Mev. state implies an oblate shape for Si^{29} and a $K = 1/2$ assignment a prolate shape.

Moments of Inertia

The values of $\hbar^2/2\mathscr{I}$ obtained above are in good agreement with that for Si^{28}, with that corresponding to a prolate shape for Si^{29} more nearly equal to the Si^{28} value. It should be noted that in heavy elements the observed moments of inertia of odd-A nuclei are systematically larger than those of neighboring even–even nuclei by amounts varying from a few per cent up to as much as 40% (Bohr and Mottelson 1955). Here again the value of $\hbar^2/2\mathscr{I}$ for the prolate sequence indicates a larger value of $\mathscr{I}$ for Si^{29} than for Si^{28} in agreement with this observation, whereas for the oblate sequence

Si^{29} is indicated as having a smaller value of $\mathcal{I}$ than Si^{28}. Because of the relatively small difference between the $\hbar^2/2\mathcal{I}$ values for the two sequences, however, these comparisons do not serve as significant evidence for either shape.

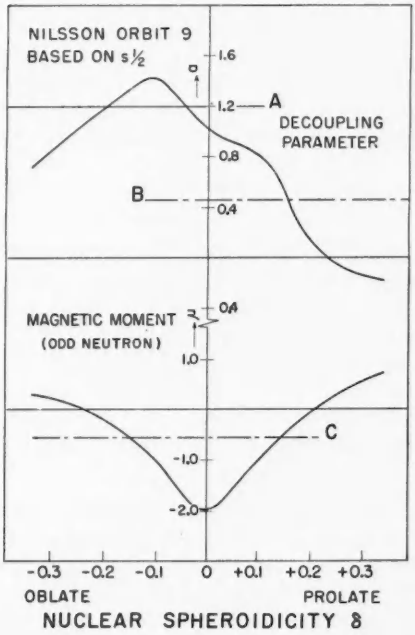

FIG. 2. Decoupling parameter and magnetic moment. The horizontal lines A, B, and C represent the values of the decoupling parameters calculated from the Si^{28} level spectrum for oblate and prolate assignments and of the ground-state magnetic moment of Si^{29} respectively.

It may be of interest to compare the values of $\hbar^2/2\mathcal{I}$ found for this mass region with that predicted for rigid rotations and the ratio of these values with the corresponding ratios for heavy nuclides. If the expression given by Bohr and Mottelson (1955) for the nuclear moment of inertia of even–even nuclei for rigid rotations is used, for Si^{28}

$$\hbar^2/2\mathcal{I}_{\text{rigid}} = 27.469A^{-5/3}[1-0.3\delta] \tag{5}$$

to first order in δ. For purposes of argument, it is convenient to disregard the δ dependence entirely here for the range of δ values of interest, namely $|\delta| < 0.2$. This gives $\hbar^2/2\mathcal{I}_{\text{rigid}} \simeq 100$ kev. and $\mathcal{I}/\mathcal{I}_{\text{rigid}} = 0.32$. If the smooth curve of $\mathcal{I}/\mathcal{I}_{\text{rigid}}$ versus $\beta = 1.06\delta$ given by Bohr and Mottelson (1955) for even–even nuclei in the region $150 \leqslant A \leqslant 188$ is extrapolated to $|\delta| = 0.15$ corresponding to Si^{28}, the predicted value of $\mathcal{I}/\mathcal{I}_{\text{rigid}}$ is approximately 0.15.

Magnetic Moment

Also in Fig. 2, the experimentally measured magnetic moment of the Si^{29} ground state of -0.555 nuclear magnetons (Dharmatti and Weaver 1951) has been superposed on a plot of this magnetic moment calculated as a function of the spheroidicity for an odd neutron. This is consistent with values of $\delta = -0.15$ and $+0.15$ and thus precludes the -0.05 value consistent with a decoupling parameter of 1.20 but does not distinguish between $\delta = \pm 0.15$.

As noted previously, Bohr and Mottelson (1953) have suggested that the departure of the Si^{29} magnetic moment from the single $s_{1/2}$ neutron value, expected in a single-particle model and found for O^{17}, may be understood in terms of a small admixture of $d_{3/2}$ into the $s_{1/2}$ ground state, consistent with an oblate shape (see Fig. 3, Nilsson orbits 8 and 9).

Level Sequence

The fact that the $Si^{28}(d, p)Si^{29}$ stripping measurements (Holt and Marsham 1953) indicate that the 3.62 Mev. state in Si^{29} has negative parity and either 5/2 or 7/2 spin is consistent only with negative spheroidicity in the Nilsson model. There is no mechanism in this model whereby this high-spin, negative-parity state (orbit 10) should lie lower than several lower-spin states of the same parity if the spheroidicity were positive. This is in fact the most striking single piece of experimental evidence available for the assignment of an oblate shape to Si^{29} on the assumption that a collective model is applicable.

Total Binding Energy

Using the Nilsson model, it is possible to calculate the total binding energy of all the nucleons in the nucleus under consideration as a function of the nuclear spheroidicity for various assumed configurations. The lowest minimum obtained in such a calculation then defines the equilibrium value of δ predicted by the model.

For a particular orbit characterized by N and Ω, where N is the total number of oscillator quanta and Ω is the projection of the single-particle total angular momentum j on the nuclear-symmetry axis, the total nuclear Hamiltonian as given by Nilsson (1955) has eigenvalues

$$E_\alpha^{N\Omega} = (N_\alpha + \tfrac{3}{2})\hbar\omega_0(\delta) + \kappa\hbar\omega_0{}^0 r_\alpha^{N\Omega}(\delta), \tag{6}$$

where $\omega_0(\delta) = \omega_0{}^0(1-\frac{4}{3}\delta-\frac{16}{27}\delta^3)^{-1/6}$; the eigenvalues $r_\alpha{}^{N\Omega}(\delta)$ are tabulated by Nilsson, and the values of $\omega_0(\delta)$ for a spherical nucleus, $\omega_0{}^0$, are given approximately by $\hbar\omega_0{}^0 \simeq 41A^{-1/3}$ Mev. $\kappa = 0.05$ is a measure of the spin–orbit interaction assumed and δ, the spheroidicity, is given by $\delta \simeq \Delta R/R_0$, where R_0 is the mean radius of the spheroid and ΔR is the difference between the major and minor semi-axes.

As shown by Nilsson in Appendix C to his paper (1955), the total Hamiltonian can be written in such a way that the total energy eigenvalues are given by

$$\mathcal{E}(\delta) = \frac{3}{4}\hbar\omega_0{}^0\left\{\sum_\alpha\left(N_\alpha+\frac{3}{2}\right)\left(1-\frac{4}{3}\delta-\frac{16}{27}\delta^3\right)^{-1/6} + \sum_\alpha \kappa r_\alpha{}^{N\Omega}(\delta)\right\} - \frac{1}{4}\sum_\alpha\langle U_\alpha\rangle, \tag{7}$$

where $\langle U_\alpha\rangle$ is the expectation value of the spin–orbit potential.

In order to examine the behavior of $\mathscr{E}(\delta)$, this function has been computed in first approximation neglecting any δ dependence of $\langle U_a \rangle$. The following procedure was employed:

(1) For a given δ the corresponding configuration was obtained by noting the sequence of filling of the individual orbits in the energy-level diagram given by Nilsson.

(2) Using this configuration, $\mathscr{E}(\delta)$ was computed for δ values in the range $-0.3 \leqslant \delta \leqslant 0.3$ by simply summing the contributions from each individual orbit containing a maximum of two neutrons and two protons.

Fig. 3 is taken from Nilsson's paper and is a plot of the energy levels of

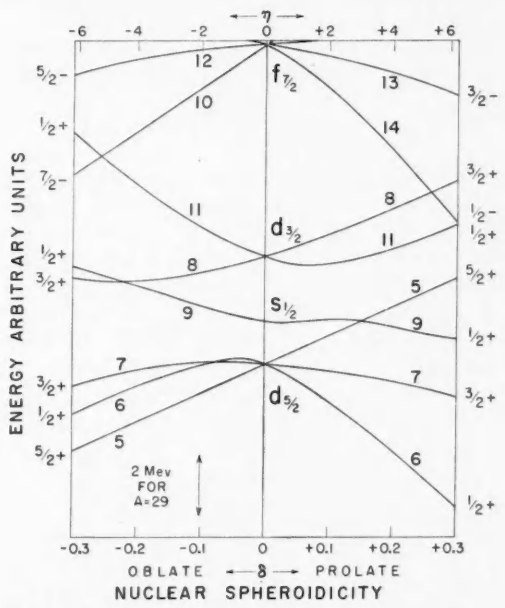

FIG. 3. Energy levels of the Nilsson model as a function of the parameters δ and η defined in the text. The numbers to the left of the figure are the orbit numbers; the notation at the $\delta = 0$ intercepts identifies the single-particle state corresponding to a spherical potential on which the particular orbits are based; the number and sign on the orbit curves themselves are the values of Ω and parity for the orbit. The rotational bands are based on these orbits with $K = \Omega$ as the lowest member of the band.

the model as a function of the spheroidicity δ. η is a parameter also used by Nilsson to characterize the nuclear spheroidicity and is by definition

$$\eta = \frac{\delta}{\kappa}\left[1 - \frac{4}{3}\delta^2 - \frac{16}{27}\delta^3\right]^{-1/6}. \tag{8}$$

The numbers on the left of the plot are the Nilsson orbit numbers, those at the $\delta = 0$ axis identify the corresponding single-particle states in a spherical

potential, and the number and sign on the individual curves give the value of Ω and the parity for that particular orbit.

(3) The values of $\mathscr{E}(\delta)$ so obtained were plotted against δ; the envelope of the resultant curves then gives the configuration of lowest energy for a particular value of δ. The minimum in this envelope defines the equilibrium spheroidicity δ_e. It should be emphasized that in this plot γ (the coordinate defined by Bohr (1952)) has a periodicity of $2\pi/3$ when only spheroidal deformations are considered. Thus the curve shown for positive values of δ is valid for $\gamma = 2n\pi/3$ and that for negative values of δ for $\gamma = (2n+1)\pi/3$, where n is integral. This problem of the γ dependence of the total energy is being investigated by Steenberg and others.

Fig. 4A is such a plot for Si^{29}. The three configurations labelled by A, B, and C on this figure are $(1\,2\,3\,4\,5\,6\,7)^4\,9^1\,[1/2+]$, $(1\,2\,3\,4\,5\,6\,7)^4\,8^1\,[3/2+]$, and $(1\,2\,3\,4\,6\,7\,9)^4\,5^1\,[5/2+]$, where these numbers refer to the corresponding

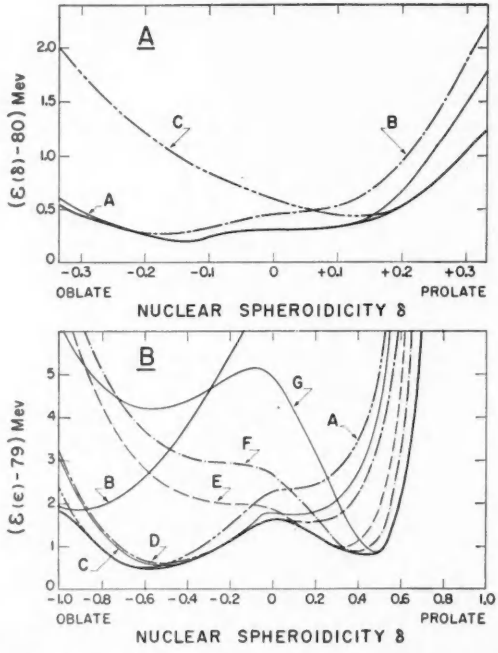

FIG. 4. Total energy predicted for Si^{29}. The Nilsson eigenvalue calculations have been extended beyond $|\delta| = 0.3$* to obtain the results shown in Part B of this figure. The configurations corresponding to the individual curves in this figure are listed in the text.

single-particle orbits in the Nilsson formulation (see Fig. 3), the superscript is the nucleon occupancy number for each orbit, and the notation in square

*We are indebted to K. Gottfried, H. McManus, and J. King for these calculations.

brackets is the corresponding predicted ground-state spin and parity. The envelope of these curves then indicates an equilibrium distortion of $\delta \simeq -0.15$, hence oblate shape, and a ground state of $1/2+$ for Si^{29}. It is of interest to note that for $-0.32 < \delta < -0.21$ the prediction for the ground state is $3/2+$, for $-0.21 < \delta < +0.13$, $1/2+$, and for $0.13 < \delta < 0.32$, $5/2+$.

It has been shown that equation (6) for $E_\alpha^{N\Omega}$ in terms of $\omega_0(\delta)$ is inaccurate because of the neglect of terms non-diagonal in N (Nilsson 1955; McManus 1957). Following Nilsson, it is possible to improve this situation appreciably by defining a new parameter

$$\epsilon = \frac{3[\sqrt{1+2\delta/3} - \sqrt{1-4\delta/3}]}{\sqrt{1-4\delta/3} + 2\sqrt{1+2\delta/3}} \approx \delta + \frac{1}{6}\delta^2 + O(\delta^3). \tag{9}$$

In terms of this parameter, the total energy eigenvalue is given (McManus and Gottfried 1956) by

$$\mathscr{E}(\epsilon) = \frac{3}{4}\hbar\omega_0{}^0\left\{\sum_\alpha \left(N_\alpha + \frac{3}{2}\right)\left(1 - \frac{1}{3}\epsilon^2 - \frac{2}{27}\epsilon^3\right)^{-1/3} + \sum_\alpha \kappa r_\alpha{}^{N\Omega}\right\} - \frac{1}{4}\sum\langle U_\alpha\rangle, \tag{10}$$

an expression which gives a good account of the equilibrium deformations of nuclei in the region $150 < A < 200$ (Mottelson and Nilsson 1955). Fig. 4B is the corresponding plot of $\mathscr{E}(\epsilon)$ as a function of the spheroidicity δ, where, in addition, the δ dependence of $\langle U_\alpha\rangle$ has been included in the calculations. The configurations here are labelled as follows: A—$(1\,2\,3\,4\,5\,6\,7)^4\,10^1$ [$7/2-$], B—$(1\,2\,3\,5\,6\,7\,10)^4\,4^1$ [$1/2-$], C—$(1\,2\,3\,4\,5\,6\,7)^4\,8^1$ [$3/2+$], D—$(1\,2\,3\,4\,5\,6\,7)^4\,9^1$ [$1/2+$], E—$(1\,2\,3\,4\,6\,7\,9)^4\,5^1$ [$5/2+$], F—$(1\,2\,3\,4\,6\,7\,9)^4\,14^1$ [$1/2-$], and G—$(1\,2\,3\,4\,6\,7\,14)^4\,9^1$ [$1/2+$]. The envelope of these curves again indicates an oblate equilibrium shape but at considerably greater spheroidicity, namely $\delta \sim -0.55$. The curves do not distinguish between $1/2+$, $3/2+$, and $7/2-$ for the ground state for this value of δ; at a value of $\delta \sim -0.15$, suggested by other measurements to be discussed and those already considered, the predicted ground state is $1/2+$, as is observed.

The effect of residual interactions has not been taken into account in equation (10). These tend (Nilsson 1955, p. 47) to reduce the deformation. Furthermore, there are likely to be corrections to the Hartree formula

$$\mathscr{E} = \sum_i T_i + \frac{1}{2}\sum_{i\neq j} V_{ij},$$

on which equation (6) is based, for the case of a finite nucleus (Skyrme 1956).*

It should be emphasized here that the value of $\kappa = 0.05$ used by Nilsson was selected to bring the model predictions into agreement with observed

*As is clear from Fig. 4A, the presumably less accurate equation (7) predicts an equilibrium spheroidicity which is in essential agreement with that indicated by the other comparisons which will be presented in this paper, namely $\delta \simeq -0.15$. On the other hand, the more accurate expression (equation (10)) indicates appreciably larger equilibrium values of δ. It would appear, however, that this agreement between the less accurate equation and experiment is not general; in the case of Al^{25} a prolate shape is predicted with $\delta \sim +0.15$ and a ground-state assignment of $5/2+$ in qualitative agreement with analysis of the experimental data (Litherland *et al.* 1957), whereas in the case of Al^{27}, which is known to have a positive quadrupole moment (Blin-Stoyle 1956) corresponding to $\delta \sim +0.3$ and a ground-state assignment of $5/2+$, the predictions are for a $3/2+$ ground state and oblate shape corresponding to $\delta \sim -0.2$.

shell regularities, particularly in heavier elements (Klinkenberg 1952). All model calculations presented in this paper with the exception of those corresponding to equation (10) were computed from the Nilsson eigenfunctions and eigenvalues as functions of η and the abscissae of the corresponding plots converted to units of δ using equation (8). Nilsson (1957) has suggested that a value of $\kappa \simeq 0.08$ may be more appropriate for the d-shell nuclei; the effect of increasing κ—that is, increasing the spin–orbit term in the potential—is to compress the δ scale on all figures in this paper with the exception of Fig. 4B corresponding to equation (10) for $\mathcal{E}(\epsilon)$, which can be shown to be roughly independent of κ. Consequently such an increase in κ is in the direction to bring the equilibrium value of δ obtained from equation (10) and from the other parameters considered here into agreement. This does not, however, remove gross discrepancies such as those just noted in the case of Al^{27}, and it has been suggested (Nilsson 1957) that introduction of the l^2 term—that is, $\mu \neq 0$—in the Nilsson formalism for the nuclear potential may be necessary. Such a term has been required for heavier elements but was neglected in the lower orbits of the original Nilsson model.

The energy difference between contributions from nucleons in neighboring Nilsson orbits in the region of Si^{29} is of the order of 50 kev. This has the consequence that the model would predict essentially constant spheroidicity for all the low bands in Si^{29} and in particular for the $K = 1/2$ and $3/2$ bands considered. It is characteristic of all these plots that the equilibrium shape of Si^{29} is essentially determined by that of the core nucleus Si^{28}.

Reduced Widths for Stripping

The Nilsson formalism allows the expansion of the eigenfunction for a single-particle state in the spheroidal potential well in terms of pure, single-particle j eigenfunctions. The coefficients c_j in such an expansion are proportional to the fractional amplitude of the corresponding j eigenfunction in that of the state. Consequently these are related to the reduced widths for neutron capture in (d, p) reactions leading to the state in question. In the case of Si^{29}, measurements of Holt and Marsham (1953) on the $Si^{28}(d, p)Si^{29}$ reaction provide the data for such a comparison.

Satchler (1955) has shown that in the strong-coupling model, because of the orthogonality of the single-particle states, capture into rotational levels is possible only if the (j_n, l_n) of the captured neutron is equal to (j, l) for the orbit into which it is captured. Writing Satchler's equation for the reduced width in the Nilsson notation (McManus 1957), one obtains for the reduced width for capture by a target I_0K_0 of a neutron (j, Ω) to form a final state I_fK_f

$$\gamma^2 = \frac{2(2I_0+1)}{2I_f+1} \times \Phi^2 \sum_j |\langle I_0 j K_0 \Omega | I_f K_f \rangle|^2 \times |c_j|^2, \tag{11}$$

where Φ is a quantity, with the dimensions of Mev. cm., which is constant for a given reaction, and is a measure of the validity of the pure single-particle picture for the stripping reaction. K admixture has been ignored in this expression. The Clebsch–Gordan coefficient is that for combination of the

angular momenta involved with specified components on the nuclear-symmetry axis and reflects the selection rule given by Satchler, since in the case of an even–even target $I_0 = K_0 = 0$, and the expression reduces to

$$|c_j|^2 \propto (2I_f+1)\gamma^2/(\delta_{j,I_f})(\delta_{\Omega,K_f}). \tag{12}$$

The extraction of the reduced widths from the experimental data has been considered by Fujimoto, Kikuchi, and Yoshida (1954), who obtain an expression for the stripping differential cross section in terms of the reduced width in a Born approximation calculation and have obtained values for the reduced widths, listed in Table I, by fitting the peak cross sections in the data of Holt and Marsham to their expressions.

TABLE I

COMPILATION OF REDUCED WIDTH DATA FROM $Si^{28}(d, p)Si^{29}$ MEASUREMENTS (HOLT AND MARSHAM 1953); IN THE PARTICULAR CASE OF Si^{29} THERE IS NO SOLUTION FOR $K = 3/2$ AND $\delta > 0$; FOR COMPLETENESS, HOWEVER, THESE VALUES ARE INCLUDED IN THE TABLE (see footnote on page 1072)

					$\lvert c_j\rvert^2$			
					$\delta = -0.15$		$\delta = +0.15$	
E_{xf} (Mev.)	l_n	I_f	γ^2 (10^{-13} Mev.cm.)	$(2I_f+1)\gamma^2$	$K=1/2$	$K=3/2$	$K=1/2$	$K=3/2$
0	0	1/2	0.25	0.50	0.34		0.43	
1.28	2	3/2	0.23	0.92	0.22	0.89	0.35	0.97
2.03	2	5/2	0.082	0.492	0.44	0.11	0.22	0.03
2.43		3/2	Stripping pattern too weak to be clearly resolved, i.e. $\lesssim$0.02		0.22	0.89	0.35	0.97
3.07	2	(5/2)	0.015	0.090	0.44	0.11	0.22	0.03
3.62	3	(7/2)	0.14	1.12				

This procedure is open to the objection that the interaction of the nucleons in the deuteron and of the outgoing nucleon with the nucleus as a whole is neglected, an approximation which tends to underestimate the reduced widths (Horowitz and Messiah 1953). However, this procedure is much simpler than the more accurate treatments suggested by Bowcock (1954) and by Tobocman and Kalos (1955) and should give a fair account of the relative values.

The values of $|c_j|^2$ listed in this table were obtained from Fig. 5, which shows these calculated squared coefficients as functions of the spheroidicity for the orbits concerned; the signs on this figure identify the appropriate sign for c_j for various ranges of δ. Comparison of the values of $(2I_f+1)\gamma^2$ with the $|c_j|^2$ does not directly distinguish between oblate or prolate shape for Si^{29}. It should be noted, however, that in either case the agreement is considerably better for a $K = 3/2$ (orbit 8) assignment to the states at 1.28 and 3.07 Mev. and a 1/2 (orbit 9) to the remaining states. As seen from Fig. 2, this requires an oblate shape.

Sum Rule for Reduced Widths

From the definition of the c_j coefficients it follows that

$$\sum_j |c_j|^2 = 1 \tag{13}$$

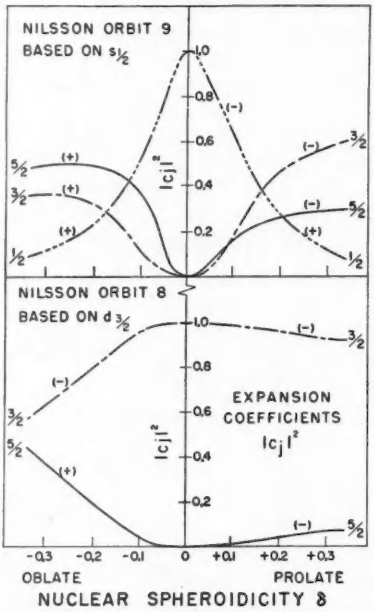

FIG. 5. Squared coefficients from expansion of single-particle eigenfunctions in the spheroidal potential in terms of pure single-particle j eigenfunctions. The + and − signs on the figures identify the sign of c_j.

for each orbit. It is therefore of interest (Litherland and McManus 1957) to examine the corresponding values of

$$\sum_j (2I_f+1)\gamma_j^2 \tag{14}$$

for both the prolate and the oblate assignments. As shown in Fig. 5, for orbit 9, j values of 1/2, 3/2, and 5/2 are possible, whereas for orbit 8 only j values of 3/2 and 5/2 are possible. In the case of orbit 10 (see Fig. 3), based on the $f_{7/2}$ state, since an $l_n = 3$ pattern was observed in the angular distribution of the protons leading to formation of the presumed 7/2− state in Si^{29} at 3.62 Mev., only the single j value 7/2 is possible in this sum. Using the data of Table I and forming the above sum, one obtains for the oblate assignment

$$\left(\sum_j (2I_f+1)\gamma_j^2\right)_9 = 1.00, \qquad \left(\sum_j (2I_f+1)\gamma_j^2\right)_8 = 1.01, \tag{15}$$

$$\text{and } \left(\sum_j (2I_f+1)\gamma_j^2\right)_{10} = 1.12,$$

whereas for the prolate assignment these quantities are ~1.91, 0.090, and 1.12 respectively. The fact that these sums are ~1.0 for the oblate assignment is

itself coincidental; however, the fact that the sums are very closely equal for this assignment and differ by as much as a factor of 20 for the other may be considered as evidence favoring the oblate shape. It is of interest to note that recent measurements on the $Si^{28}(d, n)P^{29}$ reaction (Calvert *et al.* 1957) yield reduced widths to levels in P^{29} corresponding to those studied here in Si^{29} which are quite similar, giving reduced widths in c.g.s. units for proton capture to form the first three states in P^{29} at 0, 1.3, and 1.92 Mev. excitation of 4.5×10^{-20}, 2.7×10^{-20}, and 1.3×10^{-20}, to be compared with widths for neutron capture to the corresponding states in Si^{29} (Holt and Marsham 1953) of 5.6×10^{-20}, 4.6×10^{-20}, and 1.1×10^{-20}. Consequently, as might be expected *a priori* for these mirror nuclei, the arguments advanced for Si^{29} should apply also to P^{29}, and in particular it would be expected that P^{29} and Si^{29} should have essentially the same shape.

In the work of Holt and Marsham the angular distribution of the protons corresponding to the formation of the 2.43 Mev. level in Si^{29} shows no prominent stripping peak, consistent with a low value for the corresponding reduced width. On the basis of the predictions of this model it is somewhat surprising, however, that this width should be reduced by so large a factor. It would be of interest to examine this angular distribution at a higher deuteron energy and over a wider angular range than is presently available to make possible an extraction of the corresponding reduced width using the Bowcock (1954) technique.

Gamma Transitions

Transition widths for the radiation associated with the de-excitation of the 2.03 and 2.43 Mev. states in Si^{29} have been computed using the Nilsson eigenfunctions: the $M1$ partial widths were computed using the expressions given by Nilsson, whereas the $E2$ partial widths were computed using a generalized expression which includes both single-particle and collective transition contributions (McManus and Sharp 1957). In the Nilsson notation, and neglecting center of mass motion, this expression for the reduced $E2$ transition probability may be written as follows:

$$(16)\quad B(E2) = \frac{5e^2}{4\pi}\left(\frac{\hbar^2}{M\omega_0}\right)\times G_{E2}{}^2 \times |\langle I2Kk|I'K'\rangle\times(1+y_{E2}{}^c) + b_{E2}(-1)^{I'+K'}\times\langle I2K-q|I'-K'\rangle|^2,$$

where the transition is assumed from a state I, K to a state I', K' and, by definition, $k = K'-K$ and $q = K'+K$.

The collective contribution is determined by the magnitude of the parameter $y_{E2}{}^c$, where

$$(17)\qquad y_{E2}{}^c = \frac{\kappa ZA^{1/3}}{G_{E2}}\eta\left(1+\frac{2}{3}\delta\right)\sum_{l\Lambda}\langle N'l|1|Nl\rangle\delta_{\Sigma\Sigma'}\,\delta_{KK'}\,a_{l\Lambda}\,a'_{l\Lambda'}\,.$$

Here again δ and η are the spheroidicity parameters used by Nilsson; the $a_{l\Lambda}$ are the normalized Nilsson eigenfunction coefficients, and all K admixtures in the state involved have been ignored. For the 2.03 Mev. transition in

Si^{29}, $y_{E2}{}^c$ ranges from -2.83 to -9.53 for $\delta = -0.1$ to -0.3 and from 8.82 to 17.7 for $\delta = +0.1$ to $+0.3$, as shown in Fig. 6. The fact that $y_{E2}{}^c$ is linearly proportional to Z shows why the collective effects are much more dominant

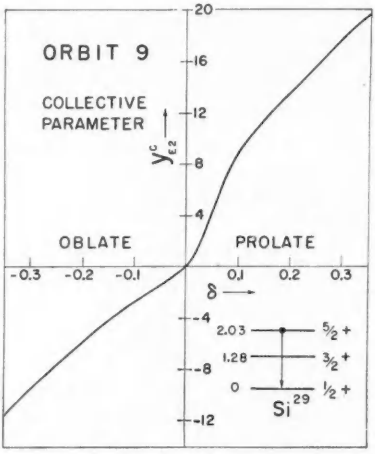

FIG. 6. The collective parameter $y_{E2}{}^c$ for the 2.03 Mev. ground-state transition in Si^{29}.

in heavy nuclei. It should be noted also that $y_{E2}{}^c$ is proportional to κ and hence to the strength of the spin–orbit interaction assumed. It was further assumed that the vibrational eigenfunctions overlap identically between these states, and use has been made of the fact that, if both initial and final states are within a rotational band, the sum $\sum_{l\Lambda}$ factor in the $y_{E2}{}^c$ expression equals unity. Fig. 7 shows the ratio of the partial transition widths thus obtained for the 0.75 Mev. cascade transition from the 2.03 to the 1.28 Mev. state. As shown in the figure, this calculation has been repeated for K assignments of both 1/2 (orbit 9) and 3/2 (orbit 8) to the 1.28 Mev. state. These are characterized here and in the following figures as oblate and prolate assignments respectively.* From this figure it is clear that for $\delta \sim -0.15$ the $E2$ width is negligibly small but that for $\delta \sim +0.15$ the widths are comparable; this relative increase in the $E2$ width reflects the behavior of the parameter $y_{E2}{}^c$ as shown in Fig. 6 and is thus largely due to an enhanced collective contribution.

As noted in the preceding paper (Bromley *et al.* 1957), an analysis of the measured triple and quadruple correlations, assuming f-wave formation and p-wave decay of the resonance involved, indicates that the 0.75 Mev. radiation is either almost entirely $E2$ or entirely $M1$ but does not distinguish between these possibilities. This would appear to support the assignment of an oblate

*The curves corresponding to an oblate assignment are also given for positive values of δ and vice versa since these shape assignments are peculiar to Si^{29} (Fig. 2) and need not hold for other nuclides to which these curves are applicable.

shape to Si^{29}, but it should be emphasized that this resonance assignment is not unique and that this argument loses some force when the rotational particle coupling is introduced to mix the overlapping bands, as will be discussed later in this section.

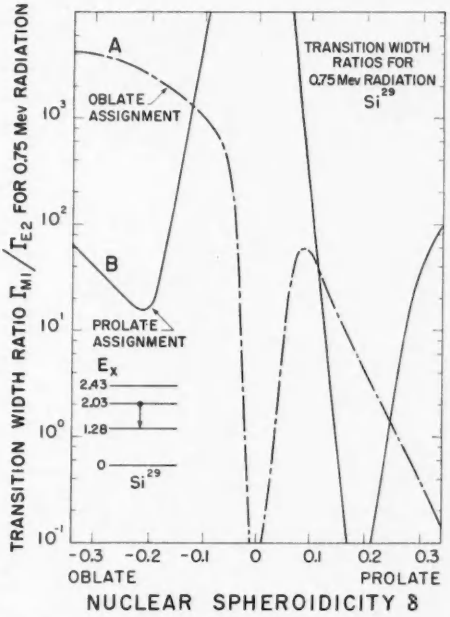

FIG. 7. Transition-width ratios for the 0.75 Mev. radiation in the de-excitation of the 5/2+, 2.03 Mev. state in Si^{29}.

Fig. 8 shows the predicted branching ratio for direct versus cascade de-excitation of the 2.03 Mev. level, again for both oblate and prolate assignments. In this ratio the total transition width to the 1.28 Mev. state has been used. It is clear from the figure that for $\delta \sim -0.15$ the predicted branching ratio is lower than the observed by a factor of $\sim$100, whereas for $\delta \sim +0.15$ the agreement is excellent. Alone, this would constitute evidence for a prolate shape for Si^{29}; further discussion of this point will follow.

Fig. 9 shows the predicted total transition widths for the three possible de-excitation modes for the 2.43 Mev. level. In each case the width shown is the sum of the partial $M1$ and $E2$ widths computed as noted previously. In the measurements on the Al^{29} beta decay (Bromley *et al.* 1957), no 1.15 Mev. radiation was detected in the associated gamma spectra. Because of the complexity of these spectra, it is not possible to fix a low upper limit to the width for this transition. On the other hand, it is possible to establish that the intensity of the 1.15 Mev. radiation is at most a factor of about 100 greater

than that of the 2.43 Mev. radiation. At a value of $\delta \sim -0.15$ the predicted intensities would be in the ratio of approximately 10^3. More accurate measurements on this branching would be required before this could be considered as

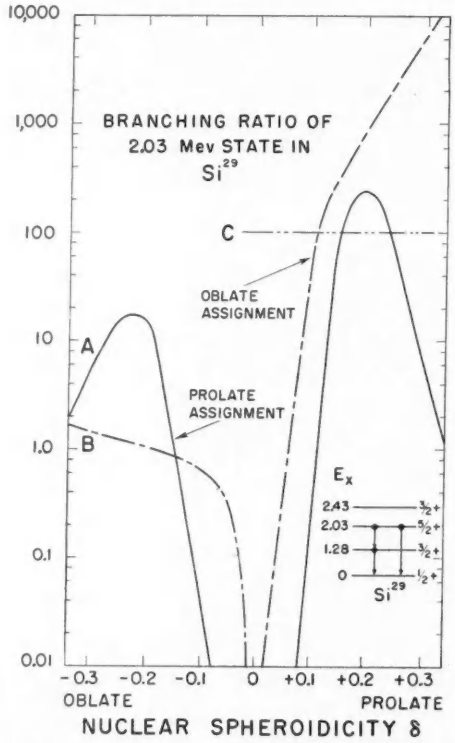

FIG. 8. Predicted branching ratio of the de-excitation of the 5/2+, 2.03 Mev. state in Si^{29}. The horizontal line indicated at C represents the experimentally determined value for this ratio.

a very significant discrepancy with the model predictions. In particular, a study of the branching ratio of the 2.43 Mev. level excited in the $Si^{29}(p, p'\gamma)Si^{29}$ reaction would be of considerable interest.

Interband Mixing

As noted previously, in all of these calculations admixtures of differing K wave functions in the states in question have been ignored. Since, on an oblate assignment, the $K = 1/2$ and $K = 3/2$ rotational bands in Si^{29} overlap appreciably, a preliminary investigation of the effect of mixing these two bands on the predicted value for the branching ratio for the 2.03 Mev. state has been carried out. The formulation of this rotational particle coupling effect developed by Kerman (1956) has been used. This is equivalent to

including a Coriolis term in the potential in which the single particle moves and, in the case of Si^{29}, mixes the $3/2+$, $K = 3/2$ state at 1.28 Mev. with the $3/2+$, $K = 1/2$ state at 2.43 Mev. and the $5/2+$, $K = 1/2$ state at 2.03 Mev. with the assumed $5/2+$, $K = 3/2$ state at 3.07 Mev. This is approximately the excitation calculated for the second, $5/2+$ member of a $K = 3/2$ rotational band based on the 1.28 Mev. state assuming the same moment of inertia as for the $K = 1/2$ band.

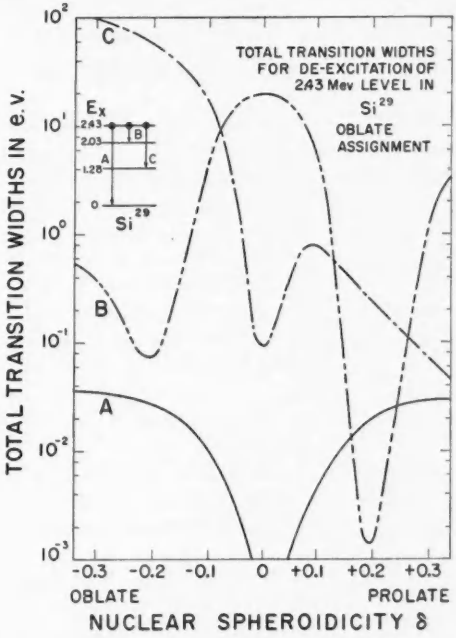

FIG. 9. Total transition widths for de-excitation of the $3/2+$, 2.43 Mev. state in Si^{29}. In each case $\Gamma_{tot} = \Gamma_{M1}+\Gamma_{E2}$; results are shown only for the oblate assignment of $K = 3/2$ to the 1.28 Mev. state.

An estimate of the magnitude of the rotation–particle coupling parameter A_K may be obtained by writing its definition in the Nilsson formalism (McManus 1957) as:

$$A_K = \left|\left(K\left|\frac{\hbar^2}{2\mathscr{I}}J_-\right|K+1\right)\right| = \frac{\hbar^2}{2\mathscr{I}}\left|\sum_j c_j^K c_j^{K+1}\sqrt{(j-K)(j+K+1)}\right|. \tag{18}$$

It should be noted that setting $K = -1/2$ in equation (18) and using the identity $c_j^{-K} = (-1)^{l+\frac{1}{2}-j}c_j^K$ (Gottfried 1956) results in

$$A_{-1/2}\,(-1)^l\left[\frac{\hbar^2}{2\mathscr{I}}\right]^{-1} = \sum_j (-1)^{j-1/2}\,(j+\tfrac{1}{2})|c_j|^2\,,$$

which is identical to the expression given by Nilsson (1955) for the decoupling

parameter a. This illustrates that the decoupling parameter can be considered as arising from the interaction of the degenerate $K = \pm 1/2$ bands (Bohr 1954). Substituting appropriately in equation (18) for the case of Si^{29}, and assuming a value of 0.40 Mev. for $\hbar^2/2\mathscr{I}$ from the previous numerical fit to the level spectrum obtained ignoring K admixture, gives $A_{1/2} \sim 0.05$ Mev. for $-0.1 > \delta > -0.15$, which is the range of interest. In this estimate the dependence of $\mathscr{I}$ on the spheroidicity has been ignored. This value of $A_{1/2}$ produces the following mixing in the 2.03 and 1.28 Mev. states:

$$\psi_{3/2}(1.28 \text{ Mev.}) = -0.0746\psi_{3/2,1/2} + 0.997\psi_{3/2,3/2}, \tag{19a}$$

$$\psi_{5/2}(2.03 \text{ Mev.}) = 0.991\psi_{5/2,1/2} - 0.132\psi_{5/2,3/2}, \tag{19b}$$

where the subscripts in the right side of these expressions characterize the unmixed states $\psi_{I,K}$.

Using the Kerman formalism, the ratio of the reduced $M1$ transition probabilities for the 2.03 to 1.28 Mev. transition calculated for this mixture to that calculated without mixing was found to vary from 0.58 at $\delta = -0.2$ to 1.28 at $\delta = -0.1$. The $I = 1/2$ ground state of Si^{29} is of necessity a pure $K = 1/2$ state, since only states of the same I can be mixed by the rotational particle coupling and no such state is possible in bands with $K > 1/2$ (coupling to higher $K = 1/2$ bands has been ignored because of the large energy separation). Consequently, the reduced $E2$ transition probability for the 2.03 Mev. transition is here only decreased by the factor $(0.991)^2$ by this coupling; the effect of the coupling on the branching ratio of the 2.03 Mev. state results, therefore, almost entirely from the effect on the $M1$ transition probabilities. From the above values it is clear that the value of $A_{1/2} = 0.05$ as calculated for Si^{29} is much too small to produce an increase in the predicted branching ratio of the order of 10^2 which would be required to remove the discrepancy between predictions and experiment.

When mixing is present—that is, $A_K \neq 0$—the level spectrum is modified from that given previously (Kerman 1956) to

$$E(I) = \tfrac{1}{2}(E_{K+1}(I) + E_K(I)) \pm \tfrac{1}{2}([E_{K+1}(I) - E_K(I)]^2 + 4A_K^2(I-K)(I+K+1))^{1/2}, \tag{20}$$

where E_K is as given in equation (4). Sufficiently detailed information on higher levels in Si^{29} is not available to allow unambiguous identification of the higher members of the $K = 1/2$ and $K = 3/2$ rotational bands. Consequently it is not possible to use the observed spectrum to solve simultaneously for all the unknowns in this expression. It is possible to arrive at an approximate upper limit for the rotational particle coupling effects characterized by $A_{1/2} \lesssim 0.17$ Mev. For purposes of orientation the branching ratio has been calculated for a value of $A_{1/2} = 0.20$ Mev. This value corresponds to mixing given by

$$\psi_{3/2}(1.28 \text{ Mev.}) = -0.269\psi_{3/2,1/2} + 0.960\psi_{3/2,3/2}, \tag{21a}$$

$$\psi_{5/2}(2.03 \text{ Mev.}) = 0.917\psi_{5/2,1/2} - 0.402\psi_{5/2,3/2}. \tag{21b}$$

The corresponding ratios of mixed to unmixed $M1$ reduced transition probabilities are 3.69×10^{-4} at $\delta = -0.2$ and 2.43 at $\delta = -0.1$. These in turn correspond to increases in the predicted branching ratio for the 2.03 Mev. state over that shown in Fig. 8 by factors of 2.28×10^{3} and 0.346. It appears, therefore, possible to account for the discrepancy between the experimentally observed branching ratio of 100 and the predicted values as shown in Fig. 8 by including rotational particle coupling effects in the calculations, although the amount of this required is appreciably greater than predicted. It should be noted that because of the κ dependence of the collective parameter $y_{E2}{}^{c}$ (equation (17)), an increase in κ, from the value 0.05 used here, would increase the transition widths for $E2$ radiation and would thus reduce the discrepancy shown in Fig. 8.

Beta Transitions

The experimental information on the positron decay of the mirror nucleus P^{29} to the low levels of Si^{29} (Roderick *et al.* 1955) and on the negatron decay of Al^{29} to these levels (Bromley *et al.* 1957) is shown on Fig. 1 and tabulated for convenience in Table II.

TABLE II

COMPILATION OF LOG *ft* DATA FOR P^{29} POSITRON DECAY (RODERICK *et al.* 1955) AND Al^{29} NEGATRON DECAY (BROMLEY *et al.* 1957)

Initial element	I	K	Final element	I	K	E_x	Log *ft* experimental	Log *ft* predicted $\delta = -0.15$	Log *ft* predicted $\delta = +0.15$
P^{29}	1/2	1/2	Si^{29}	1/2	1/2	0	3.723 ± 0.007	3.72	3.71
				3/2	1/2	1.28	5.03 ± 0.11	4.70	4.80
				3/2	3/2	1.28	5.03 ± 0.11	3.94	4.23
				5/2	1/2	2.03	$\geqslant 5.15$	—	—
				3/2	1/2	2.43	$4.51^{+0.17}_{-0.32}$	4.70	4.80
				3/2	3/2	2.43	$4.51^{+0.17}_{-0.32}$	3.94	4.23
Al^{29}	5/2	5/2	Si^{29}	3/2	3/2	1.28	5.2 ± 0.1		
				3/2	1/2	1.28	5.2 ± 0.1		
				5/2	1/2	2.03	>6.5		
				3/2	1/2	2.43	$\lesssim 5.2$		
				3/2	3/2	2.43	$\lesssim 5.2$		

The *ft* value for allowed beta transitions may be written in the form

$$ft = B\{(1-x)|\textstyle\int 1|^2 + x|\int \sigma|^2\}^{-1}, \tag{22}$$

and, for those first-forbidden transitions which are of a pure Gamow–Teller type, that is, $\Delta\pi = (-1)^{\Delta I-1}$, $\Delta I \neq 0$,

$$ft = B\{x|\textstyle\int \sigma|^2\}^{-1}, \tag{23}$$

where $|\int 1|^2$ and $|\int \sigma|^2$ represent the Fermi and Gamow–Teller matrix elements respectively,

$$B = 2\pi^3\hbar^7 \ln 2/g^2 m_e{}^5 c^4, \tag{24}$$

and the Fermi and Gamow–Teller coupling constants are given by $g(1-x)^{1/2}$ and $gx^{1/2}$ respectively.

The analysis of Kofoed-Hansen and Winther (1956) indicates best values of $B = 2787 \pm 70$ and $x = 0.560 \pm 0.012$.

The Nilsson formalism allows the computation of the matrix elements, $|\int 1|^2$ and $|\int \sigma|^2$, and hence of the *ft* values as a function of the spheroidicity δ for transitions of the sort listed above. Where possible these calculations have been carried out for the P^{29} decay transitions with the results shown in Figs. 10 and 11.

It is not possible to carry out similar calculations for the case of Al^{29} within the Nilsson formalism since almost certainly Al^{29} has prolate shape, and the Nilsson normalizations exclude the possibility of calculating widths between states with differing values of δ. The assignment of $I = K = 5/2$ to the Al^{29} ground state follows from shell-model considerations (Mayer and Jensen 1955) and from the observation that the beta decays to the $1/2+$ ground state of Si^{29} are not observed (Endt and Kluyver 1954), as would be expected for a $\Delta I = 2$ forbidden transition. If Al^{29} is assigned to orbit 5 in the Nilsson plot, as are Al^{25}, Mg^{25}, and Al^{27}, for example, then it is clear from Fig. 3 that, as in the case of these three nuclides, a prolate shape is indicated. With the $K = 5/2$ assignment to Al^{29}, all transitions to low-lying members of the $K = 1/2$ band are also K forbidden. This would appear to be substantiated in the case of the transition to the 2.03 Mev. level for which the experimental $\log ft$ value is >6.5. From normal beta-decay considerations the presumed $5/2+ \rightarrow 5/2+$ transition should be expected to have a $\log ft$ value of ~ 4.5. On the other hand the transitions to the assumed $I = K = 3/2$ state in Si^{29} at 1.28 Mev. and to the $I = 3/2$, $K = 1/2$ state at 2.43 Mev. are observed with $\log ft$ values of 5.2 ± 0.1 and $\lesssim 5.2$ respectively, although that to the 2.43 Mev. state should be K forbidden. A possible explanation for this behavior may well involve the rotational particle coupling (R.P.C.) mixing of these states as considered in the preceding section. Appreciable admixture of $K = 1/2$ and $K = 3/2$ in the eigenfunctions of both of these states would avoid violation of the K selection rule in this beta decay and would explain qualitatively the fact that the observed $\log ft$ values of 5.2 are somewhat greater than might be expected *a priori* for pure K-allowed transitions with $\Delta I = 1$. If this explanation is valid, there exists, however, the remaining problem of explaining why the K selection rule appears to operate effectively on the transition to the 2.03 Mev., $5/2+$, $K = 1/2$ state, since introduction of R.P.C. would also mix this state with the $5/2+$, $K = 3/2$ state at 3.07 Mev. as discussed previously, and thus relax the K-selection-rule inhibition. Without detailed calculations it is not possible to do more than comment on this discrepancy; it may well be that the inhibition remaining would be adequate to account for the $\log ft > 6.5$ value quoted previously. It should be emphasized that the Al^{29} ground state might be expected to be essentially pure $K = 5/2$, since the only neighboring bands in the Nilsson model, away from $\delta = 0$, are those with $K = 1/2$, which therefore do not mix in first order with the $K = 5/2$ band (Kerman 1956).

The agreement between model predictions and experiment is relatively good in the case of the P^{29} decay as shown in Figs. 10 and 11. The ground-

state transition indicates spheroidicities of $\delta = \pm 0.15$; that to the 1.28 Mev. state, $\delta = -0.07$ or $+0.09$ for an assumed $K = 3/2$ assignment and $\delta = \pm 0.13$ for an assumed $K = 1/2$ assignment. The observed $\log ft \geqslant 5.15$ for the transition to the 2.03 Mev. state is consistent with its $\Delta I = 2$ second-forbidden nature; the transition to the 2.43 Mev. state indicates spheroidicities $\delta = \pm 0.18$ for an assumed $K = 1/2$ assignment, and, finally, for a

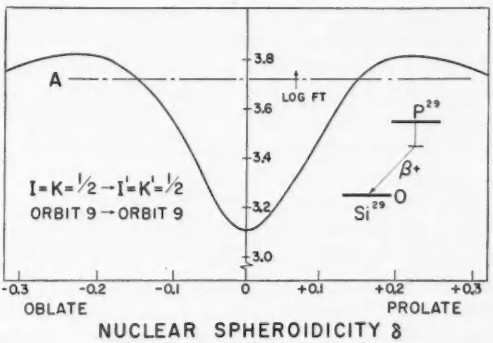

FIG. 10. Predicted log *ft* values for the P^{29} beta decay to the ground state of Si^{29}. The horizontal line A represents the experimentally observed log *ft* value for the transition shown on the inset level diagram.

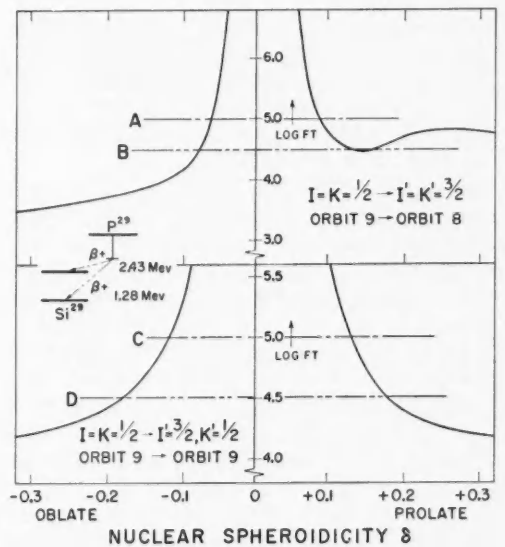

FIG. 11. Predicted log *ft* values for beta decay of P^{29} to low levels in Si^{29}. Horizontal lines A and C represent the experimentally observed log *ft* value for the P^{29} decay to the 1.28 Mev. state in Si^{29}; B and D represent that for decay to the 2.43 Mev. state in Si^{29}.

$K = 3/2$ assignment, δ has one of three possible values, namely -0.08, $+0.13$, or $+0.16$. Unfortunately these data are effectively symmetric in spheroidicity and thus, while indicating the magnitude of the deformation, do not distinguish between the two possible shapes. Particularly in the case of the P^{29} mirror transition to the Si^{29} ground state it might be expected that the Nilsson model should be particularly applicable, since both of these states have $K = 1/2$ and cannot have appreciable admixtures of higher K values, since only states of the same I are mixed by the R.P.C. and none of these exists for higher K bands. As shown in Fig. 3, if P^{29} is assigned to orbit 9, then for oblate shape the nearest $K = 1/2+$ bands are those based on orbits 11 and 6, both of which are relatively remote in energy. It should be noted in Fig. 10 that the calculated $\log ft$ value drops to its minimum value, ~ 3, characteristic of superallowed transitions for $\delta = 0$, and rises above this value with increasing distortion.

The quantitative agreement evidenced for the P^{29} transitions, while not excellent, may well reflect the fact that none of the transitions considered is K forbidden in first order. It has been assumed in the beta-transition calculations that Si^{29} and P^{29} have identical shapes, which is consistent with the available data and in particular with the results of the $Si^{28}(d, n)P^{29}$ measurements of Calvert *et al.* (1957) noted previously.

CONCLUSIONS

Before discussing the results of this study of Si^{29} it may be of value to recapitulate the motivation for, and then to summarize the results of, the detailed comparisons just described. First, these comparisons were intended as a detailed examination of the applicability of this particular model to this nuclide; and second, to the extent that this applicability may be established, it was hoped that the comparisons would lead to a determination of the sign and magnitude of the spheroidicity of Si^{29}. The results may be summarized as follows:

(*a*) The decoupling parameter a, on a $K = 3/2$ assignment to the 1.28 Mev. state, is consistent with either $\delta = -0.2$ or $\delta = -0.05$; on a $K = 1/2$ assignment to this state, $\delta = +0.15$ (Fig. 2).

(*b*) For these same two assignments, the indicated values of $\hbar^2/2\mathscr{I}$ are 0.40 and 0.31 Mev. respectively, to be compared with a value of 0.32 Mev. for Si^{28}.

(*c*) The ground-state magnetic moment is consistent with $\delta = \pm 0.15$ (Fig. 2B).

(*d*) The $\log ft$ value for the P^{29} beta transition to the Si^{29} ground state is consistent with $\delta = \pm 0.15$ (Fig. 10).

(*e*) The $\log ft$ value of the P^{29} beta transition to the 1.28 Mev. state in Si^{29}, on a $K = 3/2$ assignment to this state, indicates $\delta = -0.07$ or $+0.09$ and, on a $K = 1/2$ assignment, indicates $\delta = \pm 0.13$ (Fig. 11A).

(*f*) The $\log ft$ value of the P^{29} beta transition to the 2.43 Mev. state in Si^{29}, on a $K = 1/2$ assignment to this state, indicates $\delta = \pm 0.18$ and, on a $K = 3/2$ assignment, indicates that δ equals one of -0.08, $+0.13$, or $+0.16$ (Fig. 11).

The conclusion to be drawn from these results is that, if the Nilsson model is applicable to the description of the Si^{29} states, then a value of $|\delta| = 0.15$ is indicated. None of the above comparisons gives significant evidence in favor of either sign for δ—that is, oblate or prolate shape. The comparisons which do suggest an oblate shape for Si^{29} are the following:

(*g*) The appearance of a (7/2, 5/2) state as the lowest-energy negative-parity state in the Si^{29} level spectrum is consistent only with oblate shape (Fig. 3).

(*h*) The comparison of the reduced widths obtained from the $Si^{28}(d, p)Si^{29}$ data with the calculated $|c_j|^2$ values is consistent with the assignment of $K = 3/2$ to the 1.28 Mev. state in Si^{29} and of $K = 1/2$ to the 2.43 Mev. state. As seen from Fig. 2, this indicates oblate shape (Table I).

(*i*) Application of the reduced-width sum rule to members of three rotational bands in Si^{29} gives excellent agreement for an assumed oblate shape and disagreement by factors of 20 for an assumed prolate shape.

(*j*) The total energy plots calculated from equations (7) and (10) both show oblate equilibrium shapes for Si^{29} and Si^{28}; in addition, that from equation (7) indicates a value of $\delta_e \simeq -0.15$ for both nuclides (Fig. 4).

(*k*) The preliminary result of the analysis of the triple- and quadruple-correlation measurements on the 0.75 Mev. stopover radiation in Si^{29}, indicating that this radiation is essentially either pure $E2$ or pure $M1$, is consistent only with oblate shape where the prediction is that this radiation is essentially pure $M1$. As noted previously, however, this is by no means a strong argument for this shape, since the resonance parameters assumed in this analysis are not unique.

It would appear reasonable to conclude, then, that Si^{29} has an oblate shape characterized by $\delta = -0.15$.* There is, however, one piece of experimental evidence which would appear to favor strongly a prolate shape, namely the observed branching ratio of the 2.03 Mev. state in Si^{29} (see Fig. 8). Introduction of R.P.C. effects with a parameter $A_{1/2} \sim 0.2$ Mev. suffices to mix the $K = 3/2$ and $K = 1/2$ bands sufficiently to remove this discrepancy; however, this value of $A_{1/2}$ is about the largest value which is allowed without completely destroying the observed level ordering in Si^{29} and is much larger than the value calculated as appropriate for Si^{29}—that is, $A_{1/2} = 0.05$ Mev.

A recent paper by Sheline (1956) analyzes the available data on Al^{28} and concludes that Al^{28} has a prolate shape and that a value of $\delta \sim +0.3$ gives reasonable agreement with the observed Mg^{28} beta-decay *ft* values. However, the *ft* value for the beta decay of Al^{28} to the first excited state of Si^{28} is smaller than would be expected. On the rotational picture Al^{28} and Si^{28} would have $(I\pi K)$ values of (3+3) and (2+0) respectively. These assignments imply that the beta transition is K forbidden, as the selection rule for allowed beta transitions, $\Delta K = 0, \pm 1$, is violated. The log *ft* value of 4.9 is, however, typical of allowed log *ft* values, which implies that either or both of the states of Al^{28} and Si^{28} involved have admixtures of other K values.

The change from prolate to oblate shape or, in the notation of Bohr and

*If one assumes a value of $\kappa = 0.08$ (Nilsson 1957) instead of the value 0.05 used throughout this paper, the indicated equilibrium value of δ is increased (equation (8)) to ~ -0.22.

Mottelson (1953), of γ from 0 to π occurs, therefore, in the region of $A = 29$ if not at $A = 29$, since, as noted previously, it is probable that Al^{29} has prolate shape whereas the evidence presented in this paper strongly suggests an oblate shape for Si^{29} and P^{29}.

It is of interest to note that all measured quadrupole moments for nuclides having single neutrons outside of otherwise closed neutron shells—for example, O^{17} $(d_{5/2})^1$, S^{33} $(d_{3/2})^1$, Se^{73} $(g_{9/2})^1$, and Xe^{131} $(d_{3/2})^1$—are negative, indicating oblate shapes. The assignment of such a shape to Si^{29} is then consistent with this pattern, which was predicted in one of the earliest collective models due to Rainwater (1951).

It should be emphasized that the foregoing statements are based on a somewhat preliminary analysis of the available experimental data as presented in Fig. 1 only within the framework of the Nilsson model. It is felt, however, that the information now available on the $A = 29$ isobaric system is strongly indicative of collective effects and that it should constitute a useful test set of data for the applicability of any detailed nuclear model in this region. The inhibition of the normally allowed beta transition from the 5/2+, Al^{29} ground state to the 5/2+, 2.03 Mev. state in Si^{29} is a case in point.

Since information is available from the $Si^{28}(d, p)Si^{29}$ measurements of Holt and Marsham (1953) on the higher levels in Si^{29}, investigation of inelastic proton scattering from Si^{29} at higher proton energies than were available for the work in the preceding paper (Bromley *et al.* 1957) would be very worth while to fix the branching ratios of these higher levels and therefore make possible a more stringent test of any theoretical treatment of this nucleus. Of particular interest, as mentioned earlier, would be a study of the branching of the 2.43 Mev. state in order to obtain data to be compared with the predictions as shown in Fig. 7. Incident proton energies in excess of 3 Mev. are required to excite this state appreciably. A direct investigation of the Al^{29} negatron decay to confirm the absence of branching to the Si^{29} ground and 2.03 Mev. states would also be desirable.

Although detailed comparisons with the Nilsson model predictions have not as yet been made, it is of interest to note that (p, γ) and $(p, p'\gamma)$ measurements leading to the analogue, odd-proton nucleus, P^{31} (Paul *et al.* 1956; Green *et al.* 1956), with low levels at 1.27 and 2.23 Mev. (Van Patter *et al.* 1956) have shown these to have 3/2+ and 5/2+ assignments respectively. The study of the gamma de-excitation branching ratio of the 2.23 Mev. state shows that less than 3% of the transitions are via the 1.27 Mev. state, the remainder being direct $E2$ transitions to the ground state. This branching ratio is very similar to that reported in the previous paper for the 2.03 Mev. state in Si^{29} and again is strongly suggestive of collective effects.

It is of interest to note that, if P^{31} is considered as an $s_{1/2}$ proton added to the Si^{30} core, the arguments previously mentioned for the possible applicability of the intermediate-coupling model are also valid here. For Si^{30} $E_2/E_1 = 1.57$ (Van Patter and Buechner 1952), and the $Al^{27}(\alpha, p\gamma)Si^{30}$ measurements of Allen, May, and Rall (1951), while not separating the de-excitation of the second and third excited states clearly, indicate a direct crossover de-excitation

of the second excited state and a cascade de-excitation of the fourth excited state at 5.07 Mev. through the third at 3.79 Mev. This is inconsistent with the assignment of the 0+, 2+, 4+ rotational sequence required by the strong-coupling model.

If the Bohr and Mottelson (1955) criterion for the transition between rotational and vibrational spectra quoted in equation (3) is applied to the case of Si^{30}, the computed critical excitation for the first excited state is 1.85 Mev., whereas the observed excitation is 2.24 Mev. (Endt and Kluyver 1954). The corresponding values for Mg^{24} and Si^{28} given previously were 3.54 and 2.22, and 1.37 and 1.77 Mev., respectively. This is consistent with the observation that Al^{25} and Mg^{25} appear to have well-defined rotational characteristics and that Si^{29} has somewhat less strongly marked rotational properties with correspondingly reduced particle-core coupling strength. By inference from these figures it might be expected that rotational effects in P^{31} may be appreciably weaker than in Si^{29}.

In conclusion, therefore, the experimental data on the $A = 29$ isobaric system, on comparison with the predictions of the Nilsson strong-coupling model, are consistent with an oblate shape for Si^{29} and a spheroidicity parameter $\delta = -0.15$. This is to be compared with values of about 0.3 for Al^{27} and -0.1 for S^{33} as obtained from the measured quadrupole moments (Blin-Stoyle 1956). These data, together with those for Mg^{25} (Gove *et al.* 1956), Al^{25} (Litherland *et al.* 1956, 1957), Al^{28} (Sheline 1956), and P^{31} (Paul *et al.* 1956), would seem to constitute reasonable evidence for the applicability of current collective models to the description of the nuclear properties in this mass region. While evidence for the applicability of the strong-coupling model to the $A = 25$ system is quite convincing, as noted above, there is some evidence which suggests that the intermediate-coupling model may have relevance for the description of the $A = 29$ and 31 systems. In the event that subsequent work shows that the latter is the case, the assignment of a particular spheroidicity δ to Si^{29} is somewhat less meaningful, since, with intermediate coupling, the nucleus may be unstable with respect to vibrations about axial symmetry —so-called γ-vibrations—which have been considered by Bohr and Mottelson (1953), Wilets and Jean (1956), and Steenberg (1956). Qualitatively, it might be argued that this is consistent with the fact that the Mg^{24} core, having four equivalent $d_{5/2}$ neutrons and four $d_{5/2}$ protons outside of the O^{16} core, would be expected to have a more stable and pronounced equilibrium spheroidal shape than the Si^{28} core corresponding to the closing of the $d_{5/2}$ shell for both neutrons and protons, which, in a pure j–j coupling picture, would be expected to have spherical symmetry.

These facts emphasize the desirability of having detailed calculations analogous to those of Nilsson for the intermediate-coupling model as well. In addition, further experimental investigation both on the nuclides studied here and on the neighboring ones would be most useful. In addition to other reactions of interest mentioned previously, a study of the reaction pairs $Si^{28}(p, p'\gamma)Si^{28}$, $Al^{27}(d, n)Si^{28}$ and $Si^{30}(p, p'\gamma)Si^{30}$, $Si^{29}(d, p)Si^{30}$ with sufficiently high incident energies to establish the assignments to the states in Si^{28} and

Si^{30} below 5 Mev. would provide crucial evidence for the applicability of the intermediate-coupling model in this region.

ACKNOWLEDGMENTS

We are indebted to H. McManus, K. Gottfried, L. G. Elliott, and W. T. Sharp for many discussions concerning this work and to A. R. Rutledge and J. M. King for assistance in many of the calculations presented.

REFERENCES

ALDER, K., BOHR, A., HUUS, T., MOTTELSON, B. R., and WINTHER, A. 1956. Revs. Mod. Phys. **28**, 432.
ALLEN, R. C., MAY, J. E., and RALL, W. 1951. Phys. Rev. **84**, 1203.
BLIN-STOYLE, R. J. 1956. Revs. Mod. Phys. **28**, 75.
BOHR, A. 1952. Kgl. Danske Videnskab. Selskab, Mat.-fys. Medd. **26**, No. 14.
——— 1954. Rotational states of atomic nuclei (Ejnar Munksgaards Forlag, Copenhagen).
BOHR, A. and MOTTELSON, B. R. 1953. Kgl. Danske Videnskab. Selskab, Mat.-fys. Medd. **27**, No. 16.
——— 1955. Kgl. Danske Videnskab. Selskab, Mat.-fys. Medd. **30**, No. 1.
BOWCOCK, J. E. 1954. Proc. Phys. Soc. (London), A, **68**, 512.
BROMLEY, D. A., GOVE, H. E., PAUL, E. B., LITHERLAND, A. E., and ALMQVIST, E. 1957. Can. J. Phys. **35**, 1042.
BROUDE, C., GREEN, L. L., WILLMOTT, J. C., and SINGH, J. J. 1956. Physica, **22**, 1139.
CALVERT, J. M., JAFFE, A. A., LITHERLAND, A. E., and MASLIN, E. E. 1955. Proc. Phys. Soc. (London), A, **68**, 1008.
CALVERT, J. M., JAFFE, A. A., and MASLIN, E. E. 1957. Proc. Phys. Soc. (London), A, **70**, 78.
DHARMATTI, S. S. and WEAVER, H. E., Jr. 1951. Phys. Rev. **84**, 843.
ENDT P. M. and KLUYVER, J. C. 1954. Revs. Mod. Phys. **26**, 95.
ENDT, P. M. and PARIS, C. H. 1956. Annual Progress Report 1955–1956, Massachusetts Institute of Technology, Cambridge, Mass. (unpublished).
FUJIMOTO, Y., KIKUCHI, K., and YOSHIDA, S. 1954. Progr. Theoret. Phys. (Kyoto), **11**, 264.
GOTTFRIED, K. 1956. Phys. Rev. **103**, 1017; American Documentation Institute Document No. 4881, Library of Congress, Washington, D.C.
GOVE, H. E., BARTHOLOMEW, G. A., PAUL, E. B., and LITHERLAND, A. E. 1956. Nuclear Phys. **2**, 132.
GOVE, H. E., LITHERLAND, A. E., and PAUL, E. B. 1957. Bull. Am. Phys. Soc. **4**, 178.
HOLT, J. R. and MARSHAM, T. N. 1953. Proc. Phys. Soc. (London), A, **66**, 467.
HOROWITZ, J. and MESSIAH, A. M. L. 1953. Phys. Rev. **92**, 1326.
KERMAN, A. K. 1956. Kgl. Danske Videnskab. Selskab, Mat.-fys. Medd. **30**, No. 15.
KLINKENBERG, P. F. A. 1952. Revs. Mod. Phys. **24**, 63.
KOFOED-HANSEN, O. and WINTHER, A. 1957. Kgl. Danske Videnskab. Selskab, Mat.-fys. Medd. **30**, No. 20.
LITHERLAND, A. E., MCMANUS, H., PAUL, E. B., BROMLEY, D. A. and GOVE, H. E. 1957. To be published.
LITHERLAND, A. E. and MCMANUS, H. 1957. Abstract, Ottawa Meeting of the Canadian Association of Physicists.
LITHERLAND, A. E., PAUL, E. B., BARTHOLOMEW, G. A., and GOVE, H. E. 1956. Phys. Rev. **102**, 208.
MAYER, M. G. and JENSEN, J. H. D. 1955. Elementary theory of nuclear shell structure (John Wiley & Sons, Inc., New York).
MCMANUS, H. 1957. Private communication.
MCMANUS, H. and GOTTFRIED, K. 1956. Private communication.
MCMANUS, H. and SHARP, W. T. 1957. Private communication.
MOSZKOWSKI, S. A. 1955. Beta- and gamma-ray spectroscopy, *edited by* K. Siegbahn (Interscience Publishers, Inc., New York), Chap. XIII.
MOTTELSON, B. and NILSSON, S. G. 1955. Phys. Rev. **99**, 1615.
NILSSON, S. G. 1955. Kgl. Danske Videnskab. Selskab, Mat.-fys. Medd. **29**, No. 16.
——— 1957. Private communication.
PAUL, E. B., BARTHOLOMEW, G. A., GOVE, H. E., and LITHERLAND, A. E. 1956. Bull. Am. Phys. Soc. **1**, 39.
RAINWATER, J. 1951. Phys. Rev. **79**, 432.
RODERICK, H., LÖNSJÖ, O., and MEYERHOF, W. E. 1955. Phys. Rev. **97**, 97.
RUBIN, A. G. 1957. Bull. Am. Phys. Soc. **4**, 232; and private communication.

SATCHLER, G. R. 1955. Phys. Rev. **97**, 1416.
SCHARFF-GOLDHABER, G. and WENESER, J. 1955. Phys. Rev. **98**, 212.
SHELINE, R. K. 1956. Nuclear Phys. **2**, 382.
SKYRME, T. H. R. 1956. Phil. Mag. **1**, 1043.
STEENBERG, N. R. 1956. Private communication.
TOBOCMAN, W. and KALOS, M. H. 1955. Phys. Rev. **97**, 132.
VAN PATTER, D. M. and BUECHNER, W. W. 1952. Phys. Rev. **87**, 51.
VAN PATTER, D. M., SWANN, C. P., PORTER, W. C., and MANDEVILLE, C. E. 1956. Phys. Rev. **103**, 656.
WEISSKOPF, V. F. 1951. Phys. Rev. **83**, 1073.
WILETS, L. and JEAN, M. 1956. Phys. Rev. **102**, 788.
WILKINSON, D. H. 1956. Phil. Mag. **1**, 127.

THE FREEZING POINTS OF HIGH PURITY METALS AS PRECISION TEMPERATURE STANDARDS

II. AN INVESTIGATION OF THE FREEZING TEMPERATURES OF ZINC, CADMIUM, AND TIN[1]

E. H. McLaren

ABSTRACT

An investigation of freezing and melting temperatures with platinum resistance thermometry on high purity zinc, cadmium, and tin has been carried out. Using appropriate techniques, plateaus of essentially constant ($< \pm 0.0001°$ C.) temperature with durations of over 1 hour are readily obtained on the cooling curves of these metals. For series of freezes on particular samples, the standard deviations of the respective plateau temperatures were found to be of the order of $\pm 0.0002°$ C. It was not possible to distinguish among the plateau temperatures of three samples selected from different distillation batches of New Jersey S.P. zinc. Evidence is presented on the long term stability ($2\frac{1}{2}$ years) of the plateau freezing temperature of S.P. zinc determined with six standard thermometers. The pressure effects on the freezing temperatures were found to be 0.0043° C., 0.0062° C., and 0.0033° C. per atmosphere for zinc, cadmium, and tin respectively.

Thermal analysis of these high purity metals reveals alloy structures and other features associated with nucleation, coring, and annealing phenomena; typical thermal curves are shown.

INTRODUCTION

Some years ago a considerable amount of work was carried out with resistance thermometers on the freezing points of metals in the range of 0° C. to 630° C.; Waidner and Burgess (1910) reported reproducibilities of the order of $\pm 0.02°$ C. on the freezing points of particular samples of zinc, cadmium, and tin and Roeser (1929) used the freezing points of zinc, lead, and tin as fixed points to investigate thermocouple temperature scales, for which purpose a reproducibility of the order of 0.01° C. was adequate.

These investigations and practices, together with the difficulties encountered in the realization of the sulphur point, suggested that the freezing points of suitable pure metals might provide useful primary and secondary fixed points in the temperature range 100° C. to 650° C. Part II of this paper reports on investigations of the freezing temperatures of high purity zinc, cadmium, and tin.

EQUIPMENT

The resistance bridge, resistance thermometers, and water triple point cells used in these experiments, together with the techniques employed with them to attain the highest practicable precision in temperature measurement, were described in Part I (McLaren 1957) of this paper.

A furnace used for metals which freeze below 500° C. is shown schematically in Fig. 1. This furnace is similar in design to those used by de Selincourt (1939)

[1]Manuscript received June 12, 1957.
Contribution from the Division of Applied Physics, National Research Council, Ottawa, Canada.
Issued as N.R.C. No. 4448.

when he made a most careful investigation of the freezing points of antimony, silver, and gold with standard Pt – Pt+10% Rh thermocouples.

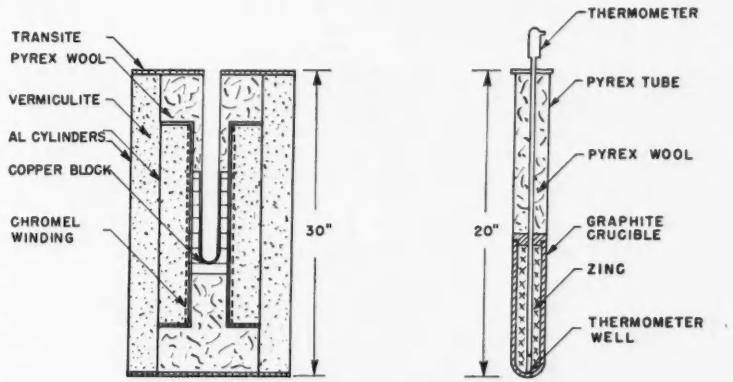

FIG. 1. Details of furnace and sample holder.

The melt, of the order of 1 kg. in weight, is placed in a cylindrical graphite crucible (Stackpole Carbon Co. grade PG-1) and covered with about 1 cm. of graphite powder (PG-1) to reduce oxidation; a hole in a removable graphite top allows either a pyrex or a graphite thermometer well to be axially located in the melt. The graphite crucible is contained in a pyrex tube which extends to the top of the furnace; this allows control of the atmosphere surrounding the melt and also provides a means for removing the crucible from the furnace. Pyrex wool insulation fills this tube from the top of the crucible to the level of the top of the furnace.

The pyrex tube fits into a heavy copper (or aluminum) block which is centered in a heavily insulated metal cylinder on which a layer of asbestos, a Chromel A strip heater, and a covering layer of asbestos are wound. These are cemented in place with water glass and cured at 150° C. until a resistance of the order of 1 megohm exists between the heater and the cylinder. The winding is powered from a regulated 115 volt a-c. supply with variac control. One furnace has end heaters as well as the main heater; the additional control they provided, however, resulted in no improvement in freezing point determinations up to 420° C.

When a zinc sample is solidifying in this furnace a freezing interface advances at nearly the same rate from the bottom, top, and walls of the crucible. This has been determined by decanting melts after various amounts of freezing at a variety of cooling rates and examining the closed cylindrical shells remaining in the crucible; a sectioned example of such a shell is shown in Fig. 2. The existence of these shells attests to the near ideal freezing environment provided by the block furnace for measuring metal freezing temperatures with a properly immersed resistance thermometer. The sensing element of the thermometer is both enclosed and shielded by the freezing interface whose temperature is

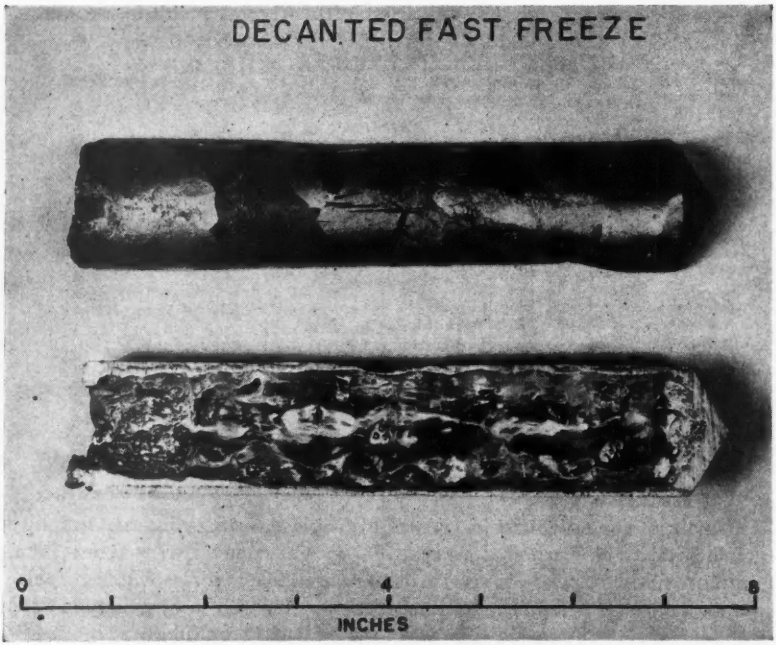

FIG. 2. Photograph of a sectioned shell of zinc remaining in the crucible on decanting the melt after partial freezing.

being measured and only a small vertical temperature gradient, due to the effect of hydrostatic pressure on the freezing temperature, exists in the liquid ahead of the interface.

EXPERIMENTAL TECHNIQUES AND THERMAL ANALYSIS

(*a*) *Zinc*

New Jersey C.P. (99.999%) and New Jersey S.P. (redistilled C.P.) zinc were studied: typical analyses of these metals supplied by Mr. E. A. Anderson of the New Jersey Zinc Co., Palmerton, Pa., are shown in Table I. The C.P. zinc is supplied in rods $\frac{1}{4}$ in. in diam. and 12 in. long and the S.P. zinc is in the form of a crystalline aggregate. The metals are carefully handled to minimize contamination, but a preliminary surface cleaning is not used. Work has been carried out with samples exposed to both air and controlled dry nitrogen atmospheres; in air graphite powder inhibits rapid oxidation of the top surface, but for sustained work it is preferable to use a neutral atmosphere.

Extensive thermal analysis was carried out under a variety of cooling and heating rates; temperature changes in the melt before transformation greater than or less than 0.1° C. per minute produced phase changes which were designated 'fast' and 'slow' respectively. With the melt held a few degrees from the transformation temperature the furnace power was adjusted to give

TABLE I

IMPURITY CONTENT OF C.P. AND S.P. ZINC

C.P. (typical)	S.P. (S.1)
Pb 0.0001%	Pb <0.0002%
Cd 0.00005	Cd <0.00005
Fe 0.0004	Cu Xf
Cu 0.00005	Mg Xf
As 0.000004	Si Xf–Vf
Sn 0.00005	

Xf—a barely detectable line.
Vf—a slightly stronger line.

a desired rate of cooling or heating and the temperature from the axially located thermometer was closely monitored as the sample changed phase.

Figs. 3(*a*) and 3(*b*) show typical cooling curves obtained from fast freezes on C.P. and S.P. zinc which clearly indicate ranges of freezing temperatures

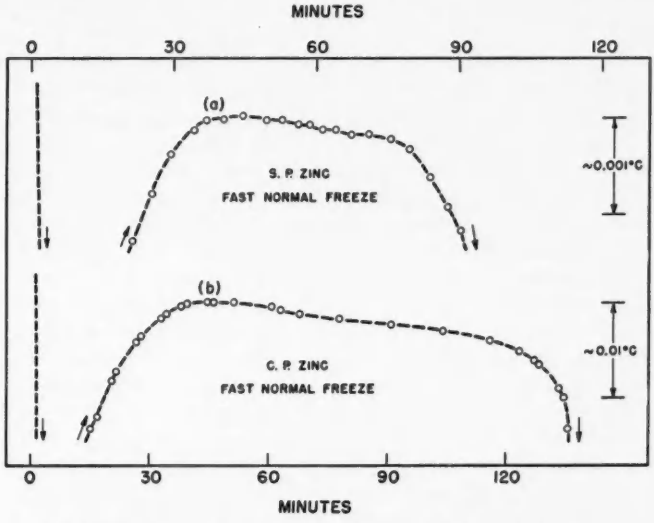

FIG. 3. Cooling curves for fast normal freezes on S.P. and C.P. zinc.

for the two samples, the freezing range being about 0.001° C. for S.P. zinc and about 0.01° C. for C.P. zinc. The smaller range of freezing temperatures for the S.P. zinc agrees qualitatively with the known impurity content of the two samples; precise correlation is not possible because the appropriate phase diagrams and impurity contents are not known sufficiently well. These ranges of transformation temperatures are demonstrated better from melting than from freezing curves (Figs. 4*a* and 4*b*) because liquidus arrests on the freezing curves are screened out by a supercooling amounting to about 0.04 deg. for these samples.

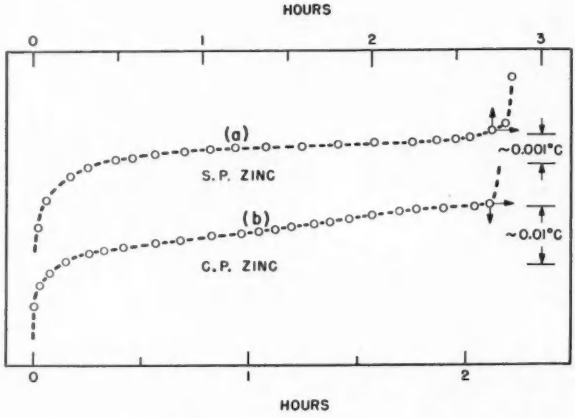

FIG. 4. Melting curves following fast normal freezes on S.P. and C.P. zinc.

Fig. 5 is a cooling curve for a slow freeze on C.P. zinc and shows the rise from supercool (recalescence), a plateau (Y–Y'), and an alloy slope. On slow freezes the duration of recalescence is relatively long and frequently exhibits erratic variations as shown in Fig. 5. During this interval nucleation and growth of the solid is presumably occurring at such a low rate that the amount of latent heat of fusion released is at times insufficient to balance the heat lost to the rest of the furnace. Eventually the growth rate becomes great enough to overcome this loss and the temperature of the melt steadily increases. On slow freezes the melt temperature eventually becomes constant (Y–Y'), varying less than 0.0001° C. for periods of time that depend on the rate of freezing; plateaus with durations varying from 10 minutes to 3 hours have been observed. The last section of a slow freezing curve is a long alloy slope of decreasing temperature which persists until all the metal is solid.

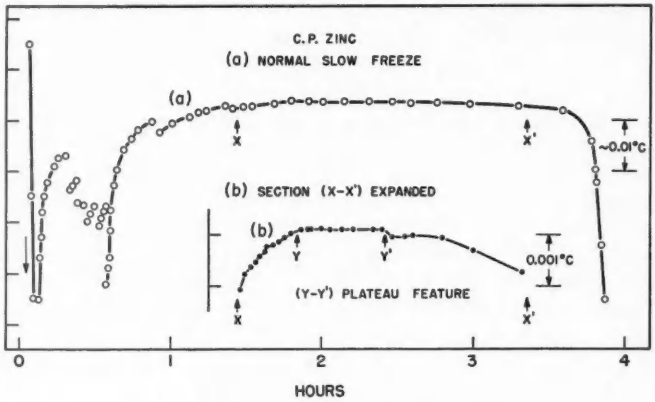

FIG. 5. Slow normal freeze on C.P. zinc.

Melting curves taken after slow freezes reveal a memory of the freezing plateaus. Fig. 6(*a*) shows a section of a cooling curve for a very slow freeze (0.04 deg. per minute before arrest) and Fig. 6(*b*) is the melting curve obtained

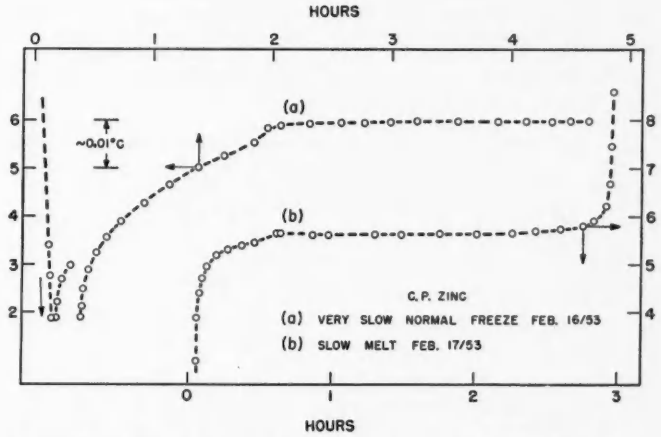

FIG. 6. Very slow normal freeze on C.P. zinc and the remelting curve showing a memory of the freezing plateau.

on the following day. In general, the plateaus obtained on melting curves after slow freezing are not quite as constant in temperature as freezing plateaus but tend to rise a few 10^{-4} deg. over their length for S.P. zinc (up to 0.003° C. for C.P. zinc); in addition the random noise at the galvanometer detector is usually higher on melting plateaus than on freezing plateaus possibly owing to small transient temperature fluctuations (equivalent to temperature changes of up to 0.0003° C. but too rapid for measurement) accompanying the release of strain energy.

The constant temperature observed on the plateaus of slow freezing curves provides an attractive index for a temperature standard, although the length of time (up to 2 hours) that the melt spends in the recalescent state would be a disadvantage in such a standard. However, it is possible to shorten this period by inducing the freeze with the following technique: the melt is allowed to cool normally until nucleation begins, then the thermometer is withdrawn from the melt for about 10 minutes, during which time it comes to room temperature, and it is then replaced. The reheating of the thermometer causes the rapid nucleation and growth of a mantle of zinc about 1 mm. thick on the thermometer well which provides a second shielding interface around the sensing coil of the thermometer and releases an amount of latent heat that rapidly raises the temperature of this interface to the plateau temperature obtained on normal slow freezes. Thereafter the mantle interface remains nearly stationary because very little heat flows across it to the insulated thermometer, the bulk of the melt freezing in a cylindrical shell from the crucible walls as in a normal freeze. Inspection of decanted mantles on C.P.

zinc reveals a cellular substructure of the kind described by Tiller and Rutter (1956) with cell diameters of the order of 2 to 5 mm. About 25 minutes are required from the end of supercool until thermal equilibria are re-established on induced freezes.

No measurable differences have been found between plateau temperatures obtained from normal and induced slow freezes on the same sample. Fig. 7

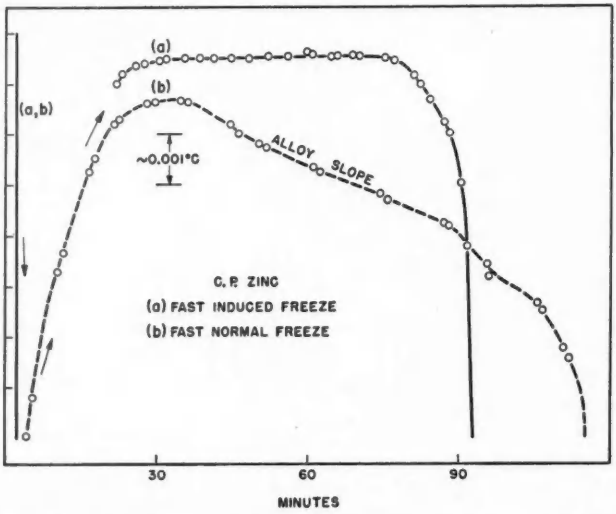

FIG. 7. Comparison between a fast induced and a fast normal freeze on the same sample of C.P. zinc.

illustrates the effectiveness of the induced freezing technique by contrasting cooling curves obtained from normal and induced fast freezes, the furnace being adjusted to give approximately the same cooling rate in both instances.

From a survey of a large number of melting and freezing curves on zinc certain general observations may be made:

Fast normal freezes yield normal alloy freezing curves.

Slow normal freezes yield curves that have, in addition to an alloy range of freezing temperatures, a plateau at constant temperature with a duration that depends on the rate of freezing, the plateau temperature being highly reproducible for a given sample.

The form of the melting curves is largely independent of the rate of melting but is strongly dependent on the nature of the previous freeze; melts following fast normal freezes yield characteristic alloy melting curves while melts following freezes, normal or induced, which developed plateau features have sections of flat contour.

The temperature at which the last of the solid melts is closely associated with the plateau freezing temperatures of that particular sample; a typical case is illustrated in Fig. 8 (*a*) and (*b*).

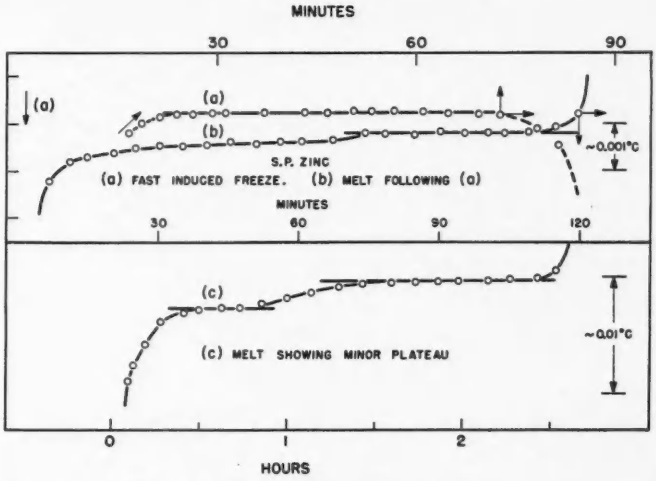

FIG. 8. Curves (*a*) and (*b*) illustrate the close agreement between the plateau freezing temperature and the liquidus break on the melting curve for a particular sample; curve (*c*) shows a melting curve with a minor plateau.

Melting curves exhibiting secondary features, such as the minor plateau at a lower temperature in Fig. 8(*c*), are occasionally observed.

The effect on the shape of the remelting curves of long homogenizing anneals near the melting temperature has not yet been determined for zinc.

(*b*) *Cadmium*

The melting and freezing curves for New Jersey S.P. (99.99+%) cadmium were very similar to those found for zinc. Figs. 9 and 10 show typical freezing and melting curves, the melting range being about 0.003° C. Plateaus of essentially constant temperature ($<\pm 0.0001$ deg.) are obtained during slow normal and induced freezes on this cadmium.

(*c*) *Tin*

Vulcan Detinning Extra Pure (99.99%) tin (Sn.3) and N.B.S. Standard Sample (42d) tin (Sn.2) were investigated: Fig. 11 (*a*) and (*b*) show typical fast and slow normal cooling curves. No constant temperature region was found, even on very slow normal cooling curves, although temperatures varying less than 0.001° C. for intervals of over an hour were obtained. Inducing freezing on the thermometer well did not result in a plateau and served only to hasten the extraction of latent heat from the sample. Failure to develop a plateau on these cooling curves of tin is presumably due to the large supercooling (variable up to 25° C. for tin compared with a few hundredths of a degree for zinc) which results in a low block temperature by the time nucleation occurs. During recalescence there is an unacceptably high rate of heat flow from the sample to the block which prevents the liquid ahead of the interface from reaching the liquidus temperature and initiating the segregation

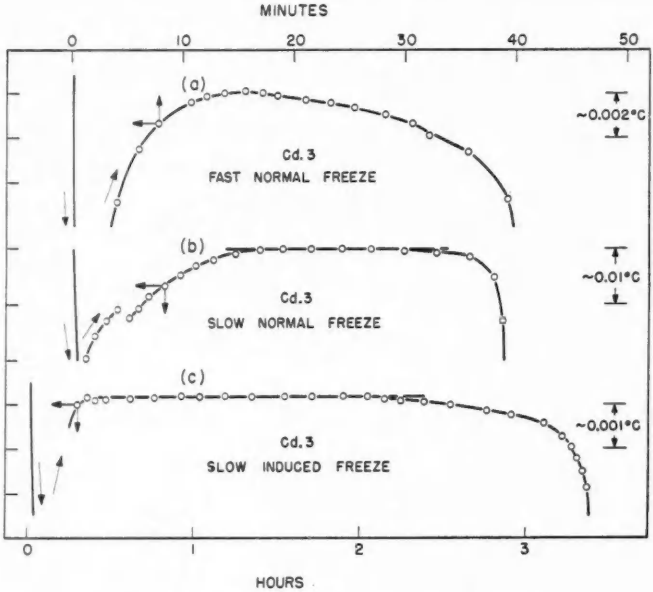

FIG. 9. Cooling curves from typical freezes on S.P. cadmium.

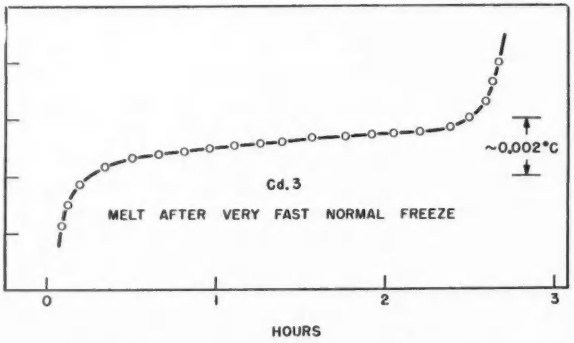

FIG. 10. Melting curve following a very fast normal freeze on S.P. cadmium.

process that is presumed to account for the plateau temperatures observed on the cooling curves for slow freezes on zinc (see Discussion).

This excessive cooling of the block can be prevented, however, in the following manner: The furnace is allowed to cool slowly (0.03° C. per minute before arrest) as in a slow normal freeze, but when the temperature of the melt approaches the freezing temperature of the tin the pyrex tube holding the crucible of tin and the thermometer is extracted into the throat of the

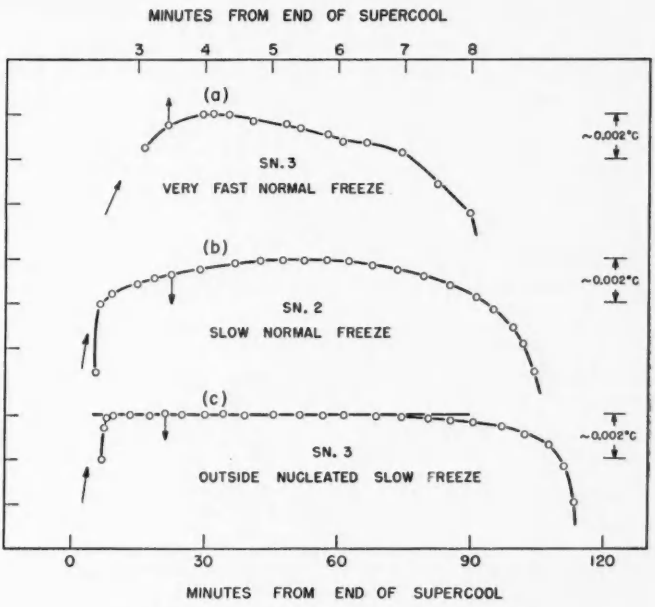

FIG. 11. Cooling curves from typical freezes on tin.

furnace until the top of the crucible is nearly level with the top of the furnace; monitoring of the melt temperatures is continued in the extracted position. The crucible is now surrounded by a region which has an average temperature many degrees below the freezing temperature of tin. The liquid around the thermometer appears to supercool to about the same extent as in a normal slow freeze, but when solidification commences the melt strikes decisively and the resulting latent heat has only to raise the mass of the melt to the liquidus temperature, the severe undercooling of the furnace block having been eliminated. Immediately the melt strikes the crucible is lowered into the slowly cooling block, which is still close to the freezing temperature, and after a few minutes of temperature equalization a cooling curve of the form shown in Fig. 11(*c*) is obtained. This is characterized by a plateau of essentially constant temperature with a duration depending on the rate of cooling of the block followed by a long alloy slope of steadily decreasing temperature which continues until the ingot is solid. The plateau temperatures on these outside nucleated freezes are highly reproducible for a particular sample of tin and, as with zinc and cadmium, provide an excellent index for a temperature standard.

Representative remelting curves obtained after various types of freezes on tin are shown in Fig. 12 and reveal a variety of plateau features, apparent alloy ranges of melting, discontinuities, and sections that suggest anomalous superheating. In marked contrast to the investigations on zinc and cadmium,

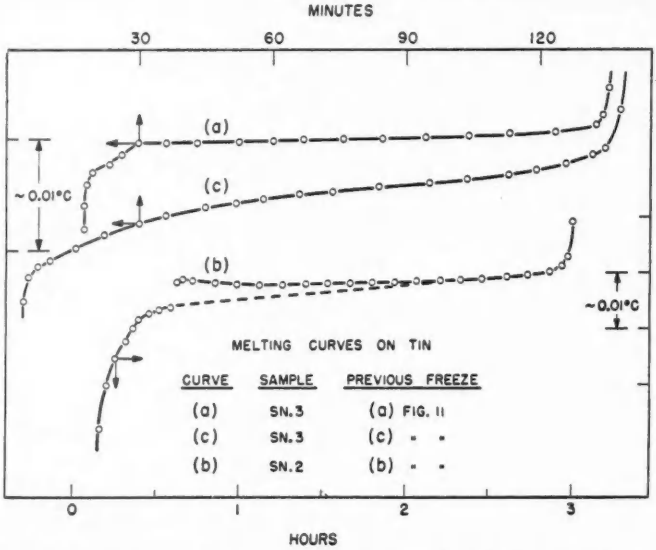

FIG. 12. Melting curves on tin. Curves (*a*) and (*c*) are after 2 hours' annealing at 215° C. and curve (*b*) is after 18 hours' annealing at 215° C.

plateau features appear on remelting curves of tin that has been rapidly frozen (Fig. 12(*a*)) while an alloy range of melting is observed on remelting material over half of which solidified at constant temperature (Fig. 12(*c*)). Also the shape of the remelting curve seems to be altered significantly by annealing

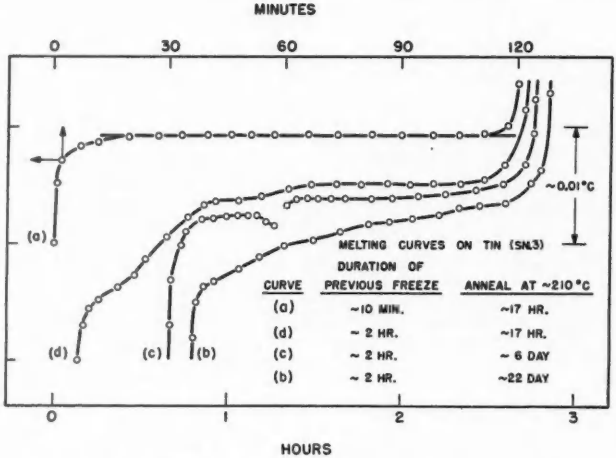

FIG. 13. Effect of annealing on the form of remelting curves of tin.

in the solid state, its effect being particularly striking on the slowly frozen material, see Fig. 13. Many curves exhibit discontinuities on the melting contour (Figs. 12(*b*) and 13(*c*)) in which the temperature abruptly rises a few thousandths of a degree and then may or may not decrease slightly before steadily rising until all the sample is melted.

REPRODUCIBILITY OF PLATEAU FREEZING TEMPERATURES

(*a*) *Zinc*

A series of induced freezes was made on three samples of S.P. zinc during a period of about 6 weeks in August and September of 1953 and the results are shown in Fig. 14. R_{TP} is the average of the thermometer resistances at

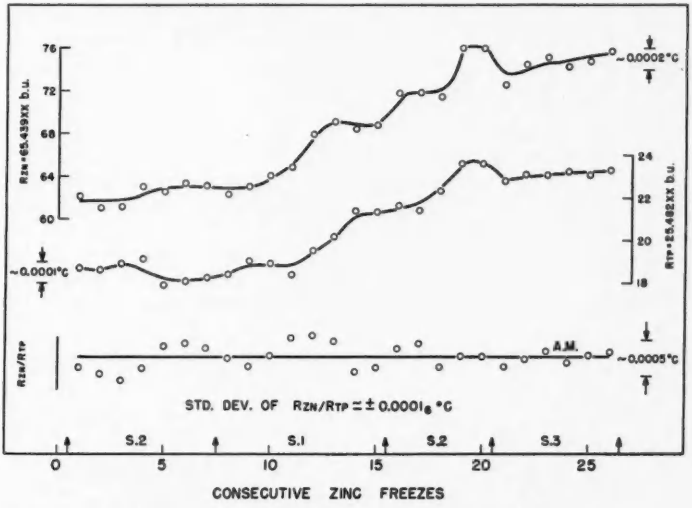

FIG. 14. Variation in R_{Zn} and R_{TP} and reproducibility of the ratio R_{Zn}/R_{TP} for a series of induced freezes on three samples, S.1, S.2, S.3, of S.P. zinc.

the triple point of water before and after the appropriate zinc freeze. R_{Zn} is the resistance of the thermometer at the plateau freezing temperature corrected to 1 atmosphere gas pressure over the melt. Both R_{Zn} and R_{TP} are zero current resistances corrected to unity bridge ratio and true bridge zero expressed in bridge units of resistance (see Part I of this paper, McLaren 1957). The mid-point of the sensing element of the thermometer was immersed about 15 cm. into the melt and no correction has been applied for the effect of this hydrostatic pressure on the value of R_{Zn}; at the time that these measurements were made successful experimental verification of the immersion pressure effect had not been realized (McLaren 1955). The recently obtained information shown in Fig. 20, see below, seems to justify a normalization of plateau freezing temperatures to an external pressure of 1 atmosphere.

The standard deviation of the ratio R_{Zn}/R_{TP} for 26 induced freezes made

on three samples S_1, S_2, S_3 of S.P. zinc from different distillation batches was $\pm 0.00016°$ C. Although these samples had been maintained at about 430° C. for 79, 52, and 13 days respectively prior to these measurements, it was not possible to distinguish between their plateau freezing temperatures, which indicates that the solution of oxide and other impurities into the melt was negligible during this period. However, heating samples for very long intervals in air results in appreciable thicknesses of oxide over the melt—which reduces the head of molten liquid over the interface at the measured level—and progressive deterioration of the graphite crucible. The use of a dry nitrogen atmosphere over the melt greatly reduced these effects.

The reproducibility of the plateau freezing temperature of particular melts of C.P. zinc also was found to be of the order of $\pm 0.0002°$ C. but the average plateau temperatures measured on individual samples of this zinc varied from a few ten thousandths to nearly 0.002 deg. lower than the plateau freezing temperature of S.P. zinc; thereby yielding additional confirmation, along with the chemical analyses and the alloy melting ranges of the two materials, that the S.P. zinc is measurably purer than the C.P. zinc.

Fig. 15 shows results, obtained from 78 freezes distributed over a much longer period, on the reproducibility of R_{Zn}/R_{TP} for a single thermometer, S.156, on the S.P. zinc. The triple point resistances used for the last three

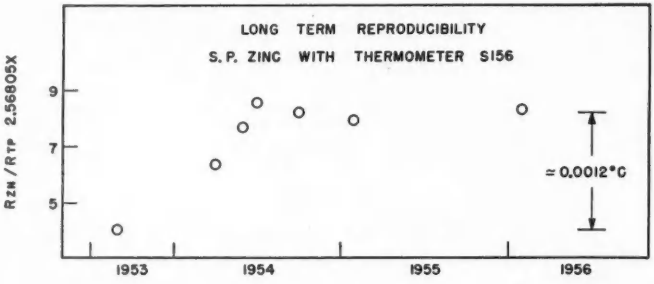

FIG. 15. Long term reproducibility of R_{Zn}/R_{TP} determined with thermometer S156 on S.P. zinc.

ratios of Fig. 14 are normalized on the highest triple point temperature measured in the triple cell intercomparisons (McLaren 1957); less reliable information on the triple cells used prior to October 1954 does not justify adjustment of the earlier triple point resistances. The R_{Zn}/R_{TP} ratio increased by 1.7 parts per million from September 1953 to February 1956, which would be equivalent to an increase of about 0.0012° C. in the freezing point of the zinc provided unaccounted changes did not occur in bridge measurements, triple cells, or the temperature coefficients of the platinum resistors over the $2\frac{1}{2}$ year interval.

An increase in the plateau freezing temperature of the S.P. zinc by the equivalent of about 0.001° C. seems unlikely for two reasons: copper, gold, and silver are the only known impurities that would raise the freezing tem-

perature of zinc and these are present only in trace amounts in the crucible and the thermometer well, the only solid materials in contact with the molten zinc; the alloy range of melting temperatures for S.P. zinc measures about 0.001° C. on new samples and on samples that have been maintained molten for nearly a year and it seems probable that the solution of sufficient copper into the zinc to raise the plateau freezing temperature by 0.001° C. would give rise to an increased range of melting temperatures of the new alloy. It is unlikely—see Part I of this paper— that differential errors in bridge calibrations or unaccounted variations in triple cell temperatures over this period could lead to an uncertainty greater than 0.0004° C. at the freezing temperature of zinc and it seems probable that the observed rise in R_{Zn}/R_{TP} was due to a change in the temperature coefficients of the platinum wire during prolonged annealing at about 430° C. During the period September 1953 to July 1954 thermometer S.156 was used for hundreds of hours in the vicinity of the freezing point of zinc and since has seen very limited service above 330° C. It is hoped that further work with secondary fixed points will determine the cause of this variation in R_{Zn}/R_{TP}.

Additional information on the long-term stability of the freezing temperatures of S.P. zinc is given in Fig. 16, which shows the variation in the ratios R_{Zn}/R_{TP} for six thermometers determined from two freezes with each thermometer in June 1954 and in February 1956 and the apparent changes in the

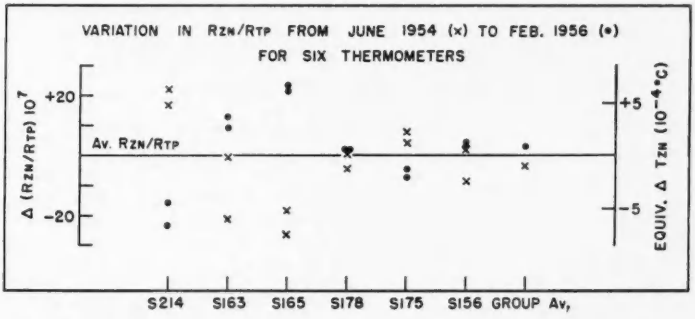

FIG. 16. R_{Zn}/R_{TP} determined from two induced freezes on S.P. zinc with each of six thermometers in June 1954 and February 1956.

zinc freezing temperature arising during the interval. As this figure contains information on only four freezes with each thermometer it cannot be used to detect with certainty a shift in the plateau freezing temperature of the zinc of less than 0.001° C.; it shows that there was no systematic change of this magnitude in the zinc freezing temperature and that any change present was probably less than 0.0003° C. The standard deviation of the 24 ratios about the average ratios for the respective thermometers was equivalent to ±0.0004° C.

(*b*) *Cadmium*

Results of a series of induced freezes on a single sample of S.P. cadmium are shown in Fig. 17. The standard deviation about the average plateau freezing temperature was equivalent to $\pm 0.00017°$ C.

(*c*) *Tin*

Results of a series of outside nucleated freezes on N.B.S. standard sample 42d tin are shown in Fig. 18. The standard deviation about the average plateau temperature was equivalent to $\pm 0.00019°$ C. Vulcan Detinning Extra

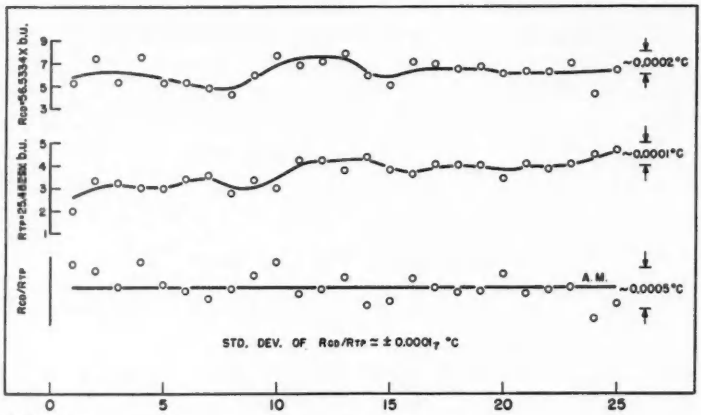

FIG. 17

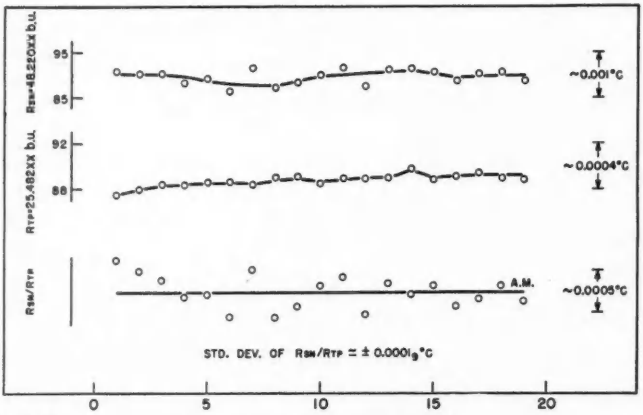

FIG. 18

FIG. 17. Variation in R_{Cd} and R_{TP} and reproducibility of R_{Cd}/R_{TP} for a series of induced freezes on a single sample of S.P. cadmium.

FIG. 18. Variation in R_{Sn} and R_{TP} and reproducibility of R_{Sn}/R_{TP} for a series of outside nucleated freezes on a single sample of N.B.S. (42d) tin.

Pure Tin also gives plateau freezing temperatures reproducible to ±0.0002 degree but the average temperature is about 0.008 degree higher than the average freezing temperature of N.B.S. tin.

PRESSURE EFFECT ON THE FREEZING TEMPERATURE

In the foregoing experiments the mid-point of the sensing element of the resistance thermometer was immersed 15 to 18 cm. in the melt, the total external pressure on the freezing interface adjacent to the sensing element being that of the atmospheric pressure over the melt plus the hydrostatic

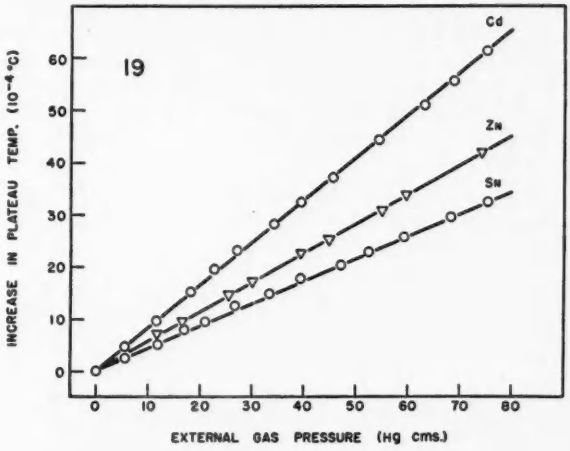

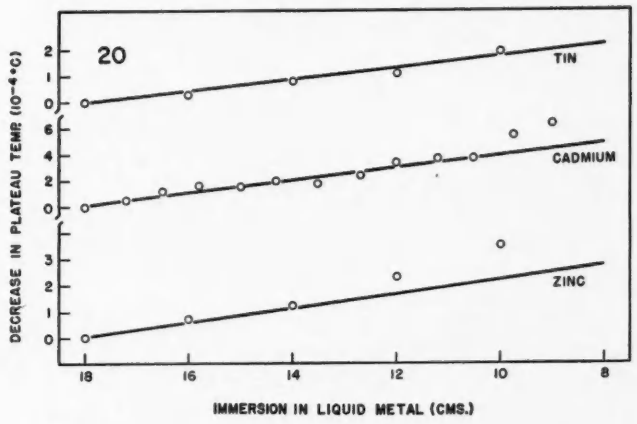

FIG. 19. Variation in plateau freezing temperature with external gas pressure.

FIG. 20. Variation in plateau freezing temperature with depth of immersion of the thermometer in the liquid metal. For tin and zinc each experimental value is the average of at least six pairs of NR commutations, while the values for cadmium were determined from single blocks of NRRN commutations.

pressure of the liquid metal. The variations of the plateau freezing temperatures with gas pressure were experimentally determined and the results are shown in Fig. 19, the increases in freezing temperatures for 1 atmosphere pressure on zinc, cadmium, and tin being 0.0043° C., 0.0062° C., and 0.0033° C. respectively. The variation in plateau freezing temperatures with immersion for these metals is shown in Fig. 20; the solid lines are deduced from the data of Fig. 19, using the liquid densities obtained from the references given in Table II. The immersion depth effect is especially difficult to measure for two reasons; the magnitude of the effect is less than 0.00005° C. per cm., which necessitates most careful interpolations on bridge balances, and the effect can be examined over only about 8 cm. of a 20 cm. melt if adequate immersion is maintained to eliminate the effect of heat conduction up the stem of the thermometer. Inspection of Fig. 20 shows that minimum immersions for a Meyers thermometer in the experimental arrangement used here are about 14, 12, and 10 cm. for the freezing points of zinc, cadmium, and tin respectively.

A comparison of the experimentally determined values of the pressure effects for 1 atmosphere for these metals with values calculated from the Clausius–Clapeyron relation is given in Table II.

TABLE II

COMPARISON BETWEEN CALCULATED AND OBSERVED CHANGES IN FREEZING TEMPERATURE FOR A PRESSURE CHANGE OF ONE ATMOSPHERE

$\Delta T_f = T_f \Delta V_{1s} \Delta P / L_f$; ΔT_f is the change in freezing temperature, T_f is the freezing temperature, ΔV_{1s} and L_f are the volume change on freezing and latent heat of fusion respectively, and ΔP is a change of pressure of one atmosphere

Metal	L_f,* 10^{10} dynes cm./mole	ΔV_{1s},† cc./mole	T_f, ° K.	$\Delta P = 1.013 \times 10^6$ dynes/cm.²	
				ΔT_f (° Calc.)	ΔT_f (° Obs.)
Zn	6.7	0.37	692.6$_8$	0.0039	0.0043
Cd	6.2	0.63	594	0.0061	0.0062
Sn	7.2	0.50	504	0.0035	0.0033

*From *Liquid Metals Handbook* (1952).
†ΔV_{1s} Zn and Sn from Saeger and Ash (1932); Cd from Matuyama (1929).

DISCUSSION

The shapes of the freezing and melting curves, revealing thermal structures inside 0.01° C. during the phase transformations on these high purity metals, yield information on the freezing process and particularly on the segregation of dissolved impurities.

For zinc and cadmium, the fast normal freezing curves and subsequent remelting curves correlate with the conventional conception of the change of state in a simple binary alloy. On the fast normal freezing curve the liquidus arrest is screened out by normal supercooling associated with difficult nucleation of the solid, gradually the rates of nucleation and grain growth increase to release sufficient latent heat to overcome the loss of heat from the melt to the cooling furnace and the melt temperature increases to a maximum, it

then falls in a nearly linear fashion with time as a normally segregated* alloy freezes in a cylindrical shell from the wall of the crucible. The rounding at the end of a freezing curve is due to both a rapidly increasing concentration of dissolved solute in the newly frozen solid and to the increasing rate of heat loss from the melt as the furnace block drops well below the melt temperature. When this ingot is remelted, melting occurs over a range of temperatures reflecting the concentration gradients of the solute laid down in the solid during the freeze and subsequently altered by any diffusion that may have occurred during the interval in which the ingot is kept solid.

The concentration gradients of dissolved solute in an ingot normally frozen in a graphite crucible are of course highly complex. Examination of a fast frozen sample after etching reveals a polycrystalline ingot containing about 100 grains varying in mean diameter from roughly 3 to 20 mm. with a preponderance of the material contained in the larger grains (see Fig. 2). The grains extend from the outside of the ingot through to the thermometer well and there is no evidence of a zone of equiaxed crystals which nucleated in the central regions owing to constitutional supercooling (Chalmers 1954). The short ingot in Fig. 21 was obtained by decanting very shortly after melting had commenced; it can be seen that shearing occurred at grain boundaries

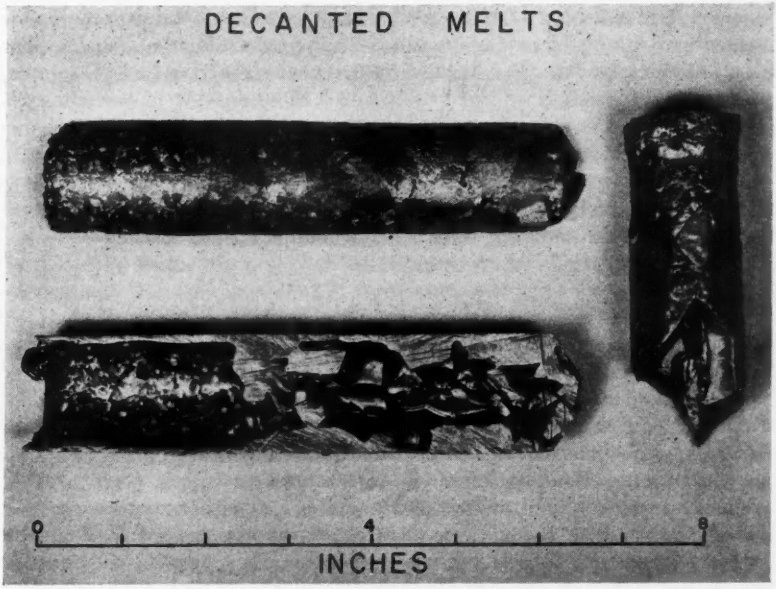

FIG. 21. Photograph of zinc ingots remaining in a crucible on decanting after partial melting.

*Normal segregation is due to a differential solubility of the solute in the liquid and the solid alloy and to a low rate of diffusion of the solute in the solid alloy.

when the ingot was forced out of the crucible and there is also evidence of marked premelting at the boundaries, presumably due to an excess of dissolved solute caused by coring, which excess results in a lowering of the melting temperature of the boundary region. The sectioned ingot in Fig. 21 was obtained by decanting after melting about half a fast frozen sample; here boundary melting had advanced to an extent that resulted in many grains being completely surrounded by liquid.

Thus both the shapes of cooling and melting curves and the observations on the ingots for normally fast frozen zinc are in general agreement with expectations for dilute alloys (Hume-Rothery *et al.* 1952; Rhines 1956). However the form of the cooling curve obtained on slow normal freezes cannot be as readily explained. The irregularities on the rise from supercool can be attributed to difficult nucleation and grain growth, but the existence of a plateau of essentially constant temperature on the cooling curve of a simple alloy implies that material of fixed concentration is being frozen out at these times. This is further substantiated by the existence of plateaus on the remelting curves taken after slow normal freezes. The agreement between the plateau temperature on a freeze with the highest temperature attained on melting suggests that the solid being laid down at the plateau freezing temperature has the concentration of solid in equilibrium with liquid at the liquidus temperature of the alloy. Therefore these results would tend to attribute the plateau temperature to an extended liquidus arrest arising from non-equilibrium segregation of the dissolved solute by the freezing interface giving rise to highly cored grains.

Tiller *et al.* (1953), Wagner (1954), and Pohl (1954) present theories on the redistribution of dissolved solute in a long single crystal normally frozen with a plane interface moving along a graphite boat with the rate of solidification controlled by adjusted temperature gradients along the boat. They assumed that diffusion of solute in the solid is negligible during the freezing times involved and treat cases in which the effects of mixing of the solute in the liquid by diffusion or convection are considered. They show that the solute concentration in the solid would rise asymptotically from the concentration in equilibrium at the liquidus temperature to a concentration equivalent to the initial average concentration of the liquid (Tiller), implying that, for long single crystals, material freezing with constant composition would solidify at the solidus temperature of the homogenized alloy.

The location of the plateau temperature on the phase diagram of the alloy is, therefore, uncertain. If in fact the plateau temperature is identical with the solidus temperature of the sample, then the close experimental agreement between the highest temperature observed on a melting curve with the plateau temperature on a freeze for a given sample suggests that the concentration of the solute in the newly frozen solid must rise very rapidly to the average concentration after freezing commences, the part of the solid containing less than this average concentration being such an insignificant fraction of the total that the remelting curves do not reveal its presence. However, this supposition raises difficulties in explaining the apparent alloy slopes on the freezing and melting curves that are observed.

The results of Pearson *et al.* (1950) on the distribution of antimony in ingots of low content germanium alloys, slowly frozen from one end, showed that over 80% of each ingot solidified with antimony contents of less than the average antimony content of the ingot and that half the material solidified with less than 1% of this amount. In the light of this work it seems likely that on freezing the low impurity content zinc used in these experiments significant amounts of solid are laid down with such a small variation in the composition of the dissolved solute that the associated range in the liquidus temperature is too small to be measured by the resistance thermometer; during these times a plateau appears on the cooling curves. On remelting this material a plateau feature appears on the melting curve which increases slightly over its length (see Fig. 6(*b*)); this measurable range of transformation temperature on a melting plateau may be due to diffusion, during the interval in which the ingot was solid, of solute into the solid that solidified at constant temperature.

This explanation of the plateau temperatures could account for the observed form of the freezing and melting curves obtained with the high purity zinc and cadmium and even the plateaus observed on slow outside nucleated tin freezes. However, the melting curves obtained on tin cannot be readily explained on this basis and it is probable that concentration gradients of dissolved chemical impurities are not the only factors that influence the apparent melting and freezing temperatures. For the polygranular cylindrical samples used in our experiments it seems that to account adequately for the redistribution of the solute on freezing we must consider the effects of preferential segregation at grain or subgrain boundaries and the influence on the solute of the self-strain in the grains introduced by freezing on cylindrical symmetry. It is possible that these effects, along with the diffusion of solute atoms and lattice defects during recrystallization, could influence freezing and melting temperatures and account for the apparent alloy range of transformation temperatures of the order of a part in 10^5 of the average melting temperature that was measured in these experiments. Melting characteristics of ingots deliberately strained either by radiation or by cold work might provide useful information on this matter.

CONCLUSIONS

This investigation has shown that it is possible, using appropriate techniques, to develop sections of very steady temperatures on the cooling curves of high purity zinc, cadmium, and tin. These plateaus have durations that are dependent on the gross rate of cooling and are reproducible to the order of $\pm 0.0002°$ C., a variation which is close to the precision limit of the measuring apparatus.

The plateau freezing temperatures for these high purity metals are thought to be due to non-equilibrium segregation of the dissolved solute.

It was not possible to distinguish among the plateau freezing temperatures of three samples of New Jersey S.P. zinc selected from separate redistillation batches of New Jersey C.P. zinc; this factor, together with the small range of melting temperatures that was observed on S.P. zinc, gives strong support

for the consideration of the plateau freezing temperature of high purity zinc as a precision alternative to the boiling point of sulphur.

The plateau freezing temperatures of particular samples of cadmium and tin have also been found to be highly reproducible and should find use as precision secondary temperature standards.

The ready experimental realization and the high reproducibility of the plateau freezing temperatures of zinc, cadmium, and tin stand severe critical comparison with the establishment and reported stabilities of the triple point of water and the standard boiling point of water and are demonstratively superior to any published data on the realization and reproducibility of the boiling point of sulphur.

A study of the freezing curves on these high purity metals has revealed structures associated with nucleation, growth, and segregation during the freezing process, and subsequent remelting curves have shown a striking dependence on the thermal history of the sample. It appears that precision thermal analysis would be a useful addition to the metallurgical methods already employed to study these phenomena.

ACKNOWLEDGMENTS

The author is grateful to Messrs. J. A. Lowdon and E. G. Murdock for their valuable assistance in carrying out these investigations and to Dr. H. Preston-Thomas for helpful comments on reading the paper.

REFERENCES

CHALMERS, B. 1954. J. Metals, **200**, 519.
HUME-ROTHERY, W., CHRISTIAN, J. W., and PEARSON, W. B. 1952. Metallurgical equilibrium diagrams (The Institute of Physics, London), Chap. 10.
MATUYAMA, Y. 1929. Sci. Repts. Tôhoku Imp. Univ. (i), **18**, 19.
MCLAREN, E. H. 1955. Comité International des Poids et Mesures, Procès-Verbaux des Séances de 1954, 24, T163.
——— 1957. Can. J. Phys. **35**, 78.
PEARSON, G. L., STRUTHERS, J. D., and THEUERER, H. C. 1950. Phys. Rev. **77**, 809.
POHL, R. 1954. J. Appl. Phys. **25**, 1170.
RHINES, F. N. 1956. Phase diagrams in metallurgy (McGraw-Hill Book Co., Inc., New York), p. 24.
ROESER, W. F. 1929. J. Research NBS, **3**, 343.
SAEGER, C. M. and ASH, E. J. 1932. J. Research NBS, **8**, 37.
DE SELINCOURT, M. 1939. Proc. Phys. Soc. **51**, 695.
TILLER, W. A., JACKSON, K. A., RUTTER, J. W., and CHALMERS, B. 1953. Acta Met. **1**, 428.
TILLER, W. A. and RUTTER, J. W. 1956. Can. J. Phys. **34**, 96.
WAGNER, C. 1954. J. Metals, **200**, 154.
WAIDNER, C. W. and BURGESS, G. K. 1910. Bur. Standards Bull. **6**, 149.

A METHOD FOR INTERPRETING THE DISPERSION CURVES OF WHISTLERS[1]

L. R. O. Storey

ABSTRACT

This paper considers how the dispersion curves of whistlers may be interpreted to provide information on the distribution of electron density with height in the outer atmosphere.

The simpler inverse problem, that of computing the dispersion curve for a given distribution, is considered first. On the assumption of longitudinal propagation in a dipole magnetic field, the dispersion curve is derived in the form of an equation relating the product $tf^{\frac{1}{2}}$ to the frequency f. The equation can be represented by a power series in f, which is useful for estimating departures from the elementary $f^{-\frac{1}{2}} - t$ relationship at frequencies where these departures are small. The coefficient of f^n in this series is termed the 'dispersion constant of order n'.

The main problem is now treated, regarding the above equation as an integral equation determining the distribution of electron density along the path. This integral equation is solved in series, making use of the same power series in f. The dispersion constant of order n is shown to be proportional to the nth moment of the distribution, suitably expressed and weighted. From the values of the moments it is possible to deduce both the initial geomagnetic latitude of the path and the distribution of electron density along it. When the observed dispersion curve is incomplete, so that only the dispersion constants of lower order can be measured, the method yields an approximation to the distribution.

1. INTRODUCTION

In some recent studies by Helliwell *et al.* (1956) whistlers recorded at a high latitude were analyzed on a 'sound spectrograph' having fine resolution in frequency. By this means features which had not been noted previously were brought out. Firstly, a whistler was not shown as a homogeneous band of noise varying steadily in mean frequency, but rather as a rapid succession of discrete traces, each representing a comparatively pure tone. Secondly, the relationship between frequency and time in any one trace departed markedly at high audio-frequencies from the simple dispersion law derived by Eckersley (1935). Instead of the frequency starting high and falling steadily, as the simple law would predict, each trace made its appearance at a medium frequency and then split into two branches, one of which fell in frequency as usual, while the other showed the reverse type of dispersion, with frequency rising. Near the initial frequency, where the two branches began, the trace was roughly parabolic; accordingly this frequency was called the 'nose frequency', and the whole phenomenon was designated as a 'nose whistler'. In a nose whistler the nose frequency was observed to fall steadily from the earlier to the later traces.

Subsequent research has established that these effects are not peculiar to high latitudes. Analyses of the 'swish' type of whistler at medium and low latitudes often show multiple traces, though less spread out in time than at high latitudes. The nose effect also occurs, but the mean nose frequency rises

[1]Manuscript received June 3, 1957.
Contribution from Defence Research Telecommunications Establishment, Defence Research Board, Shirley Bay, Ottawa, Ontario.

with decrease in latitude and may lie well above audibility. The relationship between frequency and time in the descending branch of the trace tends to Eckersley's law at the lowest frequencies, and often conforms to it quite well throughout the audio range to which earlier measurements were confined. This accounts for the effect escaping previous notice. It now appears, however, that all normal whistlers are, in fact, nose whistlers.

The presence of discrete traces in the analysis of a whistler is understood to mean that the ionization in the outer atmosphere is not homogeneous, but contains irregularities in the form of long columns of enhanced electron density, extended up the lines of magnetic force, which act as ducts and channel the waves into discrete paths. A lightning stroke illuminates a wide area at the base of the ionosphere, launching waves into many such paths. The paths which start from the high-latitude edge of the illuminated area are the longest and go out furthest from the earth; they therefore correspond to the later traces. Conversely the earlier traces belong to paths starting from points in the area at lower magnetic latitudes.

The explanation of the nose effect, and the accompanying departures from Eckersley's dispersion law at high frequencies, was advanced independently by Helliwell *et al.* (1956) and by Ellis (1956). In deriving the simple law the electron gyro-frequency was assumed to be much greater than the wave frequency everywhere along the path, but for a wave frequency sufficiently high this assumption must fail near the top of the path where the gyro-frequency is least. In this situation the wave excites the gyro-resonant circular motion of the electrons round the lines of force, and as a result suffers much group delay over and above that predicted by the simple law. This extra delay accounts for the nose effect. If the propagation is longitudinal then the upper frequency limit of the rising portion of a whistler trace, where the delay becomes infinite, is equal to the gyro-frequency at the very top of the path. The nose lies at a somewhat lower frequency. The higher the initial geomagnetic latitude of the path the lower is the gyro-frequency at the top of it, and hence the lower the nose frequency of the corresponding trace; this fact explains the decrease in nose frequency from the earlier to the later traces in a nose whistler, and also the general decrease in mean nose frequencies in whistlers observed at higher latitudes.

Helliwell *et al.* (1956) have considered what other factors besides the gyro-frequency at the top of the path go into determining the nose frequency. They find that the nose frequency must lie between the gyro-frequency and one quarter of it, but that the exact relation between the two frequencies depends on how the density of ionization varies along the path. If most of the ionization were concentrated at the lower ends of the path the nose frequency would take the higher value, while if it were concentrated around the top the lower value would apply. Hence, it appears that study of the location of the nose frequency or, more generally, the entire shape of the upper part of a whistler trace should yield information not only on the gyro-frequency at the top of the path but also on the distribution of ionization along it.

This paper has the limited aim of considering what information is contained

in a single whistler trace, and how it can be extracted. The relationship between the frequency of the trace and the time after the initial lightning stroke will be referred to as the 'dispersion curve', while the term 'dispersion law' will be used for any analytical expression intended to represent it.

The matter of the paper is arranged as follows. In Section 2 it is shown how to calculate the dispersion law when the path and the distribution of ionization are given; this problem is the inverse of that forming the subject of the paper, and is, of course, much simpler. The equation for the dispersion law is required because it is also the integral equation relating an observed dispersion curve to the unknown distribution which gave rise to it. In Section 3 this integral equation is rearranged to prepare it for solution. A formal solution, applicable to a hypothetical case where the dispersion curve is complete and measured exactly, is derived in Section 4. The case of incomplete data is treated in Section 5, and approximate methods of solution given. Finally the methods are discussed and criticized in Section 6.

The argument is illustrated throughout by working a numerical example. For this purpose a particular distribution of ionization was assumed, and the dispersion law was calculated for a particular path. Attempts were then made to estimate the gyro-frequency at the top of the path and to recover the distribution, using only the information in the lower part of the dispersion curve, the part which is most likely to be reliable in practice. Diagrams show the progressive improvement in the estimates as more and more of the curve is taken into account.

2. THE GENERAL DISPERSION LAW*

In this section a general expression is derived for the dispersion law, relating it to the distribution of ionization along the path of the whistlers through the outer atmosphere.

The group delay t experienced by a wave packet of mean frequency f in travelling through a dispersive, anisotropic medium is given by

$$t(f) = \frac{1}{c} \int \mu'(f) \cos \alpha \, ds, \tag{1}$$

where c is the velocity of light, μ' the group refractive index, α the angle between the wave normal and the ray, and the integral is taken along the ray path of which ds is an element. The value of the group refractive index depends on the angle θ between the wave normal and the magnetic field, and on the relative values of the wave frequency, the local gyro-frequency f_H, and the local critical frequency f_0 which specifies the density of the ionization. The relationship between wave normal and ray directions may also depend on frequency, so in general the ray path is different for different frequencies.

*This section recapitulates in part the argument of an earlier paper by Storey (1956) which was concerned with heavy ion effects in whistlers. No account has been taken of ion effects here, since although there are theoretical grounds for expecting them to occur, they have not yet been observed experimentally and in any case are likely to be small. If their presence should be confirmed, some attempt might have to be made to estimate and allow for them before analyzing records by the methods of this paper.

Before the general dispersion law can be derived some assumptions have therefore to be made about the shape of the ray path and about the variation along the path of the gyro-frequency f_H and the angle θ. Some further assumptions restrict slightly the types of distribution which can be handled. These assumptions are now listed.

1. Ray Path

It will be assumed that all frequencies are propagated longitudinally, the mean wave normal direction being parallel to the magnetic field (i.e. $\theta = 0$). Then all their ray paths are the same and follow a magnetic line of force exactly (i.e. $\alpha = 0$). The dispersion law will be calculated for 'short whistlers' which have traversed the path along the line of force once only; for 'long whistlers' the calculated delay times should be doubled.

2. Geomagnetic Field

The geomagnetic field will be represented in the usual way as being due to a dipole situated at the center of the earth. A line of force then has the equation

$$r/r_0 = \cos^2 L/\cos^2 L_0, \tag{2}$$

where r is the distance from the center of the earth, L is the geomagnetic latitude, and r_0, L_0 are the corresponding coordinates for the point where the line intersects the earth's surface.

The gyro-frequency f_H, which is proportional to the field strength, varies with position according to the law

$$f_H = f_e(r_0/r)^3(1+3\sin^2 L)^{\frac{1}{2}}, \tag{3}$$

where f_e ($\simeq 0.8$ Mc./s.) is its value at ground level on the magnetic equator.

3. Distribution of Ionization

The distribution will be assumed symmetrical about the geomagnetic equator, with the ionization sufficiently dense for the condition $f_0 \gg (ff_H)^{\frac{1}{2}}$ to hold everywhere. Since the highest frequency present in the whistler is equal to the gyro-frequency at the top of the path (f_m, say), the condition will be well satisfied at all frequencies if $f_0 \gg (f_m f_H)^{\frac{1}{2}}$.

In the worked example which illustrates the method of the paper the path will start from geomagnetic latitude $L_0 = 55°$. The distribution suggested by Dungey (1954) will be adopted, as in a previous paper by Storey (1956), to which reference should be made for details; this distribution is graphed as the broken line in Fig. 5.

On the first two assumptions, the equation for the dispersion law becomes

$$t(f) = \frac{1}{c}\int \mu'(f)\, ds, \tag{4}$$

where ds is now an element of the line of force.

On the third assumption, the group refractive index for the extraordinary mode in longitudinal propagation is given approximately by

$$\begin{aligned} \mu' &\simeq \frac{1}{2}\frac{f_0 f_H}{f(f_H - f)^{3/2}} \\ &= \tfrac{1}{2} f_0 (ff_H)^{-\frac{1}{2}} \{1 - f/f_H\}^{-3/2}. \end{aligned} \tag{5}$$

This expression is due to Helliwell *et al.* (1956). The term outside the curly brackets in Eq. (5) will be recognized as the simpler approximation much used in earlier studies of whistlers, while the bracketed factor represents the correction for electron gyro-resonance.

Thus the general equation for the dispersion law is

$$t(f) = \frac{1}{2c} \int f_0 (f f_H)^{-\frac{1}{2}} \{1 - f/f_H\}^{-3/2} \, ds. \tag{6}$$

For frequencies such that $f \ll f_H$ everywhere along the path, it reduces to

$$t(f) \simeq \left\{ \frac{1}{2c} \int f_0 f_H^{-\frac{1}{2}} \, ds \right\} f^{-\frac{1}{2}} = D f^{-\frac{1}{2}}, \tag{7}$$

which is Eckersley's simple form.

Fig. 1 shows the dispersion law calculated for the particular path and distribution of ionization assumed above. The full curve is the general exact

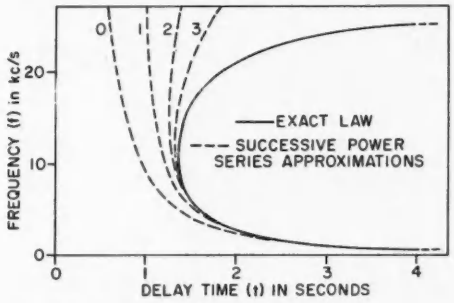

FIG. 1. Calculated dispersion law ($L_0 = 55°$).

law, showing the nose effect, while the broken curve labelled "0" is the simple approximate form; the two are seen to converge at the lower frequencies.

It is instructive to examine further the discrepancy between the general and approximate dispersion laws by expressing the former as a relationship between the product $tf^{\frac{1}{2}}$ and the frequency since, according to the latter, this quantity should be independent of frequency and equal to the 'dispersion', D. In this form the equation reads

$$tf^{\frac{1}{2}} = \frac{1}{2c} \int f_0 f_H^{-\frac{1}{2}} \{1 - f/f_H\}^{-3/2} \, ds. \tag{8}$$

Fig. 2 shows the exact dispersion law of Fig. 1 plotted out in this way. Starting from the value D at zero frequency, the quantity $tf^{\frac{1}{2}}$ rises steadily with increasing frequency and becomes infinite at the upper limiting frequency f_m. In this particular instance f_m is about 29 kc./s., and the nose frequency about 11 kc./s.

Now the simple dispersion law can be described completely by specifying the one constant D, but for the general law this is not possible. Nevertheless, if the interest is only in frequencies below some moderately high value where

the deviations from the simple law are not too great, this lower part of the general law can be described to fair accuracy by specifying just a small

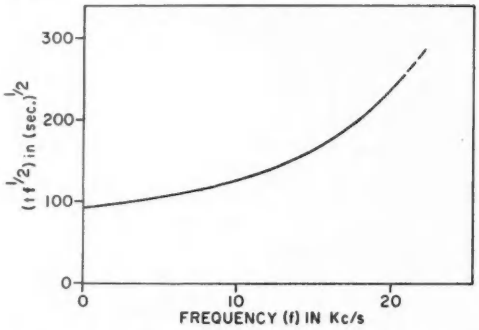

FIG. 2. Exact dispersion law as a graph of $tf^{\frac{1}{2}}$ against f.

number of constants. These constants are the coefficients in the power series for $tf^{\frac{1}{2}}$ as a function of f, viz.

$$tf^{\frac{1}{2}} = D_0+D_1f+D_2f^2+\ldots+D_nf_n+\ldots. \tag{9}$$

Their values are obtained from Eq. (6) by expanding the bracketed correction factor in ascending powers of f. The result is that

$$D_n = \frac{A_n}{2c}\int f_0 f_H^{-(n+\frac{1}{2})}\,ds, \tag{10}$$

where

$$A_n = (2n+1)!/(2^n n!)^2. \tag{11}$$

The coefficient D_n, which has dimensions of $(\text{time})^{n+\frac{1}{2}}$, will be called the 'dispersion constant of order n'. D_0, the dispersion constant of zero order, is identical with the 'dispersion' D as originally defined. Since there are known methods by which a power series can be fitted to a smooth graph, such as that of $tf^{\frac{1}{2}}$ against f, the dispersion constants are measurable parameters of a whistler trace.

In Fig. 1 the utility of the closer approximations provided by the first few terms in the series is illustrated by the broken lines labelled 1, 2, and 3. These show the results obtained by taking terms up to and including those in f, f^2, and f^3 respectively. The third-order approximation is seen to follow the exact curve fairly well up to the nose frequency. Conversely, from the part of a dispersion curve lying below the nose it should be possible to determine the first four dispersion constants, i.e. those from D_0 to D_3.

3. THE INTEGRAL EQUATION

In the preceding section the dispersion law was derived as a relation between the product $tf^{\frac{1}{2}}$ and the frequency (Eq. 8), which relation is also the integral equation for determining an unknown distribution of ionization from the

observed dispersion curve. This section is concerned with rearranging it into a form suitable for solution.

Now the variables s and f_H are mutually related through the assumptions about the ray path and the geomagnetic field. The first step must therefore be to eliminate one or the other or to express both in terms of some third variable.

The point now to be made is the key to the whole argument which follows. It is that since there exists no direct measure of position on the ray path, and ionization at different levels can only be distinguished insofar as the local gyro-frequencies are different, the distribution of ionization is most appropriately discussed in terms of some function of the gyro-frequency as the independent variable. Consideration of the form of the integral equation suggests that the reciprocal of the gyro-frequency is a suitable function to adopt. This quantity has the dimensions of time, and will be denoted by the symbol τ_H:

$$\tau_H = f_H^{-1}. \tag{12}$$

For longitudinal propagation in a dipole field, the dependence of τ_H on position is found from Eq. (3) to be

$$\tau_H = \tau_e(r/r_0)^3(1+3\sin^2 L)^{-\frac{1}{2}}, \tag{13}$$

where $\tau_e = f_e^{-1}$.

In terms of τ_H the integral equation reads

$$tf^{\frac{1}{2}} = \frac{1}{c}\int_0^\infty \left\{ f_0 \tau_H^{\frac{1}{2}} \frac{ds}{d\tau_H} \right\} (1-f\tau_H)^{-3/2}\, d\tau_H. \tag{14}$$

The integration has been taken from zero to infinity with the understanding that the term $ds/d\tau_H$ is zero outside the range of values of τ_H covered by the path. The lower limit of this range is τ_0, the value on the earth's surface at the start of the path:

$$\tau_0 = \tau_e(1+3\sin^2 L_0)^{-\frac{1}{2}}. \tag{15}$$

The upper limit is τ_m, the value at the summit:

$$\tau_m = \tau_e \sec^6 L_0. \tag{16}$$

Note that since this integration covers only half the path, the coefficient in front of the integral sign has had to be doubled.

In the form of Eq. (14), the integral equation is seen to relate the dispersion curve to the bracketed expression immediately following the integral sign on the right-hand side. As this expression plays a large part in the subsequent analysis, it is convenient to give names to it and to the factors of which it is composed.

The critical frequency f_0, expressed as a function of τ_H, will be called the 'distribution function'. Since the quantity τ_H increases uniformly up a line of force (see Eq. 13), the distribution function possesses the same general features as the relation between critical frequency and height.

The second factor

$$w(\tau_H) = \tau_H^{\frac{1}{2}}\, ds/d\tau_H \tag{17}$$

will be called the 'weighting function', since it represents the weight assigned in the integration to the critical frequency at different levels. The weighting function exists only in the range $\tau_0 \leqslant \tau_H \leqslant \tau_m$, and it rises to infinity as τ_H approaches τ_m. In so doing it gives quantitative expression to the fact that the ionization near the top of the path plays the largest part in determining the properties of a whistler.

The complete expression, being the product of these two factors, will be called the 'weighted distribution'. The distribution function, weighting function, and weighted distribution are graphed in Fig. 3 for the particular path and distribution assumed previously.

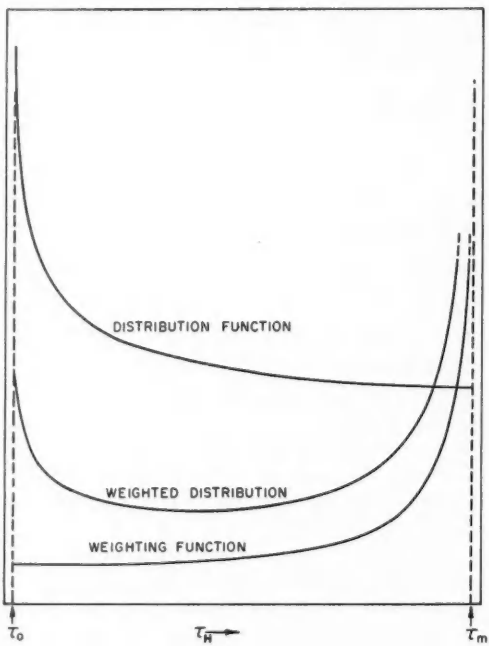

FIG. 3. Weighting function for $L_0 = 55°$, assumed distribution function, and weighted distribution.

4. THE FORMAL SOLUTION

The integral equation (Eq. 14) connecting the observed dispersion curve with the unknown weighted distribution now needs to be solved. The author has not yet succeeded in finding an analytical solution. However, the utility of the power series approximations for the dispersion law developed in Section 2

suggested that it might be worth while to seek a solution in series, and this approach has proved more fruitful.

The first step in deriving the series solution is to express the dispersion constants (Eq. 10) in terms of the variable τ_H, so that

$$D_n = \frac{A_n}{c} \int_0^\infty \tau_H{}^n \{f_0 w(\tau_H)\}\, d\tau_H, \tag{18}$$

$$= \frac{A_n}{c} c_n, \quad \text{say.} \tag{19}$$

These equations express the following useful result: the dispersion constant of order n is proportional to the nth moment of the weighted distribution. This moment has been denoted by the symbol c_n, while the coefficients A_n are those given by Eq. (11). The values of the moments can be obtained from the measured dispersion constants by means of Eq. (19).

The problem now becomes that of inferring the shape of a curve from the values of its successive moments. It will be considered first in an idealized form, where the values of all the moments are assumed to be known accurately.

The problem of synthesizing a function from a table of moments is one familiar to statisticians. It does not always have a unique solution. The conditions for uniqueness have been investigated by Kendall (1940), who finds that a sufficient pair of conditions is for the zero-order moment (i.e. the area) of the function to be finite and the function itself equal to zero above some finite upper limit of the independent variable. These conditions cover the weighted distribution function, the upper limit of τ_H being τ_m.

The unique solution, where such exists, can be found with the aid of the Fourier transform or, in statistical parlance, the characteristic function (Arley and Buch 1950). The Fourier transform of the unknown function has a power series representation in which the coefficient of the nth term is proportional to the moment c_n.

The formal solution for the weighted distribution would therefore proceed as follows: from the measured values of the dispersion constants D_n the moments c_n are calculated; these moments give the coefficients in the power series for the Fourier transform, and hence the transform itself; an inverse Fourier transform then yields the weighted distribution.

The weighted distribution would be interpreted in this way. Firstly, the lower and upper limits τ_0 and τ_m both identify the geomagnetic latitude at which the whistler path started. Knowing the path, the weighting function can be calculated. Next, the weighted distribution is divided by the weighting function, and their quotient is the distribution function; this function, it will be remembered, specifies the variation of the critical frequency with τ_H in the range between τ_0 and τ_m. Finally τ_H can be converted to height, again from knowledge of the path, and the critical frequency is obtained as a function of height. To sum up, from the weighted distribution it is possible to infer both the initial geomagnetic latitude of the path and the variation of critical frequency along it.

Unfortunately, the formal solution, though mathematically sound, is of no use in practice because it requires the values of all the dispersion constants to be known accurately. Often, however, the whistler trace is missing at the higher frequencies, so that only a few dispersion constants of low order can be determined. Even if the higher order constants were measurable their values would be suspect, because the assumptions about the ray path become progressively less valid as the frequency rises. Moreover, the Fourier transform of the weighted distribution cannot be reconstructed satisfactorily from just a few terms in its series representation.

These facts suggest that it would be better to seek a method of solution which, though less general than the formal method, would by the same token be related more closely to the particular nature of the problem in hand and would still be applicable when the data were incomplete. Inevitably, a method based on incomplete data can only yield approximate solutions. One such approximate method of solution is developed in the next section.

5. AN APPROXIMATE SOLUTION

5.1. Method of Solution

It will now be assumed that the only data obtainable from the whistler trace are the first few dispersion constants of low order. The aim is to deduce from their values approximations for the initial geomagnetic latitude of the path and for the distribution of ionization.

The first question, then, is how to identify the path. The way to proceed is suggested by the presence of the infinity in the weighted distribution at the upper limit τ_m. Evidently the values of the high-order moments, in which large weights are assigned to the function at high values of τ_H, are determined almost entirely by its shape just below this infinity (i.e. by conditions near the top of the path). More specifically, the ratio of any moment to the next lower moment tends to the limit τ_m as the order n tends to infinity. Now the value of τ_m measures the initial latitude of the path, by Eq. (16). When the moments of high order are not known, τ_m can be estimated by forming the ratios of the low-order moments and then extrapolating them to infinite order. How best to perform this extrapolation is discussed in Section 5.2. Once the initial latitude L_0 has been estimated, the weighting function can be calculated from the geometry of the path.

The next subsection, Section 5.3, deals with the problem of how to recover the distribution. The fact that the high-order moments tend to a constant ratio, and so become almost redundant, encourages the hope that the shape of the distribution can be recovered fairly well from the low-order moments alone. However, it is obvious that if only a certain number of moments are known, then only this number of parameters of the distribution can be determined. A reasonable procedure is to assume some smooth functional form for the distribution with the shape controlled by the given number of parameters, and then to adjust their values so that, when the distribution function is multiplied by the calculated weighting function, the resultant weighted distribution has the correct moments.

5.2. Identification of the Ray Path

It is hoped to identify the ray path by extrapolating to infinite n the ratio c_n/c_{n-1}, which will be called ρ_n. The problem is to find a way of graphing the variables in a form suitable for extrapolation. A straightforward graph of ρ_n against n would clearly not be suitable, as the extrapolation would have to be made over an infinite range of the independent variable. Clearly the independent variable must be some function of n which tends to a finite limit as n tends to infinity, while its relation to the dependent variable should be such that the graph reduces to a straight line at large n. To find a form of graph which meets these requirements, it is necessary to examine how the ρ_n depart from their limiting value τ_m when n is large but finite.

Now the moments of high order are determined chiefly by that part of the weighted distribution function which lies just below τ_m. In this region the function can be shown to vary with τ_H roughly as follows:

$$\{f_0 w\} \simeq k_0 \left(\frac{\tau_H}{\tau_m - \tau_H}\right)^{\frac{1}{2}} \left\{1 + 2k_1 \frac{\tau_m - \tau_H}{\tau_m}\right\}. \tag{20}$$

The constants k_0 and k_1 depend on the detailed shape of the weighting and distribution functions around τ_m, but there is no need to know their values.

By use of this expression the following approximation is obtained for the moment ratios, applicable when n is large:

$$\rho_n = \frac{c_n}{c_{n-1}} \simeq \left\{1 - \frac{k_1}{(n+1)(n+2)}\right\}\left(\frac{2n+1}{2n+2}\right) \tau_m. \tag{21}$$

Hence

$$\left(\frac{2n+2}{2n+1}\right) \rho_n \simeq \left\{1 - \frac{k_1}{(n+1)(n+2)}\right\} \tau_m. \tag{22}$$

It therefore appears that a graph of $[(2n+2)/(2n+1)]\rho_n$ against $1/[(n+1)(n+2)]$ should reduce at small values of the abscissa to a straight line cutting the ordinate axis at the value τ_m. Hence this is a suitable way to plot the moment ratios for extrapolation to infinite n. Fig. 4 shows the moment ratios for the whistler trace of Fig. 1 plotted out in this way.

The extrapolation of the graph can be performed algebraically by fitting a polynomial to the plotted points. The more points there are, the closer will be the estimate of τ_m. The first and crudest approximation is that based on ρ_1 alone, the second is based on ρ_1 and ρ_2, and so on. In each approximation the estimate of τ_m is a linear function of the moment ratios involved. The first three approximations are these:

(23) 1st approx. $\tau_m \simeq 1.333\rho_1$,

(24) 2nd approx. $\tau_m \simeq 2.400\rho_2 - 1.333\rho_1$,

(25) 3rd approx. $\tau_m \simeq 4.082\rho_3 - 3.600\rho_2 + 0.571\rho_1$.

When the moment ratios for the whistler trace of Fig. 1 are inserted in these

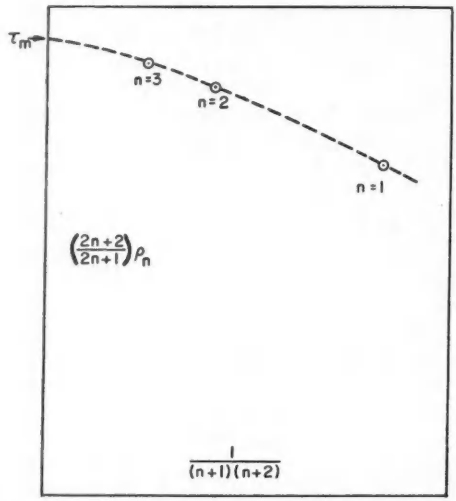

FIG. 4. Graph for estimating τ_m by extrapolation of the moment ratios.

expressions, the errors in the estimates of τ_m and of the corresponding values of L_0 are found to be as given in Table I.

TABLE I

ACCURACY OF IDENTIFICATION OF THE RAY PATH

Order of approximation	Percentage error in τ_m	Error in L_0
1	−46	−4° 25′
2	+ 6	+0° 24′
3	+ 1	+0° 4′

5.3. Recovery of the Distribution

Now that the initial geomagnetic latitude of the path has been estimated, the weighting function follows. There remains the problem of reconstructing the distribution function. The requirement for a satisfactory solution is that, when multiplied by the weighting function, the resulting weighted distribution should have moments as observed. Suppose that the known moments run from c_0 up to some particular c_n, a total of $(n+1)$ moments. The procedure is to assume for the distribution function a plausible algebraic form governed by $(n+1)$ disposable parameters, and then to adjust the values of these parameters until the observed and calculated moments agree.

The particular form that will be adopted for the distribution function is a power series in τ_H containing terms up to the nth power, with the coefficients of these terms as the required $(n+1)$ disposable parameters:

$$f_0(\tau_H) = \phi_0 + \phi_1 \tau_H + \ldots + \phi_n \tau_H^n$$

$$= \sum_{i=0}^{i=n} \phi_i \tau_H^i, \quad \text{say.} \tag{26}$$

With this assumption, the jth moment of the weighted distribution is given by

$$c_j = \sum_{i=0}^{i=n} \int_0^\infty \tau_H^j \{\phi_i \tau_H^i w\} \, d\tau_H$$

$$= \sum_{i=0}^{i=n} \phi_i \int_0^\infty \tau_H^{i+j} w \, d\tau_H$$

$$= \sum_{i=0}^{i=n} \phi_i b_{i+j}, \tag{27}$$

where the b_k are the moments of the weighting function, defined in the same way as those of the weighted distribution, viz.

$$b_k = \int_0^\infty \tau_H^k w(\tau_H) \, d\tau_H. \tag{28}$$

For each value of j, from 0 to n, there is an equation of the form (27). The complete set of $(n+1)$ linear simultaneous equations, relating the unknown parameters ϕ_i to the observed moments c_j, may be written in the symbolic form

$$c_j = b_{ij}\phi_i, \tag{29}$$

where $b_{ij} = b_{i+j}$, the suffixes (i, j) run from 0 to n, and summation takes place over the repeated suffix on the right-hand side. The elements of the square symmetric matrix b_{ij} are the first $(2n+1)$ moments of the weighting function (i.e. those from b_0 up to b_{2n}).

This set of equations may be solved by inverting the matrix. Symbolically,

$$\phi_j = b_{ij}^{-1} c_i. \tag{30}$$

Since the matrix b_{ij} is symmetric, its inverse will be symmetric also.

The parameters ϕ_j, thus determined, are substituted into the power series of Eq. (26) to provide the final solution for the distribution function. This function can be converted into a plot of critical frequency (and hence electron density) against height by using Eq. (2) and Eq. (13), with the estimated value of L_0, to translate the values of τ_H into the corresponding heights.

Fig. 5 shows the results of applying this method of analysis to the whistler trace of Fig. 1. The broken line is a graph of electron density against height for the assumed true distribution, while the full lines show the successive attempts to recover it. The number attached to each line is the order of the approximation, that is to say, the order of the highest dispersion constant that was included in the analysis; approximations up to the third have been calculated, the correct path ($L_0 = 55°$) being assumed in each case. Thus the zeroth approximation is simply the value of electron density which, if

constant along the path, would produce the observed value of D_0; the higher approximations show a progressively improving fit to the true distribution.

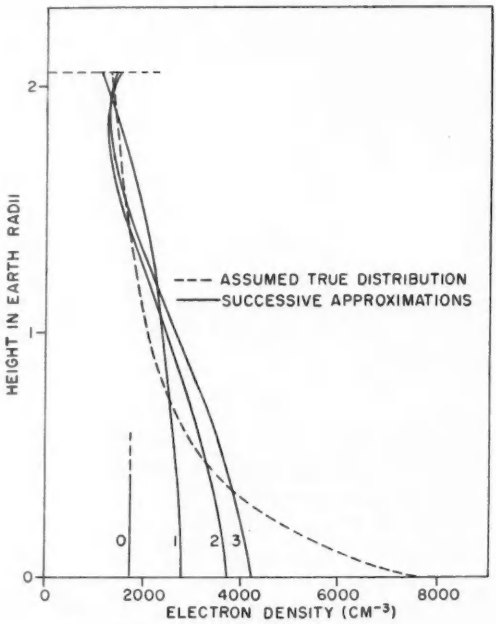

FIG. 5. Recovery of the distribution.

6. DISCUSSION

Having arrived at a method for interpreting the dispersion curves of whistlers, some discussion should be given of the systematic errors which arise in its use through basing the analysis on a limited number of dispersion constants.

The errors in τ_m and in the distribution function will be discussed separately although, since the value of τ_m is used to calculate the weighting function for recovering the distribution, errors here will be reflected in the distribution also. Indeed, when only D_0 is measured so that no estimate can be made of τ_m, the whistler trace contains no internal evidence about the distribution whatsoever. The situation is relieved by the fact that whistlers are not usually received from lightning strokes at magnetic latitudes very different from that of the receiving point (Storey 1953), so the location of this point (and of the stroke, if measured) provides a rough estimate for L_0, making a zero-order approximation possible.

Since a general discussion of the likely errors appeared too difficult, the best that could be done was to examine those arising in the particular example used to illustrate the method, and to hope that they are fairly representative of those likely to occur in practice.

As regards τ_m, it must be emphasized again that the first two dispersion constants are needed before any estimate of this quantity can be made. The first approximation, based on these moments alone, is poor. However, when dispersion constants of higher order are taken into account, the approximations converge rapidly to the true value. Because τ_m is a rapidly-varying function of the initial magnetic latitude L_0, the fractional errors in L_0 are much less than those in τ_m.

As regards the distribution function, the following points may be noted by inspecting the graphs of Fig. 5.

Firstly, all approximations give much better estimates of the electron density near the top of the path than lower down. Even the zeroth approximation comes within 30% of the density of the very top. This fact is a consequence of the greater weight assigned by the weighting function to the higher levels.

Secondly, in the first and higher approximations the general trend of the curves reproduces that of the actual distribution, namely, a decrease in electron density with height.

Thirdly, the second and third approximations show some spurious structure in the form of an increase of electron density with increasing height near the top of the path. This structure arises because the assumed distribution function (Fig. 3) is not one that can be represented easily by a few terms in a power series. To fit the observed moments the approximations are obliged to overshoot the true curve and then come back. It follows that detailed features of the approximations are not to be taken too literally.

Fourthly, the approximations fail to reproduce the middle part of the distribution particularly well through attempting to follow the steep increase of electron density with decreasing height that has been assumed to occur at low levels.

Besides these systematic errors there will, in fact, be others due to the original assumptions not being wholly correct, together with random errors due to inaccuracy of the measured data. Because somewhat complex operations are performed on the data it is hard to give any account of the effects of their inaccuracy, which seem best assessed by practical experience. Neither can systematic errors due to incorrectness of the initial assumptions be discussed within the framework of the preceding analysis. A full report on this work is now being prepared in which consideration is given to how the method can be generalized to take account of propagation in directions inclined to the magnetic field (Storey 1957*a*). Tables of the functions required in the analysis are in preparation also (Storey 1957*b*).

ACKNOWLEDGMENTS

This work was performed at the Radio Physics Laboratory, Defence Research Board, Ottawa, under project PCC No. D48-28-01-02. The author would like to acknowledge the value of discussions with Dr. L. L. Campbell of this laboratory and Dr. R. O. Skinner of the University of Saskatchewan. He is also indebted to Miss M. O'Grady, formerly of this laboratory, for help with the numerical calculations.

REFERENCES

ARLEY, N. and BUCH, K. R. 1950. Introduction to the theory of probability and statistics (Chapman and Hall, Ltd., London), p. 61.
DUNGEY, J. W. 1954. Pennsylvania State University Scientific Report No. 69.
ECKERSLEY, T. L. 1935. Nature, **135**, 104.
ELLIS, G. R. 1956. J. Atm. and Terrest. Phys. **8**, 338.
HELLIWELL, R. A., CRARY, J. H., POPE, J. H., and SMITH, R. L. 1956. J. Geophys. Research, **61**, 139.
KENDALL, M. G. 1940. Ann. Math. Stat. **11**, 402.
STOREY, L. R. O. 1953. Phil. Trans. Roy. Soc. London, Ser. A, **246**, 113.
——— 1956. Can. J. Phys. **34**, 1153.
——— 1957*a*. R.P.L. Project Report No. 23-4-1 (In preparation).
——— 1957*b*. R.P.L. Project Report No. 23-4-2 (In preparation).

CRITICAL STUDY OF VIBRONIC INTERACTION CALCULATIONS[1]

ANDREW D. LIEHR

ABSTRACT

A detailed study of the published non-empirical and semiempirical calculations of vibronic (vibrational-electronic) interactions in the $^1B_{1u}$ and $^1B_{2u}$ states of benzene is carried out. It is found that, in all but the most detailed non-empirical theory of vibronic interactions (Liehr and Moffitt 1957*a*), the Goeppert-Mayer and Sklar (1938) benzene electronic wave functions are too crude to adequately describe such interactions. Also, it is shown that the previously proposed semiempirical theories of vibronic interactions (Craig 1950; Liehr 1955; Liehr and Moffitt 1957*b*; Murrell and Pople 1956) are derivable from the more exact theory of Liehr and Moffitt (1957*a*) only with the aid of rather "herculean" assumptions.

§1. INTRODUCTION

In a recent paper Liehr and Moffitt (1957*a*) derived a general formula for the description of the interaction of vibrational and electronic motions in polyatomic molecules. They have also indicated the simplifications of this formula which arise if the electronic wave functions utilized in its numerical evaluation are exact solutions of the molecular Schrödinger equation. However, they have not explicitly demonstrated the superiority of their general formulation over the afore-mentioned simplified formulations. In this paper it will be shown that, at least in the case of benzene, the simplified formulations are inadequate for the description of the observed vibronic effects. Also, the manner in which the general formalism of Liehr and Moffitt (1957*a*) may be reduced to the previously published semiempirical formulations of Craig (1950), Liehr (1955), Liehr and Moffitt (1957*b*), and Murrell and Pople (1956) will be pointed out.

A. NON-EMPIRICAL CALCULATIONS

§2. DESCRIPTION OF VIBRONIC INTERACTIONS UNDER THE ASSUMPTION THAT EXACT ELECTRONIC WAVE FUNCTIONS ARE AVAILABLE

If one assumes that the complete molecular electronic wave function, $\Psi_K(\mathbf{r}_i, \mathbf{s}_a)$, may be expanded in terms of a suitable set of configurational functions, $\Theta_j(\mathbf{r}_i, \mathbf{s}_a)$, at each nuclear configuration, $\{\mathbf{s}_a\}$, we may write (Liehr 1955; Liehr and Moffitt 1957*a*):

$$\Psi_K(\mathbf{r}_i, \mathbf{s}_a) = \sum_j \Theta_j(\mathbf{r}_i, \mathbf{s}_a) C_{jK}(\mathbf{s}_a). \tag{1}$$

The expansion coefficients, $C_{jK}(\mathbf{s}_a)$, may be determined from a variational principle: to the the first-order in the nuclear displacements, $\mathbf{s}_a$, they are given by (Liehr and Moffitt 1957*a*):

$$C_{jk}' = \sum_a \mathbf{s}_a \cdot \nabla_{\mathbf{s}_a=0} C_{jk}(\mathbf{s}_a) = \frac{-(\mathscr{H}')_{jk} - (\Theta_j|\mathscr{H}_0 - E_K^0|\Theta_k)}{E_j^0 - E_K^0}, \qquad j \neq k, \tag{2}$$

[1]Manuscript received May 13, 1957.
Contribution from Bell Telephone Laboratories, Inc., Murray Hill, New Jersey, U.S.A.

where $\mathscr{H}(\mathbf{r}_i, \mathbf{s}_a)$ is the electronic Hamiltonian, and

$$(\mathscr{H}')_{jk} = \int \Theta_j^*(\mathbf{r}_i, 0) \sum_a \mathbf{s}_a \cdot \nabla_{\mathbf{s}_a=0} \mathscr{H}(\mathbf{r}_i, \mathbf{s}_a) \Theta_k(\mathbf{r}_i, 0) dT_{\text{el}}, \tag{3}$$

$$(\Theta_j|\mathscr{H}_0 - E_K^0|\Theta_k)' = \sum_a \mathbf{s}_a \cdot \nabla_{\mathbf{s}_a=0} \left\{ \int \Theta_j^*(\mathbf{r}_i, \mathbf{s}_a) \left[\mathscr{H}(\mathbf{r}_i, 0) - E_K(0) \right] \times \Theta_k(\mathbf{r}_i, \mathbf{s}_a) dT_{\text{el}} \right\}. \tag{4}$$

The use of equations (1) and (2) in the computation of the intensity of the vibronically allowed benzene ${}^1A_{1g} \rightarrow ({}^1B_{1u}, {}^1B_{2u})$ spectral transitions has been shown (Liehr and Moffitt 1957*a*) to yield excellent results (see Table I).

TABLE I

COMPARISON OF THE OBSERVED INTENSITIES (IN TERMS OF THE OSCILLATOR STRENGTH f) AND THOSE COMPUTED NON-EMPIRICALLY, USING THE SINGLE CONFIGURATION ENERGY OF PARR, CRAIG, AND ROSS (1950) AND THE SINGLE CONFIGURATION ${}^1A_{1g} \rightarrow {}^1E_{1u}$ INTENSITY VALUE OF BEVAN AND CRAIG (1951)

	Intensities calculated on the basis of Eq. (2)	Intensities calculated on the basis of Eq. (6)	Intensities calculated on the basis of Eq. (7)	Experimental intensities
${}^1A_{1g} \rightarrow {}^1B_{1u}$	0.257	0.0626	0.0690	0.094[a]
${}^1A_{1g} \rightarrow {}^1B_{2u}$	0.00269	0.198	0.208	0.0014[b]

[a]Hammond and Price (1955).
[b]Klevens and Platt (1953–54).

We now wish to examine the effects of assuming that the electronic wave functions, $\Theta_j(\mathbf{r}_i, 0)$, are exact solutions of the electronic Schrödinger equation

$$\mathscr{H}(\mathbf{r}_i, 0)\Theta_j(\mathbf{r}_i, 0) = E_j(0)\Theta_j(\mathbf{r}_i, 0),$$

that is,

$$\mathscr{H}_0\Theta_j^0 = E_j^0\Theta_j^0. \tag{5}$$

If we substitute equation (5) into equation (2), we see that we obtain a new formula for the first-order approximation to the "mixing" coefficients $C_{jK}(\mathbf{s}_a)$ (Liehr 1955; Liehr and Moffitt 1957*a*):

$$C_{jK}' = \frac{-(\mathscr{H}')_{jK} - (E_j^0 - E_K^0)(\Theta_j^0|\Theta_k')}{E_j^0 - E_K^0}, \qquad j \neq k. \tag{6}$$

Hence, we can determine the goodness of the presently available wave functions, Θ_j^0, by comparing the results of vibronic interaction calculations as obtained from equations (2) and (6). This has been done by the author for the case of benzene: the results are tabulated in Table I. A detailed discussion of the computations involved in numerically evaluating equation (2) may be found in the paper of Liehr and Moffitt (1957*a*), and those involved in evaluating equation (6) may be found in the thesis of Liehr (1955).

We see from Table I that equations (5) and (6) are very poor approximations if the benzene wave functions of Goeppert-Mayer and Sklar (1938) are employed. This result is not unexpected as previous dipole-length calculations

of the intensity of the electronically allowed benzene $^1A_{1g} \rightarrow {}^1E_{1u}$ spectral transition based on these same wave functions have also yielded poor results (Mulliken 1939; Bevan and Craig 1951; Wolfsberg 1955; Moscowitz 1957). When the assumption that the $^1E_{1u}$ and $^1A_{1g}$ Goeppert-Mayer and Sklar electronic wave functions are molecular eigenfunctions is dropped, either by the performance of a configuration interaction calculation (Bevan and Craig 1951), or by a dipole-velocity transition probability calculation (Wolfsberg 1955; Moscowitz 1957), improved results are obtained for the predicted $^1A_{1g} \rightarrow {}^1E_{1u}$ intensity.

§3. DESCRIPTION OF VIBRONIC INTERACTIONS UNDER THE ASSUMPTION OF SPATIALLY FIXED ELECTRONIC WAVE FUNCTIONS

If the basis functions $\Theta_j(\mathbf{r}_i, \mathbf{s}_a)$ are assumed to be spatially invariant, we have that $\Theta_j(\mathbf{r}_i, \mathbf{s}_a)$ equals $\Theta_j(\mathbf{r}_i, 0)$. In this event, since the second term on the right-hand side of equation (2), $(\Theta_j|\mathcal{H}_0 - E_K{}^0|\Theta_k)'$, vanishes, the first-order mixing coefficient is given by[2]

$$C_{jK}' = -(\mathcal{H}')_{jK}/(E_j{}^0 - E_K{}^0), \qquad j \neq k. \tag{7}$$

In the case of benzene the terms $(E_j{}^0 - E_K{}^0)(\Theta_j{}^0|\Theta_k')$ which differentiate equations (6) and (7) are, in absolute magnitude, roughly 1/20 the numerical value of the corresponding terms $(\mathcal{H}')_{jK}$ (Liehr 1955). Hence, for benzene the difference between equations (6) and (7) is rather trivial, both being very bad approximations to equation (2) (see Table I).

Before closing this section it is of interest to note that, within the original Born–Oppenheimer (1927) approximation, the terms $(\Theta_j{}^0|\Theta_k')$ alone should determine the intensity of a vibronically allowed spectral transition. In the case of benzene Sponer and Herzfeld (1952) have shown that these terms, taken by themselves, yield extremely poor approximations to the benzene $^1A_{1g} \rightarrow {}^1B_{2u}$ spectral intensity.[3] However, recently Liehr (1957*a*) has shown that when the Born–Oppenheimer approximation is modified so as to take explicitly into account the inexactitude of presently available electronic wave functions, it actually requires that equation (2) be used to determine the intensity of vibronically allowed transitions, and hence it does yield good predictions of the benzene "forbidden" intensities.

B. Semiempirical Calculations

§4. DESCRIPTION OF VIBRONIC INTERACTIONS UNDER THE ASSUMPTION OF DIPOLE POTENTIALS

In all the thus far reported semiempirical vibronic interaction calculations (Craig 1950; Murrell and Pople 1956; Liehr 1955; Liehr and Moffitt 1957*b*) equation (7) has been utilized to determine the first-order mixing constants C_{jK}'. This procedure is quite reasonable in view of the many assumptions

[2] This equation is also obtained if one assumes that the functions $\Theta_j(\mathbf{r}_i, \mathbf{s}_a)$ and $\Theta_k(\mathbf{r}_i, \mathbf{s}_a)$ of equation (6) are orthogonal eigenfunctions for all nuclear displacements $\{\mathbf{s}_a\}$.

[3] This may also be seen from the numerical values of these matrix elements as tabulated by Liehr (1955).

required to set up a semiempirical formalism for the computation of vibronic interactions.

The first semiempirical formalism proposed for the description of vibronic interactions was published by Craig (1950). In a valence bond computation of the extent of vibronic interactions in the $^1B_{2u}$ state of benzene, he proposed that the net interaction of the benzene π-electrons with the vibrating carbon nuclei is essentially of a dipolar character—each carbon atom acting towards the π-electrons on its non-neighbors as a small dipole, but being completely screened by the combined σ- and π-electron density from the π-electrons on its neighbors. This assumption gave striking agreement with the experimental findings for the $^1B_{2u}$ state of benzene (see Tables II, III, and IV).[4]

Recently Murrell and Pople (1956) transcribed Craig's model into the molecular orbital framework.[5] They did not, however, carry over Craig's nearest neighbor screening hypothesis. As a result their agreement with experiment is less striking than that obtained by Craig (see Tables II, III, and IV).

The question now arises as to how these semiempirical dipole models compare with the somewhat more rigorous quantum mechanical calculation based on the direct evaluation of equation (7), $\mathscr{H}'$ being taken as

$$\mathscr{H}' = \sum_a \mathbf{s}_a \cdot \nabla_{\mathbf{s}_a=0} \mathscr{H}(\mathbf{r}_i, \mathbf{s}_a) = \sum_a \mathbf{s}_a \cdot \nabla_{\mathbf{s}_a=0} \mathscr{V}_{e-n}(\mathbf{r}_i, \mathbf{s}_a). \tag{8}$$

We have already discussed in Section A the case when the π-electron–nuclear potential, $\mathscr{V}_{e-n}(\mathbf{r}_i, \mathbf{s}_a)$, is that of Goeppert-Mayer and Sklar (1938), and have seen that in this case equations (7) and (8) yield poor results. In this section we shall seek to obtain improved results from equation (7) by assuming a coulomb potential (this amounts to keeping only the first term in the Goeppert-Mayer and Sklar potential):

$$\mathscr{V}_{e-n}(\mathbf{r}_i, \mathbf{s}_a) = -\sum_a Z_a e^2 / |\mathbf{r}_a(i) - \mathbf{s}_a|. \tag{9}$$

In equation (9), Z_a is the "effective charge" at carbon atom a as seen by the ith $2p\pi$ electron, and $|\mathbf{r}_a(i)|$ is the distance that this electron is from the equilibrium position of carbon atom a. We shall show that by appropriately choosing Z_a this more exact calculation will reduce to those of Craig (1950) and Murrell and Pople (1956).

The substitution of equation (9) into equation (8) yields

$$\mathscr{H}' = \sum_i \sum_a Z_a e^2 \mathbf{r}_a \cdot \mathbf{s}_a / |\mathbf{r}_a(i)|^3. \tag{10}$$

When equations (10) and (7) are used jointly, the first-order mixing parameters C_{jK}' may be determined. If the parameters C_{jK}' thus determined are used to compute the intensity of the benzene $^1A_{1g} \rightarrow \{^1B_{1u}, ^1B_{2u}\}$ transitions, we obtain the numerical results given in Table II. As the computational

[4]L. E. Lyons (private communication) has also employed this model, with and without the screening assumption, in a valence bond calculation of the vibronic intensity of the benzene $^1A_{1g} \rightarrow \{^1B_{1u}, ^1E_{2g}\}$ spectral transitions (see Craig, D. P. 1953. Revs. Pure and Appl. Chem. (Australia), **3**, 207).

[5]L. E. Lyons and D. P. Craig (unpublished) have also transcribed the original Craig model into the molecular orbital framework (private communication from Profs. Lyons and Craig).

procedures utilized in this calculation are very similar to those given by Liehr (1955) and Liehr and Moffitt (1957*a*), we shall not repeat them here. Suffice it to say that if one sets $I_0(\bar{x}) = (Z^2e^2/a_0)J_0(\bar{x})$ and $I_1(\bar{x}) = (Z^2e^2/a_0)\bar{J}_1(\bar{x})$ (for the definitions of the $I_j(\bar{x})$ $(j = 0, 1)$, see Liehr (1955) and Liehr and Moffitt (1957*a*); for the definition of $J_0(\bar{x})$ and $\bar{J}_1(\bar{x})$ see Liehr (1955, 1957*b*)) in equations (2.4–5 and 6) of Liehr and Moffitt (1957*a*) and sets a_P, b_P ($P = \mathbf{u}, \bar{\mathbf{u}}$) equal to zero in equations (2.4–14) and (2.6–6 and 7) of this same reference, one obtains the results given in Tables II and IV.

TABLE II

COMPARISON OF THE VARIOUS CHARGE–DIPOLE MODEL INTENSITIES (IN TERMS OF THE OSCILLATOR STRENGTH f), USING THE EXPERIMENTAL ENERGY DIFFERENCES (PARR, CRAIG, AND ROSS 1950) AND THE EXPERIMENTAL $^1A_{1g} - {}^1E_{1u}$ INTENSITY (HAMMOND AND PRICE 1955)

	Intensities calculated with $Z_a = 1$ in Eqs. (10) and (7)	Intensities calculated using Craig's screening assumption in Eqs.(10) and (7), and $Z_a = 0.6$	Intensities calculated using assumption of zero overlap, etc., in Eqs. (10) and (7), $Z_a = Z$
$^1A_{1g} \rightarrow {}^1B_{1u}$	0.035	0.097	0.17 Z^2
$^1A_{1g} \rightarrow {}^1B_{2u}$	0.147	0.005	0.17 Z^2

	Intensities calculated by Craig (1950)	Intensities calculated by Murrell and Pople (1956)	Intensities calculated by Liehr (1955) and Liehr and Moffitt (1957*b*)
$^1A_{1g} \rightarrow {}^1B_{1u}$	0.07[a]	0.398	With benzene $^1A_{1g}$ normal coordinates 0.08 With Wilsonian symmetry coordinates 0.02 With internal symmetry coordinates 0.02
$^1A_{1g} \rightarrow {}^1B_{2u}$	0.0014	0.0119	$\sim 10^{-2} f(^1A_{1g} \rightarrow {}^1B_{1u})$

[a]Lyons (private communication). See footnote 4.

We see from Table II that the choice of Z_a equal to a constant, say Z, for all a $(a = 0, 1, 2, 3, 4, 5)$, yields extremely poor results for the intensity of the $^1A_{1g} \rightarrow \{{}^1B_{1u}, {}^1B_{2u}\}$ spectral transitions of benzene. The main reason for this discrepancy is that the integral describing the interaction of the π-electron charge cloud on atom a, $\phi_a{}^2$, with the dipolar potential of atoms $a \pm 1$ (that is, the integral $J_0(\bar{x}_{01})$ of Liehr (1955, 1957*b*); we have here taken $\bar{x}_{01} = 3.18x_{01}/a_0$, where $x_{01} = 1.40$ Å) is about three times as large as the corresponding integral describing the interaction of the "exchange" charge cloud of atoms a and $a \pm 1$, $\phi_a\phi_{a\pm1}$, with the dipolar potential of atoms $a \pm 1$ (that is, the integral $\bar{J}_1(\bar{x}_{01})$ of Liehr (1955, 1957*b*)). Since the charge–dipole interaction thus makes the "even" perturbations $\int \phi_a \mathscr{H}' \phi_b dT_{\text{el}}$, $a+b$ even, much larger than the "odd" perturbations $\int \phi_a \mathscr{H}' \phi_b dT_{\text{el}}$, $a+b$ odd, a $^1A_{1g} \rightarrow {}^1B_{2u}$ intensity which is larger than the corresponding $^1A_{1g} \rightarrow {}^1B_{1u}$ intensity is favored (see Moffitt 1954). Hence, the dipole interaction hypothesis cannot, without some modification, account for the intensity of the benzene $\{^1A_{1g} \rightarrow {}^1B_{1u}, {}^1B_{2u}\}$ spectral transitions.

If we adopt the admittedly heuristic screening mechanism of Craig (1950), thus taking Z_a equal to zero for charge–dipole interactions between neighboring atoms (that is, set $Z_a J_0(\bar{x}_{01})$ equal to zero for the "even" perturbations), we obtain very striking agreement with experiment. In Table II, we have given the results of such a calculation for benzene. We wish to here emphasize that the "goodness" of any semiempirical calculation is to be judged solely on its conceptual simplicity, physical reasonableness, and its agreement with experiment. We see from Table II that Craig's screening mechanism, which is devised solely to take into account the neglected electron correlation terms,[6] satisfies these criteria quite well.

Let us now compare the Murrell and Pople (1956) semiempirical formalism with the more exact calculation based on equations (7) and (10). Murrell and Pople employed the charge–dipole model of vibronic interactions in the molecular orbital framework,[5] assuming zero overlap between the atomic wave functions. As Moffitt (1954) has shown, the assumption of zero overlap in the benzene vibronic interaction calculation is equivalent to the assumption that the vibronic interactions of the $^1B_{2u}$ state of benzene are determined solely by "even" perturbations, and that those of the $^1B_{1u}$ state are determined solely by "odd" perturbations. Murrell and Pople have further assumed that of the "even" perturbations one need only consider the terms $\int \phi_a \mathscr{H}' \phi_a d\tau_{el}$, and that of the "odd" perturbations one need only consider the terms $\int \phi_a \mathscr{H}' \phi_{a\pm 1} d\tau_{el}$.[7] The integrals describing both the "even" and the "odd" perturbations were then evaluated by the method of Craig (1950) (without the assumption of screening, however).

If we likewise assume in equations (7) and (10) that the overlap is zero and that only the terms $\int \phi_a \mathscr{H}' \phi_a d\tau_{el}$ need be kept in the "even" perturbations, we obtain the results given in Tables II and IV.[8] We see that if we are to obtain agreement with experiment for the $^1A_{1g} \rightarrow {}^1B_{2u}$ benzene intensity we must employ an effective charge Z_a of about 0.1 for the "even" perturbations (the intensity is proportional to the square of the effective charge Z_a if Z_a is a constant, equal to Z say, for all a). Hence, the Murrell and Pople semiempirical formalism can not be transcribed as readily into the more "rigorous" framework of equations (7) and (10) as can the formalism of Craig. However, it is apparent from Tables II and IV that the Murrell and Pople calculation more than adequately satisfies our previously proposed "goodness" criteria for semiempirical computations.

§5. DESCRIPTION OF VIBRONIC INTERACTIONS UNDER THE ASSUMPTION OF LENNARD-JONES RESONANCE POTENTIALS

Recently Liehr (1955) and Liehr and Moffitt (1957*b*) have computed the effects of vibronic interactions in the benzene $^1B_{1u}$ and $^1B_{2u}$ states under the

[6]A detailed discussion of the effects of this neglect may be found in Section 2.8 of Liehr (1955).

[7]In evaluating these latter terms Murrell and Pople employed the approximation that the product $\phi_a \phi_{a\pm 1}$ is approximately equal to the overlap of ϕ_a and $\phi_{a\pm 1}$ times the product $\phi_{a'} \phi_{a''}$, $\phi_{a'}$ being an atomic orbital located midway between ϕ_a and $\phi_{a\pm 1}$.

[8]In evaluating the "odd" perturbations we have retained all of the terms $\int \phi_a \mathscr{H}' \phi_b d\tau_{el}$, $a+b$ odd, however.

assumption that all "even" perturbations are zero[9] (this is equivalent to assuming that the effective charge Z_a vanishes for "even" perturbations because of screening effects), and that all "odd" perturbations are describable by the variation of the Lennard-Jones (1937) approximation for the "resonance" integrals, $\int \phi_a \mathcal{H} \phi_b d\tau_{el}$. The results obtained for the intensity of the "forbidden" benzene $^1A_{1g} \rightarrow \{^1B_{1u}, ^1B_{2u}\}$ spectral transitions by use of these assumptions are quite satisfactory (see Tables II and IV). Hence, it seems that the assumptions inherent in the semiempirical scheme of Liehr and Moffitt also take good account of the neglected electron correlation terms.[6]

§6. DISCUSSION

From the results of Section A we see that extreme caution must be used in employing single configuration antisymmetrized molecular orbitals for the calculation of quantities dependent on the exact form of the electronic wave functions. These single configuration functions, although sometimes yielding good estimates of the molecular energies, are not good approximations to the solutions of Schrödinger's equation. Hence, we cannot really expect these functions to predict correctly the more intimate properties of the electronic structure of molecules, such as the intensities of spectral transitions.

In Section B we have seen that the deficiencies of the single configuration functions may be partly compensated for by any of several semiempirical "dodges". Which of these "dodges" will be the most useful in future calculations is hard to say. Probably some combination of them will prove to be the best means of correlating spectral intensities in homologous series of compounds. One such combination would be to use the Craig screened charge–dipole model for the computation of intensities due to "even" perturbations and the Liehr–Moffitt resonance integral model for the computation of "odd" perturbations. If the benzene calculation is a true indication of which semiempirical assumptions need to be made in order to compute "forbidden" intensities, one must use the unscreened charge–dipole model only with due caution.

Before concluding this paper we must make some comments concerning the calculation of the distribution of vibronic intensity among the various vibrational sublevels. In Tables III and IV we have tabulated the vibrational

TABLE III

COMPARISON OF THE NON-EMPIRICAL PREDICTED RATIO OF VIBRONIC INTENSITIES DUE TO THE 521 cm^{-1} ($f^{(e)}$) AND 1470 cm^{-1} ($f^{(s)}$) VIBRATIONAL FREQUENCIES WITH THE EXPERIMENTALLY OBSERVED RATIO (GARFORTH, INGOLD, AND POOLE 1948)

	$f^{(e)}/f^{(s)}$ by Eq. (2)	$f^{(e)}/f^{(s)}$ by Eq. (6)	$f^{(e)}/f^{(s)}$ by Eq. (7)	$f^{(e)}/f^{(s)}$ Exptl.
$^1A_{1g} \rightarrow {}^1B_{1u}$	0.25	0.33	0.33	—
$^1A_{1g} \rightarrow {}^1B_{2u}$	0.33	507	311	~100

[9]The assumption as to the vanishing of "even" perturbations is unnecessary for the description of vibronic interactions in the $^1B_{1u}$ state if one also assumes zero overlap, as did Liehr and Moffitt. However, this assumption is quite necessary for the description of vibronic interactions in the $^1B_{2u}$ state.

sublevel intensity distribution for the benzene $^1B_{1u}$ and $^1B_{2u}$ states, as obtained by the various methods described in this paper. The most striking feature of

TABLE IV

COMPARISON OF THE VARIOUS SEMIEMPIRICAL PREDICTED RATIOS OF VIBRONIC INTENSITIES $f^{(6)}$ AND $f^{(8)}$

	$f^{(6)}/f^{(8)}$ by Eqs. (10) and (7)	$f^{(6)}/f^{(8)}$ by Eqs. (10) and (7) with Craig's screening assumption	$f^{(6)}/f^{(8)}$ by Eqs. (10) and (7), with zero overlap, etc.
$^1A_{1g} \rightarrow {}^1B_{1u}$	1.54[a]	21[a]	18[a]
$^1A_{1g} \rightarrow {}^1B_{2u}$	235[a]	61[a]	254[a]

	$f^{(6)}/f^{(8)}$ Craig (1950)	$f^{(6)}/f^{(8)}$ Murrell and Pople (1956)	$f^{(6)}/f^{(8)}$ Liehr (1955) and Liehr and Moffitt (1957*b*)	
$^1A_{1g} \rightarrow {}^1B_{1u}$	—	0.3[b]	With benzene $^1A_{1g}$ normal coordinates	0.15[a]
			With Wilsonian symmetry coordinates	0.3[a]
			With internal symmetry coordinates	0.3[a]
$^1A_{1g} \rightarrow {}^1B_{2u}$	230[b]	4.5[b]	—	

[a]Using the $^1B_{2u}$ vibrational frequencies, $\nu_6 = 521\ \text{cm}^{-1}$ and $\nu_8 = 1470\ \text{cm}^{-1}$ (Garforth, Ingold, and Poole 1948).

[b]Using the $^1A_{1g}$ vibrational frequencies, $\nu_6 = 606\ \text{cm}^{-1}$ and $\nu_8 = 1596\ \text{cm}^{-1}$ (Herzberg 1945).

Table III (non-empirical calculations) is on the one hand the relative insensitivity of the vibrational intensity distribution in the $^1B_{1u}$ state to calculational procedure, and on the other hand the extreme sensitivity of the $^1B_{2u}$ vibrational intensity distribution to these same computational procedures. In Table IV (semiempirical calculations) both the $^1B_{1u}$ and $^1B_{2u}$ vibrational intensity distributions vary strongly from one computational method to another. Thus, from the wide variety of predicted distributions obtained from both the non-empirical and semiempirical methods, and their general disagreement, we see that we cannot place very much faith in any of the presently available methods of computing such intensity distributions. Seemingly, even though we may correct for the gross inaccuracies in the single configuration antisymmetrized molecular orbital wave functions by employing judicious calculational procedures, we cannot correct their more basic defect of being poor solutions of the molecular Schrödinger equation.

ACKNOWLEDGMENT

The author would like to thank Dr. Albert J. Moscowitz for his aid in the numerical computation of both the charge–dipole interaction integrals and the benzene normal coordinates.

SUMMARY OF SYMBOLS

$\Psi_K(\mathbf{r}_i, \mathbf{s}_a)$	Kth complete molecular electronic wave function.
$\mathbf{r}_i$	electronic coordinates.
$\mathbf{s}_a$	nuclear displacement of atom a from its equilibrium position.
$\Theta_j(\mathbf{r}_i, \mathbf{s}_i)$	jth configurational electronic wave function.
$C_{jk}(\mathbf{s}_a)$	expansion coefficient for the expansion of the $\Psi_K(\mathbf{r}_i, \mathbf{s}_a)$ in terms of the $\Theta_j(\mathbf{r}_i, \mathbf{s}_a)$.
C_{jK}'	first-order term in the power series expansion of $C_{jK}(\mathbf{s}_a)$.
$\mathscr{H}(\mathbf{r}_i, \mathbf{s}_a)$	electronic Hamiltonian at the nuclear configuration $\{\mathbf{s}_a\}$.
$\nabla_{\mathbf{s}_a=0}$	gradient operator evaluated at the configuration $\mathbf{s}_a = 0$.
E_j^0	energy eigenvalue associated with the functions Θ_j, when $\mathbf{s}_a = 0$; that is, associated with the functions Θ_j^0.
E_K^0	energy eigenvalue associated with the functions Ψ_K when $\mathbf{s}_a = 0$.
$(\mathscr{H}')_{jK}$	defined by equation (3).
$(\Theta_j\|\mathscr{H}_0 - E_K^0\|\Theta_k)'$	defined by equation (4).
Θ_k'	first-order term in the expansion of $\Theta_k(\mathbf{r}_i, \mathbf{s}_a)$ in powers of $\mathbf{s}_a$.
$\mathscr{H}'$	first-order term in the expansion of $\mathscr{H}(\mathbf{r}_i, \mathbf{s}_a)$ in powers of $\mathbf{s}_a$.
$\mathscr{V}_{e-n}(\mathbf{r}_i, \mathbf{s}_a)$	π-electron–nuclear potential energy.
$\mathbf{r}_a(i)$	coordinates of electron i as measured from the equilibrium position of atom a.
Z_a	"effective charge" associated with atom a.
e	electronic charge.
a_0	Bohr radius.
ϕ_a	$2pz$ atomic orbital associated with carbon atom a.
f	total electronic oscillator strength.
$f^{(l)}$	electronic oscillator strength associated with the excitation of the normal mode having the frequency ν_l.
$\bar{x}_{01} = 3.18x_{01}/a_0$	dimensionless carbon–carbon bond distance, x_{01}, in the benzene excited states.
$I_j(\bar{x}_{01})$	integrals, defined in Liehr (1955) and Liehr and Moffitt (1957*a*), describing the extent of vibronic interactions in benzene.
$J_0(\bar{x})$ and $J_1(\bar{x})$	two simpler integrals, defined in Liehr (1955, 1957*b*), occurring in the expansion of the $I_j(\bar{x})$ integrals.
a_P, b_P	the constants which describe the total vibronic interaction energy of benzene.

REFERENCES

BEVAN, C. W. L. and CRAIG, D. P. 1951. Trans. Faraday Soc. **47**, 564.
BORN, M. and OPPENHEIMER, R. 1927. Ann. Physik, **84**, 457.

CRAIG, D. P. 1950. J. Chem. Soc. 59.
GARFORTH, F. M., INGOLD, C. K., and POOLE, H. G. 1948. J. Chem. Soc. 505.
GOEPPERT-MAYER, M. and SKLAR, A. L. 1938. J. Chem. Phys. **6**, 645.
HAMMOND, V. J. and PRICE, W. C. 1955. Trans. Faraday Soc. **51**, 605.
HERZBERG, G. 1945. Infrared and Raman spectra (D. Van Nostrand Co., Inc., New York).
KLEVENS, H. B. and PLATT, J. R. 1953–54. Technical Reports of the Laboratory of Molecular Structure and Spectra, University of Chicago, Chicago, Ill.
LENNARD-JONES, J. E. 1937. Proc. Roy. Soc. (London), A, **158**, 280.
LIEHR, A. D. 1955. The interaction of vibrational and electronic motions in some simple conjugated hydrocarbons, Thesis, Harvard University, Cambridge, Mass. (Copies of this thesis are available from the author upon request.)
——— 1957*a*. Annals of Physics, **1**, 221.
——— 1957*b*. Z. Naturforsch. A (To be published).
LIEHR, A. D. and MOFFITT, W. E. 1957*a*. Z. Naturforsch. A (To be published).
——— 1957*b*. J. Chem. Phys. (To be published).
MOFFITT, W. E. 1954. J. Chem. Phys. **22**, 320.
MOSCOWITZ, A. J. 1957. On optical activity—hexahelicene, Thesis, Harvard University, Cambridge, Mass., Appendix VII. (Copies of this thesis are available from Dr. Moscowitz upon request.)
MULLIKEN, R. S. 1939. J. Chem. Phys. **7**, 353.
MURRELL, J. N. and POPLE, J. A. 1956. Proc. Phys. Soc. (London), A, **69**, 245.
PARR, R. G., CRAIG, D. P., and ROSS, I. G. 1950. J. Chem. Phys. **18**, 1561.
SPONER, H. and HERZFELD, K. F. 1952. Z. Physik, **133**, 41.
WOLFSBERG, M. 1955. J. Chem. Phys. **23**, 793.

THE EFFECT OF INTERACTIONS ON THE ANGULAR DISTRIBUTION OF γ-RAYS FROM AN ASSEMBLY OF ORIENTED NUCLEI[1]

J. M. DANIELS

ABSTRACT

The angular distribution of γ-radiation from an assembly of nuclei oriented by the magnetic h.f.s. method can be very much modified by interactions between the radioactive ions and other paramagnetic ions in the crystal. In order to calculate the effect of these interactions, an operator Γ is derived which represents the angular distribution of γ-rays from a radioactive nucleus. The angular distribution at any temperature is given by $\mathrm{Spur}(\Gamma\rho)$, where ρ is the statistical matrix $\exp(-\mathfrak{H}/kT)/\mathrm{Spur}[\exp(-\mathfrak{H}/kT)]$, $\mathfrak{H}$ being the Hamiltonian for the whole crystal. For a high temperature approximation, ρ is expanded in powers of $1/T$. It is found that, for alignment by the magnetic h.f.s. method, the first term which contains interaction parameters is that in $1/T^4$, and an expression is given for the contribution of interactions to this term.

At very low temperatures, perturbation theory is used to estimate the effect of interactions on the lowest nuclear energy state, and hence on the angular distribution of γ-rays. It is found that, if an external magnetic field is applied along a principal axis of the g-tensor of the radioactive ions, interactions have no influence on the angular distribution of γ-rays in the limit of large fields. It is also shown that Bleaney's restriction, that for a successful nuclear orientation experiment the broadening of the levels should be less than the hyperfine splitting, is not necessary in this case.

1. INTRODUCTION

A method of producing an assembly of oriented nuclei by cooling a single crystal of a paramagnetic substance was first suggested by Bleaney (1951*a*, *b*) and established by the group working at the Clarendon Laboratory, Oxford (Daniels *et al.* 1951; Bleaney *et al.* 1954). Early in this work serious discrepancies were observed between the observed and calculated γ-ray polar diagrams (Ambler *et al.* 1953; Grace *et al.* 1954). The most striking effect of this type (Grace *et al.* 1954) was observed in the emission of γ-rays from Mn54 included as an impurity in $Ce_2Mg_3(NO_3)_{12}.24H_2O$, where the observed anisotropy of γ-radiation was much lower than predicted, and actually decreased as the temperature fell below 0.003° K., the Curie temperature of the salt. Application of an external magnetic field of a few hundred gauss parallel to the trigonal axis of the crystals (which is also the axis of nuclear alignment) resulted in an increase of the anisotropy of γ-radiation to a more understandable value, and a disappearance of the dip at 0.003° K. The conclusion was drawn from these observations that the decrease in anisotropy in zero external field is due to magnetic interactions between the manganese and the cerium ions, and this effect has been unofficially christened the "solid state effect". The presence of the solid state effect, so far quantitatively unexplained, has thrown considerable doubt on the validity of determinations of nuclear magnetic moments by the method of nuclear orientation. The large

[1]Manuscript received April 23, 1957.
Contribution from the Department of Physics, University of British Columbia, Vancouver, B.C.

value of the solid state effect in cerium magnesium nitrate is most distressing because this salt is, from almost all other aspects, the ideal substance for nuclear orientation experiments. The object of this paper is to examine this "solid state effect" in a quantitative manner.

The method used is to deduce an operator Γ which represents the γ-ray polar diagram. The statistical matrix ρ is $\exp(-\mathfrak{H}/kT)/\mathrm{Spur}[\exp(-\mathfrak{H}/kT)]$, where $\mathfrak{H}$ is the total Hamiltonian of the system, and the polar diagram of the assembly is given by $\mathrm{Spur}(\Gamma\rho)$, which can be expanded in a series of powers of $1/kT$. The formulae involved are rather complicated to be written down explicitly, but the method is described in sufficient detail to enable any particular case to be worked out.

An attempt to deal with the solid state effect has been made by Steenberg (1954), in which the effect of interactions on the values of $\overline{I_z}$ and $\overline{I_z^2}$ is first calculated, and the effect on the anisotropy of γ-ray distribution is deduced from these using formulae derived in Steenberg (1952). It should be noted that the formulae of Steenberg (1952) are not of universal application since, in effect, the off-diagonal elements of Γ are ignored. Fortuitously, in most of the cases of axial symmetry which are treated in Steenberg (1952), the off-diagonal elements do not enter. When, however, interactions are to be considered, the positions of the nearest neighbors are important, and an ion which in the absence of interactions had axial symmetry may no longer have this axial symmetry. Under these circumstances, the off-diagonal terms of Γ cannot justifiably be ignored. The complete description of an assembly of nuclei requires, of course, a knowledge of all the elements of the statistical matrix; i.e. $(2I+1)^2$ real numbers. Alternatively, the assembly can be described by specifying all the "moments" up to those of order $2I$, again $(2I+1)^2$ in number. These are $1; \overline{I_z}, \overline{I_x}, \overline{I_y}; 3\overline{I_z^2}-I(I+1), \overline{I_x^2-I_y^2}, \overline{I_xI_y}, \overline{I_yI_z}, \overline{I_zI_x}$; etc. and it is easily seen that in the case of z-axial symmetry most of these vanish. Steenberg's treatment ignores those moments which vanish under cases of axial symmetry, and this is equivalent to his neglect of the off-diagonal elements of Γ. Because Steenberg's formulae are applicable only in the restricted cases where symmetry ensures the irrelevance of the neglected elements, it is therefore preferable to derive the polar diagram of γ-rays directly from Γ and ρ rather than through the intermediary of $\overline{I_z^2}$, etc.

A general expression for Γ has been derived by Cox and de Groot (1953). Unfortunately, they have expressed Γ not in the usual representation with I_z diagonal, but in terms of Fano's irreducible tensors. This formulation reduces the usefulness of their formulae for our purposes; hence the problem of deriving Γ is treated in this paper *ab initio*. The method of deriving Γ is not altogether original, and can be found scattered in various other publications. It is reproduced in the appendix to this paper because I think this would be convenient for those who wish to work out specific examples.

2. CALCULATION OF THE ANGULAR DISTRIBUTION AND THE EFFECT OF INTERACTIONS AT HIGH TEMPERATURES

First we require an operator Γ which represents the angular distribution of γ-radiation intensity. A method of obtaining such an operator is given in

the appendix. It is sufficient here to note that such an operator can be found, and that it has the following properties which we shall need:

(*a*) It is Hermitian.

(*b*) With m_1 and m_2 nuclear magnetic quantum numbers,

$$\langle m_1|\Gamma|m_2\rangle = (-1)^{m_1+m_2}\langle -m_2|\Gamma|-m_1\rangle; \tag{2.1}$$

This follows from the symmetry properties of Wigner coefficients and spherical harmonics.

If Γ is a normalized operator (i.e. $\int\langle m|\Gamma|m\rangle\, d\Omega = 1$), we can write $\Gamma = \Gamma'+1/4\pi$, where in this case $\mathrm{Spur}(\Gamma') = 0$. The use of $\Gamma'+1/4\pi$ instead of Γ involves no loss of generality, but simplifies the subsequent algebra considerably.

Let us now consider one radioactive nucleus in an ion (whose variables will be denoted by the subscript 0) in a crystal containing a large number of other ions all interacting by means of magnetic dipole and/or exchange coupling. Let the Hamiltonian of ion zero alone be $\mathfrak{H}_0$, and the rest of the total Hamiltonian be $\mathfrak{H}_1$. Then the angular distribution is given by

$$\mathrm{Spur}\{\Gamma\exp[-(\mathfrak{H}_0+\mathfrak{H}_1)/kT]\}/\mathrm{Spur}\{\exp[-(\mathfrak{H}_0+\mathfrak{H}_1)/kT]\}$$
$$= \frac{1}{4\pi} + \mathrm{Spur}\{\Gamma'\exp[-(\mathfrak{H}_0+\mathfrak{H}_1)/kT]\}/\mathrm{Spur}\{\exp[-(\mathfrak{H}_0+\mathfrak{H}_1)/kT]\}.$$

For a "high temperature" approximation we shall expand this in a power series of $1/kT$, evaluating the Spurs in any convenient representation since they are invariant to unitary transformations. This is the technique first introduced by van Vleck (1937).

Writing τ for $-1/kT$, and bearing in mind that $\mathfrak{H}_0$ and $\mathfrak{H}_1$ do not necessarily commute, we see that

$$\mathrm{Spur}\{\Gamma'\exp[-(\mathfrak{H}_0+\mathfrak{H}_1)/kT]\}/\mathrm{Spur}\{\exp[-(\mathfrak{H}_0+\mathfrak{H}_1)/kT]\}$$
$$= \frac{\mathrm{Spur}\{\Gamma'+\Gamma'(\mathfrak{H}_0+\mathfrak{H}_1)\tau + \Gamma'(\mathfrak{H}_0+\mathfrak{H}_1)^2\tau^2/2 + \dots\}}{\mathrm{Spur}\{1+(\mathfrak{H}_0+\mathfrak{H}_1)\tau + (\mathfrak{H}_0+\mathfrak{H}_1)^2\tau^2/2 + \dots\}}$$

is of the form

$$(B\tau+C\tau^2+D\tau^3+E\tau^4+\dots)/(\alpha+\gamma\tau^2+\delta\tau^3+\epsilon\tau^4+\dots).$$

Note that the constant in the numerator vanishes, since $\mathrm{Spur}(\Gamma') = 0$ by definition; and that the coefficient of τ in the denominator vanishes because $\mathrm{Spur}(\mathfrak{H}) = 0$, a property of the particular Hamiltonians used. This last expression can be evaluated in series:

$$\tau\frac{B}{\alpha} + \tau^2\frac{C}{\alpha} + \tau^3\left(\frac{D}{\alpha} - \frac{B\gamma}{\alpha^2}\right) + \tau^4\left(\frac{E}{\alpha} - \frac{C\gamma}{\alpha^2} - \frac{B\delta}{\alpha^2}\right) + \dots. \tag{2.2}$$

In order to evaluate the parameters B, C, α, γ, etc., we need to know $\mathfrak{H}_0$ and $\mathfrak{H}_1$. For $\mathfrak{H}_0$ the usual expression is

$$g_{\parallel}\beta H_z S_z + g_\perp\beta(H_x S_x + H_y S_y) + D\{S_z^2 - \tfrac{1}{3}S(S+1)\}$$
$$+ AS_zI_z + B(S_xI_x + S_yI_y) + P\{I_z^2 - \tfrac{1}{3}I(I+1)\}; \tag{2.3}$$

see for example Bleaney (1951*b*). This will be written in tensor notation:

$$(2.4) \qquad \mathcal{H}_0 = H_\sigma R_{0\sigma\rho} S_{0\rho} + D_{0\lambda\mu} S_{0\lambda} S_{0\mu} + F_{0\epsilon\eta} S_{0\epsilon} I_{0\eta} + Q_{0\gamma\delta} I_{0\gamma} I_{0\delta}$$

using the dummy suffix summation convention for Greek suffixes. The rest of the Hamiltonian, $\mathcal{H}_1$, can be written in tensor notation:

$$(2.5) \qquad \mathcal{H}_1 = \sum_{(ij)} P_{ij\alpha\beta} S_{i\alpha} S_{j\beta} + \sum_{p\neq 0} R_{p\sigma\xi} H_\sigma S_{p\xi} + \sum_{q\neq 0} D_{q\theta\phi} S_{q\theta} S_{q\phi} + \sum_{u\neq 0} F_{u\psi\chi} S_{u\psi} I_{u\chi} + \sum_{v\neq 0} Q_{v\omega\pi} I_{v\omega} I_{v\pi} .$$

The tensor notation is used because it is easier to manipulate in the more complicated expressions, and it comprehends both dipole–dipole and exchange interactions when appropriate values are given to the P's as explained in Daniels (1953).*

Note that $\mathrm{Spur}(\mathcal{H}) = 0$. This is obvious for the terms linear in S, and is true also for the terms quadratic in the S's and I's, because the coefficients are chosen for this to be so. Also from (2.1), $\mathrm{Spur}(\Gamma' \mathcal{H}) = 0$ if the Q_0's are all zero. We shall further assume that the Q_0's are all zero; this case corresponds to nuclear alignment by the magnetic h.f.s. mechanism (Bleaney 1951*a*). If the Q's are not zero, the electric h.f.s. mechanism (Pound 1949) also plays a part in the nuclear alignment and the resulting anisotropy has a different character and temperature dependence.

We shall now consider the various terms in the series expansion of the expression for the polar diagram:

(i) *The Constant Term*

This is $\mathrm{Spur}(\Gamma')/\mathrm{Spur}(1) = 0$.

(ii) *The Term of Degree One*

This is $-(1/kT)\mathrm{Spur}(\Gamma' \mathcal{H})/\mathrm{Spur}(1) = 0$

(note that this term would not vanish if the Q_0's did not vanish).

(iii) *The Term of Degree Two*

This is $(1/2k^2T^2)\mathrm{Spur}(\Gamma' \mathcal{H}^2)/\mathrm{Spur}(1)$.

Putting $\mathcal{H} = \mathcal{H}_0 + \mathcal{H}_1$, this term becomes

$$\frac{1}{2k^2T^2}\left[\frac{\mathrm{Spur}(\Gamma'\mathcal{H}_0{}^2)}{\mathrm{Spur}(1)} + \frac{\mathrm{Spur}(\Gamma'\mathcal{H}_1{}^2)}{\mathrm{Spur}(1)} + \frac{\mathrm{Spur}\{\Gamma'(\mathcal{H}_1\mathcal{H}_0 + \mathcal{H}_0\mathcal{H}_1)\}}{\mathrm{Spur}(1)}\right].$$

The first term is that which would be there in the absence of interactions, and we shall not be interested in this any further. The second term vanishes because Γ' and $\mathcal{H}_1$ operate in different vector spaces, and hence

$$\frac{\mathrm{Spur}(\Gamma'\mathcal{H}_1{}^2)}{\mathrm{Spur}(1)} = \frac{\mathrm{Spur}(\Gamma')}{\mathrm{Spur}(1)} \frac{\mathrm{Spur}(\mathcal{H}_1{}^2)}{\mathrm{Spur}(1)} = 0.$$

*As examples of how familiar interactions can be written in this tensor notation, isotropic exchange, familiarly $J_{ij}\, \mathbf{s}_i \cdot \mathbf{s}_j$, can be written $P_{ij\alpha\beta} = J_{ij}\, \delta_{\alpha\beta}$. Magnetic dipole coupling between isotropic dipoles, familiarly $\boldsymbol{\mu}_i \cdot \boldsymbol{\mu}_j / r_{ij}{}^3 - 3(\boldsymbol{\mu}_i \cdot \mathbf{r}_{ij})(\boldsymbol{\mu}_j \cdot \mathbf{r}_{ij})/r_{ij}{}^5$, becomes

$$P_{ij\alpha\beta} = \mu_i \mu_j \left[\frac{\delta_{\alpha\beta}}{r_{ij}{}^3} - 3\frac{r_{ij\alpha} r_{ij\beta}}{r_{ij}{}^5}\right]$$

and so on.

The last term represents the modification of the γ-ray polar diagram due to interactions; and we can show that it vanishes also. This is because each term in $\Gamma' \mathfrak{H}_1 \mathfrak{H}_0$ is of one of two kinds, either:

(*a*) it is a term like $\Gamma' \mathfrak{H}_0 P_{tj\alpha\beta} S_{t\alpha} S_{j\beta}$, which has as a factor an $S_{j\beta}$ ($j \neq 0$) to degree one, and hence has zero Spur, or

(*b*) it is a term like $\Gamma' \mathfrak{H}_0 D_{q\theta\phi} S_{q\theta} S_{q\phi}$ ($q \neq 0$), which contains a set of factors $D_{q\theta\phi} S_{q\theta} S_{q\phi}$ with zero Spur.

Hence interactions do not alter the polar diagram of γ-rays as far as the term of second degree in $1/kT$.

(iv) *The Term of Degree Three*

The term of degree three can be considered in exactly the same manner as the term of degree two. First of all, a number of terms in the expansion vanish because they have as factors $\mathrm{Spur}(\Gamma')$, $\mathrm{Spur}(\Gamma' \mathfrak{H})$, or $\mathrm{Spur}(\mathfrak{H})$, all of which are zero. The remaining terms can be split up as before, putting $\mathfrak{H} = \mathfrak{H}_0 + \mathfrak{H}_1$ into:

(*a*) a term involving Γ' and $\mathfrak{H}_0$ only (the term which would be there in the absence of interactions),

(*b*) a term involving Γ' and $\mathfrak{H}_1$ only, which vanishes identically as in the $(1/kT)^2$ case,

(*c*) an interaction term.

The interaction term is

$$-\frac{1}{6k^3T^3}\frac{\mathrm{Spur}(\Gamma'\mathfrak{H}_0\mathfrak{H}_1\mathfrak{H}_0)+2\mathrm{Spur}(\Gamma'\mathfrak{H}_0{}^2\mathfrak{H}_1)+3\mathrm{Spur}(\Gamma'\mathfrak{H}_0\mathfrak{H}_1{}^2)}{\mathrm{Spur}(1)}.$$

This term also vanishes. The parts of it which involve $\mathfrak{H}_1$ to the first degree as a factor vanish for the same reasons that such terms did in the $(1/kT)^2$ case. That those parts which involve $\mathfrak{H}_0$ as a factor to the first degree only vanish can be seen by dividing them again into two categories:

(*a*) terms like $T = D_{0\lambda\mu} S_{0\lambda} S_{0\mu} P_{0j\alpha\beta} S_{0\alpha} S_{j\beta} P_{0j\gamma\delta} S_{0\gamma} S_{j\delta}$ which do not have zero Spur but which contain no nuclear variable for ion 0; since they operate in a different vector space from Γ',

$$\frac{\mathrm{Spur}(\Gamma' T)}{\mathrm{Spur}(1)} = \frac{\mathrm{Spur}(\Gamma')}{\mathrm{Spur}(1)} \frac{\mathrm{Spur}(T)}{\mathrm{Spur}(1)} = 0,$$

and hence these terms vanish from the interaction term;

(*b*) terms which contain nuclear variables of ion 0; from (2.4) they contain $I_{0\sigma}$ to degree one only (the Q_0's are zero), and since both $\mathrm{Spur}(I_{0\sigma})$ and $\mathrm{Spur}(\Gamma' I_{0\sigma})$ are zero, these terms vanish also.

Thus interactions do not alter the polar diagram of the γ-rays as far as the term in $(1/kT)^3$.

(v) *The Term of Degree Four*

This is the first term which gives a non-vanishing contribution due to interactions. Proceeding as in the previous two cases, we find the interaction term to be

$$\frac{\mathrm{Spur}\{\Gamma'(\sum \mathfrak{H}_0{}^3\mathfrak{H}_1+\sum \mathfrak{H}_0{}^2\mathfrak{H}_1{}^2+\sum \mathfrak{H}_0\mathfrak{H}_1{}^3)\}}{24\,\mathrm{Spur}(1)}$$
$$-\frac{\mathrm{Spur}(\Gamma'\mathfrak{H}_0{}^2)\mathrm{Spur}(\mathfrak{H}_1{}^2)+\mathrm{Spur}(\Gamma'\mathfrak{H}_1{}^2)\mathrm{Spur}(\mathfrak{H}_0{}^2)}{4\{\mathrm{Spur}(1)\}^2}$$
$$-\frac{\begin{bmatrix}\mathrm{Spur}\{\Gamma'(\mathfrak{H}_0\mathfrak{H}_1+\mathfrak{H}_1\mathfrak{H}_0)\}\mathrm{Spur}(\mathfrak{H}_0\mathfrak{H}_1+\mathfrak{H}_1\mathfrak{H}_0)\\ +\mathrm{Spur}\{\Gamma'(\mathfrak{H}_0{}^2+\mathfrak{H}_1{}^2)\}\mathrm{Spur}(\mathfrak{H}_0\mathfrak{H}_1+\mathfrak{H}_1\mathfrak{H}_0)\\ +\mathrm{Spur}\{\Gamma'(\mathfrak{H}_0\mathfrak{H}_1+\mathfrak{H}_1\mathfrak{H}_0)\}\mathrm{Spur}(\mathfrak{H}_0{}^2+\mathfrak{H}_1{}^2)\end{bmatrix}}{4\{\mathrm{Spur}(1)\}^2}.$$

In this formula, an expression like $\sum \mathfrak{H}_0{}^3\mathfrak{H}_1$ means the sum of all possible terms obtained by permuting the factors; in this case $\mathfrak{H}_0{}^3\mathfrak{H}_1 + \mathfrak{H}_0{}^2\mathfrak{H}_1\mathfrak{H}_0 + \mathfrak{H}_0\mathfrak{H}_1\mathfrak{H}_0{}^2 + \mathfrak{H}_1\mathfrak{H}_0{}^3$. The whole of the last term vanishes, because each of its three parts has as a factor either $\mathrm{Spur}\{\Gamma'(\mathfrak{H}_0\mathfrak{H}_1-\mathfrak{H}_1\mathfrak{H}_0)\}$ or $\mathrm{Spur}(\mathfrak{H}_0\mathfrak{H}_1+\mathfrak{H}_1\mathfrak{H}_0)$ and these have been shown to vanish in the discussion of the $(1/kT)^2$ case. The terms which involve $\mathfrak{H}_1$ or $\mathfrak{H}_0$ to the first power (e.g. $\mathrm{Spur}(\Gamma'\sum \mathfrak{H}_0{}^3\mathfrak{H}_1)$) also vanish as explained in the discussion of the $(1/kT)^3$ case. The expression $\mathrm{Spur}(\Gamma'\mathfrak{H}_1{}^2)$ is also zero, because Γ' and $\mathfrak{H}_1$ operate in different vector spaces; hence $\mathrm{Spur}(\Gamma'\mathfrak{H}_1{}^2) = \mathrm{Spur}(\Gamma')\mathrm{Spur}(\mathfrak{H}_1{}^2) = 0$. Thus, the interaction term reduces to

$$(2.6)\qquad \frac{\mathrm{Spur}(\Gamma'\sum \mathfrak{H}_0{}^2\mathfrak{H}_1{}^2)}{24\,\mathrm{Spur}(1)}-\frac{\mathrm{Spur}(\Gamma'\mathfrak{H}_0{}^2)\mathrm{Spur}(\mathfrak{H}_1{}^2)}{4\{\mathrm{Spur}(1)\}^2}.$$

In this expression, only the terms in $\mathfrak{H}_1{}^2$ which involve a subscript 0 need be considered; the rest give no contribution, for if T be such a term $\mathrm{Spur}(\Gamma'\sum \mathfrak{H}_0{}^2T^2) = 6\,\mathrm{Spur}(\Gamma'\mathfrak{H}_0{}^2)\mathrm{Spur}(T^2)$ since $\Gamma'\mathfrak{H}_0{}^2$ and T operate in different vector spaces. For the same reason, they must also be quadratic in the I's. There are thus only six kinds of terms which need be considered:

They are of the form $\mathrm{Spur}(A)\mathrm{Spur}(B)$ or $\mathrm{Spur}(AB)$ where

$$A = \Gamma' F_{0\epsilon\eta}F_{0\lambda\mu}I_{0\eta}I_{0\mu}S_{0\epsilon}S_{0\lambda}$$

and

$$(a)\qquad B = P_{0j\alpha\beta}S_{0\alpha}S_{j\beta}P_{0j\gamma\delta}S_{0\gamma}S_{j\delta}$$

$$(b)\qquad \text{or}\quad P_{0j\alpha\beta}S_{0\alpha}S_{j\beta}R_{j\sigma\xi}H_{\sigma}S_{j\xi}$$

$$(c)\qquad \text{or}\quad P_{0j\alpha\beta}S_{0\alpha}S_{j\beta}D_{j\theta\rho}S_{j\theta}S_{j\phi}.$$

The values of $\mathrm{Spur}(B)$ and $\mathrm{Spur}(AB)$ are zero when B has the form given in (b) and (c) above, since the S_0's occur as a product of an odd number of factors. To evaluate the other terms, we note that

$\mathrm{Spur}(S_i{}^4) = (1/15)S(S+1)(2S+1)(3S^2+3S-1)$ and $\mathrm{Spur}(\sum S_iS_iS_jS_j) = (2/15)S(S+1)(2S+1)(3S^2+3S-1)$ $(i \neq j)$. Performing the algebra, we find eventually that the interference term of degree four in $1/kT$ is

$$(2.7)\qquad \frac{1}{12.45k^4T^4}\,S_0(S_0+1)\frac{\mathrm{Spur}(\Gamma'I_{0\eta}I_{0\mu})}{(2I_0+1)}$$
$$\times\sum_j S_j(S_j+1)[(3S_0{}^2+3S_0-1)(F_{0\epsilon\eta}F_{0\alpha\mu}P_{0j\epsilon\beta}P_{0j\alpha\beta}+F_{0\epsilon\eta}F_{0\epsilon\mu}P_{0j\epsilon\beta}P_{0j\epsilon\beta})$$
$$-(2S_0{}^2+2S_0+1)F_{0\epsilon\eta}F_{0\epsilon\mu}P_{0j\alpha\beta}P_{0j\alpha\beta}].$$

(vi) *Terms of Higher Degree*

Since the Spur of the sum of the permutations of a product of angular momentum operators is zero if the number of factors is odd, and since the Spur of $\Gamma' \times$(the permutations of an odd number of I_0's) is zero (from 2.1), we can draw a number of qualitative conclusions about the nature of the interference terms of higher degree:

(*a*) these terms are all of even degree in H,

(*b*) they must contain at least two F's, and one P; hence the lowest term which involves H is the term in H^2/T^5.

(vii) *A Case Which Can Be Treated Exactly*

If $S_0 = \frac{1}{2}$, $B = g_\perp = 0$ in the spin-Hamiltonian of the radioactive ion (equation (2.4)) we can show that the angular distribution of γ-rays is affected neither by interactions nor by an external field. Let us consider first for simplicity the case where the external field is zero—where the external field is not zero, only trivial modifications need be made to this argument. Here $\mathfrak{H}_0 = AS_zI_z$ commutes with $\mathfrak{H}_1$. The exponential $\exp\{(\mathfrak{H}_0+\mathfrak{H}_1)/kT\}$ can therefore be factorized, and the angular distribution can be written:

$$\frac{1}{4\pi} + \frac{\mathrm{Spur}\{\Gamma' \exp(-\mathfrak{H}_0/kT)\exp(-\mathfrak{H}_1/kT)\}}{\mathrm{Spur}\{\exp(-\mathfrak{H}_0/kT)\exp(-\mathfrak{H}_1/kT)\}} . \tag{2.8}$$

The vector space representing the crystal is the outer product of three spaces, the vector space of the nucleus of ion 0, the spin space of ion 0, and the rest. Denoting by Spur_N and Spur_1 the Spurs of operators in the first and third of these spaces, the second term of (2.8) can be written:

$$\frac{\left[\begin{array}{l}\mathrm{Spur}_N\{\Gamma' \exp(-AI_z/2kT)\}\mathrm{Spur}_1\{\exp(-\mathfrak{H}_1(S_{z0} = \frac{1}{2})/kT)\} \\ +\mathrm{Spur}_N\{\Gamma' \exp(AI_z/2kT)\}\mathrm{Spur}_1\{\exp(-\mathfrak{H}_1(S_{z0} = -\frac{1}{2})/kT)\}\end{array}\right]}{\left[\begin{array}{l}\mathrm{Spur}_N\{\exp(-AI_z/2kT)\}\mathrm{Spur}_1\{\exp(-\mathfrak{H}_1(S_{z0} = \frac{1}{2})/kT) \\ +\mathrm{Spur}_N\{\exp(AI_z/2kT)\}\mathrm{Spur}_1\{\exp(-\mathfrak{H}_1(S_{z0} = -\frac{1}{2})/kT)\}\end{array}\right]} .$$

Now $\exp(\pm AI_z/2kT) = \cosh(AI_z/2kT) \pm \sinh(AI_z/2kT)$.

But $\sinh(AI_z/2kT)$ is an "odd" function of I_z, hence $\mathrm{Spur}_N\{\sinh(AI_z/2kT)\} = 0$ and from the symmetry properties of Γ' (2.1), $\mathrm{Spur}_N\{\Gamma' \sinh(AI_z/2kT)\} = 0$. Thus

$$\frac{\mathrm{Spur}_N\{\Gamma' \exp(-AI_z/2kT)\}}{\mathrm{Spur}_N\{\exp(-AI_z/2kT)\}} = \frac{\mathrm{Spur}_N\{\Gamma' \exp(AI_z/2kT)\}}{\mathrm{Spur}_N\{\exp(AI_z/2kT)\}}$$

$$= \frac{\mathrm{Spur}_N\{\Gamma' \cosh(AI_z/2kT)\}}{\mathrm{Spur}_N\{\cosh(AI_z/2kT)\}} .$$

So that the angular distribution of γ-rays is independent of the factors $\mathrm{Spur}_1\{\exp(-\mathfrak{H}_1/kT)\}$ representing interactions.

This result is also obvious in the simpler picture of replacing the interactions by an equivalent "internal" magnetic field. Only the component of the field parallel to the z-axis of ion 0 can polarize this ion, and it is easily seen that the Zeeman pattern for this ion is very simple, and there is no change in angular distribution due to an applied magnetic field.

This result can be used to check the accuracy of other formulae, e.g. putting $S_0 = \frac{1}{2}$, $g_\perp = B = 0$, in (2.7) should, and does, give $0 = 0$.

3. THE EFFECT OF INTERACTIONS AT LOW TEMPERATURES

At very low temperatures, the angular distribution approaches a limiting value, and a knowledge of this limiting value is of interest, as it, along with a knowledge of the lowest orientation state of the nuclei, gives information on the decay scheme of the radioactive nucleus. The limiting polar diagram can be, and frequently is, affected by interactions. Interactions have, in general, three effects:

(i) The energy of the nuclear orientation states is changed.

(ii) The wave functions of all the states, and in particular of the lowest state, are changed.

(iii) The energy states of the radioactive nucleus are spread out into a "group", since each state of the radioactive nucleus is combined with a variety of different states of the other ions in the crystal.

We can show that the low temperature limiting form of the polar diagram of γ-rays is independent of interactions, provided an external magnetic field is applied along a direction which is a common principal axis of the F tensors and g tensors of all the radioactive ions, and the external field is large enough to produce a Paschen-Back effect (decoupling of the hyperfine coupling so that S_z and I_z are good quantum numbers) in the radioactive ions. Since the g tensor and the F tensor have the same symmetry as the immediate surroundings of the ion, they have the same principal axes.

If we take the x, y, z axes to be principal axes of the F and g tensors of ion 0, the Hamiltonian becomes:

$$\mathfrak{H} = g\beta HS_z + ZS_zI_z + XS_xI_x + YS_yI_y + (\text{interaction terms}).$$

The first two terms of this expression are diagonal, and the first term is by far the largest, by hypothesis. Because of the particular choice of axes, $XS_xI_x + YS_yI_y$ have matrix elements which connect only states of high energy (e.g. $S_z = +\frac{1}{2}$) with states of low energy (e.g. $S_z = -\frac{1}{2}$). The interaction terms do not contain the nuclear variables, and hence they do not mix the nuclear states. They are of two kinds, those which connect nuclear states with very different energies (like $XS_xI_x + YS_yI_y$ does), and those which connect nuclear states with the same energy (i.e. the same nuclear state combined with different ionic states in the crystal). These latter terms are responsible for broadening the nuclear levels into "groups". We will now proceed in the standard way of perturbation theory, first diagonalizing the submatrices with equal diagonal elements (or treating the broadening of the levels into groups).

Since the interaction terms do not contain the nuclear variables, the submatrices for each group have identical off-diagonal elements. This means that the density of states in each group is the same function of energy, i.e. all the groups have the same shape, and further the nuclear wave function

is unchanged. We see that, if two groups have the same shape, but are displaced in energy by an amount ϵ, the ratio of populations of the groups is $e^{-\epsilon/kT}$. This is true even if the groups are so wide that they overlap and cannot be resolved.

Bleaney (1951*a*) postulated a criterion for a successful nuclear orientation experiment, that the interactions should be so weak that the hyperfine structure should be resolved in paramagnetic resonance. We see that, in this case, Bleaney's criterion is, in fact, not necessary at all.

The change of energy of the nuclear levels is a second order effect, and is of little importance at the lowest temperatures, where only the lowest level is appreciably populated. The mixing of nuclear states has a much greater effect on the γ-ray polar diagram. We see that only the terms $XS_xI_x+YS_yI_y$ can mix different nuclear states. The first order change in the wave function is given by the well-known perturbation formula:

$$|m\rangle + \frac{|n\rangle\langle n|XS_xI_x+YS_yI_y|m\rangle}{E_m-E_n},$$

where $|m\rangle$ is the zero order wave function, and $|n\rangle$ is the wave function mixed in. $E_m-E_n \simeq g\beta H$. Thus the first order wave functions are of the form

$$|m\rangle + \frac{\alpha}{H}|n\rangle$$

and the polar diagram of γ-rays is

$$\left\langle m + \frac{\alpha}{H}n \middle| \Gamma \middle| m + \frac{\alpha}{H}n \right\rangle = \langle m|\Gamma|m\rangle + 2\,\mathrm{Re}\,\frac{\alpha}{H}\langle m|\Gamma|n\rangle + O\left(\frac{1}{H^2}\right).$$

The constant α can be easily evaluated in special cases; the important qualitative conclusion is that, at low temperatures and high fields, the polar diagram approaches that which it would have at infinite field with no interactions, and that the difference between the observed polar diagram and the limiting polar diagram is proportional to $1/H$. We thus have a useful rule for extrapolating the polar diagrams and anisotropics obtained at low temperatures in external magnetic fields.

4. CONCLUSION

In this work, we have examined the problem of the effect of interactions in the solid state on the γ-ray polar diagram of a radioactive nucleus oriented by Bleaney's method. The problem has been treated both in a high temperature and in a low temperature approximation. At high temperatures, the polar diagram can be expanded in a series of powers of $1/T$. The first term which shows the influence of interactions is the term in $1/T^4$. The first term which shows the effect of a magnetic field on interactions is that in H^2/T^6. Formulae are given (equation (2.7)) for the influence of interactions on the term in $1/T^4$. In general, the effect of interactions is almost impossible to estimate at arbitrary temperatures. When it is desired to obtain a value of the magnetic moment of a radioactive nucleus from measurements of γ-ray anisotropy, it seems most logical to base such an estimate on measurements of anisotropy made at relatively high temperatures, corrected for interactions.

At very low temperatures, if a magnetic field is applied along a common principal axis of the hyperfine coupling tensors and the g-tensors of all the radioactive ions, the polar diagram of γ-radiation is modified by interactions only very little if the external field is large enough. For large external fields, the difference between the polar diagram with and without interactions is inversely proportional to the external field. It is shown that Bleaney's criterion (Bleaney 1951*a*) of the size of interactions which influence the anisotropy of γ-radiation from oriented nuclei is unnecessarily stringent in this case.

In this paper, only the formulae are given for working out the effect of interactions. Applications of these formulae to the published results of nuclear orientation experiments will be presented in a forthcoming paper.

ACKNOWLEDGMENTS

This work was carried out during the tenure of a grant-in-aid from the National Research Council of Canada, to whom grateful acknowledgment is made.

APPENDIX

THE CONSTRUCTION OF A MATRIX TO REPRESENT THE γ-RAY DISTRIBUTION

In vacuum, a gauge can be found in which the electromagnetic scalar potential vanishes. The vector potential $\mathbf{A}$ then satisfies the wave equation $\nabla^2\mathbf{A} = (1/C^2)\partial^2\mathbf{A}/\partial t^2$. Observing that this is also Schrödinger's relativistic wave equation for a particle of rest mass zero, we may assume that the vector potential $\mathbf{A}$ plays the same part as Schrödinger's ψ function. It is to be noted that a uniform vector field has the same geometrical properties as the wave functions of a particle of spin 1 (Blatt and Weisskopf 1952). If $\mathbf{i}$, $\mathbf{j}$, $\mathbf{k}$ are the unit vectors along the x, y, z axes respectively, the eigenstates of the vector field for which the spin components along the z-axis are $+1$, 0, and -1 units are, respectively, $\alpha_1 = -(1/\sqrt{2})(\mathbf{i}+i\mathbf{j})$, $\alpha_0 = \mathbf{k}$, and $\alpha_{-1} = (1/\sqrt{2}) \times (\mathbf{i}-i\mathbf{j})$. Hence, the fact that a photon is described by a vector wave function implies, *ipso facto*, that it has an intrinsic spin of unity.

We therefore proceed to construct photon wave functions $\chi_L{}^M$ with total angular momentum L and z-component M, from product states of the spin wave functions (α's) with orbital wave functions (i.e. normalized spherical harmonics $Y_l{}^m(\theta, \phi)$). One such wave function is

$$\chi_L{}^M = \sum_{m=-1}^{+1} C^{LL1}_{M(M-m)m} Y_L{}^{M-m}(\theta,\phi)\alpha_m .$$

Here $C^{LJj}_{M(M-m)m}$ is a Wigner (or Clebsch–Gordan) vector addition coefficient, also denoted in the literature by the symbol $(J, j, M-m, m \mid J, j, L, M)$. Other possible expressions for such a photon wave function are

$$\chi_L{}'^M = \sum_{m=-1}^{+1} C^{L(L+1)1}_{M(M-m)m}\ Y^{M-m}_{L+1}(\theta,\phi)\alpha_m$$

and

$$\chi_L{}''^M = \sum_{m=-1}^{+1} C^{L(L-1)1}_{M(M-m)m}\ Y^{M-m}_{L-1}(\theta,\phi)\alpha_m .$$

It is further convenient to classify the photon wave functions according to parity. Now $\chi_L'^M$ and $\chi_L''^M$ have the same parity, and $\chi_L{}^M$ has the opposite parity; hence we have as possible photon wave functions $\chi_L{}^M$ and $A\chi_L'^M+B\chi_L''^M$. There is a further restriction, that an electromagnetic wave is a transverse wave; hence **A** is perpendicular to **r**, the radius vector from the origin. This relation is satisfied identically by $\chi_L{}^M$ but not by $\chi_L'^M$ or by $\chi_L''^M$. However, there exists a unique ratio A/B for which the wave function $A\chi_L'^M+B\chi_L''^M$ represents a transverse wave, and this combination is an acceptable photon wave function. The wave functions as so constructed are described in terms of Cartesian vector components **i**, **j**, **k**. It is, however, more convenient to use the unit vectors **r**, **θ**, **φ** appropriate to spherical polar coordinates; denoting by $|+\rangle$ and $|-\rangle$ the eigenstates $-(1/\sqrt{2})(\boldsymbol{\theta}+i\boldsymbol{\phi})$ and $(1/\sqrt{2})(\boldsymbol{\theta}-i\boldsymbol{\phi})$. When this transformation is made, it is noted that the vector **r** never appears in the formulae, because the electromagnetic wave is transverse, and that the expressions for the photon wave functions are much simpler than before. The wave function $\chi_L{}^M$ describes what is generally known as magnetic radiation of multipole order 2^L, the combination $A\chi_L'^M+B\chi_L''^M$ denotes what is generally known as electric radiation of multipole order 2^L. General formulae for these wave functions with Cartesian vector components are given by Goertzel (1946), and formulae for **E** and **B** in spherical polars are given by Tolhoek and Cox (1953); in Table I are explicit expressions for the normalized wave functions of electric and magnetic dipole and quadrupole radiations.

We can now construct a matrix for Γ using this method of Spiers (1949). Suppose, for example, that we have a nucleus of spin J, in a state with $J_z = M$. Let this nucleus decay first by a β emission in which 1 unit of angular momentum is carried off, and finally by a γ-ray of multipole order 2^L, ending in a nucleus of spin zero. Let $\psi_J{}^M$ be the wave function of the initial nucleus, $\beta_1{}^m$ a wave function of the β–neutrino pair, $\theta_L{}^\mu$ a wave function of the γ-emitting nucleus, and ϕ_0 the wave function of the final nucleus. Then the initial nuclear state $\psi_J{}^M$ can be written as

$$\psi_J{}^M = \sum_{M=m+\mu} C^{JL1}_{M\mu m}\,\theta_L{}^\mu\beta_1{}^m .$$

This equation expresses the law of conservation of angular momentum. $\theta_L{}^\mu$ can be further decomposed into ϕ_0 and a χ giving:

$$\chi_J{}^M = \sum_{M=m+\mu} C^{JL1}_{M\mu m}\beta_1{}^m\phi_0\chi_L{}^\mu .$$

The probability density function $\psi_J{}^{M*}\psi_J{}^M$ can now be written in terms of $\beta_1{}^m\phi_0\chi_L{}^\mu$, and in this expression we evaluate the inner products of all the irrelevant variables, i.e. the β's, ϕ_0, and the photon spin states. What is left is a polynomial in $\cos^2\theta$ which expresses the angular distribution of γ-radiation intensity from the pure state $\psi_J{}^M$. We note that all the cross terms vanish on account of the orthogonality of the β wave functions. This is the matrix element $\langle\psi_J{}^M|\,\Gamma|\psi_J{}^M\rangle$. By considering the probability density function u^*u of a mixed state $u = a\psi_J{}^M+b\psi_J{}^N$, and comparing this with the formal expansion

of $\langle u|\Gamma|u\rangle$, it is easily seen that the off-diagonal element $\langle\psi_J{}^M|\Gamma|\psi_J{}^N\rangle$ is precisely $\psi_J{}^{M*}\psi_J{}^N$ when the inner products of irrelevant variables have been evaluated.

TABLE I

NORMALIZED PHOTON WAVE FUNCTIONS

The phases are arranged according to the convention of Condon and Shortley

(*a*) *Dipole*

$$\chi_1{}^1 = \sqrt{\frac{3}{16\pi}}\left\{\pm\frac{1+\cos\theta}{\sqrt{2}}|+\rangle + \frac{1-\cos\theta}{\sqrt{2}}|-\rangle\right\}e^{i\phi}$$

$$\chi_1{}^0 = \sqrt{\frac{3}{16\pi}}\sin\theta\{\pm|+\rangle - |-\rangle\}$$

$$\chi_1{}^{-1} = \sqrt{\frac{3}{16\pi}}\left\{\pm\frac{1-\cos\theta}{\sqrt{2}}|+\rangle + \frac{1+\cos\theta}{\sqrt{2}}|-\rangle\right\}e^{-i\phi}$$

Upper signs denote $E1$ radiation, lower signs denote $M1$ radiation.

(*b*) *Quadrupole*

$$\chi_2{}^2 = \sqrt{\frac{5}{16\pi}}\sin\theta\left\{\mp\frac{1+\cos\theta}{\sqrt{2}}|+\rangle - \frac{1-\cos\theta}{\sqrt{2}}|-\rangle\right\}e^{2i\phi}$$

$$\chi_2{}^1 = \sqrt{\frac{5}{16\pi}}\left\{\pm\frac{2\cos^2\theta+\cos\theta-1}{\sqrt{2}}|+\rangle - \frac{2\cos^2\theta-\cos\theta-1}{\sqrt{2}}|-\rangle\right\}e^{i\phi}$$

$$\chi_2{}^0 = \sqrt{\frac{5}{16\pi}}\sqrt{3}\sin\theta\cos\theta\{\pm|+\rangle - |-\rangle\}$$

$$\chi_2{}^{-1} = \sqrt{\frac{5}{16\pi}}\left\{\mp\frac{2\cos^2\theta-\cos\theta-1}{\sqrt{2}}|+\rangle + \frac{2\cos^2\theta+\cos\theta-1}{\sqrt{2}}|-\rangle\right\}e^{-i\phi}$$

$$\chi_2{}^{-2} = \sqrt{\frac{5}{16\pi}}\sin\theta\left\{\pm\frac{1-\cos\theta}{\sqrt{2}}|+\rangle + \frac{1+\cos\theta}{\sqrt{2}}|-\rangle\right\}e^{-2i\phi}$$

Upper signs denote $E2$ radiation, lower signs denote $M2$ radiation.

This technique for finding Γ is easily extended to mixed multipole γ-transitions (and in fact to all other kinds of mixed transition). In the case where a γ-emitting nucleus $\phi_J{}^M$ decays to a nucleus $\phi_j{}^m$ emitting a coherent mixture of γ-rays of multipole order L and l, we can express the decomposition of $\theta_J{}^M$ as:

$$\theta_J{}^M = a\sum_{M=m+\mu} C^{JjL}_{Mm\mu}\,\phi_j{}^m\chi_L{}^\mu + b\sum_{M=m+\mu} C^{Jjl}_{Mm\mu}\,\phi_j{}^m\chi_l{}^\mu.$$

The ratio a/b must be real, in order that the interaction Hamiltonian responsible for the decay shall be Hermitian; $(a/b)^2$ is what is generally known as the (intensity) mixing ratio of the two multipole components. It should be noted that apart from the χ's not all the terms in the decomposition of $\theta_J{}^M$

are orthogonal; hence in the evaluation of $\theta_J{}^{M*}\theta_J{}^{M}$, an interference term (cross term) will appear. This interference term frequently is the dominant term in the angular distribution of the γ-radiation.

Finally, it is possible to discuss the polarization characteristics of the radiation using this method. In this case we observe the radiation in a fixed direction (i.e. θ and ϕ are parameters of direction) through an instrument, and we can represent the response of the instrument by means of an operator P. If the radiation can be represented by $\chi = \alpha|+\rangle+\beta|-\rangle$ the intensity of the radiation which passes the instrument is given, formally, by $\langle\chi|P|\chi\rangle$. In the representation in which $|+\rangle$ is $\begin{pmatrix}1\\0\end{pmatrix}$ and $|-\rangle$ is $\begin{pmatrix}0\\1\end{pmatrix}$, and hence χ is $\begin{pmatrix}\alpha\\\beta\end{pmatrix}$, the operators representing instruments which pass respectively only left-hand circularly polarized radiation, right-hand circularly polarized radiation, radiation polarized in the plane containing the z axis (i.e. **E** and **A** lie in this plane), and radiation plane polarized perpendicular to this are

$$\begin{pmatrix}0&0\\0&1\end{pmatrix}, \begin{pmatrix}1&0\\0&0\end{pmatrix}, \begin{pmatrix}\frac{1}{2}&-\frac{1}{2}\\-\frac{1}{2}&\frac{1}{2}\end{pmatrix}, \text{ and } \begin{pmatrix}\frac{1}{2}&\frac{1}{2}\\\frac{1}{2}&\frac{1}{2}\end{pmatrix}.$$

The operators representing more complicated instruments can be obtained using the fact that each instrument can be represented as a vector on the Poincaré sphere, and the operator representing this instrument can be expressed as $\frac{1}{2}(1+\boldsymbol{\sigma})$ where $\boldsymbol{\sigma}$ is the Pauli spin operator representing this vector on the Poincaré sphere (see, for example, Fano 1949).

REFERENCES

AMBLER, E., GRACE, M. A., HALBAN, H., KURTI, N., DURAND, H., JOHNSON, C. E., and LEMMER, H. R. 1953. Phil. Mag. **44**, 216.

BLATT, J. M. and WEISSKOPF, V. F. 1952. Theoretical nuclear physics (John Wiley & Sons, Inc., New York), p. 796.

BLEANEY, B. 1951*a*. Proc. Phys. Soc. A, **64**, 315.

——— 1951*b*. Phil. Mag. **42**, 441.

BLEANEY, B., DANIELS, J. M., GRACE, M. A., HALBAN, H., KURTI, N., ROBINSON, F. N. H. and SIMON, F. E. 1954. Proc. Roy. Soc. (London), A, **221**, 170.

COX, J. A. M. and DE GROOT, S. R. 1953. Physica, **19**, 683.

DANIELS, J. M. 1953. Proc. Phys. Soc. A, **66**, 673.

DANIELS, J. M., GRACE, M. A., and ROBINSON, F. N. H. 1951. Nature, **168**, 780.

FANO, U. 1949. J. Opt. Soc. Am. **39**, 859.

GOERTZEL, G. 1946. Phys. Rev. **70**, 897.

GRACE, M. A., JOHNSON, C. E., KURTI, N., LEMMER, H. R., and ROBINSON, F. N. H. 1954. Phil. Mag. **45**, 1192.

POUND, R. V. 1949. Phys. Rev. **76**, 1410.

SPIERS, J. A. 1949. Directional effects in radioactivity (National Research Council, Chalk River, Ontario).

STEENBERG, N. R. 1952. Proc. Phys. Soc. A, **65**, 791.

——— 1954. Phys. Rev. **93**, 678.

TOLHOEK, H. A. and COX, J. A. M. 1953. Physica, **19**, 101.

VAN VLECK, J. H. 1937. J. Chem. Phys. **5**, 320.

A NOTE ON THE PROPAGATION OF THE TRANSIENT GROUND WAVE[1]

JAMES R. WAIT

It is the purpose of this note to present some calculations for the waveforms of the ground-wave field radiated from a transient electromagnetic source on the surface of the earth. The variations of the source dipole moment are taken to be ramp, step, and impulse functions, in turn. This illustrates in a graphic way the influence of the source on the radiated waveform.

For harmonic excitation the vertical electric field can be written

$$E(\omega)e^{i\omega t} = \frac{i\mu\omega P(\omega)}{2\pi D}\left[1 - \frac{ic}{\omega D} - \frac{c^2}{\omega^2 D^2}\right]e^{-i\omega D/c}\, W(\omega)e^{i\omega t}, \tag{1}$$

where $P(\omega) = \int_0^\infty p(t)e^{-i\omega t}dt$ is the spectrum of the source moment $p(t)$, D is the distance from the source to the observer on the surface of the earth, $\mu = 4\pi\times10^{-7}$, $c = 3\times10^8$, and W is a function which accounts for the effects of diffraction and finite ground conductivity. Using the Van der Pol–Bremmer theory (Bremmer 1949), it is not difficult to show that

$$W(\omega) \cong (2\pi X)^{\frac{1}{2}}e^{-i\pi/4}\sum_{s=0}^{\infty}\frac{e^{-i\tau_s X}}{2\tau_s - 1/\delta^2}, \tag{2}$$

where $X = (\omega a/c)^{\frac{1}{2}}D/a$, a is the radius of the earth, δ is a function of the ground conductivity, and τ_s are roots of a complicated transcendental equation. Methods of computing τ_s are given by Bremmer. It can thus be assumed that $W(\omega)$ and, consequently, $E(\omega)$ are known functions of ω. Therefore, the transient field response $e(t)$ is obtained by the Fourier transformation

$$e(t) = \frac{1}{2\pi}\int_{-\infty}^{+\infty}E(\omega)e^{i\omega t}d\omega. \tag{3}$$

If the source was a ramp function,

$$\begin{aligned} p(t) &= P_1(t/t_0) && \text{for } t > 0, \\ &= 0 && \text{for } t < 0, \end{aligned}$$

then

$$P(\omega) = P_1(1/i\omega)^2/t_0.$$

If the ground was flat and perfectly conducting, $W(\omega) = 1$, and consequently the response is given by

$$e_1(t) = \frac{P_1\mu_0}{2\pi D t_0}A_1(t'), \tag{4}$$

[1]Presented at V.L.F. Symposium, Boulder, Colorado, Jan. 23–25, 1957.

where $t' = t - D/c$

and $A_1(t') = 1+(c/D)t'+(c/D)^2(t')^2/2 \quad$ for $t' > 0$,

$= 0 \quad$ for $t' < 0$.

That is, for times $t' \ll D/c$, the response is characterized by a step function. The terms proportional to t' and $(t')^2$ are related to the induction and static field respectively. The principal effect of diffraction is to round off the leading edge of the step. The induction and static fields are only slightly affected by diffraction. For this reason it is convenient to express the response for the "ramp" source on a spherical earth as follows

$$e(t) = \frac{P_0\mu_0}{2\pi D t_0} A_1(t')\, B_1(t'). \tag{5}$$

$B_1(t')$ is now the waveform of the radiation field, which, on a flat ideally conducting earth, would be a step. It can be seen that for $t' > 0$

$$B_1(t') = \frac{1}{2\pi}\int_{-\infty}^{+\infty} \frac{W(\omega)}{i\omega} e^{i\omega t'}\, d\omega \tag{6a}$$

$$= 1 - \frac{1}{2\pi}\int_{-\infty}^{+\infty} \frac{1-W(\omega)}{i\omega} e^{i\omega t'}\, d\omega \tag{6b}$$

$$= 1 + \frac{2}{\pi}\int_{0}^{\infty} \frac{\operatorname{Im} W(\omega)}{\omega} \cos \omega t'\, d\omega, \tag{6c}$$

where Im signifies that the imaginary part is to be taken.

The latter integral has been evaluated by numerical means for a distance D of 1506 miles over sea water ($\sigma \cong 4$ mhos/meter) using available data (Wait and Howe 1956) for $W(\omega)$ as a function of ω. $B_1(t')$ is plotted in Fig. 1

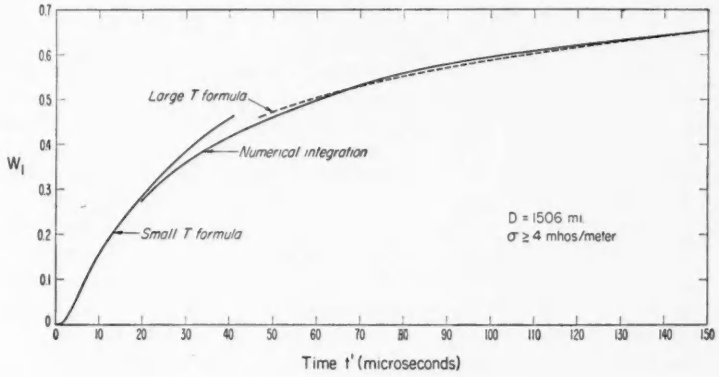

FIG. 1. Ground wave response for a ramp current source.

as a function of t' in milliseconds. For this range of t, the curves would be indistinguishable from those for a perfectly conducting earth ($\sigma \cong \infty$). This suggests that an analytical approach might be used as a check. In this case, since $\delta \cong \infty$,

$$W(\omega) \cong W^{\infty}(\omega) = (2\pi X)^{\frac{1}{2}} e^{-i\pi/4} \sum_{s=0}^{\infty} \frac{e^{-iX\tau_s^{\infty}}}{2\tau_s^{\infty}}, \tag{7}$$

where
$$\tau_0^{\infty} = 0.808\, e^{-i\pi/3},$$
$$\tau_1^{\infty} = 2.577\, e^{-i\pi/3},$$
$$\tau_2^{\infty} = 3.824\, e^{-i\pi/3},$$
$$\tau_4^{\infty} = 4.892\, e^{-i\pi/3},$$
$$\tau_s^{\infty} \cong \tfrac{1}{2}[3\pi(s+\tfrac{1}{4})]^{2/3} e^{-i\pi/3} \qquad \text{for } s \geqslant 5.$$

and $X = (\omega a/c)^{\frac{1}{2}}(D/a)$.

The response is then given by

$$B_1(t') \cong \frac{1}{2\pi} \int_{-\infty}^{+\infty} \frac{W^{\infty}(\omega)}{i\omega} e^{i\omega t}\, d\omega. \tag{8}$$

Since (Wait 1956*a*)

$$W^{\infty}(\omega) = 1 - \frac{\pi^{\frac{1}{2}}}{8}(1+i)\, g^{3/2} + \frac{7i}{120} g^3 + \frac{\pi^{\frac{1}{2}} 7(1-i)}{2048} g^{9/2} \tag{9}$$
$$\pm \text{ terms containing } g^6,\ g^{15/2}, \text{ etc.},$$

where
$$g = (\omega D/c)(\omega a/c)^{-2/3},$$

the integration can be carried to yield the asymptotic expansion valid for large t:

$$B_1(t') \sim 1 - \frac{1}{4\sqrt{2}.T^{1/2}} + \frac{7}{2048\sqrt{2}} \frac{1}{T^{3/2}} \tag{10}$$
$$\pm \text{ terms containing } T^{-5/2},\ T^{-7/2}, \text{ etc.},$$

where
$$T = t'ca^2/D^3.$$

Another approach is to evaluate the integral in equation (8) by the conventional saddle-point method (Morse and Feshbach 1953); this leads to

$$B_1(t') \sim \frac{3}{2^{3/2}} \sum_{s=0}^{\infty} \exp\left(-\frac{2}{3^{3/2}} |\tau_s^{\infty}|^{3/2} \frac{1}{T^{1/2}}\right) \Big/ |\tau_s^{\infty}|^{3/2}, \tag{11}$$

which is valid only for $T \ll 1$ since the exponent $i[-\tau_s X + \omega t] = f(\omega)$ must be large at the saddle point.

The responses $B_1(t')$ using the large T approximation (equation (11)) are shown plotted for $D = 1506$ miles in Fig. 1 along with the curve obtained by numerical integration. It is seen that the saddle-point evaluated response departs considerably from the rigorous numerical curve when T becomes comparable to unity.

The numerical results discussed above are for a "ramp" source. One particular advantage of such a model is that the radiation field is ideally a step

function. As indicated previously (Wait 1956*b*) the response so calculated can be readily extended to more complicated source waveforms. For example, in the case of a step-function current source, that is,

$$p(t) = P_2 \quad \text{for } t > 0,$$
$$= 0 \quad \text{for } t < 0,$$

the response of the radiation field is

$$e_2(t) = \frac{P_1\mu_0}{2\pi D}\left(\frac{a^2c}{D^3}\right) W_2(t'), \tag{12}$$

where

$$W_2(t') \sim \left[\frac{1}{8\sqrt{2}}\frac{1}{T^{5/2}} - \frac{21}{4096\sqrt{2}}\frac{1}{T^{5/2}} + \cdots\right] \tag{13}$$

and

$$W_2(t') \cong \frac{3}{2^{5/2}} \cdot \frac{1}{T}\sum_{s=0}^{\infty} \frac{\beta_s}{T^{1/2}} \frac{\exp(-\beta_s/T^{1/2})}{|\tau_s^{\infty}|^{4/2}} \tag{14}$$

for small T, where $\beta_s = (2/3^{3/2})|\tau_s^{\infty}|^{3/2}$.

The response for an impulse current source, or

$$p(t) = P_3\delta(t)$$

is

$$e_3(t) = \frac{P_3\mu_0}{2\pi D}\left(\frac{a^2c}{D^3}\right)^2 W_3(t'), \tag{15}$$

where

$$W_3(t') \cong -\left[\frac{3}{16\sqrt{2}.T^{5/2}} - \frac{105}{8192\sqrt{2}.T^{7/2}} + \cdots\right] \tag{16}$$

for large T, and where

$$W_3(t') = \frac{3}{2^{7/2}}\frac{1}{T^2}\sum_{s=0}^{\infty} \frac{\beta_s}{T^{1/2}}\left[\frac{\beta_s}{T^{1/2}} - 3\right]\frac{\exp(-\beta_s/T^{1/2})}{|\tau_s^{\infty}|^{3/2}} \tag{17}$$

for small T.

Using the above formulas, responses for the ramp-function, step-function, and impulse-function sources are computed and plotted in Fig. 2 as a function of the time parameter T. For convenience, a small chart is shown in Fig. 3 which relates actual time t' and the parameter T for various ranges D for an earth whose effective radius is $4/3 \times 6360$ km. While the preceding discussion has been confined to a perfectly conducting earth, the results are not modified for propagation over sea water ($\sigma \cong 4$ mhos/meter) when t is greater than about 1.0 microsecond. The influence of ground conductivity on the ramp-function responses has been studied and reported elsewhere (Wait 1956 *b*, *c*).

The computations in this paper have been carried out by William E. Briggs and Alyce M. Conda. Their assistance is appreciated. The application of the saddle-point method to calculate the small T responses was suggested by Prof. J. B. Keller of New York University (private communication).

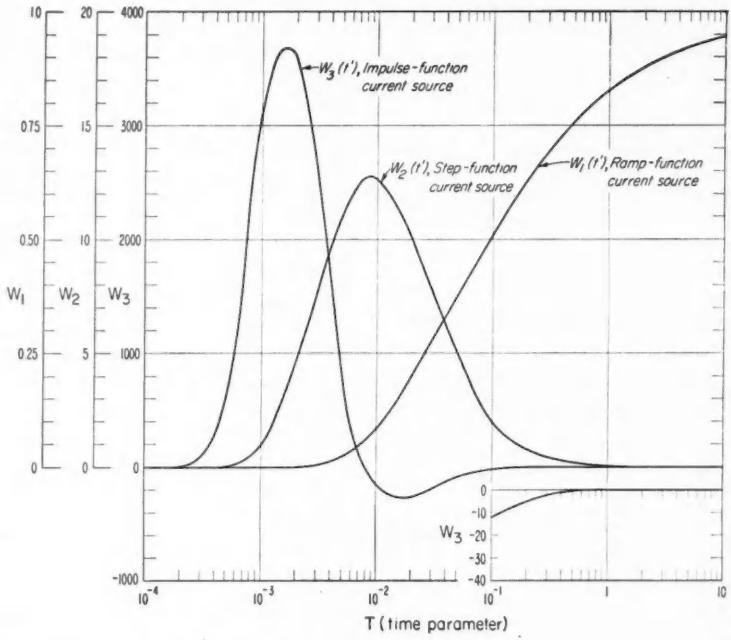

FIG. 2. Ground wave response for a transient dipole source on a spherical earth.

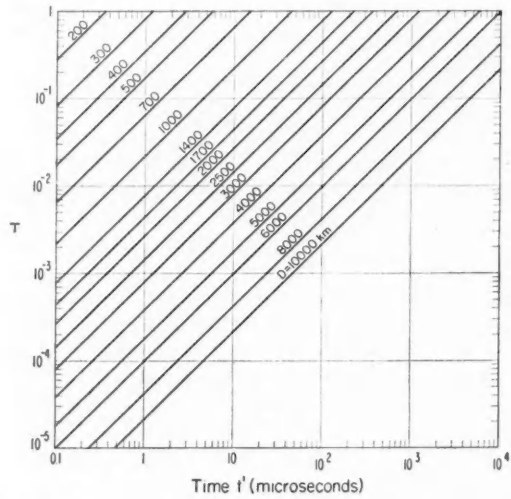

FIG. 3. The time parameter T vs. actual time t' for various distances D.

BREMMER, H. 1949. Terrestrial radio waves (Elsevier Publishing Co., Amsterdam).
MORSE, P. M. and FESHBACH, H. 1953. Methods of theoretical physics (McGraw-Hill Book Co., Inc., New York), p. 440.
WAIT, J. R. 1956*a*. Currents excited on a conducting surface of large radius of curvature, Trans. I.R.E., MTT-4, pp. 144–145.
——— 1956*b*. The transient behavior of the electromagnetic ground wave on a spherical earth, N.B.S. Report No. 3595 (Trans. I.R.E., AP-4, April 1957).
——— 1956*c*. Can. J. Phys. **34**, 27.
WAIT, J. R. and HOWE, H. H. 1956. Amplitude and phase curves for ground wave propagation in the band 200 c./s. to 500 kc./s., N.B.S. Circular No. 574.

RECEIVED JUNE 3, 1957.
NATIONAL BUREAU OF STANDARDS,
BOULDER, COLORADO.

ON THE MECHANISM OF ELECTROLYTIC RECTIFICATION

ARCHIBALD W. SMITH

The phenomenon of rectification at oxide-covered electrodes of aluminum, tantalum, niobium, and zirconium is well known but, to date, has not received a satisfactory explanation. Anderson (1943), Scholte and van Geel (1953), and Haring (1952) have proposed theories in which currents in the oxide are assumed to be electronic, and which depend on the existence of space charge barriers to explain rectification. The theory presented in this note is similar to these, but more careful account has been taken of the electronic structure of the metal and oxide. Shinohara and Hoshino (1952) have assumed that the reverse current is ionic, but have not reconciled this assumption with the relatively higher fields needed for ionic flow during formation of the oxide film. Vermilyea (1956) has suggested that rectification occurs only at "singularities" (weak spots) in the film. However, further experimental evidence is needed to establish this definitely, and it seems preferable at present to assume that the current density is more or less uniform over the surface.

To illustrate the current–voltage characteristics of anodic oxide rectifiers, a curve for the system aluminum/aluminum oxide/electrolyte/platinum is shown in Fig. 1. In obtaining this curve, a piece of aluminum foil was anodized at 200 volts for 1 hour, giving a film approximately 2.6×10^{-5} cm. thick. The electrolyte was a 5% solution of boric acid with ammonium hydroxide added to make pH $\approx$ 5.8. The current–voltage curve was taken by decreasing the reverse voltage (starting at the formation voltage), passing through zero current, and then increasing the voltage in the forward direction. Current readings were taken about 30 seconds after changing the voltage, except at low voltages, where several minutes were allowed. Reverse currents drifted slowly downward, while forward currents drifted upward, especially above 3 or 4 volts. Before plotting, the zero-current (i.e. open-circuit) voltage of the system (usually in the range ±0.5 volts) was subtracted from the applied voltage. The main variation between samples was a displacement of the straight part of the reverse curve parallel to the current axis. For instance, at 40 volts, the current varied from 5×10^{-9} to 10^{-7} amp./cm.^{2} The form of the reverse curve is similar to that found by Charlesby (1953).

It will be assumed here that at voltages below the formation voltage, the current in an anodic oxide film is electronic rather than ionic in nature. This

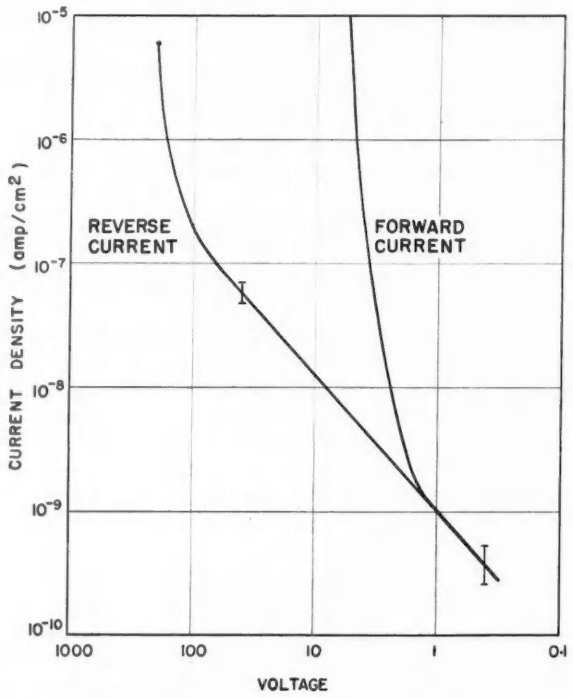

FIG. 1. Smoothed current–voltage curves for an aluminum oxide film formed to 200 volts Vertical lines indicate spread of experimental points about straight line.

assumption is almost certainly true for the reverse current (Charlesby 1953), but under some conditions the forward current may contain a small ionic component (Dekker and Urquhart 1950; Scholte and van Geel 1953). The question now arises as to whether the oxide is an insulator or a semiconductor. It has been assumed previously that the oxide must be semiconducting in order to explain the observed conduction. However, with the high fields which exist in the films even at low applied voltages, adequate conduction through the oxide is possible even if it is an insulator. As an example, consider an insulator 4×10^{-5} cm. thick, with ohmic contacts, a gap of 0.1 ev. between the equilibrium Fermi level and the conduction band, an electron mobility of 100 cm.^{2}/volt sec., and no traps. Under these conditions, Ohm's law holds up to approximately 75 volts, and if 1 volt is applied across the film, a current of 2×10^5 amp./cm.^{2} is obtained (Lampert 1956). This may be compared with the value of 10^{-9} amp./cm.^{2} obtained from the current–voltage curve of Fig. 1.

As there is no irrefutable evidence that the anodic oxides are semiconducting, and since the same oxides in bulk are insulators under most conditions, the anodic layers will be treated as insulators in this note.

Whether it is an insulator or a semiconductor, conduction through the oxide film can occur only if carriers can be injected into the valence or conduction band. In principle, carrier injection may take place at either the metal/oxide or the oxide/electrolyte interface. The experiments of Brattain and Garrett (1955) on germanium/electrolyte systems suggest that the injection of holes or electrons occurs at insulator/electrolyte interfaces during electrolytic discharge of ions. On the other hand, experiments at this Laboratory on anodic oxide films with contacts of evaporated aluminum (in place of the electrolyte) indicate that there is no appreciable conduction from the metal to the oxide for either the aluminum or the tantalum systems. The currents through the metal/oxide/metal systems in both directions were found to be very much smaller than the observed reverse currents in metal/oxide/electrolyte systems. Thus, neither the reverse nor the forward current can originate from carrier injection at the metal/oxide interface. This result can be interpreted in an elementary way by assuming that the Fermi level of the metal falls near the center of the forbidden band of the oxide, as illustrated in Fig. 2. If the width of the forbidden band is greater than about 3 ev., the density of electrons and holes injected by the metal is not sufficient

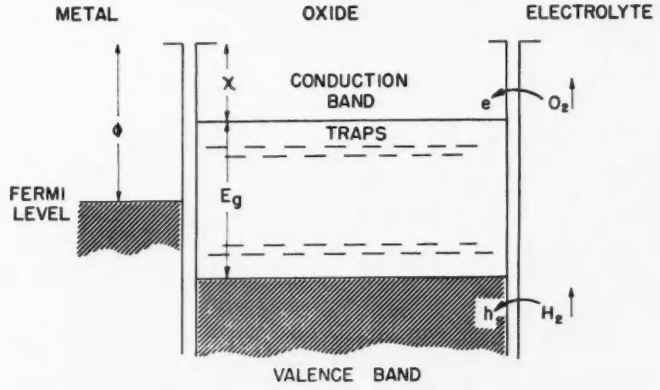

FIG. 2. The energy levels of an oxide film in contact with a metal and an electrolyte. The injection of electrons (e) and holes (h) is shown at the oxide/electrolyte interface.

to account for the observed reverse currents. It is estimated that the width of the forbidden band, E_g, is 3.5 ev. and 6.5 ev. and the work function, ϕ, 4.1 ev. and 3.8 ev., respectively, for the tantalum and aluminum systems, with the depth of the conduction band, χ, about 2 ev. in both cases.

The mechanism of rectification will now be discussed on the basis of the above remarks. The situation is illustrated in Fig. 2. No attempt has been made in this figure to show the effect of space charge in the film. When the

metal/oxide electrode is anodic, hydroxyl ions (OH^-) at the oxide/electrolyte interface inject electrons into the conduction band and gaseous oxygen is evolved. These electrons will be moved through the oxide to the metal by the field in the oxide, and constitute the reverse current. The high barrier at the metal/oxide interface prevents holes from flowing out of the metal and taking part in the electrolytic process. When the metal/oxide electrode is cathodic, hydrogen ions (H_3O^+) at the oxide/electrolyte interface inject holes into the valence band, giving rise to the forward current. The current can be controlled either in the body of the oxide or at its surface. It has already been noted above that if carriers can freely enter an insulating film, relatively large currents can be passed. This suggests that the current is mainly controlled at the oxide/electrolyte interface, with the body properties of the oxide playing only a secondary role. To obtain the observed direction of rectification, the rate of evolution of oxygen by a reaction involving electron transfer to the conduction band must be much smaller than that of hydrogen by hole transfer to the valence band. The postulation of a slow reaction with anions at the conduction band has been found necessary previously to explain rectification at germanium/electrolyte surfaces (Brattain and Garrett 1955).

If this mechanism is correct, the relation between current and voltage for the oxide film should be given by the theory of overvoltage at electrodes (Bockris 1951). The net current flowing through an electrode is given by the difference of the currents flowing in each direction across the electrode/electrolyte, namely,

$$i = \vec{i} - \overleftarrow{i} = Ae^{-U/kT} \sinh(e/kT)\alpha(V - V_0),$$

where A is the collision factor and U the activation energy for the reaction, α is the fraction of the applied voltage V which affects the reaction, V_0 depends on properties of the surface and solution, e is the ionic charge, k the Boltzmann constant, and T the absolute temperature. There are two limiting cases: (1) If $\alpha(V - V_0) \gg kT/e$, then $\vec{i} \gg \overleftarrow{i}$ and $V = a - (kT/\alpha e)\ln i$, where a is independent of i. This is the Tafel equation which is obeyed when hydrogen is liberated at a metallic cathode (Bockris 1951). It gives an approximate fit to the part of the forward curve above 2 volts in Fig. 1. The part below 2 volts is probably determined by the change-over from the anodic to the cathodic process. (2) If $\alpha(V - V_0) \ll kT/e$ then $\vec{i} \approx \overleftarrow{i}$ and $i = cV$. This fits the linear part of the reverse curve in Fig. 1, which has a slope only slightly greater than 1 on the log–log plot. The curvature above 80 volts may be due to the attainment of the condition $\alpha(V - V_0) \approx kT/e$ or to the onset of ionic conduction in the film, or both.

The reverse current is probably determined by the discharge of an ion present as an impurity, rather than by the hydroxyl ion (Charlesby 1953; Haring 1952). The addition of chloride ions, for example, increases the reverse current in aluminum oxide films (Muriset 1952), and the current–voltage relation during the liberation of chlorine is observed to be linear at low current

densities (Chang and Wick 1935). Thus the data of Fig. 1 are not inconsistent with the proposed mechanism, but a more detailed comparison with experimental results would be necessary to establish its validity.

Electroluminescence in aluminum oxide films can be explained within the same framework as rectification. Certain observations on electroluminescence are well established (Anderson 1943) and may be summarized as follows: When the metal/oxide electrode is anodic, a continuous glow is observed. This glow is a function of the cell current and the film thickness. If the electrode is switched suddenly from anode to cathode, a flash is observed, but there is no continuous cathodic glow. If the polarity is again reversed, a flash is observed, followed by the steady-state anodic glow. Manganese appears to act as an activator.

The anodic glow probably arises from collisions of electrons in the conduction band with luminescence activator centers, which are excited or ionized (cf. Destriau and Ivey 1955). The high fields usually encountered in anodic oxide films should certainly be adequate to produce visible radiation by this process. The absence of cathodic glow is explained as follows: When the metal/oxide electrode is cathodic, conduction is by holes. The optical electrons of the activator centers and electrons in the conduction band and in traps will be captured by holes, or removed at the oxide/electrolyte interface. Once all such electrons have been removed, there will be no further excitation of the spectral band in question.

In conclusion, the author wishes to thank Dr. J. H. Simpson for valuable discussions of the problem.

ANDERSON, S. 1943. J. Appl. Phys. **14**, 601.
BOCKRIS, J. O'M. 1951. Overpotential, *in* Electrical phenomena at interfaces, *edited by* J. A. V. Butler (Methuen & Co., London).
BRATTAIN, W. H. and GARRETT, C. G. B. 1955. Bell System Tech. J. **34**, 129.
CHANG, F. T. and WICK, H. 1935. Z. physik. Chem. **172**, 448.
CHARLESBY, A. 1953. Proc. Phys. Soc. B, **66**, 533.
DEKKER, A. J. and URQUHART, H. M. A. 1950. J. Appl. Phys. **21**, 708.
DESTRIAU, G. and IVEY, H. F. 1955. Proc. I.R.E. **43**, 1911.
HARING, H. E. 1952. J. Electrochem. Soc. **99**, 30.
LAMPERT, M. A. 1956. Phys. Rev. **103**, 1648.
MURISET, G. 1952. J. Electrochem. Soc. **99**, 285.
SCHOLTE, J. W. A. and VAN GEEL, W. CH. 1953. Phillips Research Repts. **8**, 47.
SHINOHARA, S. and HOSHINO, R. 1952. J. Fac. Sci. Hokkaido Univ. Ser. II, **4**, No. 2.
VERMILYEA, D. A. 1956. J. Appl. Phys. **27**, 963.

RECEIVED FEBRUARY 20, 1957.
ELECTRONICS LABORATORY,
DEFENCE RESEARCH BOARD,
OTTAWA, ONTARIO.

Under this heading brief reports of important discoveries in physics may be published. These reports should not exceed 600 words and, for any issue, should be submitted not later than six weeks previous to the first day of the month of issue. No proof will be sent to the authors.

Determination of an Absolute Pair Production Cross Section by Relative Measurements

Using a method which involves only relative measurements we have determined an absolute cross section for the pair production process in lead at 1.12 Mev. The principal advantage of this method over an earlier one (Standil and Moore 1956) is that experimental errors are reduced by about a factor of four.

The experimental arrangement is shown in Fig. 1. Gamma rays from the Zn^{65} source fall on a target which consists of a thin lead disk surrounded by $\sim$1 mm. of graphite (T). The graphite thickness is such that all positrons produced in the lead must stop in the target. The two single-channel scintillation spectrometers with gates set on the annihilation peaks then detect, in coincidence, the oppositely directed annihilation quanta.

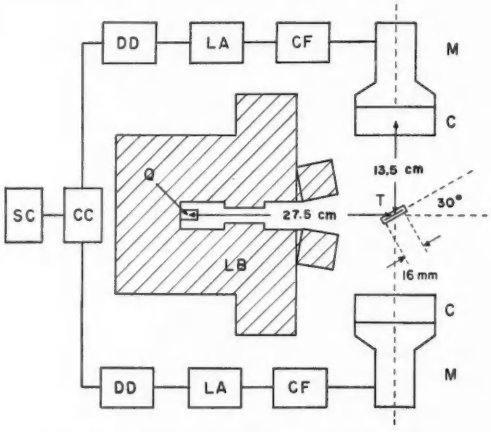

FIG. 1. The experimental arrangement (not to scale).

T	target	CF	cathode follower
LB	lead	LA	linear amplifier
Q	Zn^{65} source ($\sim$27 mc.)	DD	differential discriminator
M	photomultiplier (Dumont 6364)	CC	coincidence circuit (resolving time 0.35 μsec.)
C	sodium iodide crystal (3.5 in. diameter by 2.0 in.)	SC	scaler

If we let $N_{12}{}^{T}$ be the observed coincidence counting rate, corrected for the primary beam and annihilation quanta absorption in the target, coincidences due to cosmic radiation, pair production in graphite, and accidentals, then we have

$$N_{12}{}^{T} = \sigma N \epsilon Q / 4\pi r^2, \tag{1}$$

where σ = pair production cross section per atom of lead,
N = number of lead atoms in the target,
ϵ = an over-all efficiency factor for the counting system,
Q = number of 1.12 Mev. gammas emitted per second from the Zn^{65} source,
r = Zn^{65} source-to-target distance.

If now the Zn^{65} source and target are removed and a positron emitter (actually $\sim$1/10 μc. Na^{22} source embedded in sufficient lucite to stop all positrons) is placed in the target position,

the observed coincidence rate, corrected for annihilation quanta absorption in the lucite, coincidences due to cosmic rays, and accidentals, will be given by

$$N_{12}{}^{S} = S\epsilon, \tag{2}$$

where S = number of positrons annihilated per second.

Combining (1) and (2) we have

$$\sigma = \left(\frac{4\pi r^2}{N_{12}{}^{S}}\right)\left(\frac{N_{12}{}^{T}}{N}\right)\left(\frac{S}{Q}\right). \tag{3}$$

The first term of expression (3), $4\pi r^2/N_{12}{}^{S}$, was readily measured with a probable error of 1%.

In Fig. 2 we have plotted (curve I) the net coincidence counting rate (background due to cosmic rays, pair production in graphite, and accidentals subtracted) vs. N, the number of lead atoms in the target. Curve II represents these data corrected for the absorption of the primary beam in the target and also for absorption in the target of the annihilation quanta. The resulting linearity of curve II serves as a check on the corrections and its slope gives us $N_{12}{}^{T}/N$, the second term of expression (3), with a probable error of 1%.

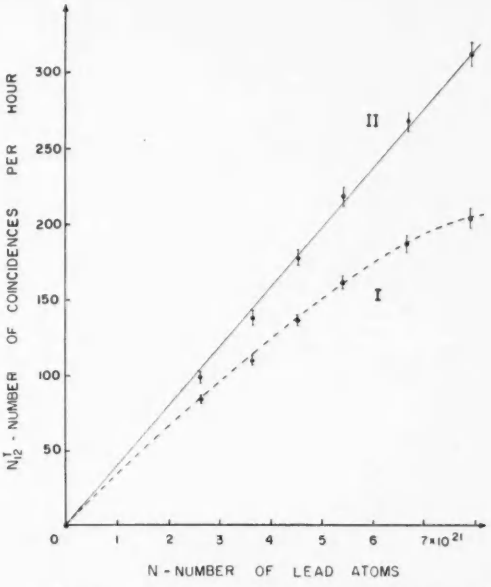

FIG. 2. Coincidence counting rate vs. number of lead atoms in target. Curve I—observed, curve II—corrected.

The term S/Q can be obtained by comparing the intensities of two gamma emitters of slightly differing energies. This is so because the decay of Na^{22} takes place essentially through positron emission and K-capture to an excited state of Ne^{22} followed by a gamma ray of 1.28 Mev. (Hollander, Perlman, and Seaborg 1953). The percentage of the decays by K-capture is reported to be 9.9±0.6% (Sherr and Miller 1954) and 10.9±1% (Allen, Burcham, Chackett, Munday, and Reasbeck 1955). If we take 10.4%, a mean of these values for K-capture, then

$$\frac{S}{Q} = 0.896\left(\frac{\text{intensity of the 1.28 Mev. gamma radiation from } Na^{22}}{\text{intensity of the 1.12 Mev. gamma radiation from } Zn^{65}}\right).$$

The ratio of intensities of these gamma sources was determined in a separate experiment using a single scintillation spectrometer calibrated as to photopeak efficiency vs. energy with the aid of similar data published by Lazar, Davis, and Bell (1956). The error in this determination is estimated to be 5% and is this large because of the difficulty of comparing a relatively strong source with a very weak one.

Our value for the pair production cross section at 1.12 Mev. in lead, after taking into account the very small effects of one-quantum and three-quanta annihilations (Jaeger and Hulme 1936; Rich 1951) and also differences in finite sizes of the target and positron emitter assembly, is 13.8 ± 1 millibarns. This is 2.4 ± 0.2 times greater than the value predicted by the Bethe–Heitler theory (based on the Born approximation, which is not valid in this case) and also greater than a value reported by Jenkins (1956), who found the cross section to be 1.8 ± 0.2 times that predicted by the Bethe–Heitler theory. Exact calculations at this energy have not been made.

ALLEN, R. A., BURCHAM, W. E., CHACKETT, K. F., MUNDAY, G. L., and REASBECK, P. 1955. Proc. Phys. Soc. A, **68**, 681.
HOLLANDER, J. M., PERLMAN, L., and SEABORG, G. T. 1953. Revs. Mod. Phys. **25**, 469.
JAEGER, J. C. and HULME, H. R. 1936. Proc. Cambridge Phil. Soc. **32**, 158.
JENKINS, T. 1956. Bull. Am. Phys. Soc. **1**, 167.
LAZAR, N. H., DAVIS, R. C., and BELL, P. R. 1956. Nucleonics, **14**(4), 52.
RICH, J. A. 1951. Phys. Rev. **81**, 140.
SHERR, R. and MILLER, R. H. 1954. Phys. Rev. **93**, 1076.
STANDIL, S. and MOORE, R. D. 1956. Can. J. Phys. **34**, 1126.

RECEIVED MAY 27, 1957.
PHYSICS DEPARTMENT,
UNIVERSITY OF MANITOBA,
WINNIPEG, MAN.

V. SHKOLNIK*
S. STANDIL

*On leave from the University of Belgrade, Yugoslavia.

CANADIAN JOURNAL OF PHYSICS

Notes to Contributors

Manuscripts

(i) **General.** Manuscripts, in English or French, should be typewritten, double spaced, on paper 8½×11 in. **The original and one copy are to be submitted.** Tables and captions for the figures should be placed at the end of the manuscript. Every sheet of the manuscript should be numbered.

Style, arrangement, spelling, and abbreviations should conform to the usage of this journal. Names of all simple compounds, rather than their formulas, should be used in the text. Greek letters or unusual signs should be written plainly or explained by marginal notes. Superscripts and subscripts must be legible and carefully placed.

Manuscripts and illustrations should be carefully checked before they are submitted. Authors will be charged for unnecessary deviations from the usual format and for changes made in the proof that are considered excessive or unnecessary.

(ii) **Abstract.** An abstract of not more than about 200 words, indicating the scope of the work and the principal findings, is required, except in Notes.

(iii) **References.** References should be listed **alphabetically by authors' names,** unnumbered, and typed after the text. The form of the citations should be that used in current issues of this journal; in references to papers in periodicals, titles should not be given and only initial page numbers are required. The names of periodicals should be abbreviated in the form given in the most recent *List of Periodicals Abstracted by Chemical Abstracts.* All citations should be checked with the original articles and each one referred to in the text by the authors' names and the year.

(iv) **Tables.** Tables should be numbered in roman numerals and each table referred to in the text. Titles should always be given but should be brief; column headings should be brief and descriptive matter in the tables confined to a minimum. Vertical rules should be used only when they are essential. Numerous small tables should be avoided.

Illustrations

(i) **General.** All figures (including each figure of the plates) should be numbered consecutively from 1 up, in arabic numerals, and each figure referred to in the text. The author's name, title of the paper, and figure number should be written in the lower left corner of the sheets on which the illustrations appear. Captions should not be written on the illustrations (see Manuscripts (i)).

(ii) **Line Drawings.** Drawings should be carefully made with India ink on white drawing paper, blue tracing linen, or co-ordinate paper ruled in blue only; any co-ordinate lines that are to appear in the reproduction should be ruled in black ink. Paper ruled in green, yellow, or red should not be used unless it is desired to have all the co-ordinate lines show. All lines should be of sufficient thickness to reproduce well. Decimal points, periods, and stippled dots should be solid black circles large enough to be reduced if necessary. Letters and numerals should be neatly made, preferably with a stencil (**do NOT use typewriting**) and be of such size that the smallest lettering will be not less than 1 mm. high when reproduced in a cut 3 in. wide.

Many drawings are made too large; originals should not be more than 2 or 3 times the size of the desired reproduction. In large drawings or groups of drawings the ratio of height to width should conform to that of a journal page but the height should be adjusted to make allowance for the caption.

The original drawings and one set of clear copies (e.g. small photographs) are to be submitted.

(iii) **Photographs.** Prints should be made on glossy paper, with strong contrasts. They should be trimmed so that essential features only are shown and mounted carefully, with rubber cement, on white cardboard with no space or only a **very** small space (less than 1 mm.) between them. In mounting, full use of the space available should be made (to reduce the number of cuts required) and the ratio of height to width should correspond to that of a journal page (4½×7½ in.); however, allowance must be made for the captions. Photographs or groups of photographs should not be more than 2 or 3 times the size of the desired reproduction.

Photographs are to be submitted in duplicate; if they are to be reproduced in groups one set should be mounted, the duplicate set unmounted.

Reprints

A total of 50 reprints of each paper, without covers, are supplied free. Additional reprints, with or without covers, may be purchased.

Charges for reprints are based on the number of printed pages, which may be calculated approximately by multiplying by 0.6 the number of manuscript pages (double-spaced typewritten sheets, 8½×11 in.) and including the space occupied by illustrations. An additional charge is made for illustrations that appear as coated inserts. The cost per page is given on the reprint requisition which accompanies the galley.

Any reprints required in addition to those requested on the author's reprint requisition form must be ordered officially as soon as the paper has been accepted for publication.

Contents

Printed in Canada *by* University of Toronto Press